

# Laser processing of metallic surfaces for controlled micro-texturing and metallic bonding

By

MUHANNAD YASSEEN AHMED OBEIDI

(B.Eng, M.Sc.)

A thesis submitted for the degree of  
Doctor of Philosophy

School of Mechanical and Manufacturing Engineering  
Faculty of Engineering and Computing  
Dublin City University

January 2018

Supervisor

Prof. Dermot Brabazon

## **Declaration**

---

I hereby certify that this material, which I now submit for assessment on the programme of study leading to the award of Doctor of Philosophy is entirely my own work, and that I have exercised reasonable care to ensure that the work is original, and does not to the best of my knowledge breach any law of copyright, and has not been taken from the work of others save and to the extent that such work has been cited and acknowledged within the text of my work.

MUHANNAD AHMED OBEIDI

ID No.:12212207

January, 2018

## Preface

---

This thesis describes original work which has not previously been submitted for a degree in Dublin City University or at any other University. The investigations were carried out in the School of Mechanical and Manufacturing Engineering, Dublin City University, during the period March 2015 to November 2017, under the supervision of Dr Dermot Brabazon. This work has been disseminated through the following publications

### Journal Articles:

- M.A. Obeidi, E. McCarthy, D. Brabazon, Methodology of laser processing for precise control of surface micro-topology, *Surf. Coatings Technol.* 307 (2016) 702–712.
- M. Ahmed Obeidi, E. McCarthy, D. Brabazon, Laser surface processing with controlled nitrogen-argon concentration levels for regulated surface life time, *Optics and Lasers in Engineering* 102 (2018) 154–160.
- M. Ahmed Obeidi, E. McCarthy, L. Kailas, D. Brabazon, Laser surface texturing of stainless steel 316L cylindrical pins for interference fit applications, *Journal of Materials Processing Tech.* 252 (2018) 58–68.
- M. Ahmed Obeidi, E. McCarthy, S.I. Ubani, I. Ul Ahad, D. Brabazon, Effect of surface roughness on CO<sub>2</sub> laser absorption by 316L stainless steel and aluminium, submitted to *Optics and Lasers in Engineering* on Nov. 8, 2017.

### Conference papers:

- M. Ahmed Obeidi, E. McCarthy, D. Brabazon, Laser Surface Texturing for High Control of Interference Fit Joint Load Bearing, 20th International Esaform Conference on Material Forming, DCU, Ireland, April 27th-29th, 2017.
- Muhannad Obeidi, Éanna McCarthy, and Dermot Brabazon, A Review of Semi-Solid Aluminium-Steel Joining Processes. 19th International Esaform Conference on Material Forming, Nantes, France, April 27th-29th, 2016, AIP Conference Proceedings Volume 1769, Article Number 030005 (2016).

Conference poster:

- M. Ahmed Obeidi, E. McCarthy, D. Brabazon, Laser Processing of Metallic Surfaces for Equisitely Controlled Micro-texture and Metallic Joint Bond Strength. 19<sup>th</sup> Sir Bernard Crossland Symposium and Postgraduate Workshop. Queen's University Belfast, Northern Ireland, United Kingdom, April 27-28<sup>th</sup>, 2016.
- M. Ahmed Obeidi, E. McCarthy, D. Brabazon, Laser surface texture of stainless steel 316L cylindrical pins for the interference-fit applications. 18th Sir Bernard Crossland Symposium and Postgraduate Workshop. University of Limerick, Ireland, April 29-30<sup>th</sup>, 2015.



## **Author's Contribution**

---

All the work in this thesis was carried out by the researcher under the supervision of Prof Dermot Brabazon and at the faculty of mechanical and manufacturing engineering at Dublin City University(DCU) and at the Advanced Processing Technology Research Centre (APT) at (DCU). The ideas, experimental design, experimental work and the collection and analysis of the data were my responsibility under the supervisor's confirmation and approval. The work in this thesis was also presented in three peer-reviewed journal papers, two conference papers and two conference posters. The inclusion of the co-authors reflects the collaborative work between the researchers. The author's contribution can be explained in the following table:

Publication title	Publication type	Researcher's contribution
Laser processing of metallic surfaces for controlled micro-texturing and metallic bonding.	PhD thesis	First author, initiation, key ideas, finding literature, experimental work and experiments design, collecting and analyzing data, manuscript development and writing up.
Methodology of laser processing for precise control of surface micro-topology.	Journal paper	First author, initiation, key ideas, theoretical calculations, experimental design and work, finding the correlations between input parameters and output results, manuscript and writing up.
Laser surface nitriding with various gas compositions for controlled surface life time.	Journal paper	First author, initiation, key ideas, manuscript and writing up.
Laser surface texturing of stainless steel 316L cylindrical pins for interference fit applications.	Journal paper	First author, manuscript and writing up.

Laser Surface Texturing for High Control of Interference Fit Joint Load Bearing	Conference paper	First author, manuscript and writing up.
A Review of Semi-Solid Aluminium-Steel Joining Processes.	Conference paper	First author, manuscript development and writing up.
Laser Processing of Metallic Surfaces for Equisitely Controlled Micro-texture and Metallic Joint Bond Strength.	Conference poster	First author, initiation, key ideas, manuscript development, writing up and presentation.
Laser surface texture of stainless steel 316L cylindrical pins for the interference-fit applications.	Conference poster	First author, initiation, key ideas, manuscript development, writing up and presentation.

Muhannad Ahmed Obeidi ..... Date:.....

Prof. Dermot Brabazon ..... Date.....

Dr. Eanna McCarthy ..... Date.....

## Acknowledgement

---

I would like to express my sincere gratitude to my supervisor Prof. Dermot Brabazon for the continuous support of my Ph.D study and related research, for his patience, motivation, and immense knowledge. His guidance helped me in all the time of research and writing of this thesis. I could not have imagined having a better advisor and mentor for my Ph.D study.

Besides my supervisor, I would like to thank my colleagues, Dr. Eanna McCarthy and Dr. Shadi Karazi for the excellent research atmosphere. Their insightful comments incentivized me to widen my research from various perspectives.

Also, I would like to thank the technical staff in DCU workshop and labs especially Mr. Michael May, Mr. Liam Domican, Mr. Dean McLoughlin, Mr. Cian Merne, Mr. James Barry, Mr. Christopher Crouch and Mr. Eoin Touhy for their support to facilitate the experimental work.

More importantly, I would like to present my appreciation to my family, my loving wife and wonderful children for being so patient, cooperative and understanding during the entire study time.

## Table of Contents

Declaration .....	II
Preface .....	III
Author's Contribution .....	V
Acknowledgement .....	VIII
Abstract.....	XXIV
List of Tables .....	XV
List of Figures.....	XVII
Chapter 1 .....	1
Introduction-Lasers and laser beams .....	1
1.1    Introduction.....	1
1.2    Laser types .....	1
1.2.1    Gas lasers .....	2
1.2.2    CO <sub>2</sub> gas laser composition .....	5
1.3    Laser beam temporal modes .....	8
1.4    Laser beam profile and transverse modes .....	9
1.5    Laser – materials interaction.....	11
1.6    Laser processing parameters .....	14
1.6.1    Pulse energy, $E_p$ .....	14
1.6.2    Laser peak power, $P_p$ .....	14
1.6.3    Duty cycle, DC .....	15
1.6.4    Average power, $P_{AV}$ .....	15
1.6.5    Laser power density (Irradiance), $I_{ir}$ .....	15
1.6.6    Pulse repetition frequency, PRF.....	16
1.6.7    Residence time and scanning speed .....	16

1.6.8	Pulse energy density (fluence), $F_p$ .....	17
1.6.9	Laser pulse width ( $\tau$ ) .....	18
1.6.10	Laser focal spot size .....	18
Chapter 2 .....		22
Literature Review- .....		22
Stainless steel alloys and Laser machining .....		22
2.1	Introduction.....	22
2.2	Types of stainless steel and their applications .....	26
2.3	Iron-iron carbide (Fe-Fe <sub>3</sub> C) phase diagram .....	29
2.4	Laser machining applications .....	33
2.4.1	Laser surface engineering (LSE).....	34
2.4.2	Laser surface cladding.....	34
2.4.3	Laser surface glazing.....	38
2.4.4	Laser surface alloying .....	39
2.4.5	Laser cold cutting .....	41
2.4.6	Laser surface polishing .....	42
2.4.7	Nitriding .....	44
Chapter 3 .....		51
Literature Review-Interference Fit .....		51
3.1	Introduction.....	51
3.2	Traditional Fastening Methods .....	53
3.3	Types of Fits .....	56
3.3.1	Press and shrink Fit .....	57
3.3.2	Stresses in the interference fit: .....	58
3.4	Commercial and commonly used fixtures .....	60

3.4.1	Spirally Coiled Pins.....	60
3.4.2	Grooved Pins .....	61
3.4.3	Other Types of Pins.....	62
3.4.4	HILTI X-BT Threaded Fastener .....	63
3.5	Aim of the study .....	65
Chapter 4 .....		66
Materials, Method and Experiment .....		66
4.1	Introduction.....	66
4.2	Equipment and materials .....	67
4.2.1	The laser system .....	67
4.2.2	Materials and preparation.....	70
4.2.3	Surface roughening by sand blasting .....	71
4.3	Preliminary screening test.....	73
4.3.1	Investigating the melting point and threshold .....	74
4.3.2	The effect of the pulse repetition frequency (PRF).....	79
4.3.3	The effect of the percentage overlap .....	80
4.4	Calculating the texture pattern angle .....	84
4.5	Design of experiment (DoE).....	87
4.5.1	Experimental procedure .....	89
4.6	Process layout .....	90
4.7	Processed samples inspection .....	91
4.7.1	The increase in samples diameter .....	91
4.7.2	Measuring the texture angle, peak-peak and peak-valley measurement.....	92
4.8	Metallographic test .....	93
4.9	Microscopic investigation.....	95

4.10	Chemical composition analysis .....	97
4.11	Measuring the meltpool depth .....	98
4.12	Measuring the micro-hardness .....	99
4.13	Residual stresses investigation.....	99
4.13.1	Elastic modulus and hardness investigation.....	99
4.14	Roughness measurements .....	101
4.15	Interfering volume calculation .....	102
4.16	Insertion and pull-out tests.....	104
4.16.1	Commercial samples test.....	105
4.17	Fatigue test .....	106
4.18	Laser nitriding.....	108
4.19	Wear test .....	109
4.20	Corrosion test.....	112
4.20.1	Calculation of the corrosion rate .....	113
4.21	Torsion test .....	114
4.22	Thermal modelling.....	114
4.22.1	Energy calculations: .....	115
4.22.2	Absorption factor calculations .....	116
4.22.3	The mathematical model .....	117
Chapter 5	.....	119
Results	.....	119
5.1	Effect of surface roughness on absorption of thermal energy .....	119
5.2	Morphology and metallography investigations .....	123
5.3	Effect of the laser processing.....	124
5.3.1	Surface morphology and cross-sectional microstructure .....	124



5.3.2	The chemical composition and EDAX test results .....	127
5.4	Resulting surface texture .....	129
5.4.1	Texture pattern angle.....	129
5.4.2	Surface roughness measurement .....	131
5.5	The melt-pool depth.....	135
5.6	Elastic modulus and nano-hardness results .....	135
5.7	The measured diameter increase, peak-valley and peak-peak distances .....	137
5.8	Interfering volume .....	146
5.9	Insertion and pull-out test .....	147
5.9.1	Insertion test results.....	147
5.9.2	Pull-out test results.....	152
5.10	Tested samples .....	156
5.11	Insertion and pull-out test of the commercial samples .....	157
5.12	Fatigue test .....	159
5.13	Wear test results .....	160
5.14	Corrosion test.....	163
5.15	Correlation strength investigation.....	164
5.16	Laser nitriding results .....	167
5.16.1	Microstructure: .....	168
5.16.2	Alteration in surface hardness - <i>Stainless steel</i> : .....	170
5.16.3	The insertion and pull-out tests of the nitrided samples .....	174
5.16.4	Corrosion test results.....	177
5.17	Torsion test .....	178
5.18	Thermal profile .....	178
5.18.1	The temperature profile and thermal history .....	179

5.18.2 Heating and cooling rates .....	181
Chapter 6 .....	184
Discussion and Conclusion.....	184
6.1 Thermal energy and absorption factor .....	184
6.2 Measured micro texture longitudinal and circumferential dimensions .....	187
6.3 The effect of the laser processing .....	188
6.4 The melt-pool depth .....	192
6.5 The chemical composition and phase change .....	193
6.6 The elastic modulus and nano-hardness .....	194
6.7 The surface roughness measurements.....	194
6.8 The diameter increase .....	196
6.9 Metallographic test results .....	197
6.10 The insertion and pull-out test.....	198
6.11 Corrosion test.....	201
6.12 Conclusions.....	202
References .....	205
Appendices .....	221
Appendix A- .....	221
Appendix B Input laser processing parameters and out-put measures.....	242
Appendix C- Metallographic arrangements .....	243
Appendix D .....	253
Appendix E.....	257
E-1 Elastic modulus test .....	257

## List of Tables

Table 2-1 Types of CO <sub>2</sub> lasers and their specifications and applications.....	23
Table 2-2 Common types of stainless steel and their applications.....	28
Table 2-3 Advantages and disadvantages of laser machining.....	33
Table 2-4 Characteristics of laser surface alloying (LSA).....	33
Table 3-1 Joints efficiencies for various processes and materials (%).....	55
Table 3-2 Spirally Coiled Pin Insertion Force (lb/dia.length).....	61
Table 3-3 Loading values for Hilti X-BT fastener stud.....	63
Table 4-1 Rofin laser system specifications .....	67
Table 4-2 Chemical composition for 316L austenitic stainless steel samples (wt%).....	70
Table 4-3 Chemical and physical properties of the grit used in the surface roughening.....	71
Table 4-4 Physical properties of SST 316L.....	74
Table 4-5 Laser processing parameters values used in the preliminary test... ..	78
Table 4-6 Lists the results for processing with different PRF .....	80
Table 4-7 The laser processing parameters applied to determine the effect of overlap on sample morphology.....	85
Table 4-8 The laser processing parameters applied in the DOE.....	88
Table 4-9 Chemical composition of the carbon steel samples used in laser nitriding.....	108
Table 5-1 The melt pool (MP) dimension.....	123
Table 5-2 The chemical composition of the as-received And processed samples .....	129
Table 5-3 parameters applied to determine the The laser processing effect of using different overlaps on the pattern angle.....	129
Table 5-4 Averages of the elastic modulus and surface hardness.....	137
Table 5-5 Lists the textured surface geometry and type.....	138
Table 5-6 ANOVA results for the diameter increase model.....	142
Table 5-7 ANOVA results for the insertion force model.....	149

Table 5-8 ANOVA results for the pull-out force model.....	153
Table 5-9 The fatigue test results for sample no. 9 at frequency of 10 Hz.....	159
Table 5-10 Wear resistance of 316L SST before and after CO2 laser Treatment.....	161
Table 5-11 The correlation strength (r) and the significance of correlation (p) of the process parameters and resulting profile and force measurements.....	165
Table 5-12 Torque test results for sample no. 9.....	178
Table 6-1 Calculated laser processing parameters with the resulting meltpool depth, average surface roughness and the pull-out force for selected samples.....	196
Table 6-2 Lists the processed samples with their related forces, interfering volume and surface hardness.....	200
Table 6-3 Table 6-3 Lists the surface hardness and the corresponding heating and cooling rates for sample no. 9 and 15.....	201
Table 6-4 manufacturing cost of the laser surface texture insertion.....	204

## List of Figures

Figure 1-1 Shows the energy levels of HeNe laser generating system .....	3
Figure 1-2 Helium-neon laser system.....	4
Figure 1-3 CO <sub>2</sub> vibrational modes: (a) symmetric stretching, (b) bending, and (c) axisymmetric stretching .....	5
Figure 1-4 Axial flow CO <sub>2</sub> laser.....	6
Figure 1-5 Show the laser working modes (a) continuous and (b) pulse mode.	8
Figure 1-6 Shows two spatial intensity distribution modes (a) TEM <sub>00</sub> fundamental Gaussian and (b) TEM <sub>01</sub> mode .....	9
Figure 1-7 Shows three different distribution modes.....	10
Figure 1-8 Shaping the Gaussian profile beam into a “top-hat” beam.....	10
Figure 1-9 The three possible scenarios of laser-material interaction.....	11
Figure 1-10 The absorption of materials to different lasers wavelength.....	12
Figure 1-11 The absorption of steel to CO <sub>2</sub> laser as a function of the oxide film thickness.....	13
Figure 1-12 Laser beam multi reflections due to surface roughness may enhance the absorption.....	13
Figure 1-13 Shows the terms used in the pulse operating mode.....	14
Figure 1-14 Schematic diagram for the laser process showing the scanning speed and direction.....	17
Figure 1-15 Focal length, spot diameter and depth of focus for a Gaussian laser beam.....	19
Figure 1-16 Geometry and intensity of the Gaussian showing the beam focus positions with reference to the sample surface.....	20
Figure 1-17 Fluence produced by focusing low energy levels into small spot sizes.....	21
Figure 2-1 Regimes of various effects during laser–material interactions and their application in laser materials processing .....	25
Figure 2-2 Iron-Iron Carbide (Fe-Fe <sub>3</sub> C) phase diagram.....	30
Figure 2-3 Schematic presentation of the microstructure for the low carbon iron alloys.....	31
Figure 2-4 Shows (a) schematic and (b) micrograph of the phases available for 0.38 wt% C steel .....	32
Figure 2-5 Classification of laser surface engineering.....	34
Figure 2-6 Arrangements for laser cladding by the (a) blown (b) coaxial powder feeding techniques .....	35
Figure 2-7 CO <sub>2</sub> Laser cladding of (a) steam turbine blade to improve erosion resistance (Juha Kauppila) and (b) cobalt based powder on a valve rim. ....	36

Figure 2-8 Hardness distribution profile along the depth of titanium Substrate.....	37
Figure 2-9 SEM of the top surface of a Ti-Si treated by LSA.....	40
Figure 2-10 A human hair textured using an excimer laser.....	42
Figure 2-11 Types of laser polishing.....	43
Figure 2-12 Shows the laser polishing principle.....	43
Figure 2-13 Shows the laser micro-polishing of a glass mould, before polishing (left) and after polishing (right).....	44
Figure 2-14 Iron-Nitrogen equilibrium phase diagram.....	45
Figure 2-15 CO <sub>2</sub> laser nitriding of 1.5919 steel using (power =1 kW, scanning speed=5 mm/s and 1 successive pass .....	48
Figure 3-1 (a) Mechanical, (b) Chemical and (c) Physical joining of parts.....	54
Figure 3-2 Tolerances between two mating parts .....	58
Figure 3-3 Interference-fit .....	58
Figure 3-4 The basic design of a spirally coiled pin.....	60
Figure 3-5 Grooved Pin.....	62
Figure 3-6 (a) Knurled and (b) Slotted Tubular Pins.....	62
Figure 3-7 HILTI X-BT Stud. (1) Shank AISI grade SST 316, (2) Threaded Sleeve (3) Metal Washer and (4) Sealing Washer.....	63
Figure 3-8 Pull-out Load-Displacement behaviour of X-BT Hilti Fastener.....	64
Figure 4-1 The CO <sub>2</sub> laser system used in this research.....	68
Figure 4-2 Experimental set up.....	68
Figure 4-3 Schematic diagram for the CO <sub>2</sub> laser scanning process of cylindrical samples.....	69
Figure 4-4 Shows 10 mm diameter stainless steel 316L cylindrical samples (a) before and (b) after roughening by shot-blasting.....	71
Figure 4-5 SEM micrographs of the side view for the cylindrical sample surface (a) before and (b) after roughening.....	72
Figure 4-6 Stainless steel flat samples with three different surface roughness of 0.02 µm (left), as-received 0.8 µm (middle) and 1.5 µm (right), processed with the same laser parameters for the investigation of the laser energy absorption.....	73
Figure 4-7 Optical micrograph of 10 mm length, 20 mm diameter cylindrical sample scanned by CO <sub>2</sub> laser of 200W, 100 Hz, 50% duty cycle, 2.5 ms residence time, -50% overlap and process time = 52 s.....	76

Figure 4-8 (a) and (b) high magnification SEM images for the sample shown in Figure 4-7.....	76
Figure 4-9 Micrographs of 316L melt pool (a) circumferential cross section, longitudinal cross sectional view, and (c) additional longitudinal cross section view showing maximum depth.....	77
Figure 4-10 (a) SEM image of 316L surface processed by 1 kW, 2250 Hz and 20% overlap and (b) shows the brown brittle oxide on the surface.....	79
Figure 4-11 Sparks generation when scanning with 500 W, -20% OV and PRF of (a) 300 Hz and (b) 1500 Hz.....	80
Figure 4-12 Overlap scanning scenarios of (a) zero, (b) positive and (c) negative values of the laser spot.....	82
Figure 4-13 Schematic diagram illustrating the three possible scanning scenarios positive, zero and negative laser spot overlap.....	84
Figure 4-14 Schematic of laser path (thin lines) and resulting texture pattern (thick lines).....	85
Figure 4-15 Schematic of three laser pulses showing the texture pattern angle $\theta_p$ .....	86
Figure 4-16 Process flow chart for the CO <sub>2</sub> laser surface texture of cylindrical samples.....	91
Figure 17 (a) Schematic diagram of the cross section view showing peak-peak width and peak-valley height, and (b) top view showing pattern direction relative to the longitudinal axis.....	92
Figure 4-18 Schematic for the sectioned cylindrical sample.....	93
Figure 4-19 SST 316L sample processed with a CO <sub>2</sub> laser (a) after grinding and polishing and (b) after treatment with Adler chemical etchant .....	95
Figure 4-20 The Carl-Zeiss EVO-LS15 SEM.....	96
Figure 4-21 Optical image for the sample shown in Figure 4 6.....	97
Figure 4-22 SEM micrographs Showing the test points where the EDAX analysis carried out on (a) as- received and (b) laser processed samples.....	98
Figure 4-23 SEM image of sample no. 9 showing the melt-pool depth.....	98
Figure 4-24 (a) The methodology used in nano-indentation and (b) SEM micrograph for the indents.....	100
Figure 4-25 3D image of the surface roughness profile for surface roughness profile.....	101
Figure 4-26 2D surface roughness profile oriented in the axial direction.....	102
Figure 4-27 Cross section of the interfering volume between the pin insertion and the hub ring.....	103

Figure 4-28 Laser textured insertion pin and the corresponding hub.....	104
Figure 4-29 Picture of the insertion and removal test arrangement on the Zwick Z-50.....	105
Figure 4-30 Commercial plain steel pin insertions.....	106
Figure 4-31 Fatigue test (a) sample assembly sketch and (b) experimental set up.....	107
Figure 4-32 Sample preparation for the metallographic study.....	109
Figure 4-33 Flat sample produced to facilitate the pin on disc wear test.....	110
Figure 4-34 Schematic of the wear testing instrument.....	111
Figure 4-35 Polarisation electrolyte cell used in the corrosion test.....	112
Figure 4-36 (a) Samples preparation for torsion test (b) testing machine.....	114
Figure 4-37 Surface temperature profile plotted for different laser power and scanning speed.....	115
Figure 4-38 (a) The theoretical propagating laser beam cross-section and (b) the incident laser beam track and melt-pool form.....	117
Figure 5-1 The laser pulse tracks on 316L SST flat samples with different surface roughness.....	122
Figure 5-2 SEM images of the as-received samples (a) and (b) surface, (c) and (d) cross section microstructure revealed by glyceresia etchant.....	124
Figure 5-3 Sample 9 surface morphology (left) and cross sectional microstructure (right).....	125
Figure 5-4 Sample 15 surface morphology (left) and cross sectional microstructure (right).....	125
Figure 5-5 Micrograph of the cross section microstructure for sample no. 9 revealed by glyceresia etchant.....	126
Figure 5-6 Micrograph of the cross section microstructure for sample no. 15.....	127
Figure 5-7 EDAX spectrum of the (a) as-received and (b,c,d) processed samples.....	128
Figure 5-8 SEM images of surfaces for sample no. (a) 19, (b) 20 and (c) 11.....	130
Figure 5-9 (a) Shows the symmetrical percentage overlap in both direction and (b) the resulting texture angle for sample no. 4 correspond to table.....	130
Figure 5-10 Graph of the recorded surface roughness against the laser irradiance, for various laser residence times, n=5.....	131
Figure 5-11 The correlation between the surface roughness and the laser power irradiance for different residence time, n=5.....	132
Figure 5-12 3D images for the surface roughness of the processed samples...	134
Figure 5-13 The effect of the residence time and Irradiance on the melt pool depth, n=8.....	135



Figure 5-14 The average elastic modulus and hardness for (a) all the indents in sample no. 9 and (b) one line of indent in sample no. 15.....	136
Figure 5-15 (a) picture and (b) SEM image showing ridged pattern processed with 500 W, 300 Hz and 20% overlap (sample 20), (c) and (d) non-ridged textured sample processed with 300W, 300 Hz and -20% overlap (sample 4).....	139
Figure 5-16 Graph of the peak-valley values of the processed samples, n=8.....	140
Figure 5-17 Graph of the peak-peak values of the processed samples with clear pattern, n=8.....	140
Figure 5-18 Graph of the average diameter increase, n= 8.....	141
Figure 5-19 The experimental and predicted diameter increase.....	144
Figure 5-20 Shows the interaction of the power and the PRF on the diameter increase for the three overlapping scenarios.....	145
Figure 5-21 Relationship between the interfering volume and the different input and output parameters.....	147
Figure 5-22 Graphs of the insertion force against insertion length of (a) eight samples and (b) for sample no. 9 with the 95% CI, n=8.	145
Figure 5-23 RSM plots for the insertion force showing the effect of PRF and laser power on the insertion force for different overlap.....	150
Figure 5-24 The actual versus predicted values of the insertion force.....	151
Figure 5-25 Graphs of the pull-out force against removal length of (a) eight samples, and (b) for sample no. 9, n=8.....	152
Figure 5-26 RSM plots for the pull-out force for the laser processing parameters at (a) -20%, (b) 0%, and (c) 20% overlap.....	154
Figure 5-27 Actual and predicted values of the pull-out force.....	155
Figure 5-28 Pictures of 316L cylindrical samples after the insertion and removal test (a) sample 9 processed with 400 W, 100 Hz, -20%, 4 ms residence time, and (b) sample 15 processed with 500 W, 300 Hz, -20%, 1.33 ms residence time.....	156
Figure 5-29 The diameter increase-pull out force test result.....	157
Figure 5-30 (a) Insertion and (b) pull-out forces plots for the commercial samples Tested in a 9.99 mm diameter hubs, n=7.....	158
Figure 5-31 Fatigue test (a) stroke-no. of cycles and (b) stroke-load data obtained from fatigue test.....	160
Figure 5-32 The surface structure of 316L SST flat samples processed in (a) and (b) argon, (c) and (d) argon-nitrogen gas shielding.....	162
Figure 5-33 Potentiodynamic polarization scan potential-current log plot indicating Tafel slope for as-received and laser	

processed samples in argon atmosphere.....	163
Figure 5-34 The perturbation graphs shows the relationship between the processing parameters and the pull-out force at overlaps of (a) -20%, (b) 0% and (c) 20%.....	167
Figure 5-35 SEM cross section micrographs of samples no. 3 and 9 processed with (a), (c) argon and (b), (d) nitrogen atmosphere.....	168
Figure 5-36 Cross-section micrographs of carbon steel processed with CO <sub>2</sub> laser of 325 W and 800 Hz revealed by nital 5% etchant.....	169
Figure 5-37 Shows the effect of the laser nitriding on the surface micro-hardness.....	170
Figure 5-38 3D RSM plots of the laser nitriding with (a) -20% and (b) 20% OV.....	171
Figure 5-39 The perturbation plot of the processing parameters and the hardness relationship.....	172
Figure 5-40 Plot of the actual and predicted data.....	173
Figure 5-41 Surface hardness of carbon steel scanned by CO <sub>2</sub> pulsed laser in argon and nitrogen gas atmosphere.....	174
Figure 5-42 Shows a comparison between the pull-out forces for the nitride and non-nitrided samples no. 3, (b) 10, (c) 15 and (d) 25.....	175
Figure 5-43 RSM graph for the relationship between the laser processing parameters and the pull-out force for samples processed in (a) argon and (b) nitrogen gas atmosphere at (-20%) pulse overlap.....	176
Figure 5-44 Potentiodynamic polarization scan potential-current log plot Tafel slope for indicating as-received and laser processed samples in argon-nitrogen gas atmosphere.....	177
Figure 5-45 (a) Objective, (b) top, and (c) side views for the temperature profile at 78 µm depth for 316L resultant from 200W, 100 Hz, 2.5ms residence time, and 50% duty cycle.....	179
Figure 5-46 Normalized temperature distribution for samples no. 9 and 15 in four depths planar from the surface.....	180
Figure 5-47 Temperature history for (a) sample no. 9 and Sample no. 15 at four depth levels.....	182
Figure 5-48 Temperature-time history profile for samples no. 9 and 15.....	182
Figure 6-1 Optical micrographs of the melt pool (a) width and depth and (b) length revealed by Adler etchant.....	185
Figure 6-2 Laser micro-polishing of a cylindrical SST sample produced by (AM) before (top left) and after (top right).....	187
Figure 6-3 Samples no. 15 (left) and 24 (right) after insertion.....	189
Figure 6-4 Graph of the average surface roughness, Ra, versus the PRF for all test conditions.....	190

Figure 6-5 PRF and pull-out force data scattering.....	191
Figure 6-6 Relationship between the residence time and the melt pool depth.....	192
Figure 6-7 Relationship between the energy density and the melt pool depth.....	193
Figure 6-8 Distribution of the full DoE set of samples showing the surface roughness versus the pull-out force.....	195
Figure 6-9 Surface hardness profile and the hard martensite of sample no. 9.....	199

**PhD Thesis by: Muhannad Ahmed Obeidi, DCU 2017**

**Laser processing of metallic surfaces for controlled micro-texturing and metallic bonding.**

**Abstract**

---

This study investigated the development of a novel method for designing high-end interference fit fasteners. In this work, a new surface laser treatment process was developed and implemented to enable enhanced usability and bond strength control of interference-fit connections. Stainless steel 316L cylindrical samples of 10 mm diameter were textured over a 10 mm length using a pulsed 1.5 kW CO<sub>2</sub> laser. The laser beam was focused one millimetre below the metal surface, with the thermal energy adjusted to bring the surface to just above the melting point to avoid the loss of the metal. Due to the localized surface melting, rotational movement of the pin and the gas jet impingement, the re-solidified metal creates raises in the sample diameter. The pin surface morphology and dimensions were precisely controlled by controlling the laser processing parameters specifically the laser beam power, the pulse repetition frequency, the rotational speed, the gas pressure, and the overlap between scan tracks. The pin was inserted into a hub hole diameter of  $10.05 \pm 0.003$  mm and pull out joint bond strengths were measured and examined. The results of this study showed that surface thus altered provided improved control of the bond strength, which is a particular novelty of this new interference fit joining method. Surface roughness, Ra, from 40 to 160  $\mu\text{m}$ , melt pool depths from 0.4 to 1.7 mm, increases in the pin outer diameter from 0.1 to 1.1 mm, and pull out forces of up to 7.51 kN were achieved. The bond joint was found to re-grip before complete separation providing a more secure joint and increased safety. This joining method allows for the possibility of joining different materials. The modified surface layer did not reveal any distinct variation in the elastic modulus or hardness across the cross section of the insertion.

## Introduction Lasers and laser beams

### 1.1 Introduction

Laser beams are the material scientist's dream. They can deliver high energy with a finite control to almost all kinds of materials [1–3]. In definition, LASER stands for Light Amplification by Stimulated Emission of Radiation. As a versatile, highly concentrated energy source, lasers brought the attention of researchers and engineers for variable applications in medicine, metallurgy, semiconductors technology and engineering. Laser beams can be generated in the broad range of wavelengths, energies and beam modes in addition to the unique property of propagation in straight lines with less or negligible divergence. These unique features made lasers preferential for metal treatment and surface modification over the conventional heat treatment methods. In laser surface modification, only a localised treatment of the surface is achieved without damaging the neighbouring and the core material properties of the substrate, high reproducibility, high speed and low cost [3,4].

The stimulated emission phenomenon can be produced from almost all materials with variant levels of power. Only a few materials can be excited to a high power capability level and produce more molecules in the excited state than in the lower-energy state and in order to achieve this, the lifetime of the excited atoms and molecules must be maintained [4,5].

### 1.2 Laser types

Lasers are divided into three types according to their lasing material [4-6]:

- a) Gas laser
- b) Liquid laser
- c) Solid laser

Dahotre [8] added a fourth type known as the semiconductor lasers even though they are based on solid material, the pumping and lasing mechanisms are different. All these types can work in two modes: the continuous wave mode (CW) in which laser beam can be emitted without interruption and the pulsed wave mode (PW) in which the beam is interrupted periodically. Since the first ruby laser development in 1960, laser action has been tested in many materials. However, the suitable materials for the commercial laser are still limited. In the review below, only the gas type of lasers would be discussed as for the main laser utilised in this work.

### 1.2.1 Gas lasers

Gas lasers are the most common type of laser. They can operate in both continuous and pulsed mode with an output power range from several kilowatts for carbon dioxide to few mill watts for helium-neon lasers and a range of wavelengths starting from ultraviolet to infrared [9]. In contrast with solid lasers, gas lasers have the advantages of: relatively low cost of gases, ease of transport and cooling, and a homogeneous and finite controlled medium and generated beam.

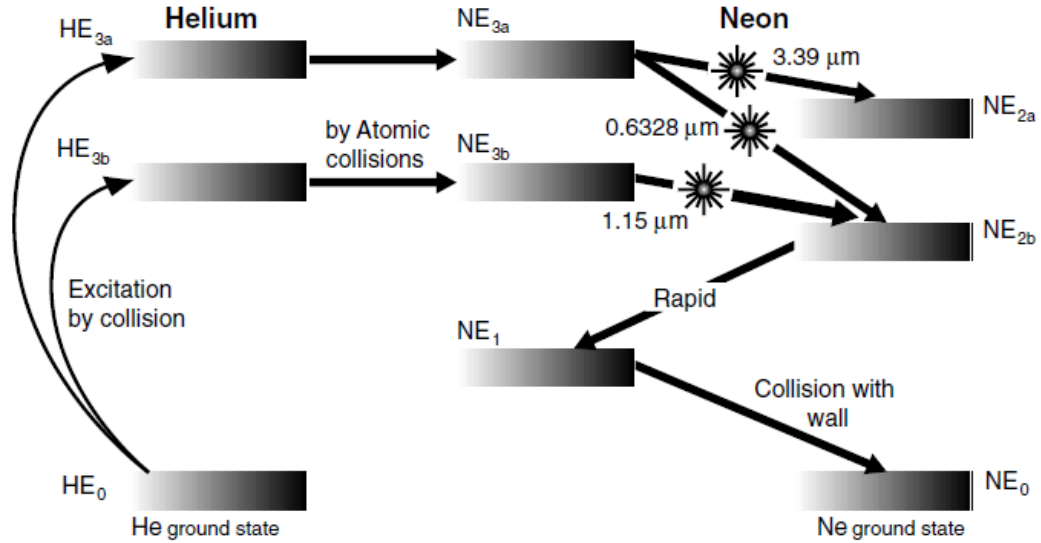
The low density of gases can be considered a minor drawback of this type of laser resulting in a maintenance scheduled for replacement of gas consumed.

Gas lasers can be classified into three types depending on the chemical composition of the active lasing medium and the energy levels of the laser transition, these are:

- a) Neutral atom lasers,
- b) Ion laser, and
- c) Molecular lasers

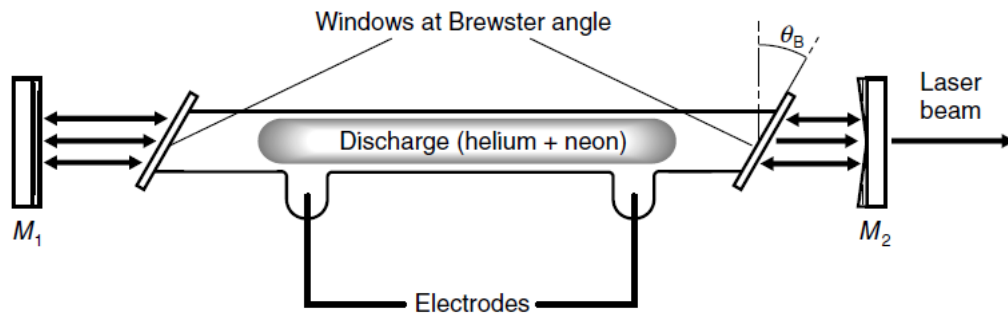
***Neutral atom lasers:*** The most common visible gas laser is the helium-neon (HeNe) laser which can be classified as one of the *neutral atom gas laser* types and has wide applications in alignment, measurements, vision, scanning, holography and optical-fiber communications. This laser can be tuned from infrared to various wavelengths. The most common frequency, is the red coloured beam which has the wavelength of 0.6328  $\mu\text{m}$ . Helium gas is first excited by electrical discharge by the aid of a DC electrical

discharge in a low-pressure tube. This energy is transferred to the neon atoms by kinetic interactions as shown in Figure 1-1.



**Figure 1-1** The energy levels of HeNe laser generating system [9]

The active medium is composed of 1:10 parts of He:Ne. The process starts by exciting the He gas atoms from the ground state to the higher energy levels of  $HE_{3a}$  and  $HE_{3b}$  which in turn would coincide with the few formerly excited atoms of Ne at  $NE_{3a}$  and  $NE_{3b}$  energy levels and transfers energy to Ne atoms in a process called resonant energy transfer. A subsequent energy inversion would take place between  $NE_{3a}$  and  $NE_{3b}$  energy levels and the lower level of neon gas atoms  $NE_{2a}$  and  $NE_{2b}$ , thus lasing action would continue to take place between the neon atoms while helium gas acts as the pumping medium. Helium atoms can maintain the metastable state for a relatively long time making the energy transfer process more efficient. The neon gas atoms in the high energy level have a decay time of 100 ns and those in the low energy levels have a decay time of about 10 ns which makes the system efficient for a continuous wave (CW) mode operation. Figure 1-2 shows a schematic diagram of this system.



**Figure 1-2** Helium-neon laser system [9]

The system is composed of the low-pressure discharge tube of 20 to 80 cm in length. The reflecting mirrors could be mounted externally or internally. The disadvantage that the external mirrors have is that the windows at the two ends of the tube reflect part of the beam resulting in losses. Internally mounted mirrors must be sealed and replaced periodically because of erosion. The power output of this type of laser is relatively small (0.5-50 mW) with an input power of 5 to 10 W with the overall efficiency of 0.02%.

**Ion laser:** In this type of lasers, an inert gas such as argon (Ar), krypton (Kr) or xenon (Xe) is used. Excitation of the gas to produce lasing is performed in two stages; gas ionization and electrons excitation to a higher energy level. The resulting laser beam has a wavelength range of 0.5 to 1.0  $\mu\text{m}$  and power of 20 W in continuous wave mode. Typical applications for these in surgery and spectroscopy require higher power than those provided by the neutral atoms lasers. Low power  $\text{Ar}^+$  ion lasers are also used in laser printers [8,9].

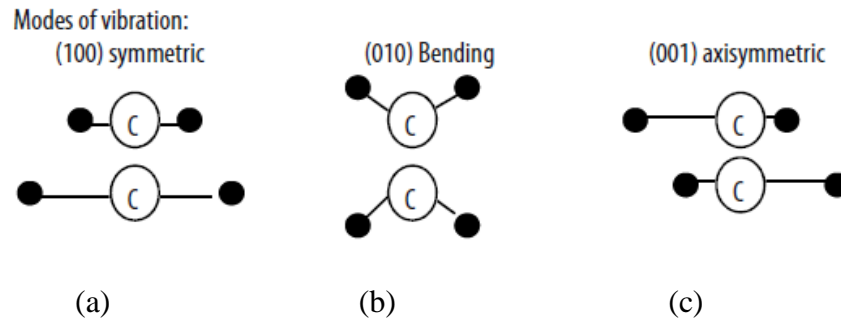
**Molecular gas laser:** In this type of laser beam, the gas molecules are used as the lasing medium. Carbon dioxide ( $\text{CO}_2$ ) and, carbon monoxide (CO) are the most common types used for laser machining. In contrast to the former two types of gas lasers, molecule gas laser derives its energy from gas molecules. The resultant overall energy of the laser-molecule is a function of four components:

1. Electronic energy, generated by electron motions around the nuclei.
2. Vibrational energy, generated by the vibration of the atoms around an equilibrium position.
3. Rotational energy, generated by the rotation of the molecule about an axis.



4. Translational energy, due to the thermal motions of the molecule.

Carbon dioxide laser is the most common laser used in materials processing and machining. The following Figure 1-3 shows the three different vibration modes that CO<sub>2</sub> molecule can undergo; symmetric, axisymmetric and bending vibration modes.



**Figure 1-3** CO<sub>2</sub> vibrational modes: (a) symmetric stretching, (b) bending, and (c) axisymmetric stretching [6].

Different energy levels are associated with these modes, and the smaller energy level comes with the rotational mode compared with the vibrational modes. Electronic, vibrational and rotational energy levels are quantized meaning they only exist when a certain level of energy is reached and therefore can produce laser oscillations. The translational energy level is not quantized and thus is not useful to produce lasers.

### 1.2.2 CO<sub>2</sub> gas laser composition

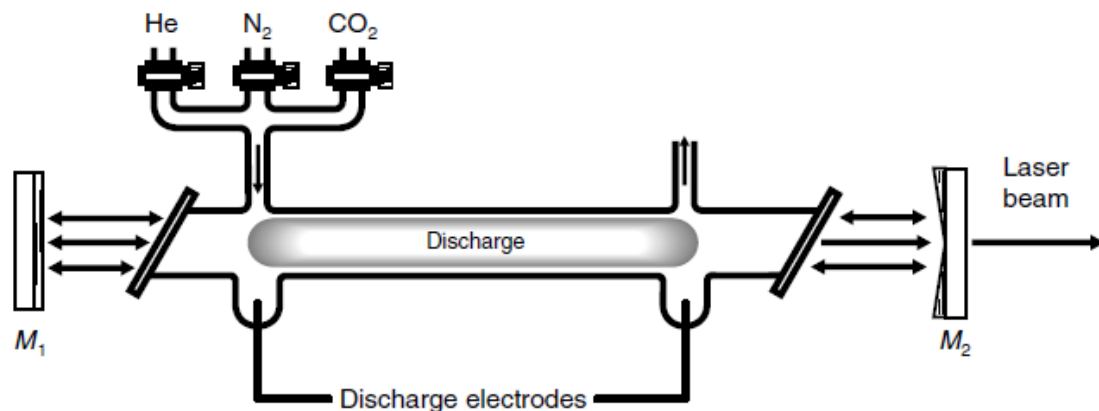
The first infrared CO<sub>2</sub> laser beam was reported by Patel in 1964 [8, 9] in pulsed discharges through pure CO<sub>2</sub>. Following experiments, Patel in 1964 succeeded in producing more efficient and more powerful laser by exciting nitrogen gas molecules and transfer the vibrational energy to the CO<sub>2</sub> molecules. The energy transfer was based on the quirky phenomenon of nitrogen molecule being oscillated in one way. Moreover, the nitrogen gas molecules can oscillate in a range of Hertz that is adequate to transfer cold CO<sub>2</sub> molecules to the axisymmetric oscillation mode (001). The lifetime of the excited N<sub>2</sub> molecules is long. They only lose energy when colliding with the tube walls, and they transfer energy to CO<sub>2</sub> even if it is not in the plasma zone. The later experiment improves the efficiency of the CO<sub>2</sub> laser for up to (15-20%). A subsequent advance occurred soon in 1965 when Patel applied the use of helium gas and found an

increase in CO<sub>2</sub> laser power from 1 mW to 10<sup>2</sup> W which represents an improvement factor of 10<sup>5</sup>.

There are several designs of CO<sub>2</sub> lasers for example:

- a) Longitudinal flow lasers
- b) Sealed tube lasers
- c) Transverse flow lasers
- d) Transversely excited atmospheric lasers (TEA)
- e) Gas-dynamic lasers

The following Figure 1-4 shows the configuration of the longitudinal (axial flow) design CO<sub>2</sub> laser as an example. This design allows for the continuous delivery of the gas mixture necessary for the removal of any dissociation products particularly CO which may results in the laser beam to be quenched. Cooling water is used for cooling the tube wall from the heat generated during the discharge.



**Figure 1-4** Axial flow CO<sub>2</sub> laser [8]

The output power does not depend on the tube diameter but it depends on the tube length and the number of reflections of the beam inside the resonator. For the laser design shown above the output power is 50-60 W/m or 50-500 W in total. Also the output power is restricted to the heat generated inside the tube walls. A modified design of the axial flow is by flowing the gas mixture through the tube and extract the heat by convection. This arrangement improves the laser efficiency and power output by up to 20 kW.

A wide range of mixing ratios can be obtained from a three-component gas mixture, but the optimum output regarding power and efficiency for  $\text{CO}_2 : \text{N}_2 : \text{He}$  was found to be 0.8 : 1 : 7. Experiments show that  $\text{CO}_2 : \text{N}_2$  ratio is essential factor for the output power more than  $[\text{CO}_2 : \text{N}_2] : \text{He}$  ratio and that setting procedure for a significant mixing ratio is to be performed by fixing the  $\text{CO}_2 : \text{N}_2$  ratio to [0.8:1] and adjust the  $[\text{CO}_2 : \text{N}_2] : \text{He}$  to find the maximum output power. Then it is possible to adjust the  $\text{N}_2$  flow rate to find the system optimum point [11].

### **Why $\text{CO}_2$ laser ?**

The  $\text{CO}_2$  laser photon energy is equal to 0.12 eV. This amount of energy is still insufficient to eject the electron from the metal surface after incident laser beam excitation. Because the motion of the metal electron is constrained by the grain and lattice boundaries and that the energy absorbed from the laser photons must be dissipated to the surrounding so that the electrons can go back to the equilibrium state, the overall effect is to convert this energy into heat. The heat generated during this process is useful for processes like surface heat treatment, welding, cutting and many types of industrial treatment and machining.

The increasing demand for lasers in material processing can be attributed to the following benefits over the traditional machining operations [13]:

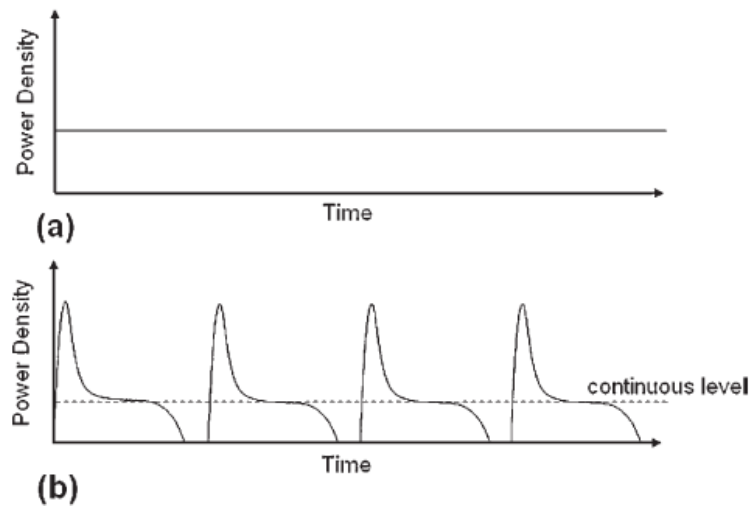
- The ability for automation
- No-contact machining, so there is no tool damage due to high load friction or wear
- High product quality
- Near-net shape production and the great reduction of finishing tasks
- Reduced processing cost
- Minimum heat affected zone.

In most material processing by laser, i.e., welding, cutting and drilling which require high energy density within a very short time, the average power, efficiency and the laser-material interaction time are important factors. The carbon dioxide, the fiber and the ND-YAG lasers are practically the best available choices due to their availability in high power ranges. Moreover, the high output power of the  $\text{CO}_2$  lasers of 0.1-50 kW

and the electric efficiency of up to 20% compensate the poor laser-material interaction due to the long wavelength of 10.64  $\mu\text{m}$ .

### 1.3 Laser beam temporal modes

Laser machining and surface modification can be performed using either the continuous (CW) or the pulsed wave mode (PW) as shown in Figure 1-5. In contrast with the continuous wave mode, the pulse wave mode discharges energy rapidly and periodically. Energy is stored in pulse mode until a threshold value is reached and then rapidly discharge in a very short duration with high density. An example of the pulse wave mode is shown in Figure 1-5 (b) and is mainly characterized by initial spikes of the peak laser power of (2-3) times the average power.



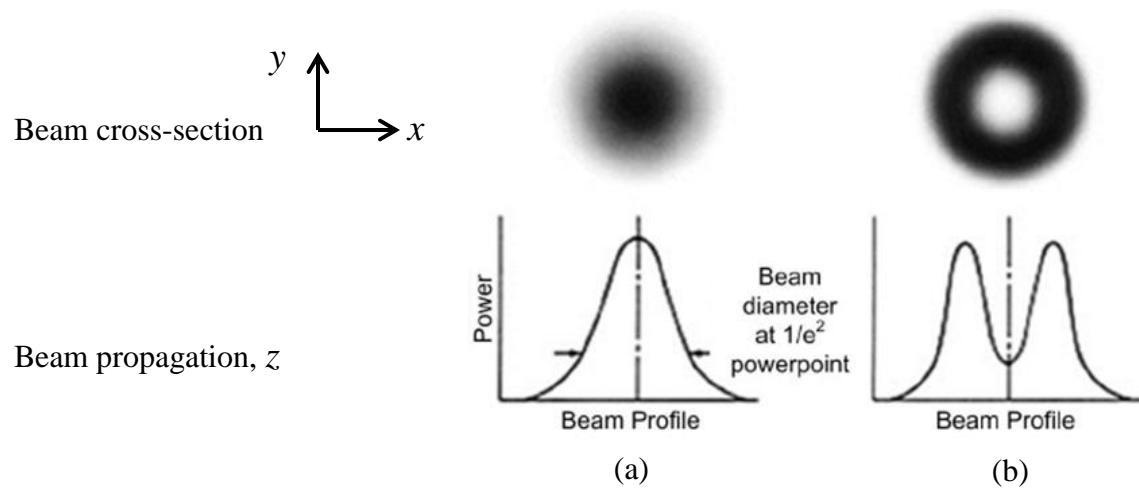
**Figure 1-5** The laser working modes (a) continuous and (b) pulse mode [8].

An additional parameter when working with (PW) mode is the pulse repetition frequency (PRF) which indicates the number of pulses per unit time and it can be in the range of a few Hertz to gigahertz. Pulse repetition frequency is an essential factor in laser treatment and machining of materials in addition to the other parameters characterising the pulse wave mode, like pulse energy, pulse width and duration time. The finite adjustment of these parameters reflects the flexibility of the process for

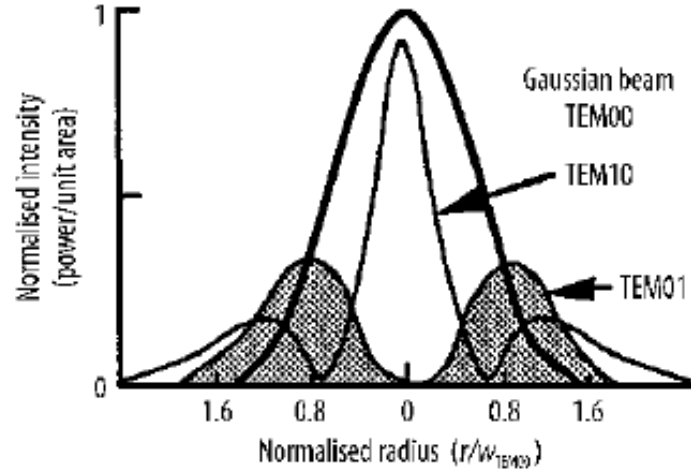
adequate multi-task materials treatment. For example, the pulse peak power in pulsed operating mode induces the high radiation absorptivity and the short duration time induces the high heating and cooling rates, the refinement of the grains and the formation of the non-equilibrium phases. The continuous wave mode is preferred over the pulsed mode when the required processed layer thickness is too high [6-8]. The surfaces treated by using the (CW) laser usually exhibit higher roughness which make it less applicable than the (PW) for applications require high wear resistance [14,15]. Continuous wave mode is recommended when processing metals with low absorptivity to the laser wave-length [16] and the processed surfaces suffer predominantly from cracks, porosity and bubbles [14][17].

#### 1.4 Laser beam profile and transverse modes

The cross-section of the laser beam exhibit a specific energy distribution profile known as the Transverse Electromagnetic Modes ( $TEM_{mn}$ ), where  $m$  and  $n$  are the number of nodes in the radial direction of the beam cross-section ( $x, y$ ). Figure 1-6 shows the  $TEM_{00}$  and  $TEM_{01}$  fundamental Gaussian spatial energy distribution modes which are commonly used in all types of laser machining processes [8-13]. Figure 1-7 shows the intensity distribution for three different operating modes. All the experimental work in this study was carried out by using a focusing lens with a Gaussian  $TEM_{00}$  distribution mode.

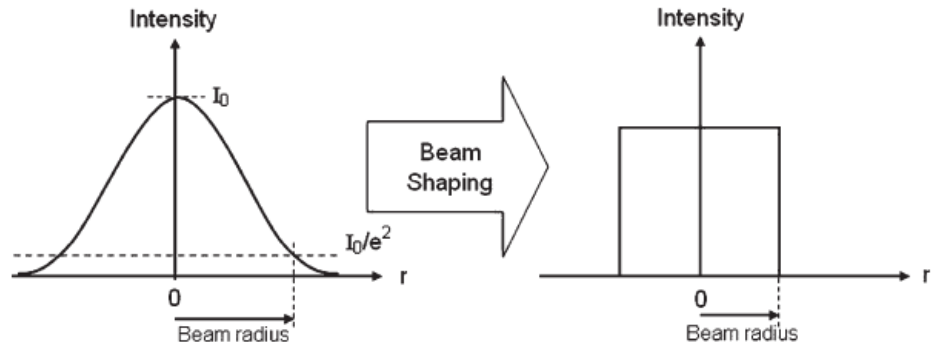


**Figure 1-6** Shows two spatial intensity distribution modes (a)  $TEM_{00}$  fundamental Gaussian and (b)  $TEM_{01}$  mode [18].



**Figure 1-7** Shows three different distribution modes [18].

For some specific applications, the beam intensity needs to be uniformly distributed. This can be achieved by using beam shaping optics. The resulting beam intensity profile is shown in Figure 1-8.



**Figure 1-8** Shaping the Gaussian profile beam into a “top-hat” beam [8]

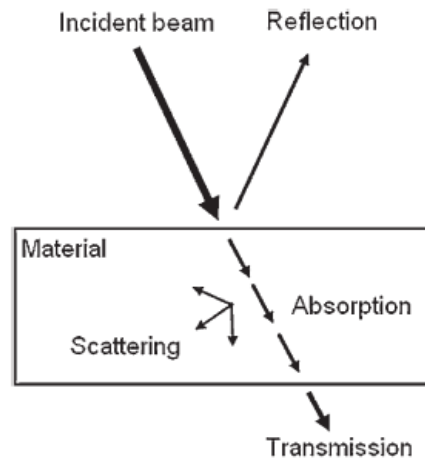
In Gaussian distribution profile the power intensity can be calculated from equation (1) [8]:

$$I = I_0 \exp \left[ \frac{-2r^2}{w^2} \right] \quad (1-1)$$

where,  $r$  is the radius of the beam,  $I_0$  is the beam intensity at the center of the beam ( $r=0$ ) and  $w$  is the beam radius when  $I=I_0/e^2$  [8].

### 1.5 Laser – materials interaction

Since laser radiation is an electromagnetic wave (i.e. oscillating transverse electric and magnetic fields), the laser processing in general can be described as an electromagnetic interaction process [6,8]. As the beam strikes the surface of the target medium, some of it would be reflected, some absorbed and some transmitted. When a laser beam strikes a surface of any matter, the electric force associated with the electric field would set the electrons of the matter to vibrate to some level. The energy gained by the electrons will be either re-radiated (reflected and/or transmitted) or absorbed and converted to heat energy, see Figure 1-9. The absorption of a metal to laser radiation depends on the metal type, the wavelength of the radiation and its intensity.



**Figure 1-9** The three possible scenarios of laser-material interaction [8]

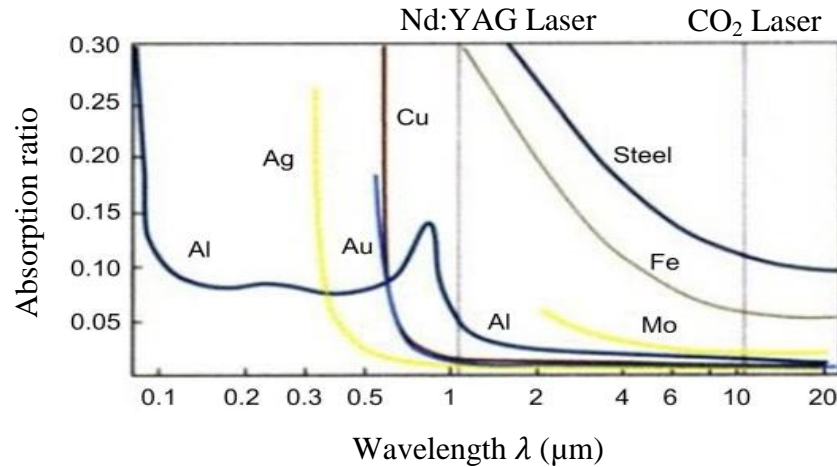
In general, reflectivity and absorptivity are correlated as follows:

For transparent materials: Reflectivity + Transmissivity + Absorptivity = 1

For non-transparent materials: Reflectivity + Absorptivity = 1

The value of each of these phenomena is a dimensionless fraction of a unity and is affected by several factors such as [6,19,20]

- a) Wavelength (see Figure 1-10)
- b) Surface temperature
- c) Surface films, i.e. contamination and oxide layers
- d) Angle of incidence
- e) Surface roughness.



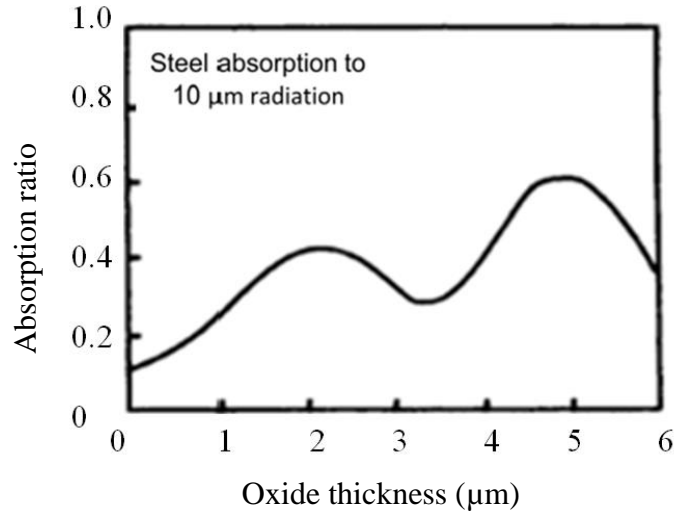
**Figure 1-10** The absorption ratio of materials to different laser wavelength [21].

**Wavelength:** Metals exhibit high absorptivity and low reflectivity at shorter wavelengths. More energetic photons can be absorbed by a greater number of bond electrons at shorter wavelengths [22]. Figure 1-10 shows that the absorptivity of iron surface (Fe) is 30% when scanned by Nd: YAG laser beam compared to 5% when processed by CO<sub>2</sub> laser.

**Temperature effect:** Metals surface absorptivity increases by the rise of the surface temperature and this action can be explained by the increase in the phonon-electron energy exchange [6,23]. The rise in energy makes the electrons prone to interact with the metal structure more than reradiate.

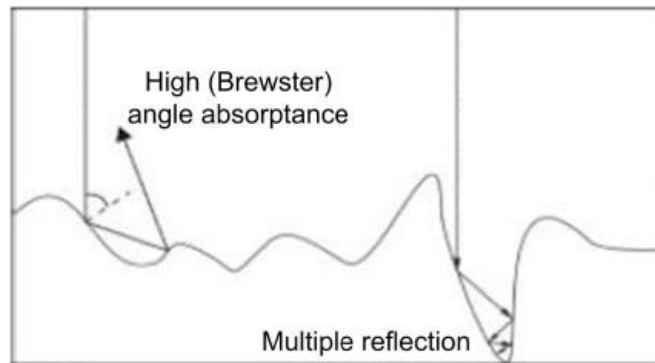
**Effect of surface films:** Absorptivity and reflectivity are surface properties thus the surface films have a significant effect. The following Figure 1-11 shows the absorptivity of steel scanned by 10.6  $\mu\text{m}$  wavelength CO<sub>2</sub> laser for different oxide film thicknesses. The plasma generated during the laser processing is an example of these films.





**Figure 1-11** The absorption ratio of steel for CO<sub>2</sub> laser wavelength as a function of the oxide film thickness [24].

**Effect of surface roughness:** Surface roughness is a crucial factor in radiation absorptivity [6,20,22,25,26]. The undulations of the high roughness surfaces would create multiple reflections for the laser beam, see Figure 1-12 in addition to the possibility of a stimulated absorption caused by the beam interference with the sideways reflected beams. Surface roughening by sand blasting can improve absorptivity to lasers for different materials [20,27]. For surface roughness smaller than the beam wavelength, the surface would be perceived as smooth.



**Figure 1-12** Laser beam multi reflections due to surface roughness may enhance the absorption [26].

## 1.6 Laser processing parameters

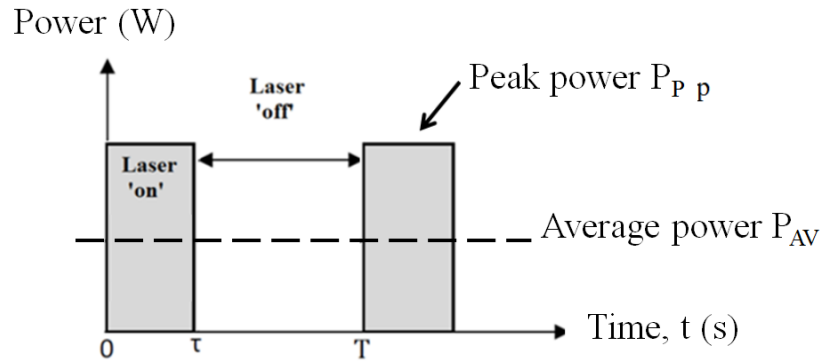
Laser surface modification of materials are influenced and controlled by a number of processing parameters. The different setting of these parameters will result in variation in surface mechanical, physical and microstructure properties of the treated material. The main laser parameters used in this research are listed below with their definitions:

### 1.6.1 Pulse energy, $E_p$

The average laser power delivered by one pulse and can be calculated by dividing the average power by the pulse repetition frequency, PRF.

$$E_p(J) = \frac{P_{AV}}{PRF} \quad (1-2)$$

where,  $E_p$  is the pulse energy (J). Several studies found that the amount of ablated material is proportional to the pulse energy [28–30]. The processed surface reached higher temperature levels when processed with short pulses for the same pulse energy [31–33].



**Figure 1-13** Schematic illustration of pulse operating mode and terms used.

### 1.6.2 Laser peak power, $P_p$

Output power is a principle parameter of a laser beam. Using the under-powered beam would result in increasing the processing time, and the process might not be executed. Moreover, using of overpowering beam power may be an excessive expense. The highest power of a CO<sub>2</sub> laser can be obtained when working in continuous wave mode while Nd:YAG laser is adopted for the highest power levels in pulsed mode operation

[7]. When working in both (CW) and (PW) mode, the average laser beam power affects the nature and scale of the resultant structure [34,35].

### 1.6.3 Duty cycle, DC

Duty cycle is the portion of time when the laser system is in operation and it represents a percentage (%) of laser pulse period. Duty cycle can be calculated as:

$$\begin{aligned}\text{Duty Cycle (DC)} &= \text{Pulse width } (\tau) \times \text{Pulse repetition frequency (PRF)} \times 100\% \\ &= (\text{Pulse width} / \text{Pulse period}) \times 100\% \\ &= (\text{Average power} / \text{Peak power}) \times 100\%\end{aligned}$$

Duty cycle affects the pulse width and then the material-beam interaction time for the same value of the peak power. The high duty cycle is recommended for welding process to prevent cracking [10][36]. Moreover, the large duty cycle was found to produce surfaces with higher roughness compared to processing by the continuous mode.

### 1.6.4 Average power, $P_{AV}$

The average power is the product of the laser power (P) and the duty cycle (DC). The average power of the laser beam significantly affects the nature and the scale of the processed material structure whether using the pulse or the continuous operating mode [37,38].

### 1.6.5 Laser power density (Irradiance), $I_{rr}$

Also known as the laser beam intensity at the incident point. It can be calculated by dividing the average power by the spot area:

$$I_{rr} \text{ (W/mm}^2\text{)} = \frac{P_{AV}}{\pi w_0^2} \quad (1-3)$$

where,  $I$  is the laser beam irradiance,  $P_{AV}$  is the average power (W) and  $w_o$  is the incident laser beam spot radius (mm). Laser beam irradiance has a significant effect on the processed surface roughness, microstructure and the thermal cycle [35,39]. High irradiance is associated by high laser beam power per unit area that would result in the increase of the molten pool size. This correlation was investigated by Stournaras et al. [40] and Choudhury and Shirely [41] during experiments on AISI 316L, Aluminium and Polymers cutting. Eltawhni et. al. [24,42], found that a reduction in CO<sub>2</sub> laser power from 1.49 kW to 1.02 kW with an increase in the cutting speeds range from 1538-1661 mm/min to 1900-2968 mm/min can be obtained when reducing the focal diameter 1.5 mm to 1 mm during cutting AISI316L austenitic stainless steel.

#### **1.6.6 Pulse repetition frequency, PRF**

In pulse wave operating mode, the pulse repetition frequency is the number of laser pulses triggered towards the sample surface per unit time (sec). Herman et. al. [43] found that the high PRF produces a better surface quality and significant reduction in the appearance of thermal stresses. PRF is greatly affected the morphology and the scale of the ablated portion [43,44]. Schaffer et al. [44,45] compare the material thermal diffusion time with the time between laser beam successive pulses. The researcher found that a heat accumulation occurs in the focal zone when using a shorter time between pulses which would result in heating up the material. Because pulse energy is inversely proportional to pulse repetition frequency, low PRF is associated with high pulse energy and hence development of thermal stresses that leads to micro cracks and flakes [43]. For this reason, it is a better controlled to implement high PRF with lower energy levels to enhance a uniform deposition and accumulation of heat.

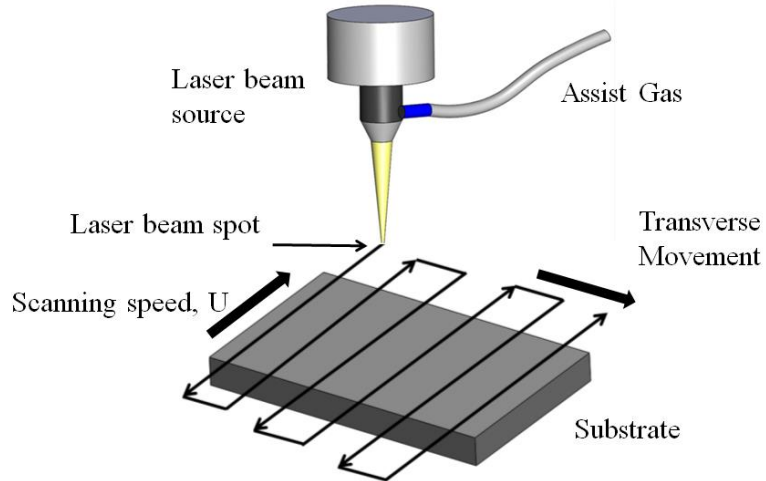
#### **1.6.7 Residence time and scanning speed**

Residence time is the laser beam-material interaction time or the time for the laser beam to be in contact with the metal surface and can be calculated as follows:

$$R(s) = \frac{\tau \times \text{PRF} \times d_s}{U} = \frac{\text{Duty Cycle} \times d_s}{U} \quad (1-4)$$

where,  $R$  is the residence time (s),  $\tau$  is the pulse width (s),  $d_s$  is the spot diameter and  $U$  is the beam scanning speed. When working in continuous mode (CW), the product of  $\tau$  and PRF would be equal to one since the duty cycle is equal to 100%.

The scanning speed is the relative speed between the metal surface and the laser beam. It is a crucial parameter in laser processing because it controls the amount of energy absorbed by the irradiated material to the laser beam energy. The higher the scanning speed, the lower energy absorbed. The following Figure 1-13 shows a schematic diagram for a sample substrate being scanned by a laser beam for the explanation of the terms indicated.



**Figure 1-14** Schematic diagram for the laser process showing the scanning speed and direction.

#### 1.6.8 Pulse energy density (fluence), $F_p$

It can be defined as the pulse energy delivered per unit area at the focal spot and is measured or specified in  $\text{J}/\text{cm}^2$  or  $\text{J}/\text{mm}^2$  in applications.

$$F_p = \frac{E_p}{\pi w^2} \quad (1-5)$$

The energy density is a significant factor controls the thermal energy delivered to the material, the melt pool size, and the consequent microstructure and surface profile. It can be controlled by adjusting the input power, spot size and the scanning speed [46]. Previous works have shown that the delivered fluence strongly affect the machined surface roughness [47,48].

#### **1.6.9 Laser pulse width ( $\tau$ )**

The time interval for the laser pulse to be active. Pulse width is a function of the duty cycle and PRF and can be calculated from the following equation:

$$\tau \text{ (s)} = \frac{\text{DC}\%}{\text{PRF}} \quad (1-6)$$

When the pulse width increases, the laser beam - material interaction time is longer, and a larger heat affected zone would be resulted and vice versa. In ultra-short pulse width ranges of femtoseconds, the heat affected features become unrelated to the spot size and they are much smaller than that of the long pulse width [49]. Moreover, in ultra-short and femtoseconds range pulses, the electrons of the processed material can acquire higher levels of energy from the laser pulse before dissipating it to the surroundings. This high energy level would create highly localized laser-induced material breakdown [50].

#### **1.6.10 Laser focal spot size**

Spot radius,  $w$ , “is the distance from the axis of the beam to the point at which the intensity drops to  $\frac{I_0}{e^2}$  from its value at the center of the beam” [8], see Figure 1-8 [9,11]. Focal spot size is a significant factor in determining the power intensity or irradiance value that is important in all types of material processing such as welding, ablation and melting.

Spot radius is corresponding to the minimum number of lenses used including the focusing. In a Gaussian beam profile, the minimum spot radius  $w$  is [8]:

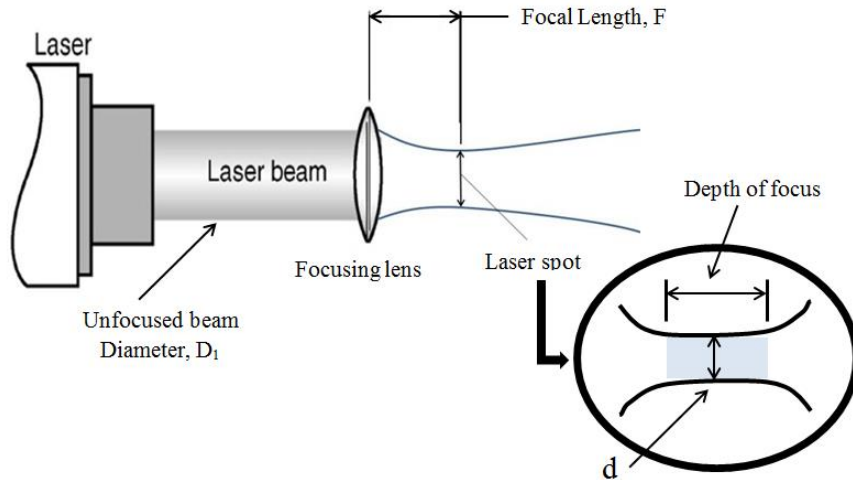
$$w = \lambda \times N \quad (1-7)$$

where,  $\lambda$  is the laser beam wavelength and  $N$  is the number of lenses, hence theoretically, the minimum spot radius can be equal to the wavelength of the laser beam when one lens is used for the diffraction. In practice, the minimum spot size is corresponding to the aberration value of the optics used and the best focusing conditions can be found by using a Gaussian beam profile.

Also, the focal spot size can be calculated as follows [7]:

$$\text{Focal spot diameter, } d = \frac{4\lambda F}{\pi D_1}$$

where;  $F$  is the focal length and  $D_1$  is the unfocused beam diameter as shown in the following Figure 1-15.

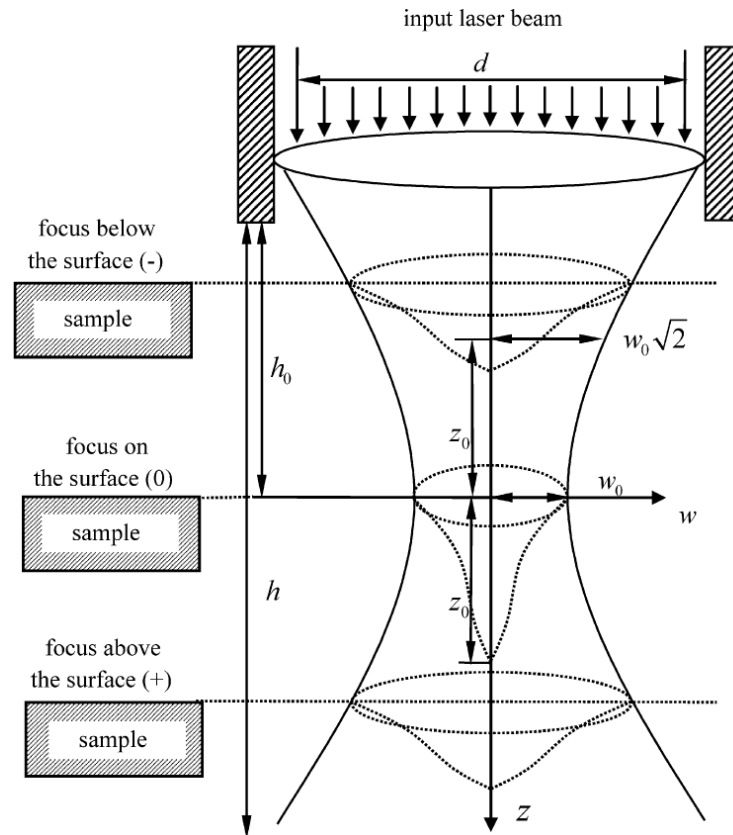


**Figure 1-15** Focal length, spot diameter and depth of focus for a Gaussian laser beam.

The focal spot size is affected by:

- a) The quality of the laser beam which is related to the laser beam divergence, the smaller the divergence, the smaller the spot size can be reached [12].
- b) Beam diffraction.
- c) The unfocused laser beam diameter, the larger the incoming beam diameter, the smaller the spot size.

The following Figure 1-16 shows the Gaussian beam characteristics with the three possible focal positioning scenarios used in materials processing. Positioning the sample surface below, above or at the beam focus allows to achieve various spot size and then various irradiance [18,22,24,25,51,52] and alters the modified layer microstructure [53–57][58].



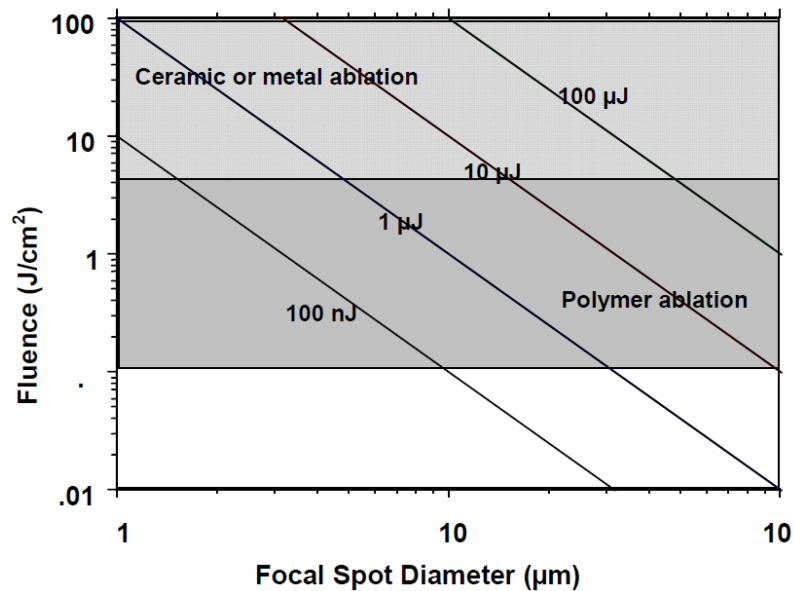
**Figure 1-16** Geometry and intensity of the Gaussian beam showing the beam focus positions with reference to the sample surface [58].



Despite the fact that the same spot size can be achieved when processing a substrate with focal position below or above the surface, the modified area was found to be larger when the laser beam focus is set below the surface. This is due to the 10% higher thermal energy absorbed when the focus is set below the surface [57, 60,61]. Adjusting different beam focus position was reported in several studies in order to obtain the required thermal energy applied and the resulting microstructure [61–65].

Irradiance is a significant parameter in all types of laser treatment. High irradiance is sufficient to melt, ablate and vaporize almost any kind of material. The maximum irradiance can be reached at the beam focal point smallest incident area.

In the following Figure 1-17, laser pulses with different energy levels between 100 nano-joules and 100 micro-joules were applied into a range of spot size between 1 and 100 microns to investigate the correlation between the focal spot size and the pulse fluence. The figure indicates that these low energy levels can be used to ablate most metals and non-metals such as ceramics when small focal spot size is applied [66].



**Figure 1-17** Fluence produced by focusing low energy levels into small spot sizes [66]

## Literature Review- Stainless steel alloys and Laser machining

### 2.1 Introduction

Laser machining can replace many conventional machining methods efficiently especially when processing (difficult-to-machine) materials like hardened parts, non-metal and composites. The advantages of laser machining are [7][67]:

- *It is a thermal process:* the high-temperature ranges that can be reached by laser processing for the machining of the parts with high hardness or brittleness which make them difficult to machined using the conventional methods.
- *It is a non-contact process:* this property reduces cost associated with high cutting forces, the need for fixtures, material damage, tool wear and machine vibrational quality control issues.
- *It is a flexible process:* when installed on a high-precision and multi-axis mechanism, laser heads are accurate and efficient to perform drilling, cutting, grooving, welding and surface heat treatment. Moreover the controlled processing parameters make the process highly repeatable. This flexibility eliminates the transportation of the workpiece for a subsequence process and the loss of accuracy.

Disadvantages of laser processing are the high thermal gradients produced which may cause localised high strain levels or changes in the material properties via phase change. Carbon dioxide, Nd:YAG and the fiber lasers are the most common laser types for machining. Each type can perform several processes when its characteristics and parameters are set appropriately. The wide range of these characteristic values indicates why lasers are a flexible tool in manufacturing and other applications. These characteristics include laser power, interaction time and irradiance (power/unit area). Among these three types of lasers the infrared CO<sub>2</sub> lasers have their advantages like; *the*

*low cost, ease of operation, high efficiency, large beam size and the non-toxic gases used* [37, 38]. CO<sub>2</sub> Lasers have become the most popular lasers because they are electrically more efficient (15-20%) and produce higher power of (0.1-50 kW) than other types of lasers [13]. The only one drawback of CO<sub>2</sub> laser is the large wavelength (10.64  $\mu\text{m}$ ) negatively affecting the absorption of the beam energy by the metal surface but the high thermal efficiency and the high output power level compensate the poor laser-metal coupling energy level.

The following Table 2-1 lists the characteristics for the different types of CO<sub>2</sub> laser and their applications.

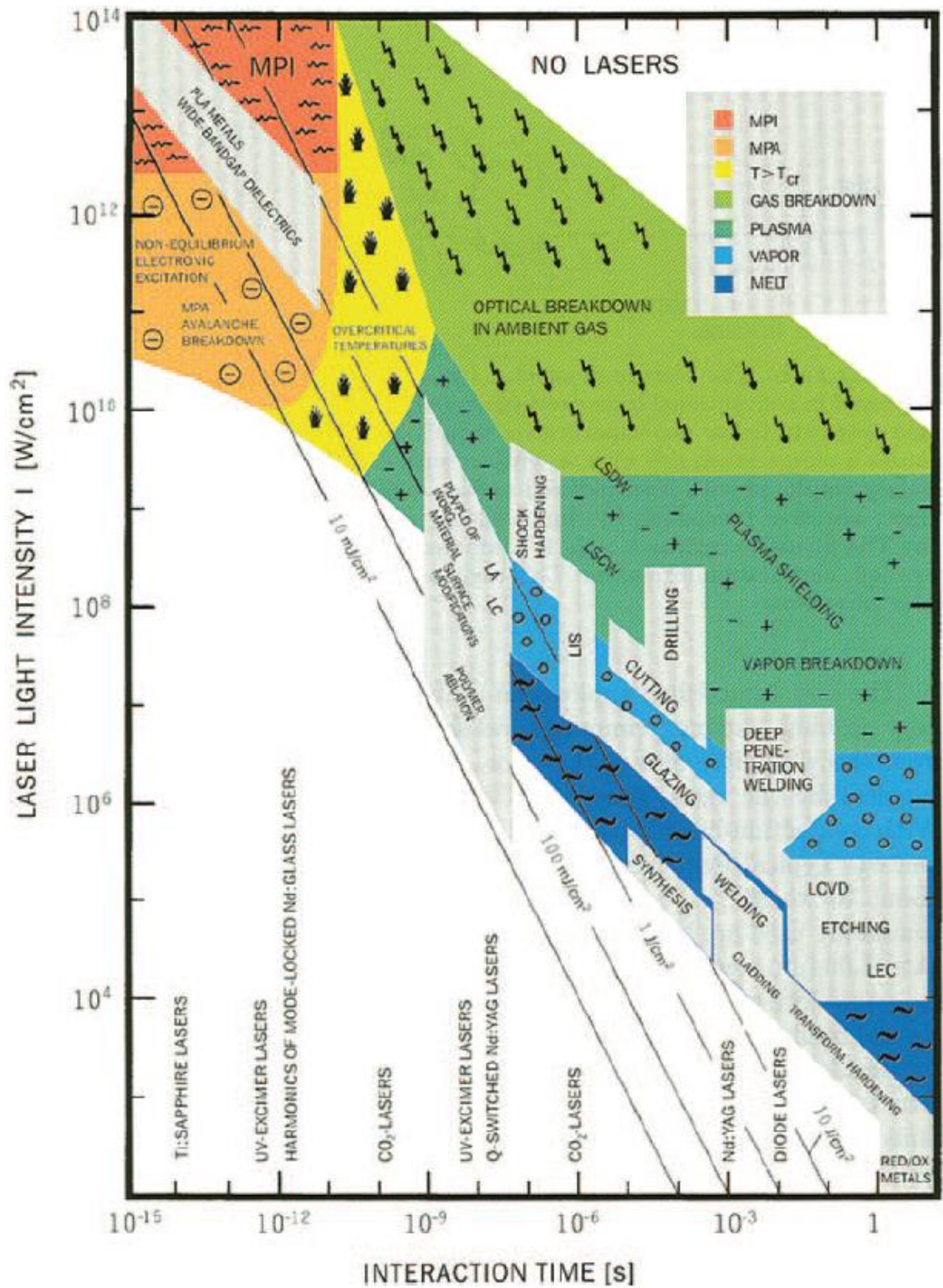
**Table 2-1** Types of CO<sub>2</sub> lasers and their specifications and applications  
as shown by W.M. Steen [6].

Property		Types of CO <sub>2</sub> lasers				
		Slow flow or sealed	Axial flow	Transverse flow	Transverse excited atmospheric pressure	Waveguide
Wavelength ( $\mu\text{m}$ )		10.6	10.6	10.6	10.6	10.6
Standard beam operating mode	CW	•	•	•		•
	Pulsed				•	•
	Q-switched					
Average output power (W)		3–100	50– 5,000	2,000–25,000		0.1–40
Output stability (percentage variation)			0.25–5	0.25–5	0.25–5	0.25–5
Pulse energy (J/pulse)					0.03–75	
Repetition rate (pulses/s)					1–300	
Beam diameter (mm)		3–4	5–70	5–70	5–100	1–2
Beam divergence (mrad)		1–2	1–3	1–3	0.5–10	10
Wall plug efficiency (%)		5–15	5–15	5–15	1–10	5
Most suitable applications	Cutting	•	•	•		
	Drilling				•	
	Part marking				•	•
	Welding		•	•		
	Cladding		•	•		
	Alloying		•	•		
	Microsoldering	•				•
	Heat treatment		•	•		
	Cleaning				•	

There exist distinct combinations of laser characteristics where the ideal laser material interaction can be reached. Figure 2-1 shows different regimes of laser-materials

interaction and their applications. The specific treatment can be determined by setting the laser power density and the laser-material interaction time (residence time) to the corresponding values [4,6]. These regimes include the following processes:

- Pulsed laser ablation/deposition, PLA/PLD
- Laser annealing, LA
- Laser cleaning, LC
- Laser-induced isotope separation, LIS
- Multiphoton absorption/ionization MPA/MPI
- Laser supported detonation/combustion waves, LSDW/LSCW
- Laser induced CVD, LCVD
- Laser induced electrochemical plating/etching, LEC
- Long pulse or CW CO<sub>2</sub> laser induced reduction/oxidation, RED/OX)



**Figure 2-1** Regimes of various effects during laser–material interactions and their application in laser materials processing [8].

This study is concentrated on the laser surface texture and modification of stainless steel 316L by melting and re-solidification. This process requires an accurately controlled amount of laser power to be induced on the metal surface and for a specific period of time in order to avoid the over-melting and ablation of material. Figure 2-1 shows that the laser intensity required for melting is  $<10^8 \text{ W/cm}^2$  and must be applied for a period of time  $>10^{-8} \text{ s}$ .

## **2.2 Types of stainless steel and their applications**

The chemical composition of stainless steel alloys contain relatively low carbon, a minimum chromium content of 10.5% and up to 30% nickel [70–73]. Chromium content might be increased for corrosion resistance enhancement as well as that of other elements like manganese, aluminium, titanium and molybdenum. Chromium is the key element in stainless steels that forms the refractory oxide protective layer and a barrier from corrosion and may repair itself if broken. Stainless steels are divided into three groups according to their metallurgical structure that forms when they are cooled from high temperatures. These are the austenitic, ferritic and martensitic stainless steel. However, only the austenitic stainless steel will be discussed here as for the 316L SST used in this study and the other groups are outside of the scope of this study.

Austenitic stainless steel (SST) is the most commonly used and accounts for more than 70% of production with type 304 the most common. They include: 301, 304, 304L, 316, 316L, 321 and 310. The basic chemical composition of 304 SST is 18% chromium and 8% nickel referring why the most popular type 304 has been called 18/8. The stable metallurgical structure at room temperature is a single-phase of austenite indicating the name of this group. The main characteristics of this group are;

- I. The ability to strengthen for up to four times by cold working
- II. High ductility
- III. Welding ability
- IV. High corrosion resistance
- V. Suitable for elevated surrounding temperatures (310-1100 °C)
- VI. Suitable for low temperatures (cryogenic boundary conditions)
- VII. Non- Magnetic

The most commonly used types of austenitic stainless steels and their applications are listed in the following Table 2-2.

**Table 2-2** Common types of stainless steel and their applications adopted from  
Steel & Tube stainless steel user guide [70].

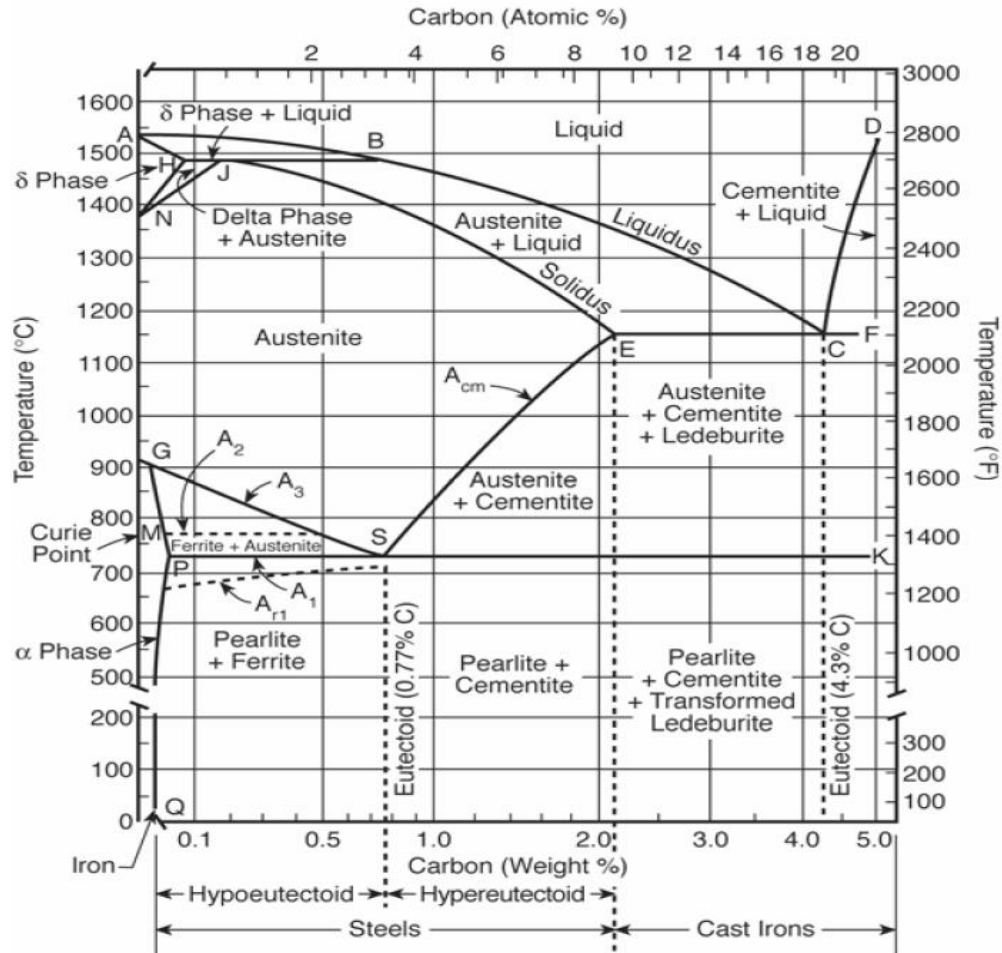
Grade	Applications	Properties
304	Architecture [exterior & interior]; food processing; handling and serving equipment; saucepans; hospital equipment; rainwater goods; household appliances; domestic sinks and laundry troughs, general deep drawing applications; brewing and dairy equipment; evaporators; drums; barrels; heat exchangers and refrigerator parts.	A general purpose austenitic corrosion resistant steel. Excellent deep drawing and cold forming qualities in the annealed condition. Can be polished to a high finish. Readily weld able for use in moderate corrosion resistant applications. Using appropriate techniques, 304 can be welded in thickness up to 12mm without subsequent heat treatment unless it is required for stress purposes.
304L	Chemical plant; food processing equipment; and for use in coal and petroleum industry.	An extra-low carbon austenitic stainless steel, with general corrosion resistance similar to 304, but with greater resistance to inter granular corrosion. Can be welded in greater thickness than 304, or heated for appreciable periods of time above 500°C without the need for subsequent solution heat treatment. Recommended when fabricating thickness in excess of 12mm, or where high heat input methods are used and subsequent solution heat treatment cannot be performed.
310	Furnace parts and equipment, baffles; heat treatment; boxes; retorts; furnace linings; heat exchangers.	Austenitic 25/20 chromium nickel steel offering excellent resistance to scaling at high temperatures. Mechanical properties in the higher temperature ranges are superior to other standard heat resisting steels. Can be employed for continuous service in the temperature range 900/950°C to 1100°C.
316	Exterior applications subject to severe industrial or marine atmospheres; chemical; textile; photographic and paper making equipment; wine vats.	More resistant to certain corrosive conditions than the standard non-molybdenum bearing austenitic stainless steel. Suitable where protection is required from highly corrosive non-oxidizing acids. Is used for plant and equipment in chemical manufacture. Has moderate deep drawing and cold forming properties. Able to be welded in thickness up to 12mm without subsequent heat treatment for most applications.
316L	Chemical plant and food processing equipment.	An extra low carbon modification for 316, with similar corrosion resistance. Intended for heavier sheet or plate fabrication where welding without subsequent heat treatment is required. Can be welded in heavy sections without the risk of inter-granular corrosion [weld decay] in the as-welded condition and also in the stress relieved condition under most circumstances. Suitable for polishing to a bright finish.



### 2.3 Iron-iron carbide (Fe-Fe<sub>3</sub>C) phase diagram

In this section, the iron-iron carbide phase diagram will be discussed to provide an understanding of the phase change during melting and re-solidification, which can be regarded as a low carbon content iron on the left hand side of the phase diagram in the following Figure 2-2.

Pure iron experience two changes in the crystalline structure before melting. Figure 2-2 shows the different phases for the carbon-steel in an equilibrium state which can be obtained by very slow (furnace) cooling from the melting temperature [74]. The pure iron at the room temperature is known as ferrite ( $\alpha$ ) with a body centred crystal structure (BCC). This phase transfer to the face centred (FCC) austenite ( $\gamma$ ) when heated for up to 912 °C. If the heating continues for up to 1394 °C, the later phase would transfer to the (BCC)  $\delta$  ferrite which persists until melting starts at 1538 °C. The temperature values indicated in Figure 2-2 are only valid for the slow heating and cooling. The high heating and cooling rates shift the transformation temperature lines  $A_1$  and  $A_3$  to higher and lower levels to be  $A_2$  and  $A_{r1}$  respectively.



**Figure 2-2** Iron-iron carbon phase diagram, carbon steel handbook [74].

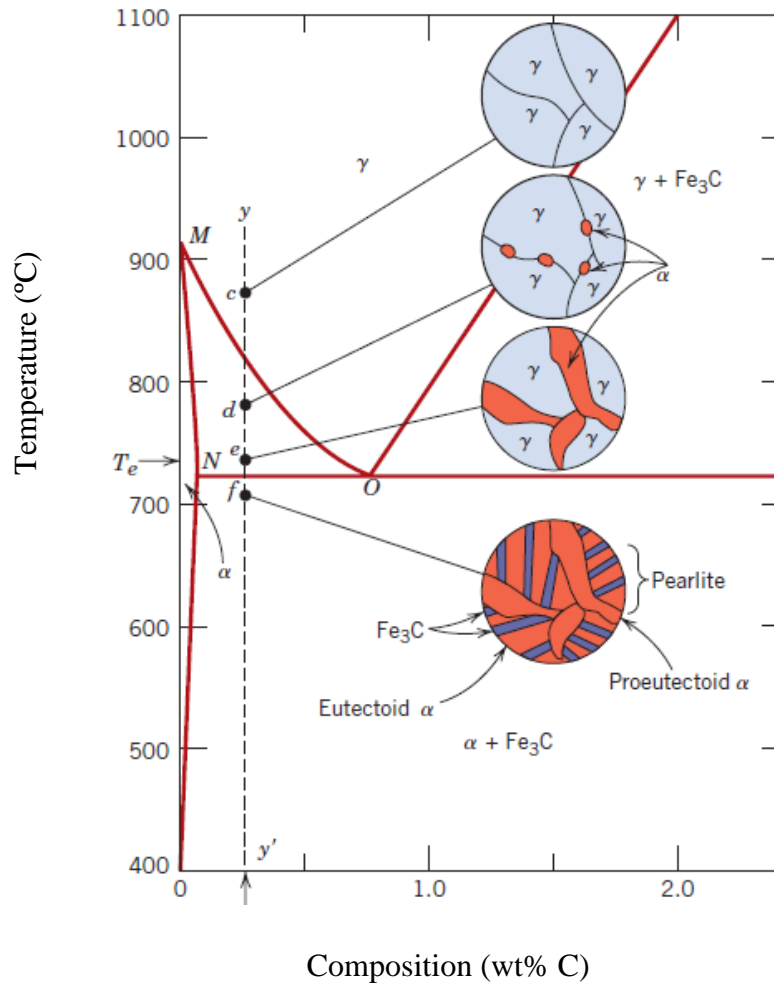
Three main zones can be classified as a ferrous alloys on the iron-carbide phase diagram based on the carbon content at room temperature:

- Iron: less than 0.008 wt% C in a ferrite  $\alpha$  phase.
- Steel: 0.008-2.14 wt% C in ferrite  $\alpha$ + cementite  $\text{Fe}_3\text{C}$ .
- Cast iron: 2.14-6.7 wt%.

Only the microstructure of the low carbon steel would be presented in this section, the other types are beyond the scope of this study knowing that stainless steel 316L is an alloys of several elements and that the following phase transform presentation is only accurate to some extent.

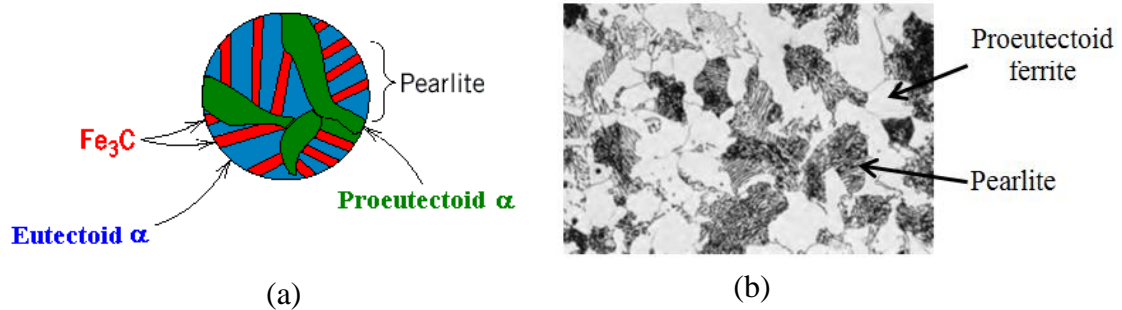
For example, the iron alloys with carbon content of 0.022-0.76 wt% C on the phase transformation diagram are known as hypo-eutectoid which means less than eutectoid in

Greek. These alloys contain pro-eutectoid formed above the eutectoid temperature and eutectoid perlite that contain eutectoid ferrite and pearlite, see Figure 2-3.



**Figure 2-3** Schematic presentation of the microstructure for the low carbon iron alloys [75].

In the equilibrium (furnace) cooling conditions along the  $yy'$  line, the  $(\alpha+\gamma)$  phase transform to the ferrite  $\alpha$  and cementite phases and a larger growth in the  $\alpha$  particles is resulted. The ferrite phase is soft and ductile due to the low carbon content. The higher carbon is concentrated in the hard cementite phase to form alternating lamellar platelets with the soft ferrite in the eutectoid pearlite, see Figure 2-4.



**Figure 2-4** (a) Schematic and (b) micrograph of the phases present at 0.38 wt% C steel [75].

The mechanical properties of pearlite are intermediate to soft, ductile ferrite and hard, brittle cementite.

The un-balanced or fast cooling from elevated temperatures alters the mechanical properties of any alloy due to the phase change and grain size change. The fast cooling does not allow for the grain growth so smaller grain size can be observed. The small grains microstructure exhibits higher strength and surface hardness compared to that of the bigger grains [76–78].

***Stainless steel 316L:*** Stainless steel alloys are made of several alloying elements, which make them highly resistant to corrosion and work in large variety of environments. The predominant alloying elements include chromium, nickel and molybdenum. The addition of the alloying elements effects physical, chemical and mechanical properties. The mechanical properties of stainless steel 316L are function of the microstructure and the thermal history. They are difficult to be hardened by heat treatment due to the low carbon content of 0.02% and can only be hardened by cold work or surface alloying for example carburizing, nitriding and cladding [75,79,80]. However, the surface hardening of stainless steel for more than ~300 HV by carburizing or nitriding is not preferred due to the formation of the stress corrosion cracking when working in high temperature water. This is caused by the precipitation of chromium carbide ( $\text{Cr}_2\text{C}_6$ ) and chromium nitride ( $\text{CrN}$ ) at the grain boundaries when stainless steel is heated between 425 and 800 °C in a phenomena called “sensitization”. This phenomena results from the degradation

of the corrosion resistance of stainless steel because of the losses of free chromium and the formation of electrolytic cells at the grain boundaries [9].

In laser processing of metal surface, the high heating/cooling rates of up to  $10^4$ - $10^{11}$  K/s [13], does not allow the low temperature phase transformation to occur. Also the high quenching caused by the cold substrate surrounding material reduces the crystallinity and increasing the chances to form the hard martensite from the soft austenite.

#### 2.4 Laser machining applications

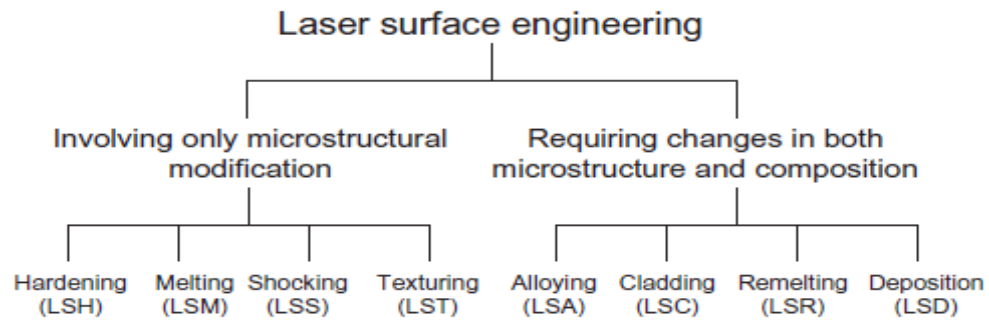
In contrast with conventional surface engineering methods, laser beams are preferred for the machining of hardened materials, ceramics and composites. The following Table 2-3 lists the strength and weaknesses of laser beam machining.

**Table 2-3** Advantages and disadvantages of laser machining [2,8,13,81]

Strength	Weakness
It is a thermal and electromagnetic process depending on the optical properties more than the mechanical of the part.	High energy needed to melt and evaporate the metal.
It is a non-contact process indicating no cutting forces and tool wear.	The high temperature required for the removal of the surface material may cause damage or decomposition of the parts made of polymer-matrix
The material to be removed is not limited by the tool force or the build-up edge.	It is a technically complex manufacturing process.
It is a flexible process and assembling the laser head on a high precision, CNC machine, a multi task processing such as drilling, welding cutting and heat treatment can be performed.	
<i>Other benefits:</i> No need for subsequent chemical cleaning and no or less after machining.	

### 2.4.1 Laser surface engineering (LSE)

Laser surface engineering (LSE) can be classified into two main types, the surface microstructural modification in which no change in material's composition occurs. This type includes processes like; hardening, melting, texturing and annealing. The other type requires changes in microstructure and in the composition of material like in cladding and alloying see Figure 2-5.



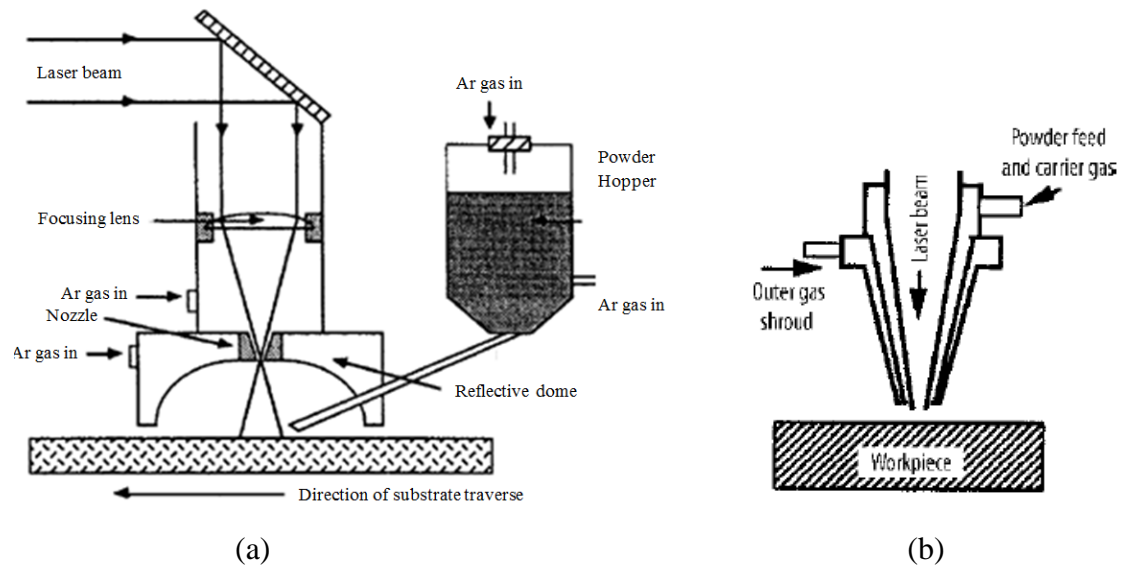
**Figure 2-5** Classification of laser surface engineering [13].

In addition to the advantages of the laser machining applications listed in Table 2-3, laser beams can deliver energy of  $1\text{-}30\text{ J/cm}^2$  or power density of  $10^4\text{-}10^7\text{ W/cm}^2$  with verity of pulses width of  $10^{-3}\text{-}10^{-12}\text{ s}$  and they can work in both pulse and continuous wave modes. The high heating and cooling rates of  $10^4\text{-}10^{11}\text{ K/s}$  and the instant re-solidification speed of up to  $1\text{-}30\text{ m/s}$  render the development of an exotic near-surface microstructure and the formation of metastable amorphous phase [13]. Several studies investigated the surface roughness of the metal parts after laser beam irradiation [69,82,83] and reported that the resulting surface roughness is proportional to the scanning speed [55], irradiance [84] and pulse width [85].

### 2.4.2 Laser surface cladding

By definition, laser cladding is the surface melting process with the addition of alloying material onto a substrate by means of laser beam as a heat source [36]. The process is usually carried out by covering a relatively inexpensive substrate material with a more expensive material to enhance wear and/or corrosion resistance [18,36]. The product would have the improvised properties of the expensive material at the surface. The

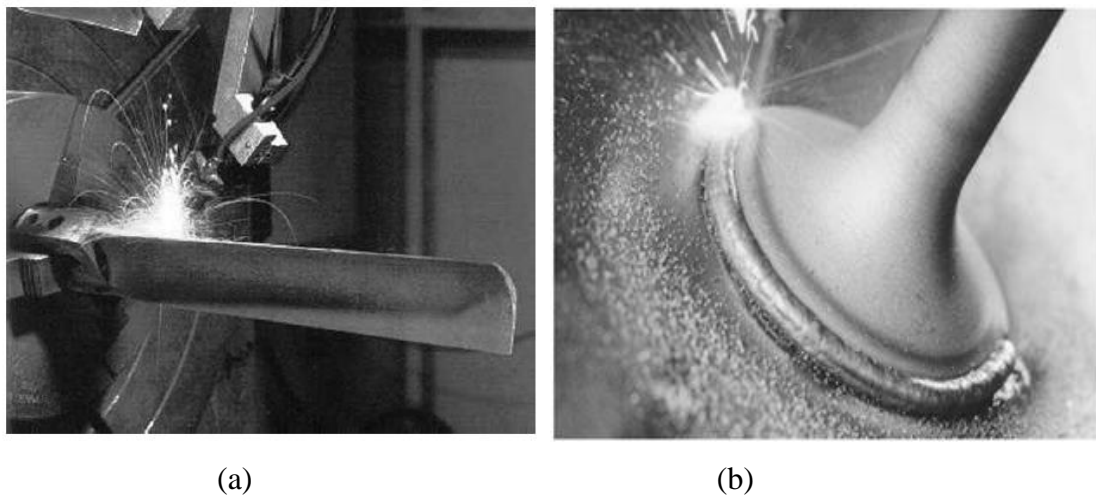
conventional approaches for cladding was represented by inert gas welding, plasma and flame spraying. The drawbacks in using these techniques were the cladding porosity, uneven cladding thickness and the damages caused by the elevated temperature, such as the dilution of cladding alloys and part distortion. These problems have been overcome or reduced by the use of laser cladding producing a better control on the part's dimensions and minimizing alloy dilution. Feeding of alloy cladding material powder may be carried out during or prior to the laser melting zone as shown in Figure 2-6. The molten powder is deposited and clad with the molten part of the substrate. The final modified surface properties can be tailored to a given application with specified improvement in hardness, wear, corrosion, and oxidation resistance.



**Figure 2-6** Arrangements for laser cladding by the (a) blown  
(b) coaxial powder feeding techniques [5].

Laser cladding process is similar to laser alloying; they only differ in the dilution amount. Whenever the percentage of dilution exceeds, 10%, the process is known as alloying more than a cladding [86]. Duhamel et al. [87] achieved melting a hard facing alloy chip onto the notch region of a turbine blade. The chip was melted by the irradiation of a CO<sub>2</sub> laser of 4.5 kW and 1.5 mm beam size for 10 s residence time. The blade is then machined to the original dimensions. Rolls-Royce adopted the blown

powder technique for laser cladding their RB- 211 series engines to replace the old method of TIG coating in which implications of achieving the final tolerances and dilution of control persist. Laser cladding is applied by several manufacturers such as aircraft engine group of GE (Cincinnati, OH, USA) and Honeywell International Aerospace Services (Norcross, GA, USA) to repair worn components. Figure 2-7 shows a CO<sub>2</sub> laser cladding process for depositing alloy powder on a rim valve. In general, most materials that tolerate laser melting would be suitable for laser cladding, i.e., stainless steel, alloys based on aluminium, titanium magnesium and nickel.



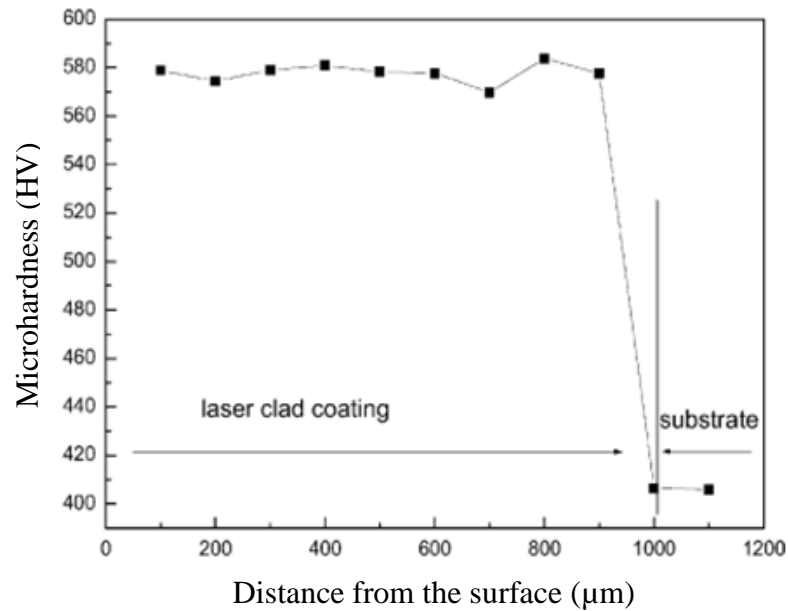
**Figure 2-7** CO<sub>2</sub> Laser cladding of (a) steam turbine blade to improve erosion resistance (Juha Kauppila) and (b) cobalt based powder on a valve rim. (Tero Kallio) (Lappeenranta University of Technology, Finland) [36].

Cladding alloys may contain tungsten carbides, cobalt, iron, titanium, silicon and ceramics, like zirconia. The selection of laser type depends on the coverage area, the thickness of cladding, bonding and the product geometry. The primary goal of the process is to produce a part with appropriate properties, strong bonding with the substrate and minimal distortion. When a large cladding surface area with several millimetres in thickness is needed, CO<sub>2</sub> laser is preferred. When high accuracy with three-dimensional components and thickness of less than one millimetre is needed, then a robot mounted diode or Nd: YAG laser light transmitted via a fiber-optic cable is preferential.



Significant levels of surface modification can be reached, for example, a uniform improvement in surface hardness and wear resistance of a BT9 titanium alloy reinforced by  $\text{Ti}_2\text{Ni}_3\text{Si}$  intermetallic composite coatings deposited by  $\text{CO}_2$  laser cladding.

Figure 2-8 shows the microhardness profile of the clad coating layer along the depth of the titanium substrate. The profile readily shows the uniform distribution of  $\text{Ti}_2\text{Ni}_3\text{Si}$  with an average hardness of approximately 580 HV [88].



**Figure 2-8** Hardness distribution profile along the depth of a laser clad titanium substrate [88].

Imperfections:

*Crevice*s: the main reason behind them is the lack of fusion often observed at the toes of overlapping clads. Also might be present when the aspect ratio (thickness/width) is too high and might be overcome by adjusting the powder feeding rate or the traverse of the workpiece.

*Cracking* since laser cladding is a thermal process hence the main reason of cracks appearance is the thermal stresses developed because of the high thermal gradients created during cooling. They could be reduced by preheating the substrate prior to treatment.

*Distortion* is caused by the residual stresses during cladding that would fail the part at any stage during work lifetime. It can be reduced by reducing the laser beam power when working with CW mode or switching to pulsed mode (PW) or a post-process heat treatment to reduce stresses.

*Porosity* which may be presents in two forms; fine porosity caused by degassing after solidification of clads. Coarse porosity which is caused by the gas pockets trapped in the centre when the outer region solidify first. The interface between the molten clads substrate surface is a source of porosity. A contaminated surface may generate vapours of volatile organic compounds that influence the wetting ability of the molten clad. Cleaning and degreasing of the surface can reduce the porosity.

*Dilution* small part of the substrate must be melted in order to form a strong metallurgical bond. The two molten metals would be mixed by convection and efficiently diluting the composition of the clad. Dilution can be controlled by adjusting the feeding rate of the alloy powder and the laser parameters. Adjustment of all parameters must be to such level that the reproducibility of the process is reachable at all time.

### **2.4.3 Laser surface glazing**

In this type of surface processing, a small portion of the metal surface is melted when scanned by a multikilowatt CO<sub>2</sub> laser. The interior of the substrate remains cold. A rapid solidification and quench occur on the molten surface after the laser beam moves on. Because of the high quench rate, the surface microstructure may result in unusual properties and very small grain size that might be useful for some specific applications. The extreme rapid cooling caused by the high thermal gradient between the surface and the bulk material results in significant microstructural alteration. The material atoms would not have sufficient time to form crystals. Instead, they freeze in random arrangements producing improvement in strength, hardness, wear and corrosion resistance [89]. The new surface can appear more glassy and hence the name of the process. Glazing is applicable for metals, and ceramics and the process is very controllable and reproducible and mainly applied for wear resistance enhancement. One example of this process is the glazing of cast iron to produce a white surface layer with

high hardness and wear resistance and the aluminium bronze glazing to enhance the corrosion resistance [18].

It is difficult to distinguish all the process parameters that promote the glazed surface formation because of the large variation of irradiance and the exposure time that can be found [13,18,25,36].

#### 2.4.4 Laser surface alloying

Laser surface alloying (LSA) is similar to laser surface melting and cladding except for the injection of another material and a higher level of power is implemented compared to cladding process [6]. The addition of the alloy material is carried out in two ways:

- a) Co-deposition in which alloy material is injected with the laser beam simultaneously resulting in a new chemical composition for the substrate surface. The alloying element could be in the form of gas, powder or wire [52,90–93].
- b) Pre-deposition where the alloying material is deposited prior to laser irradiation.

The characteristics of (LSA) process are listed in the following Table 2-4:

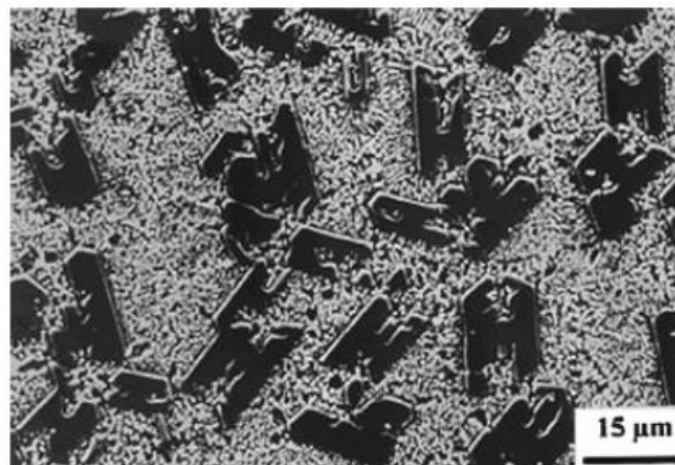
**Table 2-4** Characteristics of laser surface alloying (LSA).

Advantages	disadvantages
Fine microstructure and homogenous mixing the melt area. Signs of inhomogeneity are recorded in fast melt tracks (0.5 m/s).	Precision in placement and good adhesion of the alloys and vast improvement in processing speeds (e.g., 70 mm/s for the power of 2 kW).
Wide range of materials is suitable for use as alloying and substrate material. The high quench rate minimizes the segregation and guarantees the formation of surface alloys, e.g., Fe-Cr-Mn [94].	Some loss of the unstable components can be expected.
The processed zone thickness is (1-2000 $\mu\text{m}$ ). Thin and rapid quenched alloys can be mad using Q-switched Nd: YAG lasers.	Some alloys may suffer cracking and porosity that limits shrouding and preheating implementing.

Gavigan et al. [95] achieved a hardness of 549 HV on a titanium substrate surface by using LSA process in a nitrogen environment. The invention was registered as a patent in the United States in 1994. A titanium shaft sample of 50 mm in diameter and 250 mm in length was preheated in a furnace of air atmosphere to a temperature of (540-650 °C). An accurate control of laser processing parameters and nitrogen gas concentration resulted in a high hardness and crack free surface compared to the conventional method of nitriding. The thickness of the processed layer crucially depends on nitrogen gas pressure and concentration in the gas mixture and a balancing percentage of an inert gas such as argon might be used. Laser nitriding of titanium could be conducted with either ND:YAG or CO<sub>2</sub> lasers of CW modes at power densities of ( $10^8$ - $10^{11}$  W/m<sup>2</sup>) [95,96].

### Applications

*Titanium* LSA is widely conducted on titanium surface to improve wear and high-temperature oxidation resistance. The treatment can be performed by either carbon or nitrogen. Titanium nitriding can be carried out by treating the titanium substrate in a nitrogen shroud using laser beam as a heat source [97–99]. The hard carbide or nitride solidifies first forming dendrites of attractive colours. Figure 2-9 shows the hyper-eutectic microstructure of a Ti substrate alloyed with Si consisting of Ti<sub>3</sub>Si<sub>3</sub> uniformly distributed in a two-phase eutectic aggregate of  $\alpha$ -Ti and Ti<sub>3</sub>Si<sub>3</sub> [100].



**Figure 2-9** SEM of the top surface of a Ti-Si treated by LSA [100].

*Nitinol*, NiTi alloy of nearly equiatomic is an excellent material for applications like stents because of its unique properties, such as super-plasticity and radiopacity. The alloy can be nitrided producing an enhanced-surface sealing and corrosion resistant surface that ameliorates the danger of nickel release [6].

*Cast-Iron* is also alloyed with chromium, silicon and carbon to make relatively cheap cast iron into superficially exotic irons.

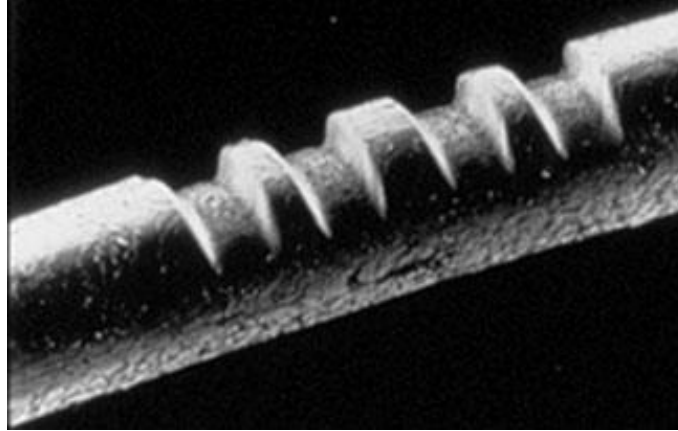
*Steel* can be alloyed with chromium, molybdenum, boron and nickel.

*Stainless steel*, carbon alloying in stainless steel by melting a pre-deposited powder.

*Aluminium*: Walker et al. [4][57] reported that the aluminium surface can be hardened by using LSA process to deposit silicon, carbon, nitrogen and nickel.

#### **2.4.5 Laser cold cutting**

This process is usually applied to organic material in addition to other material that are difficult to cut like ceramic. Organic materials can absorb ultraviolet laser efficiently, and because these materials are thermal insulators, the cutting edge is well defined with minimum amount of debris and thermal damage [6,9,101,102]. The photon energy in the ultraviolet range of radiation is 3.5 to 6.5 eV which is similar to the bond energy for most organic materials. When a photon with this level of energy, high power and ultra-short pulses of picoseconds strike this bond, the bond breaks and the material disappears with no heating which indicates the high quality of the process. Ultraviolet radiation has the lower wavelength in the biologically hostile range of radiation. The next higher radiation energy would be X-rays and  $\gamma$ -rays. The technique has wide application in electronics manufacturing and marking. Figure 2-10 shows a human hair been textured using this technique. This technique suggests a high range of medical applications represented by microsurgery.

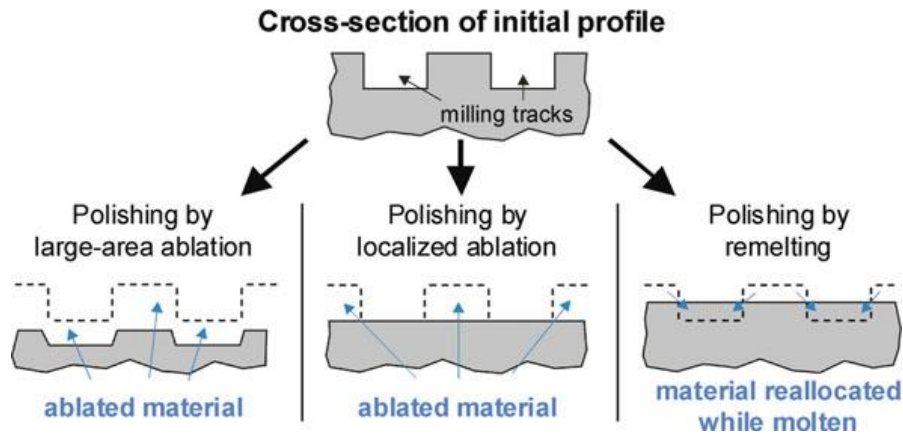


**Figure 2-10** A human hair textured using an excimer laser [6].

#### **2.4.6 Laser surface polishing**

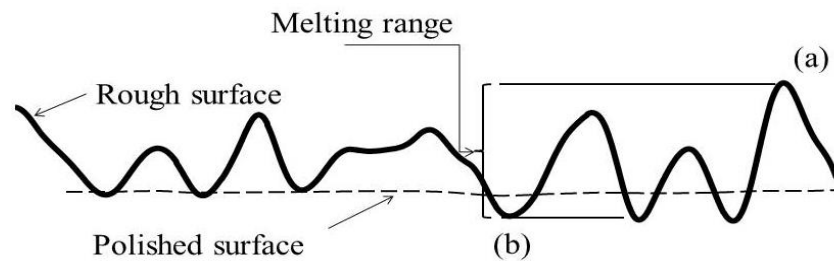
In addition to the mechanical and tribological properties, physical properties and visual impression of mechanical and artificial parts are also important in most applications in addition to the customer demand. It is a finishing process by which the surface roughness is reduced to enhance wear, removing oxide layer, adjust tolerances ..etc. Conventional mechanical polishing methods include grinding by means of abrasive discs and machining by using high speed lathe and/or milling machines. These processes are limited sometimes due to the high effort required because of the low feeding rates especially when applied on parts with high surface hardness or a complicated geometry [103–106] in addition to the tool wear and damage. Laser polishing is a new method in which the metal surface is irradiated with high power density and ultra-short laser pulses. Laser polishing can be classified into three types as can be seen in the following Figure 2-11:

- a) Polishing by large area ablation in which a large range area over the whole surface is melted and ablated.
- b) Polishing by localised ablation. In this process only the undesired rough and prominences are melted by laser beam down to a set surface level. This process require high control on the applied power density and the coordination of the portions under ablation.
- c) Polishing by re-melting.



**Figure 2-11** Types of laser polishing.

The following Figure 2-12 shows the re-melting process in more detail. This method is the most common laser polishing process in which no material ablation occurs mostly [107], the power density is calculated and adjusted to melt the metal surface in a nanometre scale. The roughness peaks (a) in Figure 2-12 are melted and the molten material imparted to the lower level valleys (b).



**Figure 2-12** Illustrates the principle of laser polishing by melting the metal between (a) and (b) of the rough surface and producing the polished surface shown in the dotted line.

Figure 2-13 presents examples for this method: a wine glass metal mould is shown before (left) and after (right) laser polishing. The polishing was carried out in the micro scale (less than 40 microns) after the milling process to enhance the gloss and shiny level finishing.



**Figure 2-13** Shows the laser micro-polishing of a glass mould, before polishing (left) and after polishing (right) [108].

#### **2.4.7 Nitriding**

Nitriding, in general, is a ferritic thermochemical treatment of diffusing nitrogen in cast iron and steel. The process was first developed in the early 1900's, and the advantages were identified in the early 1920's. The modified nitrided parts must have the enhancement of the following surface properties [109–111]:

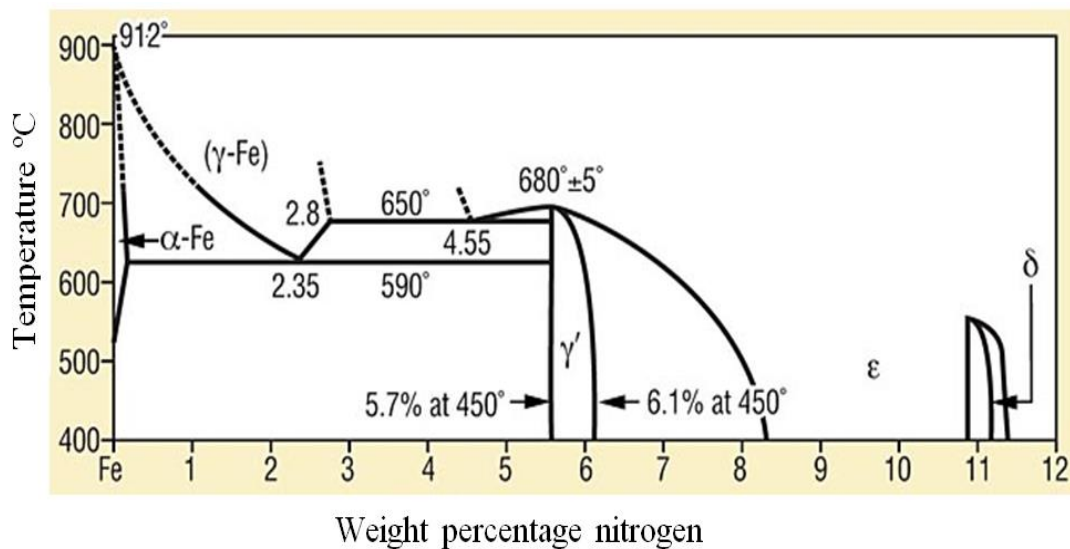
- High wear resistance
- High corrosion resistance
- High compressive strength
- Abrasive wear resistance

Nitriding is regarded as the simplest method of surface hardening and applied often in industry for example: automotive, aircraft, turbine generation system and bearings. Many mechanical parts and tools are nitrided to modify their chemical and tribological properties such as toothed-gears, camshafts, cylinders and bio-implants. The advantageous characteristic of the process is that there is no phase change from ferrite or cementite (depending on the chemical composition) to austenite during the entire treatment. Hence, there is no phase change from austenite to martensite because of the free cooling of treated parts compared to quenching. Also, the molecular structure does not alter from the body-centred cubic (BCC) to face centred cubic (FCC). There is only a negligible growth in the dimensions caused by nitrogen diffusion. The major



drawback of the process is the presence of surface residual stresses induced by the elevated temperatures that may cause bending or twisting [112].

Figure 2-14 shows the iron-nitrogen equilibrium diagram. The solubility of nitrogen in iron is a factor of temperature. Absorption of  $N_2$  in iron is up to 6.1% at temperature of 450 °C and the formation of the  $\epsilon$  phase is induced. The solubility is decreased at a temperature of 680 °C. The formation of the  $\delta$  phase is induced from 11 to 11.35% Ni at temperatures below 500 °C.



**Figure 2-14** Iron-nitrogen equilibrium phase diagram [113].

The process in general is controlled by a number of parameters such as treatment temperature, processing time and gas flow rate. Gas nitriding hardening has developed fast to produce alternative nitriding methods like salt bath and ion nitriding. In salt bath nitriding, nitrogen gas is replaced with a molten salt rich with nitrogen. A steel part is placed in the molten salt and heated up. The liberated nitrogen gas is absorbed by the steel surface producing a better, thicker and uniform metallurgical formed case. The process is carried out in a relatively higher temperatures of 585 °C and shorter processing time of 90 minutes compared to gas nitriding of up to 75 hours. Also, the process required low capital and operation cost, lower operating skill level, less space area and easy to start and shutdown. Other common types of nitriding are plasma

nitriding and ion-beam nitriding, which can decrease the time and temperature needed compared to gas nitriding [114]. The composition of the salt used in this process is a combination of sodium and potassium cyanide [113,115]. The treated parts are manufactured to the nearest net shape, hardened by quenching, tempered to high temperatures (590-650 °C), machined to the final dimensions before nitriding. The nitrided surface is hard in nature and difficult to machine for this reason it is crucial avoiding cracks and any dimension detriment. The induced nitrided layer has significant high hardness, fatigue resistance and can work efficiently in particular corrosive environments.

### **Laser nitriding**

The development of laser and its employment in industry in recent years make it a very powerful and competent tool for many applications like; cutting, welding, drilling, glazing and heat treatment. The use of laser irradiation in metal nitriding was first investigated by Katayama et al. [116] and since then it has been investigated for various materials and by using different laser systems. Laser nitriding is the irradiation of metal surface in a nitrogen containing atmosphere and used to produce surface hardening in the surface layers of steel alloys containing elements that incubate the forming of nitride like aluminium, chromium molybdenum and vanadium [43, 44].

Aluminium for example is approved to form a very hard constituent when used as alloying element with steel in the range of 1 to 1% [112]. Several studies reported large improvement in the hardness and corrosion resistance on iron, aluminium, titanium and other materials by the formation of FeN, AlN and TiN layer after laser nitriding [97,109].

Nitriding of steel alloys according to their alloying elements is robust compare to ordinary steels hence; special steel alloys have been developed. As a process, parts are heated to temperatures of 525 to 675 °C in ammonia atmosphere (containing nitrogen and hydrogen gas) for 10 to 40 hours. The nitrogen gas diffuses into the surface metal of the steel forming a modified hard layer of approximate thickness of 650 micron.

The advantages of the process are:

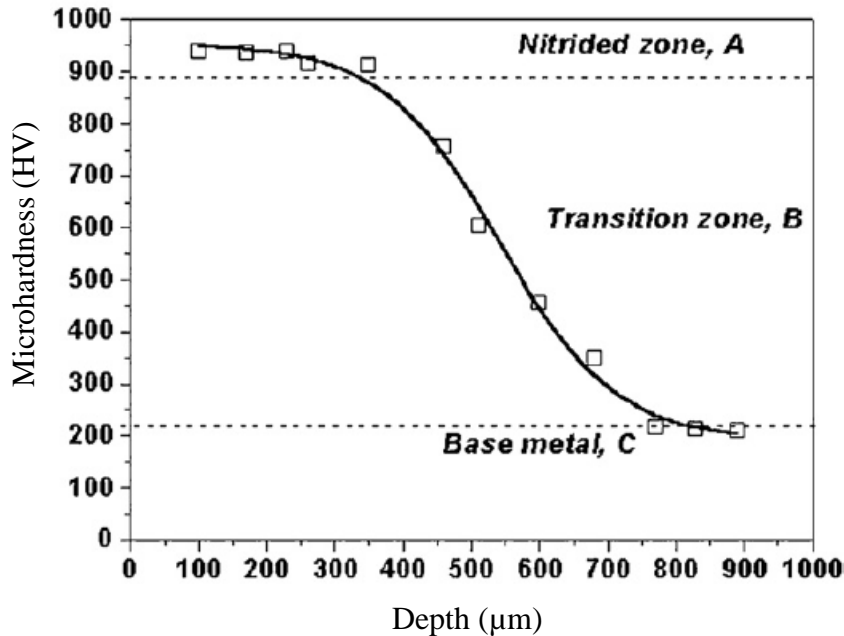
- There is no phase change from ferrite to austenite or from austenite to cementite because the heating temperature is below the phase transformation temperature

so there is no molecular structure change as in the conventional methods such as carburizing [112].

- No subsequent process is needed such as quenching and there for no warp or cracks are developed.
- The processed parts exhibit enhanced hardness, slide wear resistance and corrosion resistance against water, salt water, crude oil and natural gas [119].
- The modified hard layer is very thin, so there is no major change in the part's dimensions restricting the process to products with high dimensional accuracy.

The main disadvantages of the process are the long processing time and that processed parts must be machined to the required dimension prior to nitriding.

Laser nitriding has been investigated previously and was found to be encouraging for the enhancement of the mechanical and tribological properties of the mechanical parts such as hardness, corrosion and wear resistance of different materials and alloys like iron, carbon steel, stainless steel, aluminium and titanium [1,109,120–122]. Some researchers have studied the influence of the main laser processing parameters on the effectiveness of nitridation of the metal surface and the optimization of these parameters with reference to the presence of cracks, pores and melt evidence [123]. Psyllaki et. al. shows that CO<sub>2</sub> laser beam power of ~1 kW in the continuous mode is optimal for the hardening of 1.5919 steel with a noticeable micro-hardness improvement from 220 to 950 HV in a significant thickness from the treated surface, see Figure 2-15.



**Figure 2-15** CO<sub>2</sub> laser nitriding of steel using (power =1 kW, scanning speed=5 mm/s and 1 successive pass [123].

The researcher indicated that using the power levels of less than 1 kW shows no significant changes while higher power levels of 1.5 kW resulted in extensive undesirable melting. Also, the study found that a higher nitride zone thickness can be reached when the nitrogen gas is delivered vertically on the substrate and that multi scans are needed when using high scanning speed.

The nitride layer is metallurgically bonded to the bulk material in a more significant form compared to the conventional nitriding methods [49,52,53]. Shuaeib et. al. [125] reported that the nitride layer thickness is between few microns to few hundred microns. Several researches in laser nitriding have been performed using vacuum chamber and then the pure nitrogen gas is pumped in [126]. To the best of our knowledge, the laser nitriding process of metals has not been optimized until the writing of this thesis. This fact has been also reported by several researchers [127–129].

Nitrogen has a very limited solubility in iron. In ferrite, nitrogen solubility is around 0.4 at.% at temperature of 592 °C. In austenite phase, it's 10.3 at.% at 650 °C while it could be up to 12 at.% in martensite phase [109]. At the iron melting temperature of 1540 °C and nitrogen gas surrounding at atmospheric pressure the solubility is nearly 0.17 at.%

but could be significantly increased by 3 times using arc discharge above the molten surface [130].

The application of 100% N<sub>2</sub> gas might result in surface cracks and brittleness. Liu and Baker [131,132] reported that the high cooling rates encourage the formation of the surface macro/micro-cracks in a laser nitrided Ti-6Al-4V alloy. Liu reported that the better selection of the main laser processing parameters might result in the reduction of the residual stresses and then the surface cracks. On the other hand, Baker [131] suggested preheating the sample prior to the laser processing would reduce the cooling rate and produce a modified surface with hardness of more than 600 HV and a high control of the presence of any cracks. An alternative way to overcome this problem is the application of diluted nitrogen usually with argon but at the expense of the hardness. Several researchers employed different mixing ratios of argon-nitrogen gas composite [131,133–138]. Selamat et. al. [137] reported the achievement of crack-free processed surface of Ti-6Al-4V using a mixing ration of 20%N<sub>2</sub>-80%Ar. The argon gas content as an assist gas is beneficial by decreasing the molten metal surface tension allowing a larger penetration for the nitrogen [139].

***Why study nitriding?*** Nitriding to improve the properties of steel has possible applications in making rolling fatigue resistant gears [140], cut blades [141], bipolar plates in proton exchange membrane fuel cells [142], and biomedical applications such as surgical instruments [143]. In the application of the interference-fit, the failure of the pin-insertion joint is most likely expected to occur by separation caused by the fretting of the textured surface peaks due to the dynamic loads. Increasing the processed surface hardness by nitriding would result in the reduction of the fretting effect and the wear of the thin lamellar section texture. This would result in the increase of the contact forces which in turn reduce the relative movement.

At the present time, there is no accurate details on the processing parameters and their values because the technique itself is still new and no amount of researches and experiments have been reported so far. Also, the treated layers properties depends on the laser-plasma-material interaction which encompass heating, convection, plasma formation, fluid dynamics, diffusion and metallurgical process. However, the minimal

dimensions of the heat affected zone related to the small laser beam spot size make it ideal to treat complex sections and parts without changing the core properties.

The present research is focused on the laser texturing of cylindrical stainless steel samples by using argon as assist gas. The success in laser nitriding of different materials by enhancing the physical and chemical properties with a crack free coating layer was the motivation factor for this study.

### 3.1 Introduction

*Interference (press) fit* fasteners are widely used in industry; e.g. bolts, rivets, positioning pins, and tapered insertion pins. They have extensive applications in automotive and aerospace because they are easy to fit, dismantle, replace, or repair. Interference fit, also known as press fit, are commonly used in industry for a hub and shaft coupling assembly, in which the hub hole is machined slightly smaller than the shaft diameter [144–146]. The difference between these diameters is referred to as the "interference". Engineers and technicians usually follow the rule of thousandths, which is 0.001 to 0.002 units of diametric interference per unit of shaft diameter. Machinists usually use the limits of 0.025 mm of interference for shaft diameters of up to 25mm, and 0.05 mm for diameters between 25 and 100 mm. The two parts are then forced together during assembly using a press, generally with the presence of lubricant oil. The friction and the difference between the two mating parts geometry create a contact pressure. Both the friction force and the contact pressure created depend on the contact area, the interference volume and the coefficient of friction, and they are responsible for the prevention of sliding or loosening during power transmission from the shaft to the hub [144,146–149]. The process of manufacture of this high precision interference is carried out on high precision lathe machines, and sometimes also employing cylindrical grinding (externally on the shaft surface) and jig grinding (for the internal grinding of the hole). The quality of the bond, as well as bonding and de-bonding forces, are extremely sensitive to these dimensions. This represents an important drawback for this process, due to the high cost of labour and machining, as well as the potential for poor bonding quality due to surface deterioration or damage from excessive surface deformation. Another drawback to be considered is the difficulty of the assembly when maintenance is needed and that the whole assembly might need replacement after a number of maintenance cycles.

*Cold expansion* is also widely used in industry. In this method a tapered mandrel is inserted in a slightly smaller hole diameter hub from one end all the way to the opposite side. During insertion, a significant plastic deformation is produced in the hole peripheral area. Moving further in the radial direction, an elastic deformation is produced in the material loaded below the yield point (elastic limit). After the insertion, the elastically deformed zone generates a compressive residual stress on the hole circumference. This compression residual stress can significantly delay the initiation and propagation of fatigue cracks, and prolong the insertion lifetime [150–152]. The technique has been employed and developed by Boeing for some applications, such as the landing gear and the engine mountings [150,152].

Another common method for joining parts is using *knurled pins*. This method is predominantly applied in die casting, and for the joining of wood, plastic, and thin sections applications [145]. In the die casting assembly, the knurled pin (mandrel) and the hub are positioned together by tooling while melted zinc alloy is injected into the void between the mating components. The shrinkage of the solidified alloy allows for a strong mechanical joining, for example, joining the mandrel to an abrasive wheel. In the force-inserted knurled pin application, the knurls lead to two types of joining during insertion. The first is the cutting joining, in which the chip cut and the formation of the knurled in the hub results due to the axial insertion of the pin into a slightly smaller diameter hub. This type of joining forms a closure in the tangential direction. The second type of joining is the forming joining, in which a radial displacement is created in the hub and generating a high groove pressure and a closure in the axial direction.

These mechanical joints usually exposed to cyclic loads and may fail by fatigue and crack propagation, as a result of the residual stresses on the pin or the hole during manufacturing and assembly. Studies in the past six decades have tried to innovate a practical solution to this problem with limited implications for the shaft-hub interference, the elastic-plastic deformation calculations, and design. Surface modification has been shown in the literature to allow for the production of components with higher hardness, wear resistance, and fatigue life [153,154]. These treatments have a variety of applications in industry and biomedical implants. Improvement of hardness and wear resistance is usually achieved by nitriding, using Physical or Chemical



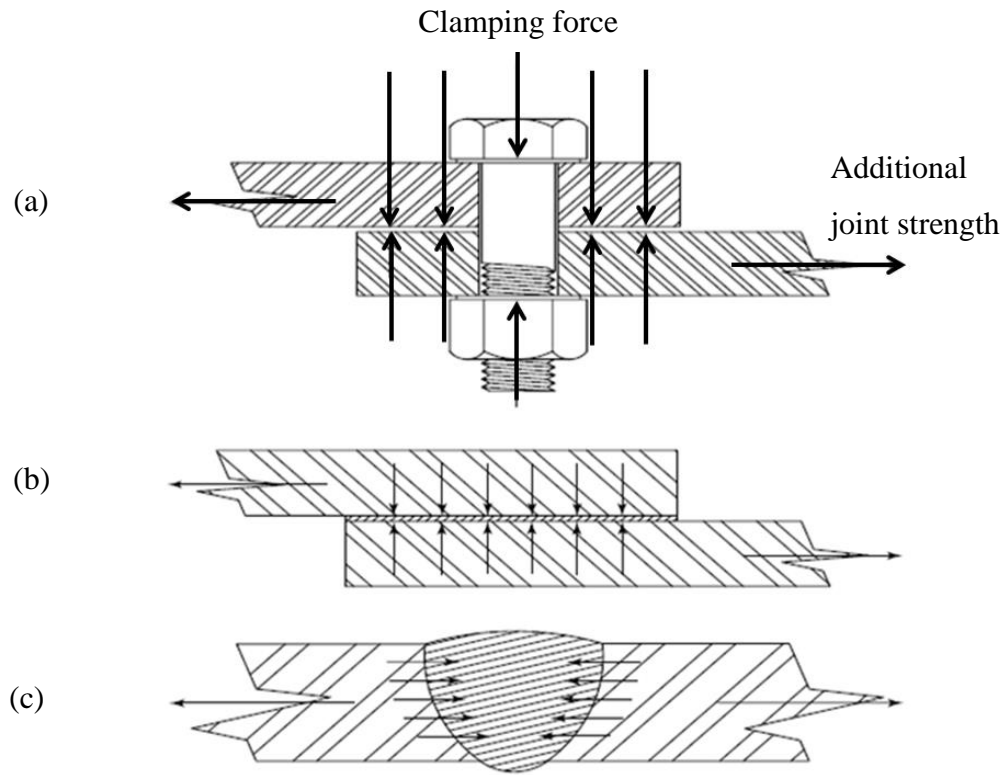
Vapour Deposition methods (PVD) or (CVD) [155]. Lasers have been used as a heat source in tool steel nitriding, and have produced useful material properties [109,156]. Despite the fact that laser nitriding is a complex process, the accurate control of the processing parameters (laser fluence, number of pulses, spot size, and the gas pressure and concentration) controls its influence in different materials [109].

In structural and component section bonding, interference fit is also used in power transmission applications, where a driver (shaft) is pressed into a hub section. Such power transmission can be achieved via direct coupling, gears, chains, keyways, spline shaft-hub, and tapered insertion. In industrial applications, the most predominant shaft-hub insertion methods used are the press fit or the shrink fit.

In this work a new surface laser treatment process was utilized to enable novel high value add press-fit connections. The novelty of this new interference fit joint design is the ability to achieve pre-defined bonding forces and bond strength. Fasteners are created by laser texturing the surface of stainless steel pins. The fastener's surface morphology and dimensions can be precisely achieved by controlling the working parameters such as laser beam power, laser spot size, pulse repetition frequency (PRF), scanning speed, and the overlap between each scan. Other interesting aspects of this approach are its ability to provide very repeatable results and with better-defined margins of quality control and safety which are critical for a number of applications, such as airplane manufacture.

### **3.2 Traditional Fastening Methods**

Fastening and Joining are mainly made in three different ways according to the bonding force namely (see Figure 3-1): (1) Mechanical, (2) Chemical and (3) Physical bonding forces, R.W. Messler [157]. In the mechanical joining, forces arise from interlocking and resulting interference between the parts when a fastener (pin) is inserted in a smaller hole diameter hub. Chemical forces arise from chemical reactions between the joined parts caused by the application of adhesive materials. The last type of joining is the physical bonding in which the attraction forces between the atoms and the oppositely charged ions and molecules lead to bonding forces in a process generally known as welding.



**Figure 3-1** Types of joining: (a) mechanical, (b) chemical and (c) physical joining of parts, adapted from [157].

Only the *mechanical joints* type would be studied here as the other types are beyond the scope of this research.

The efficiency of the joint can be represented as the effectiveness of the joint compared to the rest of the structure when supporting the applied loads. The following Table 3-1 lists the joint efficiencies based on static strength for the most common types of joints and materials and calculated as:

$$\text{Joint efficiency} = \frac{\text{Joint stress}}{\text{Structure stress}} \times 100\%$$

where, the joint stress is the stress resulted on the bolts (in the case of the mechanical joint) and the structure stress is the stress experienced on the rest of the structure material at the joint due to the load applied.

**Table 3-1** Joints efficiencies for various processes and materials (%) [157]

<i>Joining Method</i>	<i>Metals</i>	<i>Ceramics</i>	<i>Glass</i>	<i>Polymers</i>	<i>Composites</i>
Mechanical Fastening	75–100+	<50	<50	50–100	50–100
Mechanical Attachment	75–100+	near 100	N/A	100+	50–100+
Adhesive Bonding					
Organic adhesive	<20	<20	<20	40–100+	20–60 (100+)*
Inorganic adhesive	N/A	50–100+	20–50+	N/A	50+
Cement/Mortar	N/A	50–100+	N/A	N/A	50–100+**
Welding					
Fusion processes	50–100+	30–80	100	100	about 50
Non-fusion processes	100	80–100	N/A	100	about 50
Brazing	40–90	20–70	N/A	N/A	about 50
Soldering	5–20	<20	10–40	N/A	UNK
Braze Welding	50–75	N/A	N/A	N/A	UNK
Thermal Spraying					
Metals/Ceramics	30–80	30–80	N/A	N/A	N/A
Polymers	<20	<20	N/A	50–100+	>50
Rivet-Bonding	75–100	N/A	N/A	100+	UNK
Weld-Bonding	25–75	N/A	N/A	100+	UNK
Weld-Brazing	50–80	N/A	N/A	N/A	UNK

From Table 3-1, it can be seen that joint efficiency varies widely. For example, joining of two flat metal plates by welding could be efficient for up to 100% when the weld is carried out in a full penetration and by using a similar composition to the base material and when the strength and stress developed at the weld is equal to that in the base material. The joint efficiency might be less than 100% when welding is performed using weaker filler material and vice versa.

Mechanical joints advantages:

- High efficiency
- Ease of disassembly, in most applications without damaging the parts
- No changes in the materials chemical composition
- Need no experience and little or no preparation
- The ability to automate the process
- Allow some degrees of freedom suitable to dynamic structures

Disadvantages:

- In some applications, sudden failure without precautions
- Stress concentration might be resulted at holes, sharp edges and welding
- Extra weights added compared to other types of joining
- Some mechanical joint are difficult to carry out or automate and need experienced labour skills.

### **3.3 Types of Fits**

There are several types of fits. Many companies and associations have drawn up standards to be used in their production. The American Standards Association (ASA) has classified the running and sliding fits based on the basic hole system. That is the nominal size is the minimum hole diameter. The tolerance on the hole diameter is always positive while the tolerance on the shaft diameter is always negative for a working fit [158]. Moreover, the American National Standard Institute has also tabulated the classes of fits according to the unilateral hole basis such that the mating parts would always exhibit the same performance throughout the range of sizes. The tables include all types and sizes that approved in the American-British-Canadian classification [159]. Theoretically an infinite number of fits might exist but the main categories that may cover most applications can be classified as:

- (RC) Running or Sliding Clearance Fit
- (LC) Locational Clearance Fit
- (LT) Transitional Clearance or Interference Fit
- (LN) Locational Interference Fit
- (FN) Force or Shrink Fit

The selection of size limits, the type of fit can be obtained according to the use of the application, and the limits of the final dimension of the mating parts can be established then.

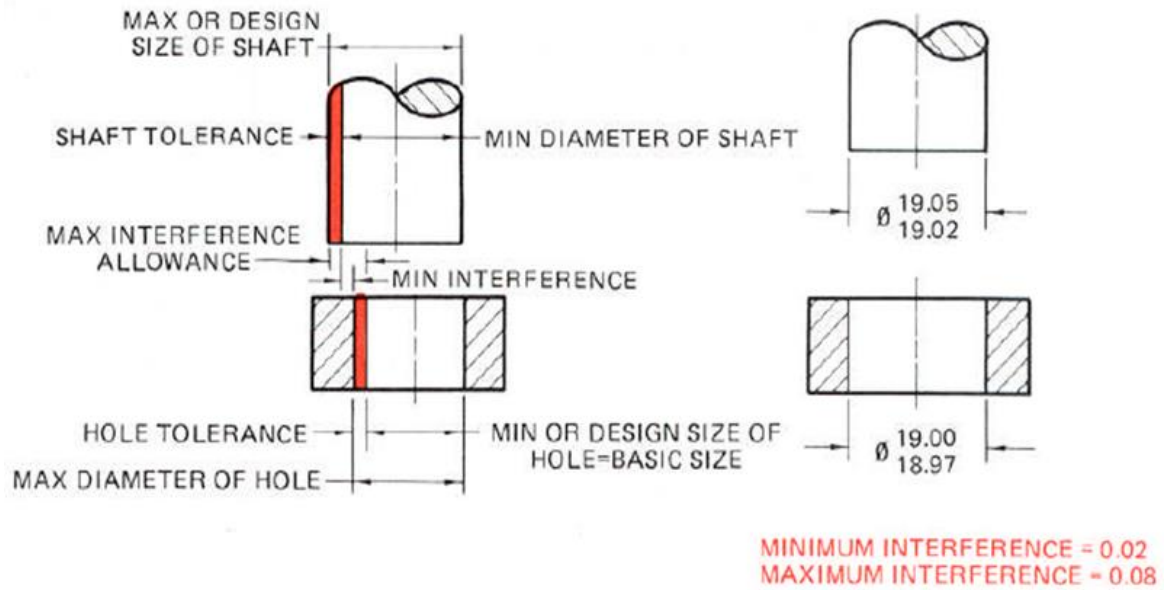
### 3.3.1 Press and shrink Fit

When the pin diameter is greater than the hole diameter, a force or pressure is required to put the mating parts together in a cold assembly. The interfering material is called the negative allowance. The American Standard Association (ASA) categorised interference-fits into five categories according to the transmitted load: FN1, FN2 and FN3 for light, medium and heavy drive fits respectively. FN4 and FN5 categories for force fit applications when mating parts can stand high stresses. When the amount of force required for assembly is impractical, shrink fits can be applied by even cooling the inner part or heating the external part or both. The implication and drawback in this techniques is miss the positioning, once parts assembled together and cool down to room temperature, they would seize so errors of assembly would result in damaging expensive parts. The other drawback here is the fact that each part was exposed to different temperature during the process. This in turn would lead to residual stresses in the assembly and further heat treatment at elevated temperature is necessary [160,161]. There is some elastic and plastic deformation on the mating parts after the assembly and existence of pressure at the interface [146][162]. The minimum and maximum interference values of a feature control the amount of variation in the size and geometric of the feature. These limits would decide the final dimension limits between the maximum and least material conditions, (MMC) and (LMC). The range of the fit feature can then vary between the established upper and lower limits of the size dimension.

The minimum and maximum interference can be calculated as follows, see Figure 3-2:

**Minimum Interference** = Lower limit dimensions of the shaft – Upper limit dimension of the hole.

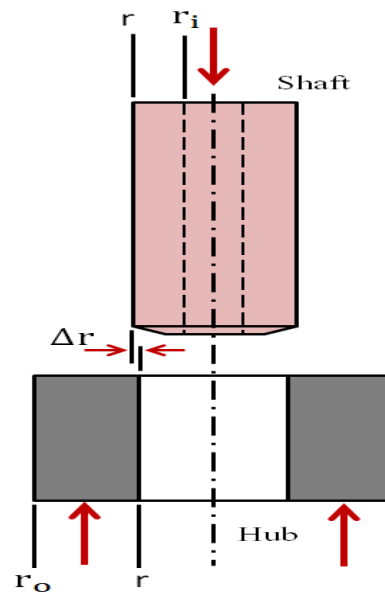
**Maximum Interference** = Upper limit dimension of the shaft - Lower limit Dimensions of the hole.



**Figure 3-2** Schematic of the tolerances between two mating parts [162].

### 3.3.2 Stresses in the interference fit:

The pressure applied on the shaft and the hub in interference fit is similar to an external and internal pressure applied on the surface of a shaft and a thick wall cylinder respectively [144].



**Figure 3-3** Schematic of an interference-fit joint design [144].

This pressure can be calculated by applying the following equation:

$$p = \frac{0.5 \delta}{\frac{r}{E_o} \left( \frac{r_o^2 + r^2}{r_o^2 - r^2} + v_o \right) + \frac{r}{E_i} \left( \frac{r^2 + r_i^2}{r^2 - r_i^2} - v_i \right)} \quad (3-1)$$

where:  $\delta$  is the diametral interference between the shaft and the hub (i.e.  $\delta = 2\Delta r$ ),  $r$  is the nominal interference radius,  $r_o$  is the hub (ring) external radius,  $r_i$  is the shaft (pin) internal diameter (applies for a hollow shafts only)  $E$  and  $v$  are the Young's modulus and Poisson's ration for the pin and the ring respectively.

The torque transmitted through the joint is a function of this pressure and can be calculated from the following equation:

$$T = 2\pi r^2 \mu p l \quad 3-2$$

Where:  $l$  is the interference engaged length and  $\mu$  is the friction coefficient which is suggested by AGMA standard to be  $0.15 \leq \mu \leq 0.2$  for a shrink and press interference fits [144].

Solving these two equations gives:

$$T = \frac{\pi l r \mu \delta}{\frac{1}{E_o} \left( \frac{r_o^2 + r^2}{r_o^2 - r^2} + v_o \right) + \frac{1}{E_i} \left( \frac{r^2 + r_i^2}{r^2 - r_i^2} - v_i \right)} \quad 3-3$$

The pressure ( $p$ ) in equation [3-1] is used to calculate the radial and tangential stresses in both the shaft and the hub.

$$\text{For the shaft} \quad \sigma_{\text{shaft tangential}} = -p \left( \frac{r^2 + r_i^2}{r^2 - r_i^2} \right)$$

$$\sigma_{\text{shaft radial}} = -p$$

For the hub

$$\sigma_{\text{hub tangential}} = p \left( \frac{r_o^2 + r^2}{r_o^2 - r^2} \right)$$

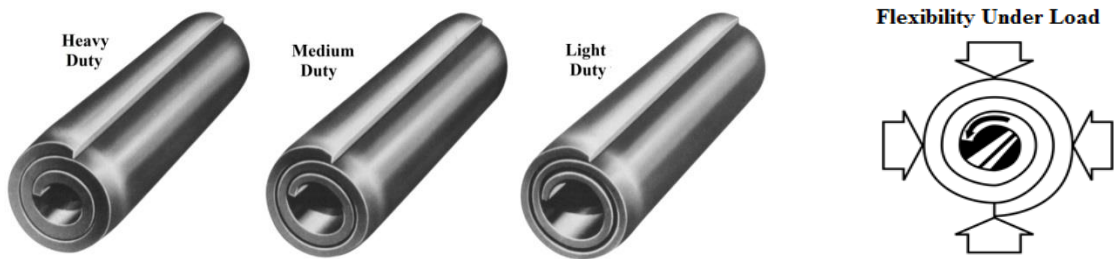
$$\sigma_{\text{shaft radial}} = -p$$

The maximum permissible values for these stresses must be less than the yield strength of the material. Reaching the yield strength would lead to the failure of the material and the hub would be loose on the shaft due to a plastic deformation.

### 3.4 Commercial and commonly used fixtures

#### 3.4.1 Spirally Coiled Pins

Among the most versatile fasteners available are the spirally coiled pins, Figure 3-4, are widely used for their flexibility both before and after insertion. This type of pins can absorb shocks and dynamic loads, reduce any damage to the hole and absorb the vibration transmitted between the assembly elements.



**Figure 3-4** The basic design of a spirally coiled pin [145].

Parmely [145], listed the different sizes of spirally coiled nickel SST and carbon steel pins and the estimated insertion force as a function of the length of engagement and hole diameter. Five sizes of the nickel stainless steel pins are listed Table 3-2. The following formula can be used to estimate the insertion force:

$$\text{Insertion Force, IF} = \frac{\text{Length of Engagement}}{\text{Hole Diameter}} \times (\text{lb/dia. length})$$



**Table 3-2** Spirally Coiled Pin Insertion Force (lb/dia.length) [145].

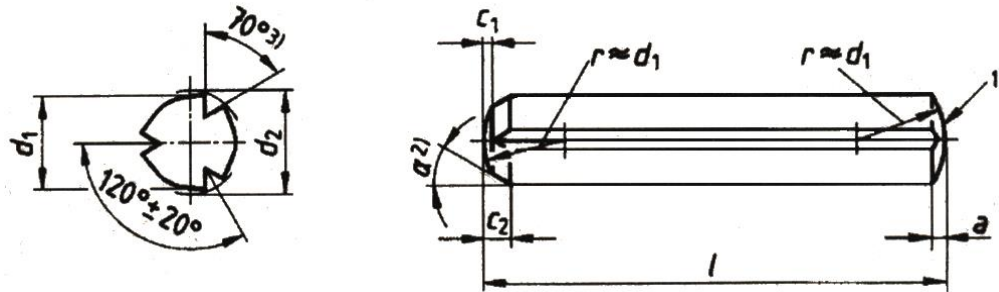
NOMINAL DIA. (in)	DUTY	INSERTION FORCE (lb/dia.length)		
		OPTIMUM	REC. MAX	ABS. MAX.
$\frac{1}{4}$	H	250	295	340
	M	100	130	160
$\frac{5}{16}$	H	350	405	465
	M	140	170	200
$\frac{3}{8}$	H	450	515	590
	M	185	220	255
$\frac{7}{16}$	H	540	630	720
	M	230	270	310
$\frac{1}{2}$	H	640	740	840
	M	275	315	360

Applying the above formula on the  $\frac{3}{8}$  in pin diameter using 10 mm length of engagement and 10.2 mm hole size gives insertion force of 441 lb  $\approx$  1.96 kN for the optimum and heavy duty conditions and 2.57 kN for the absolute maximum and heavy duty conditions. The pull-out force is almost 55% of the insertion force when exerted opposite to the insertion direction while it starts at the same magnitude of the insertion force and decreases as the removal progresses when applied in the same direction.

### 3.4.2 Grooved Pins

Grooved pins are basically solid pins in design with three parallel, equally spaced grooves impressed longitudinally on the pin surface as in Figure 3-5. During manufacturing, the tool penetrates the pin surface to certain depth and displacing some amount of the metal without cutting. The displaced metal forms a raised portion on both sides of the groove while the tool is moving along the axis of the pin and an expanded diameter from the nominal diameter. When the grooved pin is pressed in a hole that is slightly bigger than the nominal diameter, the metal in the raised portion is forced back inside the grooves constituting a radial force against the hole wall. This force is radially

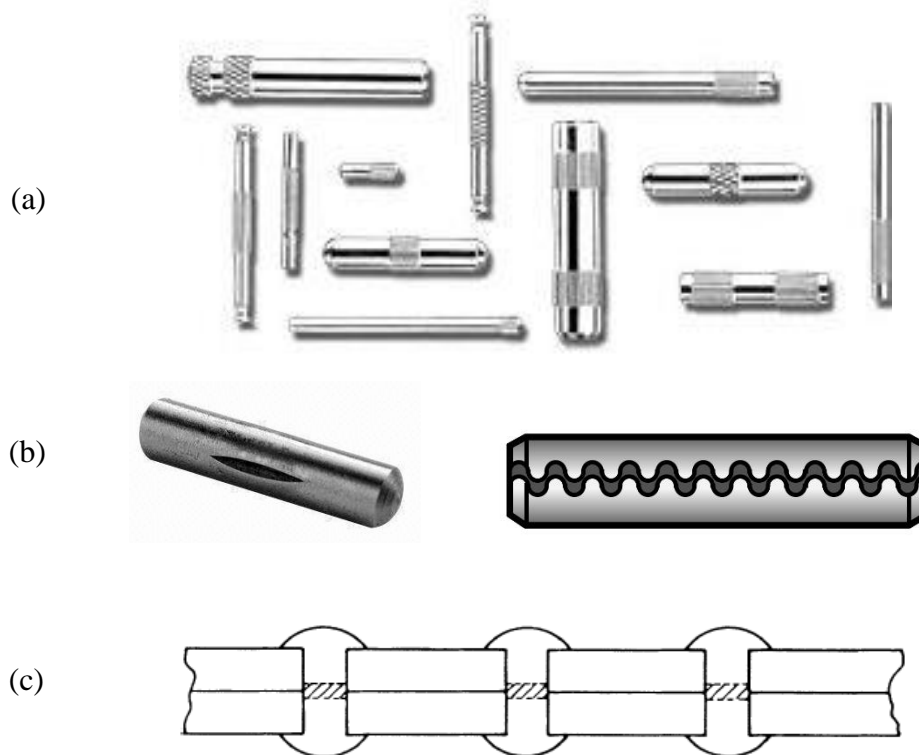
balanced by the six flutes on each side of the groove and is powerful enough to enable a self locking fastener.



**Figure 3-5** Schematic of a grooved pin design [145].

### 3.4.3 Other Types of Pins

The following Figure 3-6 shows different types of commonly used pin insertions, interference press fit fasteners and rivets:

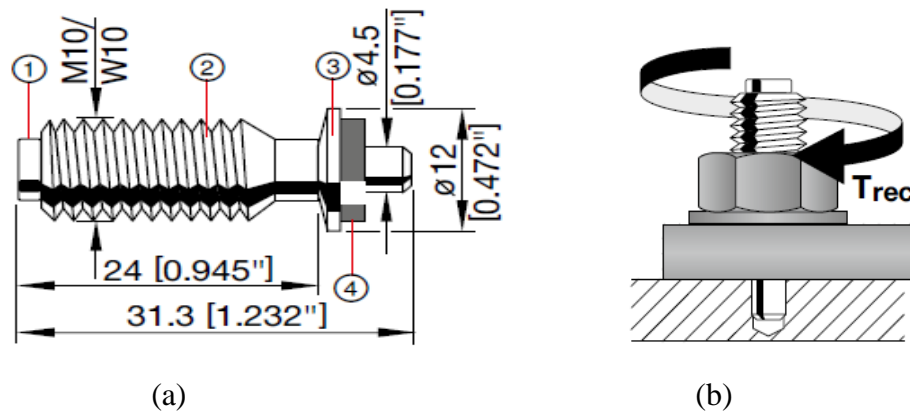


**Figure 3-6** (a) Knurled, (b) Slotted Tubular Pins and (c) riveted joints [145].

Figure 3-6 (a) shows samples of the knurled pins which used widely in wooden and plastic applications and other assemblies with thin sections because they have many knurls in the contact area. Figure 3-6 (b) shows the slotted or spring pins which are tough and durable fasteners.

### 3.4.4 HILTI X-BT Threaded Fastener

One practical example is the Hilti X-BT threaded stud fastener which is widely used in industry and construction with high loading and pull-out values. It can also be used to fasten high strength and thick steel, blocked end and no through penetration of the base metal. Figure 3-7 shows the principle design for this stud with an explanation of the main parts.



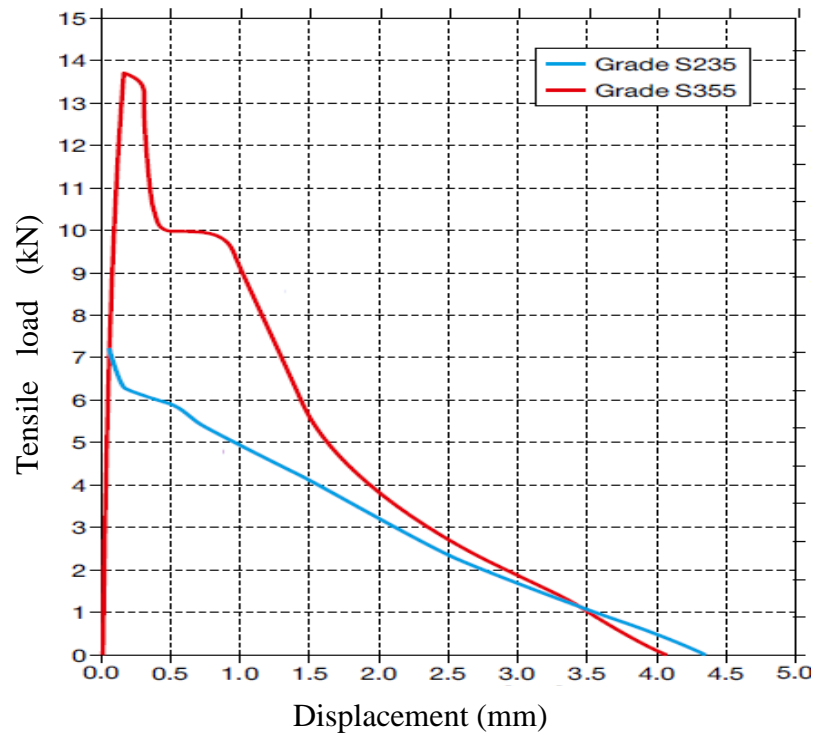
**Figure 3-7** HILTI X-BT Stud. (1) Shank AISI grade SST 316, (2) Threaded Sleeve (3) Metal Washer and (4) Sealing Washer [163].

The recommended loads for steel grade S235, S355, grade 50 and stronger steels are listed in the following Table 3-3:

**Table 3-3** Loading values for Hilti X-BT fastener stud [163].

Load Type	Steel: S235, A36	Steel S355, 50 and stronger Steel
Tension, kN	1.8	2.3
Shear, kN	2.6	3.4

The following Figure 3-8 shows the pull-out tensile test for X-BT stud. The test were applied on two different grades of steel for the base metal, S235 and S355. Six and five fasteners were used in each test respectively. The two curves indicates a higher load value of 2.7 kN/fastener for the higher grade of S355 steel compared to the lower grade steel S235 with 1.2 kN.



**Figure 3-8** Pull-out Load-Displacement behaviour of X-BT Hilti Fastener [163].

The graph indicates a very high stiffness (kN/mm) up to the maximum load and a sudden drop in the pull-out force indicating the failure of the assembly. No significant grip can be seen until the parts are fully disengaged.

The bond strength of the conventional interference fit joints is highly depending on the interfering material and surface finish. In order to reach the final dimensions at the interface area high precision machines and techniques must be employed including milling, lathe, grinding, presses and heat treatment. Moreover, the parts in the aforementioned techniques are manufactured to bigger diameters and then machined to the design dimensions in a subsequent process which cost time and money in addition to

the material being removed. Also, none of the work found in the literature reported a design of experiment approach to explain the relation between the most effecting parameters or even nominating them.

To address this gap in knowledge, the work in this thesis investigated the laser surface texturing of the insertion pins as a novel method for this application. The experimental work and the produced samples will be tested according to a design of experiment model. This model will allow for the cross relating between the different processing parameters and the response; increase in diameter, bond strength and mechanical properties. In order to achieve this, the following aims were set.

### **3.5 Aim of the study**

The aim of this study can be summarized as follows:

- i. To produce a surface texture on a 316L SST cylindrical samples with a pre-defined surface roughness, diameter increase, surface morphology and cross sectional microstructure.
- ii. To produce interference fit joints with enhanced capability due to this texture such that insertion and pull-out forces can be pre-defined and produced with tighter tolerance levels.
- iii. To obtain and optimise the most significant laser processing parameters and their ranges of activity which couple with the optimal responses supported by a DoE model.
- iv. To characterise the produced samples for the surface mechanical properties, change in chemical composition, modified layer depth, hardness and residual stresses.
- v. To test the produced samples for the insertion and pull-out forces and for the fatigue and dynamic loading performance.
- vi. To optimize the process by testing the repeatability of the process and results, identify and minimize the error values and to examine the effect of the laser process on the wear and corrosion resistance of the modified layer.
- vii. To model the thermal field from the laser beam pulses to provide a better understanding for the modified layer depth, heating and cooling rates which have a direct effect on the surface hardness.

### 4.1 Introduction

This study focuses on the surface texturing, via surface melting of stainless steel samples by applying high laser power with a short residence time. Most tests were carried out on stainless steel 316L pins of 10 mm diameter. The objective of these experiments was to investigate the effect of the laser processing parameters on the samples topography, microstructure and increase in diameter. From the literature and previous studies, a range of laser processing parameters was selected, and preliminary screening tests were performed. Different power levels and percentage of overlapping laser spots were examined by the aid of various combinations of transverse and rotational speeds of the sample and the pulse repetition frequency. A full breakdown of the preliminary tests are explained in the following sections with the effect of each processing parameter on the output responses. The results were statistically analysed by using design of experiment techniques and Design Expert software. Based on the results obtained from the preliminary screening tests three levels,  $3^n$ , full factorial design of experiment was modified. The number of processing parameters,  $n$ , was equal to 3 for this work. The measured output response was always the increase in sample diameter, the insertion and removal forces with no or less presence of oxide and material loss and a consistent surface texture. It was found that the processing parameters with the most significant effect on the response and their ranges are the laser power 300 to 500 W, PRF 100 to 300 Hz and the percentage overlapping laser spots -20 to 20%. Other laser processing parameters were investigated as well and were found to have no or limited effect. Such parameters include laser spot size and position of the focus point; over, on or below the metal surface. Moreover, the effect of the assist gas pressure and the duty cycle were tested. These processing parameters were fixed to the values, which produce the best responses as will be explained in the following sections.

## 4.2 Equipment and materials

### 4.2.1 The laser system

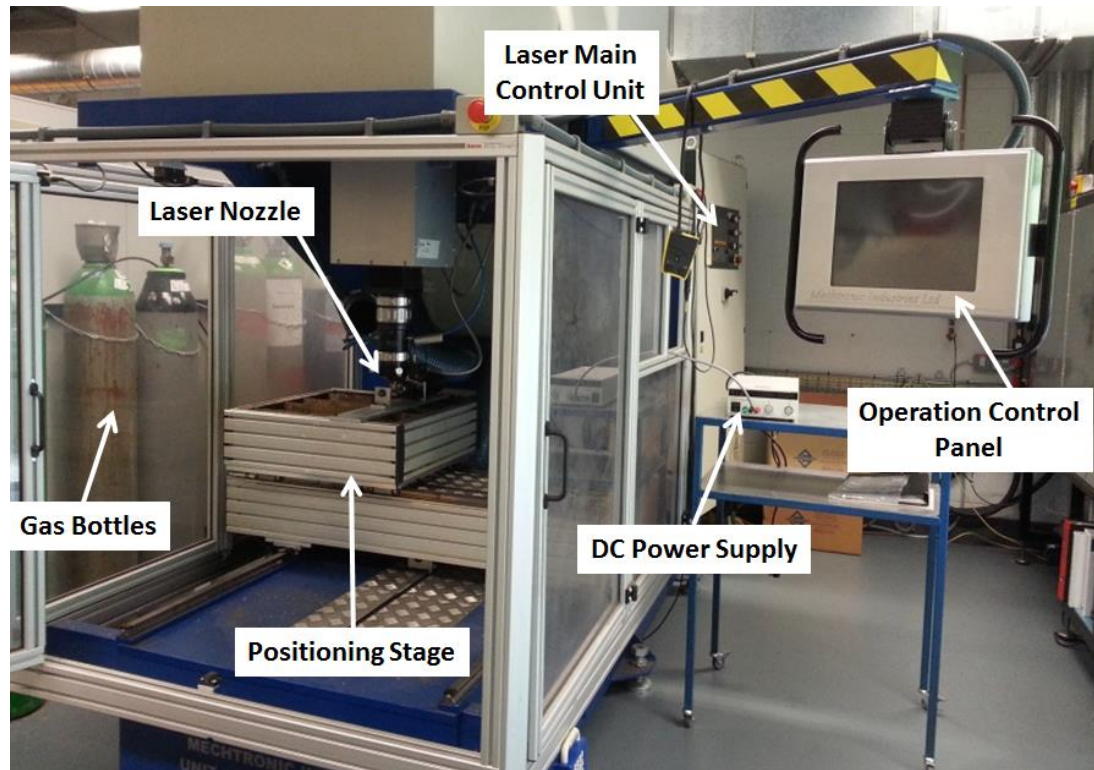
A CO<sub>2</sub> laser system from Rofin DC-015 was used in this study. CO<sub>2</sub> lasers are versatile and practical and able to produce a wide range of power starting from few watts to several kilo-watts [164–166]. The specifications of the laser system used are listed in Table 4-1. The system is capable to work in both pulsed and continuous wave modes.

**Table 4-1** Rofin laser system specifications.

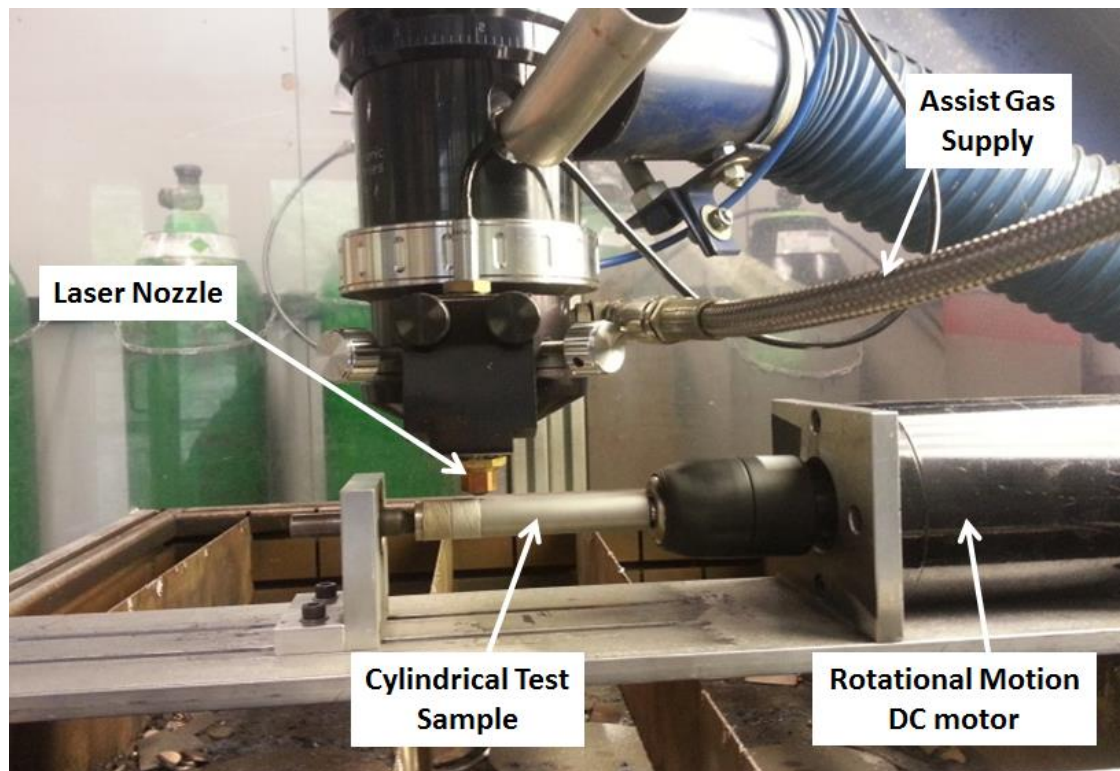
Rofin DC-015 CO <sub>2</sub> Laser System	
Maximum Power	1500 W
Operating Modes	Pulsed or Continuous
Output Wavelength	10.64 $\mu\text{m}$
Maximum PRF	5000 Hz
Beam Mode	Gaussian TEM <sub>00</sub>
Beam Propagation and Quality Parameter, $M^2$	1.11
Spot Diameter Used	0.2 mm

Figure 4-1 shows the main features of the laser system and the instruments employed in this research. These are:

- The main positioning stage:  
This part represents the carrier of the sample and the sample holder. The stage can be moved in two perpendicular axes in the horizontal plane X-Y.
- The control console:  
controls and displays the speed and distance travelled by the stage.
- The laser nozzle assembly (Figure 4-2):  
This assembly carries the focusing lens of (127 mm) focal length and 0.2 mm spot diameter. The entire assembly is mounted on an independent vertical axis named the Z-axis with a stroke length of 150 mm of vertical displacement to facilitate the laser beam spot positioning. The vertical displacement of the Z-axis can also be monitored on the console display.



**Figure 4-1** The CO<sub>2</sub> laser system used in this research.



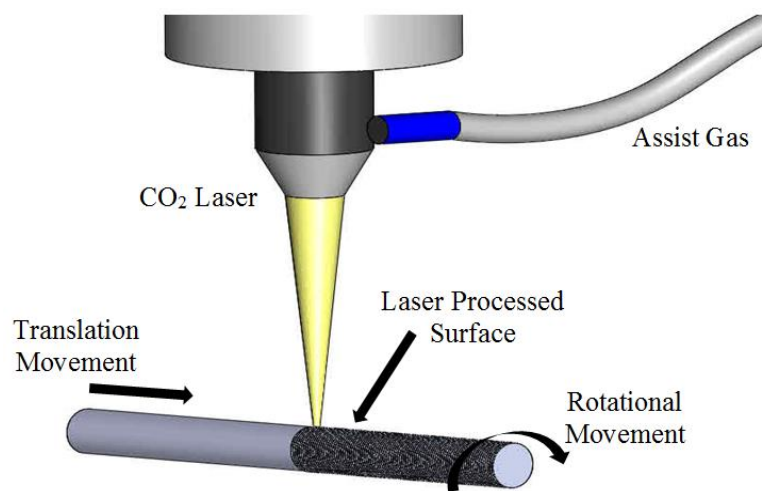
**Figure 4-2** Experimental set up.



A minimum gap of 1 mm is required between the nozzle and the sample surface to allow for the expansion of the material and to leave safe passage for the plasma fumes induced from the laser melting of the material. The assembly is also provided with an assist gas supply. The laser assist gas is a crucial factor in the laser processing of materials. Depending on the gas type, pressure and flow rate, a large variation on the mechanical and chemical properties of the processed surface can be obtained. The function of the assist gas is to:

- Protect the laser focusing lens from any damage caused by the laser induced plasma, fumes and small ablated particles.
- Inert gases like argon are usually used to reduce oxidation of the heat affected zone (HAZ) which may initiate surface cracking [63][167].
- Other types of gases like nitrogen can be used for nitriding and surface hardening.
- The assist gases helps to increase cooling rates.

Figure 4-3 shows a schematic diagram of the laser process utilised in this study. The cylindrical pin samples were rotated with a DC motor which was used to provide an adjustable speed range from 0 to 5000 rpm. The main positioning stage provided translational speed within the range of 0 to 5000 mm/min.



**Figure 4-3** Schematic diagram for the CO<sub>2</sub> laser scanning process of cylindrical samples.

Argon gas was delivered in line with the laser beam during processing. The pin sample was supported by a freely rotating centre bearing opposite to the DC motor, to prevent sample off centre spinning, see Figure 4-2.

#### 4.2.2 Materials and preparation

During the preliminary tests, stainless steel 316L pin samples of different diameters were used during the preliminary test in order to investigate the reproducibility of the process and the ability to reflect the laser pulse coordination on different sample diameters, its effect on the results and for the validation of the correlations derived in this study. The cylindrical samples were employed here over the flat samples as this allowed for achieving higher scanning speeds, which would provide two interacting parameters; the rotational and the translational speed. This provided a suitable shape for an interference fit pin as one possible final application. The fresh samples were 10, 12, 16, and 20 mm in diameter, and were cut into lengths to allow translational scans of 10 mm length along the pin with different laser processing parameters. The laser parameters examined were the power (W), pulse repetition frequency PRF (Hz), the percentage of overlapping laser spots (%), the duty cycle, the laser spot size, the laser beam focus position whether located above, on or below the sample surface and the assist gas pressure. An important measured outcome response was the increase in the samples diameters (mm). This increase in diameter results from the controlled surface melting and re-solidification.

Table 4-2 lists the chemical composition of the as received austenitic stainless steel AISI 316L. The material was supplied by ACEROS INOXIDABLES OLARRA, see *Appendix A*.

**Table 4-2** Chemical composition for 316L austenitic stainless steel (wt%).

Cr	Mn	Si	P	S	C	Mo	Ni	N	Cu	Co	Fe
17.0	1.77	0.34	0.033	0.029	0.018	2.06	11.1	0.029	0.34	0.15	Bal

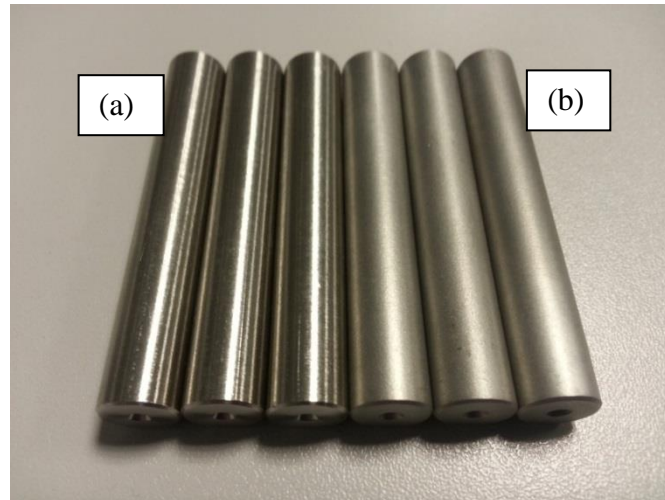
### 4.2.3 Surface roughening by sand blasting

As explained in section 1.5 and in order to improve the laser energy absorption, samples were sandblasted prior to CO<sub>2</sub> laser irradiation by using Guyson Honite-13 as a blasting media. The following Table 4-3 lists the chemical and physical properties of the blasting media particles:

**Table 4-3** Chemical and physical properties of the grit used in the surface roughening

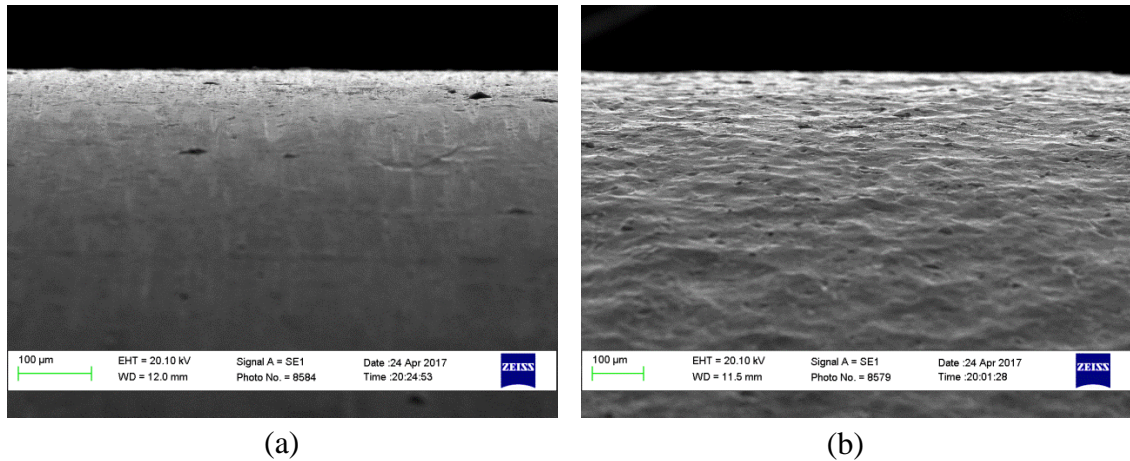
Chemical composition (Soda-lime glass beads)	SiO <sub>2</sub>	Na <sub>2</sub> O	CaO	MgO	Iron
	<75%	<15%	<10%	<5%	Free (<1%)
Physical properties	Shape	Size ( $\mu\text{m}$ )	Colour	Sp. Gravity	Hardness (Mohs)
	Spherical	106-212	White	2.4-2.6	5

An increase in the average surface roughness from 0.8 to ~3  $\mu\text{m}$  was achieved and measured using contact probe stylus profilometer, Civil Instruments TR200. Figure 4-4 shows the SST 316L cylindrical samples before and after the shot-blast roughening.



**Figure 4-4** Shows 10 mm diameter stainless steel 316L cylindrical samples (a) before and (b) after roughening by shot-blasting.

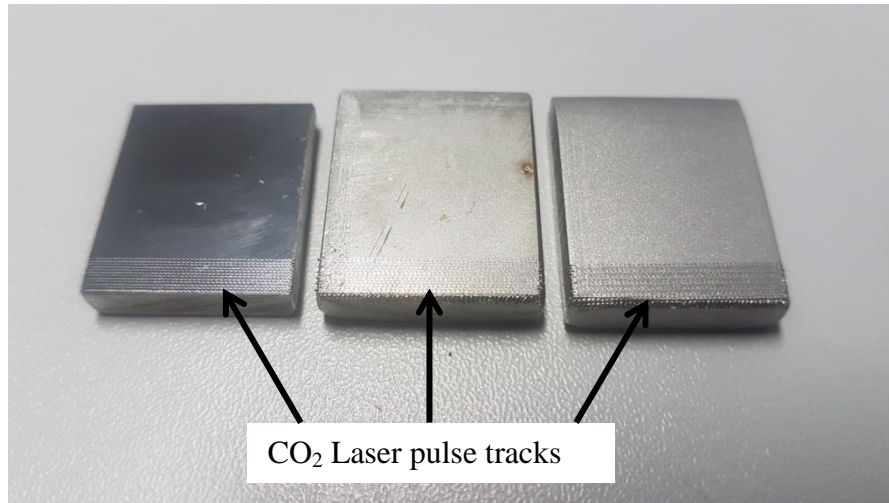
Figure 4-5 (a) and (b) show SEM micrographs for the samples surface before and after gritting and roughening.



**Figure 4-5** SEM micrographs of the side view for the cylindrical sample surface (a) before and (b) after roughening

The chemical composition was also tested in order to investigate whether the gritting particles are embedded on the metal surface, which might affect the laser processing and results. The tests were carried out by using energy dispersive analysis x-ray (EDAX) from (FEI Ltd, Hillsboro, USA). The test shows that no grit blast materials resided on the surface after the roughening process.

An in situ experiment was performed in order to investigate the effect of the surface roughness on the thermal energy absorbed from laser beam radiation. Three flat samples made of 316L SST were sectioned into 25×20×4 mm blocks as shown in Figure 4-6. The first sample was polished down to a surface roughness of 0.02 µm. The second sample was kept fresh and the last one was roughened for up to 1.5 µm by using the method explained formerly.



**Figure 4-6** Stainless steel flat samples with three different surface roughness of 0.02  $\mu\text{m}$  (left), as-received 0.8  $\mu\text{m}$  (middle) and 1.5  $\mu\text{m}$  (right), processed with the same laser parameters for the investigation of the laser energy absorption.

The three samples were processed by applying the same laser processing parameters of 200 W, 100 Hz, 50% DC and scanning speed of 2387 mm/min.

### 4.3 Preliminary screening test

The screening test was performed first to identify the most significant laser processing parameters, their range of values and their relationship with the increase in pin diameter as a response. A 10 mm length scans were carried out on 10, 12, 16 and 20 mm diameter stainless steel 316L samples with different settings of the selected laser processing parameters. The three parameters used in this test are the laser power, the pulse repetition frequency and the percentage of overlapping laser spots. In order to obtain estimated values for the laser processing parameters for the test initiation, and to keep this range within the capabilities of the equipment used in the test, i.e. laser machine power and axes speeds, theoretical calculations were carried out as discussed below.

#### 4.3.1 Investigating the melting point and threshold

Starting from calculating the thermal energy needed to trigger melting the sample surface and the physical properties of SST 316L relevant to these calculations are listed in Table 4-4 [168,169]:

**Table 4-4** Physical properties of SST 316L

Density, $\rho$ kg/m <sup>3</sup>	Thermal conductivity, $k$ (W/m.K)	Specific heat capacity, $C_p$ (J/kg.°C)	Thermal diffusivity, $\alpha$ (m <sup>2</sup> /s)
8000	16	500	$3.8 \times 10^{-6}$

From Fourier's law, the thermal energy,  $Q$ , needed to initiate the surface melting is equal to:

$$Q = C_p \times (T_m - T_o)$$

where,  $C_p$  is the specific heat for stainless steel, 500 J/kg·K,  $T_m$  and  $T_o$  are the melting temperature, 1445 °C, and the surrounding temperature respectively. These values give a specific energy of 711.5 kJ/kg required for melting. Laser parameters applied during a melt volume assessment test were a power of 200 W, PRF of 100 Hz, duty cycle of 50%, laser beam focus diameter of 0.2 mm, and an applied negative overlap of -50% so that the gaps between laser incident pulses could be clearly measured. Using the values listed in Table 4-4 along with the pulse width,  $\tau$ , of 5 ms allows calculation of the diffusion length as:

$$L_D = \sqrt{\alpha \times \tau} = \sqrt{3.8 \times 10^{-6} \times 5 \times 10^{-3}} = 137.8 \mu\text{m}$$

Approximating the volume of metal melted as a cylindrical volume of diameter equal to the laser beam spot size of 0.2 mm and a depth of 137.8  $\mu\text{m}$ , then the mass,  $m$ , affected by the laser beam can be calculated as:

$$m = \rho \times \text{volume} = 8000 \times \pi \times (0.1 \times 10^{-3})^2 \times 137.8 \times 10^{-6} = 3.46 \times 10^{-8} \text{ kg}$$

Multiplying this mass by the specific energy gives 24.64 mJ of energy which is required by each laser pulse for surface melting. This is a useful initial approximation of energy required for surface melting.

Because of the large wavelength of the CO<sub>2</sub> laser beam and the high reflectivity of the substrate, a photonic energy absorption coefficient of 3% was assumed [171, 25]. A PRF value of 100 Hz and duty cycle of 50% were employed for the calculation of the laser power needed.

The peak power attributed to these values can be found as:

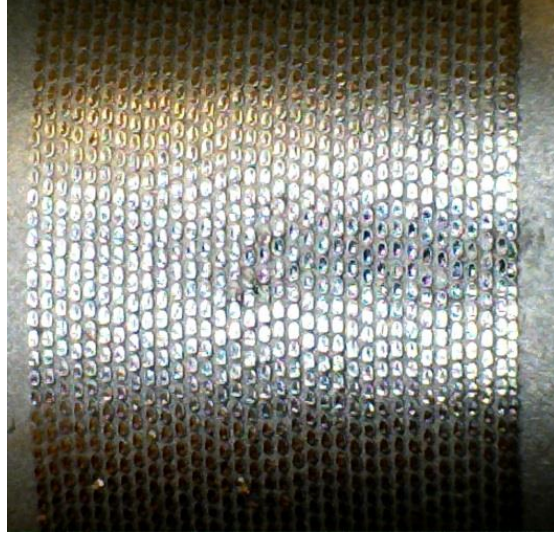
$$\text{Power (W)} = \frac{\text{Thermal energy required for melting (J)}}{\text{Processing time (s)} \times \text{Absorption ratio}}$$

$$= \frac{24.64 \times 10^{-3}}{\frac{0.5}{100} \times 0.03} = 164 \text{ W}$$

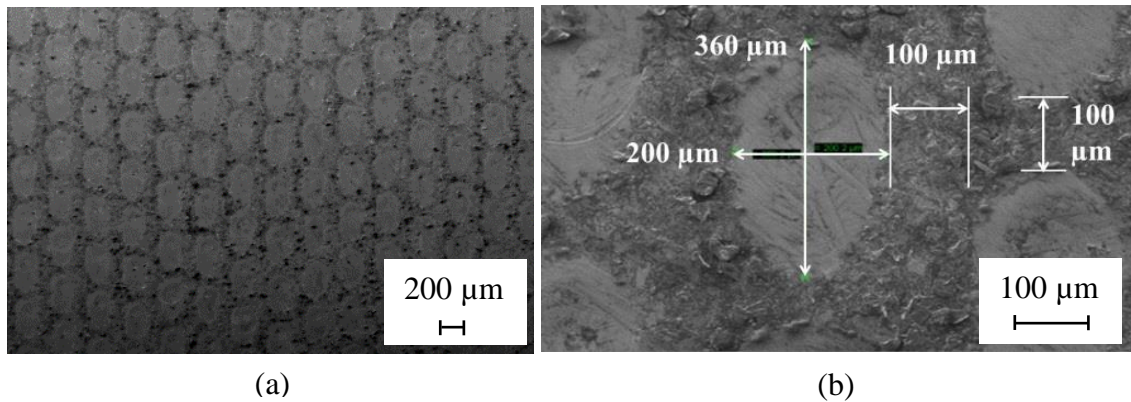
The absorption ratio in the above equation, is a dimensionless value, see section 1.5. Because the assist gas acts as a coolant, and stainless steel is more reflective than steel, a higher laser beam power of 200 W was applied in order to compensate for these heat losses.

The first experiment was carried out by using laser beam power of 200 W, PRF of 100 Hz and -50% overlap, see Figure 4-7. The large negative overlap provided distinct, well-spaced melt pools. This allowed for examination of the relationship between the laser parameters, and the melt pool geometry and pattern. These laser processing parameters were just sufficient to melt small thin regions on the pin surface. An optical micrograph of the re-solidified melt pools is shown in Figure 4-7 and a SEM images of an individual melt pool in Figure 4-8. The melt pool is observed to be 200 μm in the longitudinal direction and 360 μm in the circumferential direction. A separation of 100 μm was measured between melt pools in both directions which is equal to the set overlap of 50% of the spot size.





**Figure 4-7** Optical micrograph of 10 mm length, 20 mm diameter cylindrical sample scanned by CO<sub>2</sub> laser of 200W, 100 Hz, 50% duty cycle, 2.5 ms residence time, -50% overlap and process time = 52 s.



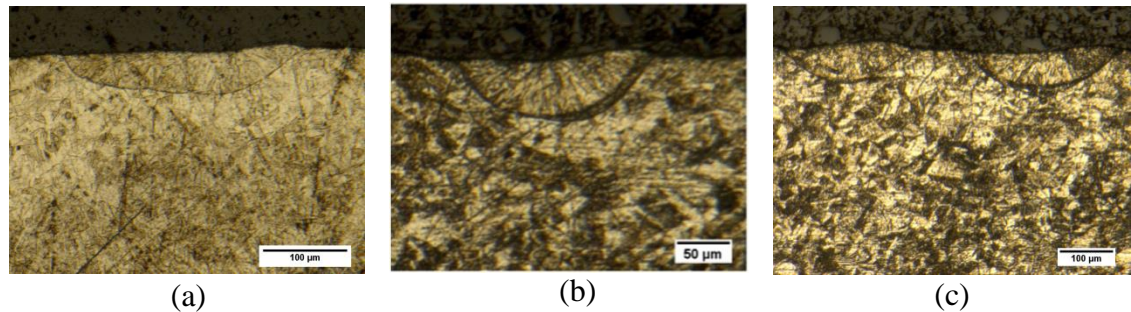
**Figure 4-8** (a) and (b) high magnification SEM images for the sample shown in Figure 4-7.

The processing parameters applied on the sample represented in Figure 4-7 where the surface was locally melted with negative overlap, correspond to each laser pulse delivering an energy of 1000 mJ. Since most metals and alloy surfaces are reasonably reflective to the longer-wavelength infrared light beams, such as CO<sub>2</sub> laser [6,51,171], the energy supplied must be several times that calculated based solely on consideration of heat capacity, latent heat of fusion, and latent heat of vaporisation. Quintino et al. [51] noted for example that iron absorbs about 5% of the energy from the CO<sub>2</sub> laser



radiation, while steel absorb closer to 12%. As the corresponding energy required for melting a cylindrical volume at the surface was approximated as 24.64 mJ. This indicates that only approximately 2.46% of the heat energy delivered was absorbed by the metal surface. A close examination of the re-solidified melt pool shape shows that it resembles an ellipse rather than a circle, even though the beam is TEM<sub>00</sub> Gaussian which should be circular. The elliptical shape can be understood to be due to the moving of the sample during laser firing. This means that the heat affected zone, HAZ, must be corrected. Moreover, the mass affected by the laser energy also need to be recalculated to the exact melt depth of 70  $\mu\text{m}$  found experimentally, see Figure 4-9.

Taking this into account and recalculating, the new affected mass should be closer to  $3.16 \times 10^{-8}$  kg, and the corresponding heat energy needed to melt this mass would be 22.5 mJ. This indicates that the approximation of 3% absorbance used in the previous calculations was acceptable.



**Figure 4-9** Micrographs of 316L melt pool (a) circumferential cross section, longitudinal cross sectional view, and (c) additional longitudinal cross section view showing maximum depth.

These absorption factor values are still lower than expected, compared to those reported by Quintino et al. [51]. This could be explained by stainless steel, as an alloy, being more reflective than other types of steel at the same wavelength, and it would therefore be expected to reflect a larger percentage of the incident visible and IR radiation than pure steel.

An assumption adopted in this consideration is that the heat loss to the surrounding by convection and radiation is negligible, and that all the absorbed pulse energy is

converted into heat energy. This assumption is reasonable because the melting process is carried out in such a short time, equal to one pulse width of 5 ms. Moreover, the PRF value of 100 Hz is the minimum value applied in this study, see Table 4-23. The PRF of 200 and 300 Hz would result in pulse widths of 2.5, and 1.6 ms respectively, thus reducing the process time and not allowing sufficient time for significant heat loss to the surroundings, which supports the assumption adopted here.

The gaps between the molten pools seen in Figure 4-8 and 4-9 in both the circumferential and the axial directions, were found to be 100  $\mu\text{m}$ . This value is half of the laser beam spot diameter of 0.2mm, which is consistent with the controlled overlap value of -50%. These gaps were consistent during the entire scanning process. The melt pool circumferential spot length, expanded to 360  $\mu\text{m}$  in the beam propagation direction due to the high circumferential speed of 2400 mm/min, see Figure 4-8. The distance, x, scanned by each pulse can be calculated as:

$$x = \text{The pulse width} \times \text{The scanning speed} = 0.005 \text{ s} \times (2400 / 60) \text{ mm/s} = 200 \text{ } \mu\text{m}.$$

For the 200  $\mu\text{m}$  diameter laser spot to translate 200  $\mu\text{m}$ , the total processed surface length would be 400  $\mu\text{m}$ . The measured melt pool is 40  $\mu\text{m}$  shorter than this which could be considered to be due to the time needed for heat energy to build up before melting is initiated. This explanation is supported by the melt pool length, see Figure 4-9 (a), which is narrower where the laser shot begins (left) than where it finishes (right). It is considered that energy accumulation is required before being sufficient for melting. From the above experiment, it was decided to consider the range of the main laser processing parameters listed in the following Table 4-5 during the preliminary test.

**Table 4-5** Laser processing parameters values used  
in the preliminary test.

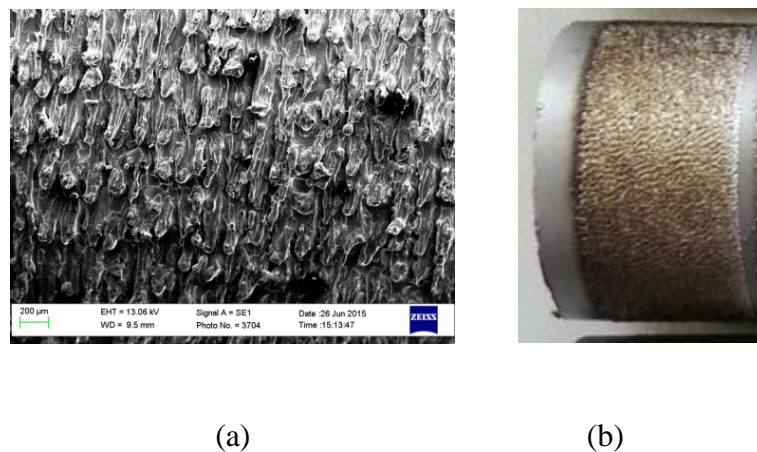
Laser Parameter	Low level	High level
Laser Power P(W)	200	1000
PRF (Hz)	100	2250
Overlap (%)	-50	500

The scanning speed is attributed to the percentage overlap applied and at the same time it is the resultant of two components; the transverse and the rotational speeds of the sample. It was noted that the rotational speeds below 10 rpm are hard to control so higher speeds were employed. The rotational speed was measured by using a dual laser-photo/contact tachometer.

The assist gas pressure was kept constant at 0.4 MPa for the first part of the test. The rotational and transverse speeds were calculated as will be explained in section 4.3.3, to produce the corresponding percentage overlap. An excel sheet was designed to perform these calculations in addition to calculating the other related terms like residence time; energy density, irradiance, fluence and pulse width, see *Appendix B*. The processed surface was examined quantitatively for the increase in pin diameter and qualitatively for the roughness and textured pattern. The following sections show a breakdown with a detailed explanation of the effect of each parameter on the results individually.

#### 4.3.2 The effect of the pulse repetition frequency (PRF)

It was found that for frequencies higher than 750 Hz, the textured surface is more likely a dendrite and knurl in general with presence of porous in between. There is a clear appearance of brown and brittle oxide that do not provide a rigid support for an interference fit. Moreover, a very limited increase in sample's diameter of 0.05 to 0.25 mm were noted, see the following Figure 4-10.



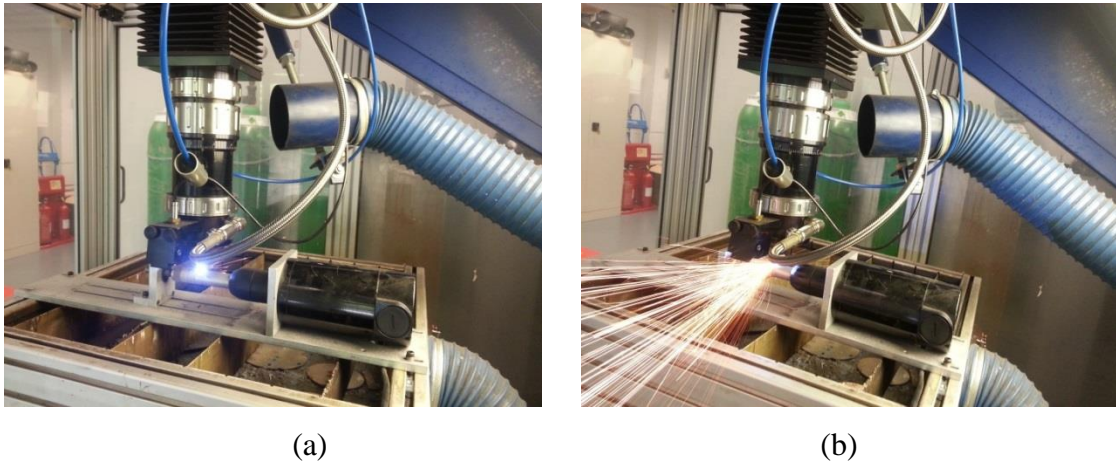
**Figure 4-10** (a) SEM image of 316L surface processed by 1 kW, 2250 Hz and 20% overlap and (b) shows the brown brittle oxide on the surface.

The following Table 4-6 is an example for the effect of the pulse repetition frequency (PRF) modulation on the increase in pin diameter.

**Table 4-6** Lists the results for processing with different PRF.

Power (W)	PRF (Hz)	OV (%)	Diameter (mm)
700	1500	-20	0.1
700	2250	-20	0.05
700	800	-20	0.25

Also, high production of sparks was observed as an indication on the material removal when values of PRF higher than 750 Hz were applied as shown in Figure 4-11.

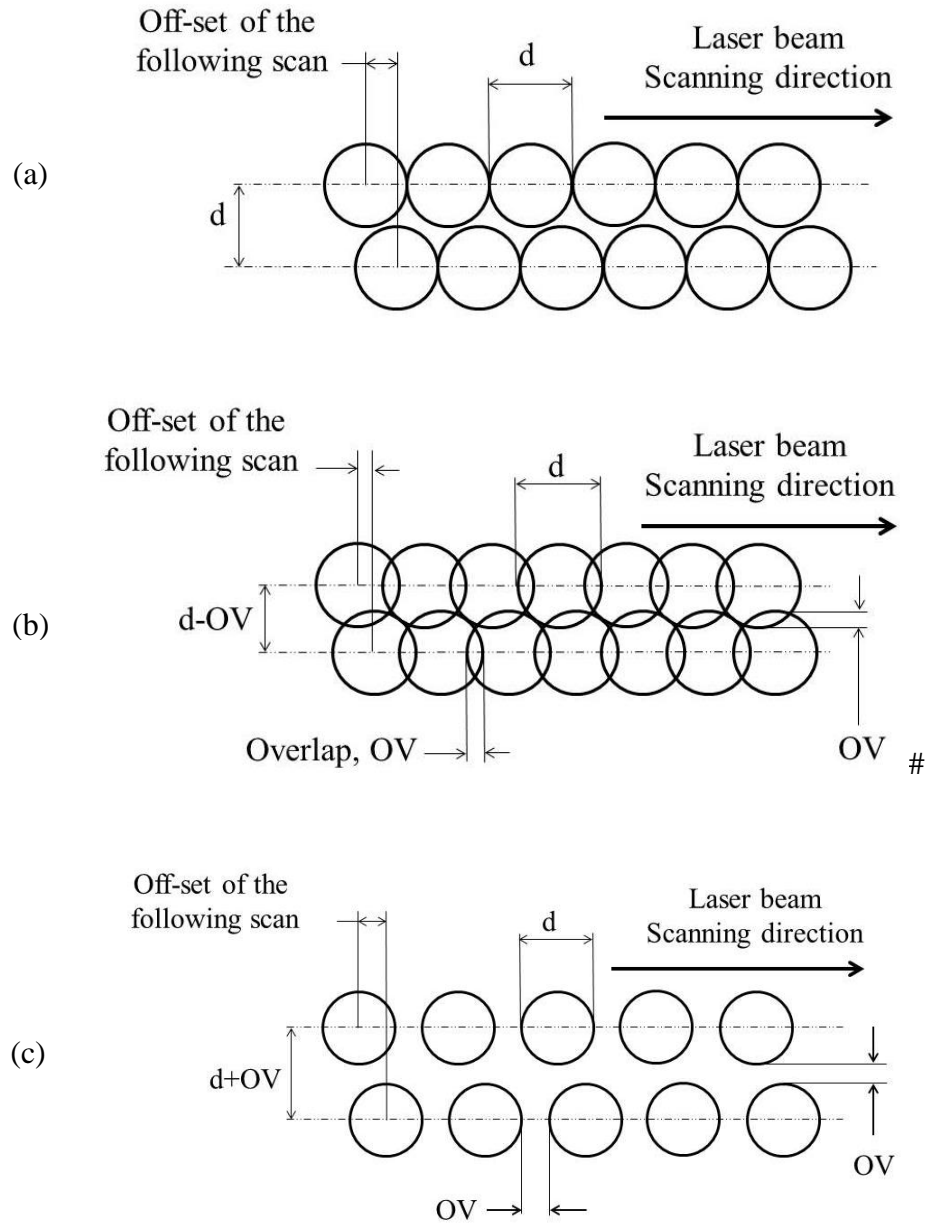


**Figure 4-11** Sparks generation when scanning with 500 W, -20% OV and PRF of (a) 300 Hz and (b) 1500 Hz.

### 4.3.3 The effect of the percentage overlap

Overlapping scans means the percentage of the beam spot diameter in which the laser spot go over a pass that has already been processed. Hence, three possible laser spot overlap scenarios can be found and they are shown on the schematic in Figure 4-12 and 4-13:

Zero overlap: indicates that the laser spots in both circumferential and axial directions were arranged such that they touch only tangentially, as shown in Figure 4-12 (a). The positive overlap occurs where the laser spots interfere with each other by a certain defined percentage, as indicated in Figure 4-12 (b), and conversely negative overlap (c), indicates the presence of unprocessed gaps between each successive laser spot. For each of these cases in this work, the rotational and translation speed were set such that the laser spots were overlapped to the same extent in the circumferential and longitudinal directions. The mathematical relationship between translation and rotational speed required to achieve these overlaps is presented below. A negative overlap test sample to compared the spot size and theoretical pre-determined spot spacing was prepared with a laser power of 200W, PRF of 100 Hz, and spot overlapping of  $-50\%$ .



**Figure 4-12** Overlap scanning scenarios of (a) zero, (b) positive and (c) negative values of the laser spot

Different values of overlap can be found by using different combinations for the linear and rotational speeds depending on the PRF value used and may be calculated as:

1. Zero Overlap Scenario:

Dividing the pin's circumference by the spot diameter to find the number of spots per one revolution of the pin gives the number of pulses/rev =  $\pi D/d$ ; where D is the pin's diameter (mm) and d is the laser beam spot diameter (mm). Multiplying by the number of revolutions per second,  $\omega$  (rpm)/60, gives the PRF (pulses per second) which results in zero overlap as follows.

$$\text{PRF} = \frac{\pi D \omega}{60d}; (\text{pulse/sec}) \quad (4-1)$$

2. For any other Percentage Overlapping Scenario:

The value for negative or positive overlap (OV) must be added to the latter equation to produce the correct PRF for other overlap situations as follows.

$$\text{PRF} = \frac{\pi D \omega (1 + \text{OV})}{60d} \quad (4-2)$$

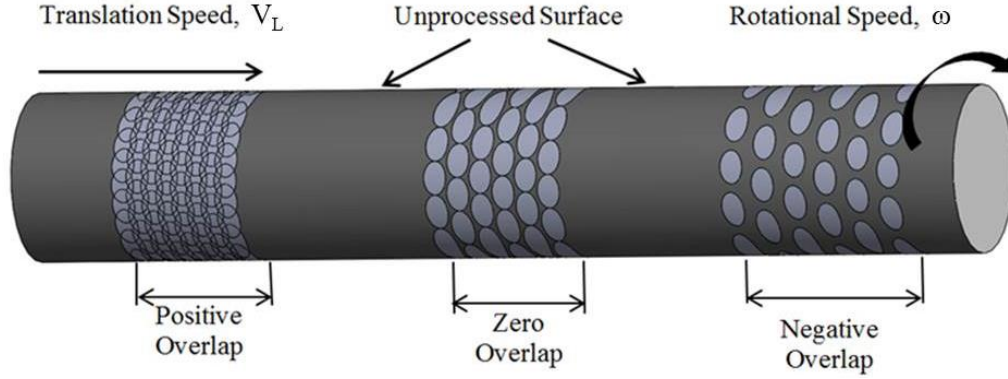
Hence, the tangential (circumferential) overlap percentage is given as:

$$\text{OV}\% = \left[ \frac{\text{PRF} \times 60 \times d}{\pi \times D \times \omega} - 1 \right] \times 100 \quad (4-3)$$

and the linear translational speed of the stage,  $V_L$ , relative to the fixed laser beam to give the same value of overlap in the axial direction can be calculated as:

$$V_L = d \times \omega \times (1 - \text{OV}), (\text{mm} / \text{min}) \quad (4-4)$$

The following Figure 4-13 shows a scheme for the three possible types of overlapping on one sample for explanation and to give closer visual comparison.



**Figure 4-13** Schematic diagram illustrating the three possible scanning scenarios positive, zero and negative laser spot overlap.

A full explanation of the preliminary screening test results are detailed in *Appendix A* showing the effect of each processing parameters on the measured result individually.

#### 4.4 Calculating the texture pattern angle

From Figure 4-14, the laser beam path on the cylinder surface is represented by the thin lines. This scanning direction is from the bottom to the top due to the rotational movement of the cylindrical sample. The thick lines represent the pattern valleys generated by the incident laser pulses and re-solidified melted pools. The circumferential distance that the laser beam travels from point A to point B (distance  $X_C$ ), can be calculated as:

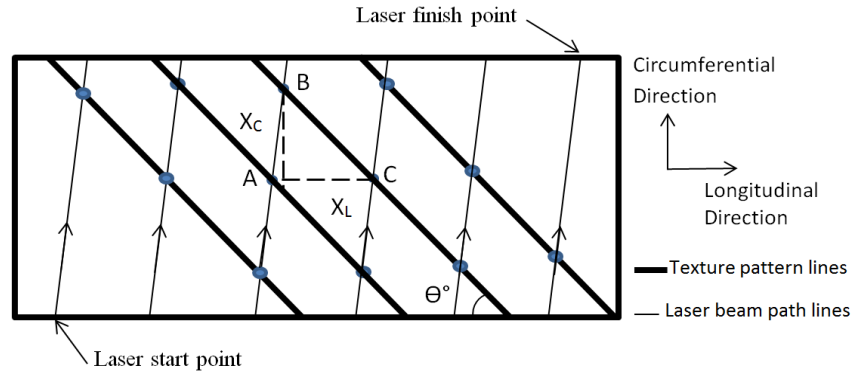
$$X_C = V_C \times \text{time for each pulse} = (\pi \cdot D \cdot \omega / 60) \times (1 / \text{PRF}) \quad (4-5)$$

where  $D$  is the diameter of the cylindrical metal sample in millimetres,  $V_C$  is the tangential speed in mm/s,  $\omega$  is the rotational speed in revolutions per minute, and PRF is the frequency in pulses per second. Similarly, in order for the laser beam to travel from point A to point C, the sample must complete one full revolution and move a longitudinal distance,  $X_L$  of

$$X_L = V_L \times \text{time required for one revolution} = V_L \text{ (mm/sec)} \times (60 / \omega) \quad (4-6)$$



A number of test samples were accordingly produced, using the parameters listed in Table 4-7, to investigate the geometry given by different levels of overlap.



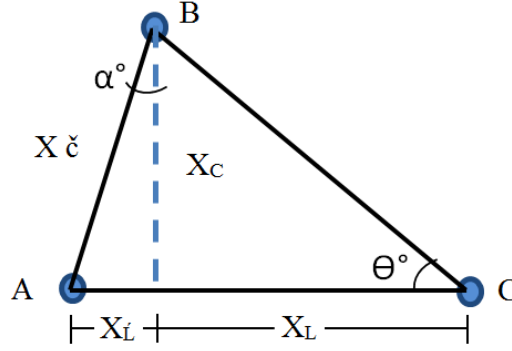
**Figure 4-14** Schematic of laser path (thin lines) and resulting texture pattern (thick lines).

Applying these equations on samples OV-1 and OV-2 listed in Table 4-7, would result in  $X_C = 0.2$  mm,  $X_L = 0.1955$  mm, and pattern angle of  $45.5^\circ$  for sample OV-1, and  $X_C = 0.166$  mm,  $X_L = 0.158$  mm, and pattern angle of  $46^\circ$  for sample OV-2; and  $X_C = 0.25$  mm,  $X_L = 0.23$  mm and pattern angle of  $47.4^\circ$  for sample OV-3.

**Table 4-7** The laser processing parameters applied to determine the effect of overlap on sample morphology.

Power (W)	PRF (Hz)	Overlap (%OV)	$\omega$ rpm	$V_L$ mm/min
500	300	0	71.6	14
500	300	20	59.68	10
500	300	-20	89.5	21

In equations(4-5) and (4-6), the inclination of the laser path when travelling from Point A to point B was neglected and the distance  $|AB|$  was counted as a vertical displacement. As a validation of this assumption, the following Figure 4-15 shows a detailed sketch for  $\Delta ABC$ .



**Figure 4-15** Schematic of three laser pulses showing the texture pattern angle  $\theta_p$ .

From the figure;  $X_L$  is the longitudinal (horizontal) component and  $X_C$  is the circumferential (vertical) component of the displacement  $X_c$ .

$$X_L = V_L \times \text{time for each pulse (1/PRF)}$$

Also,

$$X_c = \sqrt{X_L^2 + X_C^2}$$

Substituting the values for OV-1 from the above Table 7 gives:

$$X_L = (14/60) \text{ (mm/sec)} \times (1/300) \text{ (sec)} = 7.77 \times 10^{-4} \text{ mm}$$

Hence;  $X_C = \sqrt{(7.77 \times 10^{-4})^2 + (0.2)^2} = 0.2 \text{ mm}$ ; and the angle  $\alpha$  is equal to  $\tan^{-1}(0.000777/0.2) = 0.22^\circ$  indicating that the approximation used earlier is accurate and acceptable.

Applying this equation on all the experimental parameters used in this study and calculating  $X_c$  gives negligible (less than  $9 \times 10^{-6} \text{ mm}$ ) differences between  $X_c$  and  $X_C$ , which supports the method of vertical displacement calculation detailed above.

#### **4.5 Design of experiment (DoE)**

Depending on the qualitative and quantitative analysis of the results from the preliminary test, the effects of the processing parameters were examined according to a  $3^3$  factorial design of experiment. The parameters levels utilized are listed in Table 4-8. From screening experiments, these laser processing parameters were chosen to be slightly above the melting threshold of SST 316L and the high levels were avoided to ensure no or minimal surface oxidation, material loss via ablation, and the result of any extreme changes in pin dimensions and mechanical properties. During the experimental work, the laser beam focal position was fixed on 1 mm below the metal surface due to the reason that no texture pattern was observed when working on or above the substrate surface. The duty cycle and the assist gas pressure were fixed on 50% and 0.3 MPa respectively, see *Appendix A*.

**Table 4-8** The laser processing parameters applied in the DOE

Experiment Order	Run Order	Power (W)	PRF (Hz)	Overlap (%OV)
1	26	400	300	0
2	24	400	200	-20
3	12	300	200	-20
4	1	300	300	-20
5	15	300	300	0
6	4	500	200	-20
7	10	300	100	-20
8	19	500	200	20
9	14	400	100	-20
10	21	400	100	20
11	23	500	300	-20
12	13	400	100	0
13	22	300	100	0
14	3	400	200	0
15	6	400	300	20
16	25	500	100	0
17	9	300	200	0
18	8	500	200	0
19	2	500	300	0
20	5	500	300	20
21	20	300	200	20
22	18	300	300	20
23	11	500	100	20
24	27	300	100	20
25	16	400	300	-20
26	17	500	100	-20
27	7	400	200	20

Based on the preliminary test results, the other processing parameters were kept at constant levels as indicated below: Duty Cycle = 50%

- Laser beam focus position 1 mm below the metal surface
- Argon assist Gas Pressure = 3 bar

A detailed explanation of these results would be presented in the next chapter.

The  $3^3$  full factorial DoE was conducted by using Design Expert 9 to analyse the relationship between the different values of the input parameters and the output sample characteristics. This model is preferred because it is more comprehensive and produces the solution with full details for the factors interaction and it can present the output data graphically. The software also provides the ability to analyse the results statistically by using the analysis of variance (ANOVA) and test the significance of each factor. The statistical analysis created by the DoE model indicates the influence of the factors and how confident the results are. For example, the F-value is an indication of factors influence, the higher the F-value the greater the factor influence. Similarly, the p-value is an indication of the significance of the model and the solution, i.e. p-value of 0.05 means that the solution is 95% significant. The R-squared indicates the variation of the measures around the mean value, the closer it is to 1, the lesser the variation of the readings.

The number of samples needed to execute the test is  $3^3 = 27$ . The full test was repeated for 3 times for reproducibility and some samples were repeated several times in order to carry out other tests. The following section discusses the experimental technique and the DoE table.

#### **4.5.1 Experimental procedure**

The experiment was carried out in the following sequence and by implementing the values indicated in Table 4-8 for each pin sample.

1. Inserting the pin sample in the DC motor chuck. A follower rotating centre holder was used at the free end of the sample to prevent the sample from any eccentric or bouncing motion. The whole assembly was fixed on the positioning stage responsible for the linear translation, see Figure 4-1.

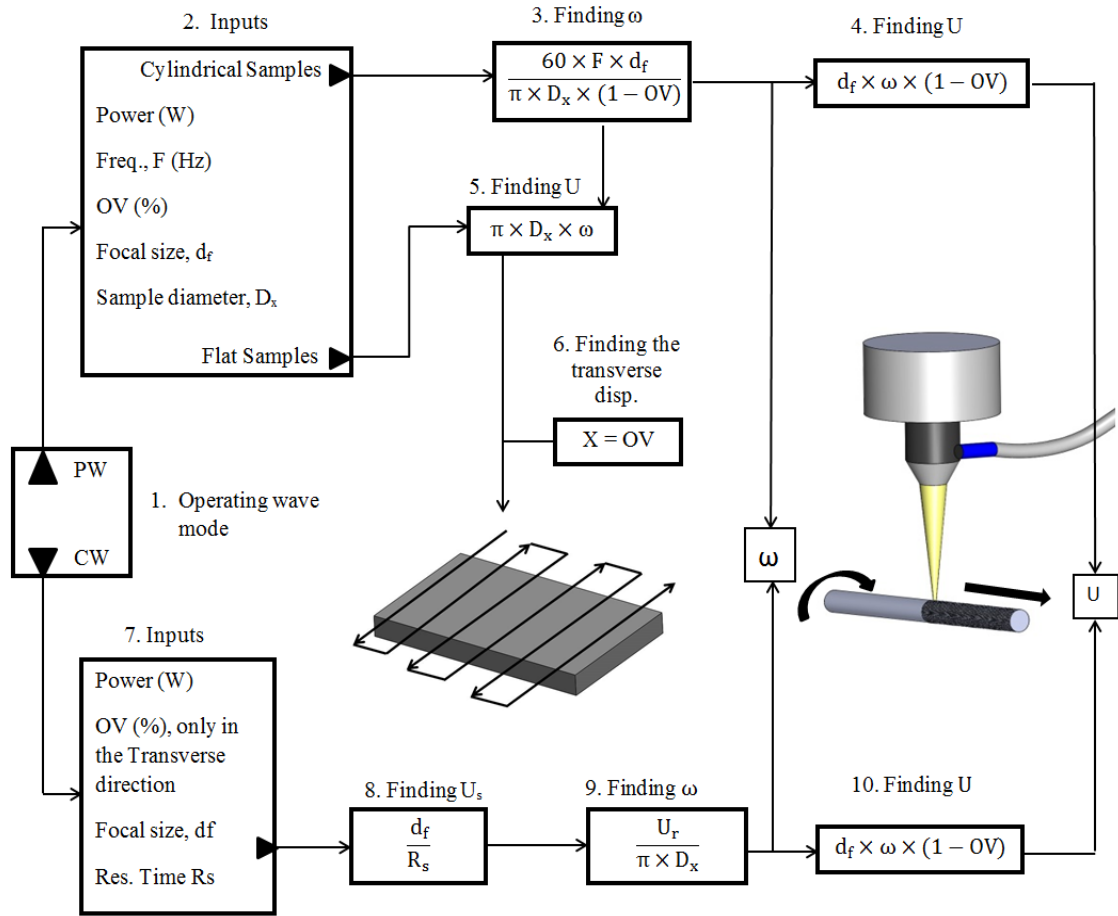
2. Processing parameters values are set by entering the laser beam power and the PRF values into the Laser Main Control Unit. Setting the assist gas pressure by using the gas regulators and monitor the pressure on the operation control. The overlap percentage is set by both adjusting the linear translation speed of the stage and the DC motor rotational speed. The rotational speed is measured by the tachometer.
3. A dry cut demonstration (without laser) can be performed to assure all other processing parameters are correctly set and engaged.
4. The sample is then completed and can be removed, labelled and taken to the next mechanical properties testing.
5. Steps 1 to 5 are repeated for the new sample and so on.

#### **4.6 Process layout**

The process layout shown in Figure 4-16 details the two operating- wave modes, pulsed PW and continuous CW (block 1). As explained earlier in this chapter, only the pulse wave mode was used in this study. The calculations corresponding to the rotational and transvers speeds can be carried-out externally and for the full set of samples in the DoE. These motion values can be entered through the operation control panel while the laser processing parameters are set by means of the laser main control unit, see Figure 4-1.

The continuous wave operating mode can be used for other types of laser processing like laser nitriding, polishing, cutting or surface texturing. When this mode is applied, the scanning speed  $U_s$  can be entered accordingly or to be calculated for a specific residence time  $R_s$  and spot size  $d_f$  value (block 8).

Moreover, the figure also shows the method used to translate the laser process applied on the cylindrical samples to produce an equivalent flat sample in order to facilitate the wear pin-on-disc (POD) and corrosion tests. In order to achieve symmetrical results, the laser processing parameters are remain constant, the equivalent linear scanning speed can be found directly from the rotational speed and the transverse distance (X) (block 6) must be equal to the applied overlap.



**Figure 4-16** Process flow chart for the CO<sub>2</sub> laser surface texture of cylindrical samples.

#### 4.7 Processed samples inspection

After laser processing, the produced samples were visually tested and by microscope to study the geometrical changes on the surface and the presence of any cracks and oxide which must be avoided. The presence of oxide can be indicated by the dark brown colour texture.

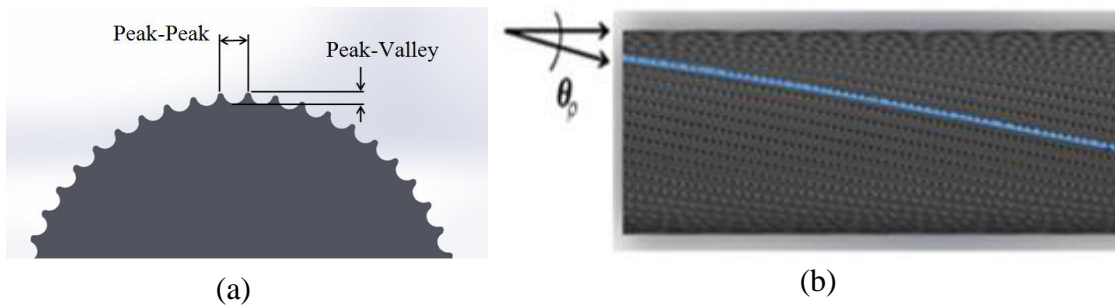
##### 4.7.1 The increase in samples diameter

The effect of the laser processing parameters on the produced samples diameter was examined by obtaining the average of 9 measurements taken on each sample. The measurement were carried out by using a 0.05 mm resolution vernier. The wide portion

of the vernier was used to measure the maximum diameter on the texture peaks while the sharp portion was used to measure the minimum diameter at the valleys. The measured diameter was plotted for each sample versus the main laser processing parameters for all the samples using statistical software, design expert 9 model.

#### 4.7.2 Measuring the texture angle, peak-peak and peak-valley measurement

The melt-pool size depends on the set laser power, spot size, traverse speed, pulse repetition frequency (PRF), and percentage overlap. The interaction between the circumferential and longitudinal speeds and the pulse repetition frequency contributes to form the pattern generated in both the circumferential and longitudinal directions. The developed texture pattern thereby has prescribed peak-to-peak widths, as well as peak-to-valley heights, see Figure 17 (a). The helical translation of the laser beam spot on the pin surface, under the wide range of possible processing parameters, provides a wide range of scanning and overlapping variations. The re-solidified molten pools construct different surface patterns with texture angle,  $\theta_p$ , see Figure 4-17 (b).



**Figure 4-17** (a) Schematic diagram of the cross section view showing peak-peak width and peak-valley height, and (b) top view showing pattern direction relative to the longitudinal axis.

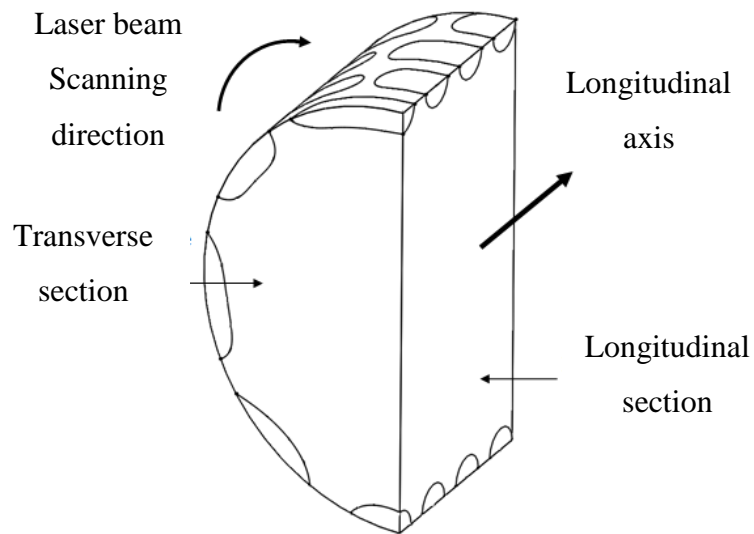
From the screening experiments, the laser processing parameters were chosen to be slightly above the melting threshold of SST 316L. High powers were avoided to ensure



minimal material loss via ablation, surface oxidation, and resulting negative extreme changes in pin dimensions and mechanical properties. Ten measurements were taken to determine the average peak-to-peak widths and peak-to-valley heights using a Keyence VHX2000E 3D digital microscope with a measurement resolution below 1  $\mu\text{m}$ . The average and 95% confidence interval of the resultant dimensional measurements were calculated. Pearson correlation coefficients were calculated between the input parameters and output responses.

#### 4.8 Metallographic test

The sample produced during the thermal energy calculation test was sectioned in the longitudinal and transverse direction with reference to the laser beam propagation direction as shown in the following Figure 4-18 using a CNC-EDM wire-cutting machine.



**Figure 4-18** Schematic for the sectioned cylindrical sample, cut by wire EDM.

The melt craters produced on this sample were just above the melt threshold and the wire cutting method was preferred over other traditional methods in order to avoid the excessive damage on the laser-processed area.

The set of samples produced from the preliminary scanning test and the full DoE test were cross-sectioned by using diamond rotating disc cutter because of the shorter time and lower cost compared to the EDM-wire cutting. Moreover, the modified layer in these samples are more clear due to the higher processing parameters level.

**Sample preparation:** A Buehler Motopol 2000 was used for the grinding and polishing process. The grinding was carried out by applying successive grades of silicon carbide grinding paper of 400, 600, 800 and 1200, with a water flow to act as a lubricant, and for flushing the loose metal and abrasive particles. Final polishing was carried out using a Textmet cloth with diamond and alumina suspensions of 9, 6, 3, and 0.05  $\mu\text{m}$  particle size sequentially. Each polishing grade was applied for 3 to 4 min with rotational speed of 150 rpm. The total thickness of the layer removed from each sample in both grinding and polishing was no less than 1 mm. This is important to avoid the influence of the cutting on the microstructure. L. Straka [172] reported that the heat affected zone, (HAZ) depth due to an EDM-wire cutting of tool steel using similar power levels was only 50 microns based on the altered hardness in the HAZ returns to the bulk material hardness.

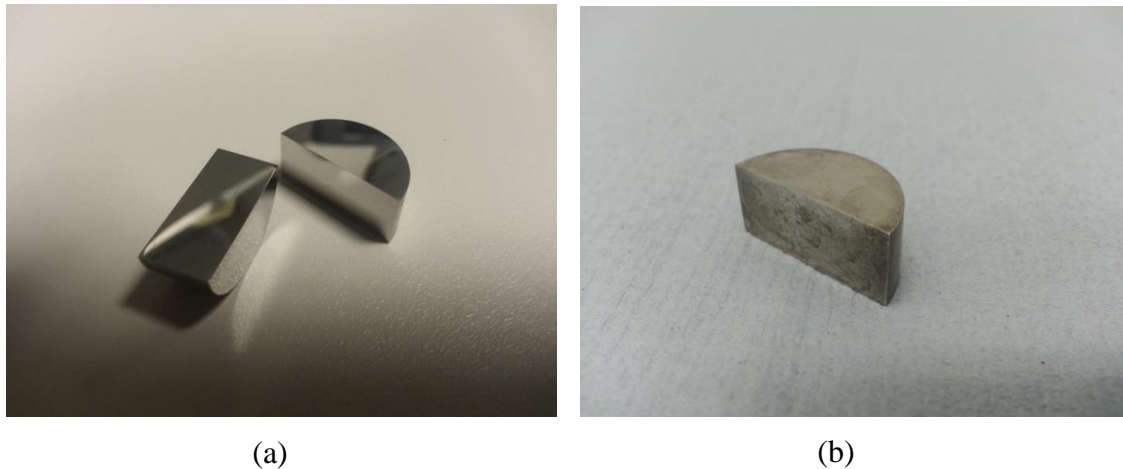
In order to enhance the visual contrast of grain boundaries, the polished layer was chemically etched. Stainless steel 316L, as an austenitic steel alloy, is significantly anti-corrosive and is difficult to etch. Two different types of chemical etchants were used in this study. A very effective etchant from Adler [173] was used to reveal the microstructure of the sample used during the preliminary test, see section 4.3 The laser processing parameters applied on this sample were near the minimum thermal energy required to trigger surface melting and no significant or clear phase change, chemical composition or grain size alteration is expected.

Adler etchant is made up of 9 g copper ammonium chloride, 150 ml hydrochloric acid, 45 g hydrated ferric chloride, and 75 ml distilled water was applied to the sample surface for 8 to 10 s using a cotton cloth and then rinsed with isopropyl alcohol (IPA).

Glyceregia etchant was used to reveal the grain boundaries and orientation for the set of samples in the DoE. Glyceregia was made up of 20 ml nitric acid, 30 ml hydrochloric acid and 20 ml glycerol and was applied for 5 to 7 sec by swabbing the cross section

area using a cotton cloth [17,19,107]. After the chemical etching, the sample was primarily washed using tap water and liquid soap solution to remove any residual chemical substances and finally with isopropyl alcohol to remove any stains or prints of water and soap.

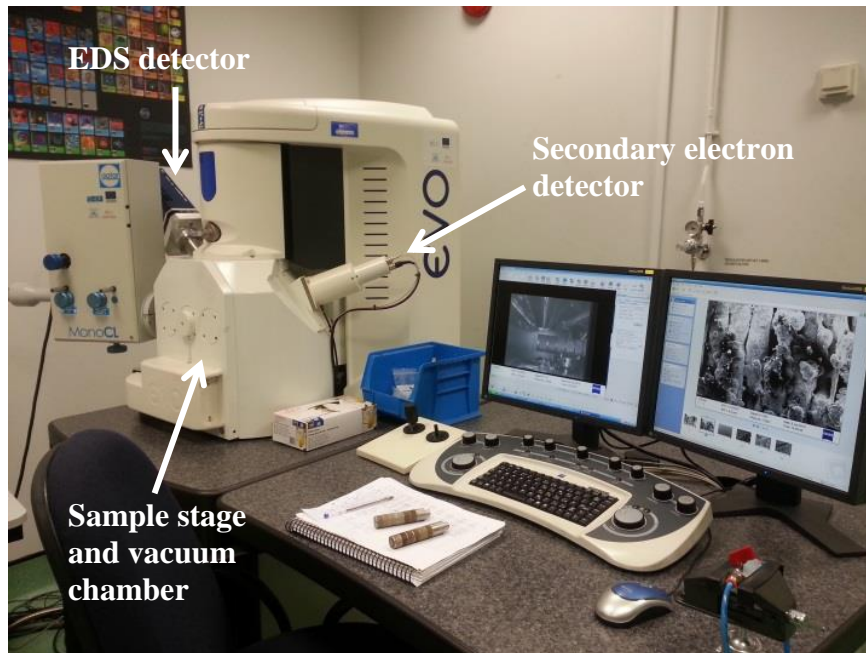
The following Figure 4-19 (a) shows the sliced sample after grinding, and polishing and (b) shows the sample after treatment with the chemical etchant.



**Figure 4-19** SST 316L sample processed with a CO<sub>2</sub> laser (a) after grinding and polishing and (b) after treatment with Adler chemical etchant.

#### 4.9 Microscopic investigation

A Carl-Zeiss EVO-LS15 scanning electron microscope, SEM, was used to reveal the modified microstructure of the cross section and the surface morphology, see Figure 4-20.



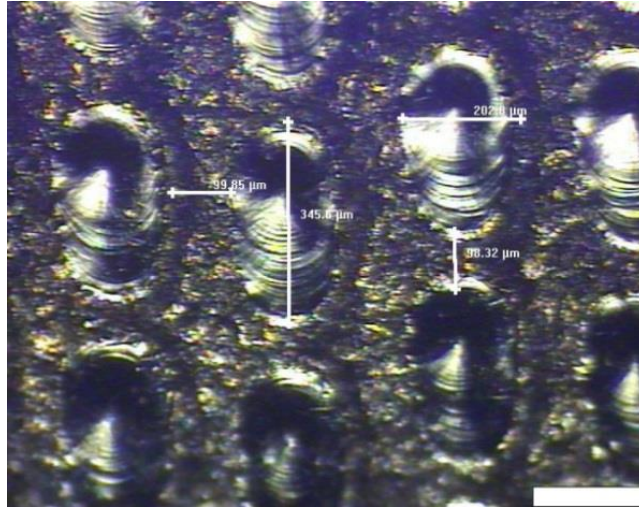
**Figure 4-20** The Carl-Zeiss EVO-LS15 SEM

The secondary electron microscope was used for the following characterisation:

- Investigating the modified surface morphology for the presence of any micro-crack that might be resulted due to the high cooling rates.
- The modified cross-section; change in grain size and orientation and phase change.

Wide range of accelerating voltage was used from (5 kV) to reveal the surface morphology up to (23 kV) to reveal the cross-section micrographs.

Also, a Reichart ME F2 universal optical microscope was used to obtain a bright field investigation and imaging for the surface morphology and cross-section microstructure, see Figure 4-21. This figure was only used for the validation of the micrograph from the SEM. The optical microscope was equipped with Buehler Omnimet Enterprise, an imbedded software driven tool that allows for the quantitative analysis of the sample image.

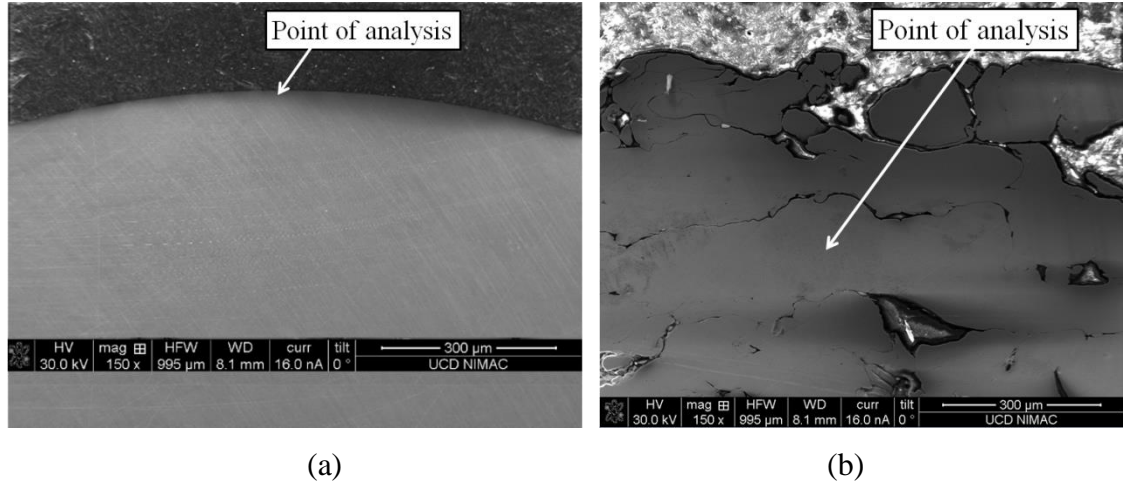


**Figure 4-21** Optical image for the sample shown in Figure 4-7

#### 4.10 Chemical composition analysis

The energy dispersive analysis x-ray (EDAX) from (FEI Ltd, Hillsboro, USA) available in the school of chemical and bioprocess engineering, UCD was used for the element analysis and the chemical composition characterisation. The samples were mounted on the stubs using double-sided carbon tape for conductivity purpose. The samples were then examined using a FEI Quanta3D FEG Dual Beam, which is composed of a combination of focused ion beam (FIB) with high resolution field emission scanning electron microscope (FEG-SEM). This combination is capable of high resolution surface imaging of 1 nm at 30 kV in addition to the fast composition analysis.

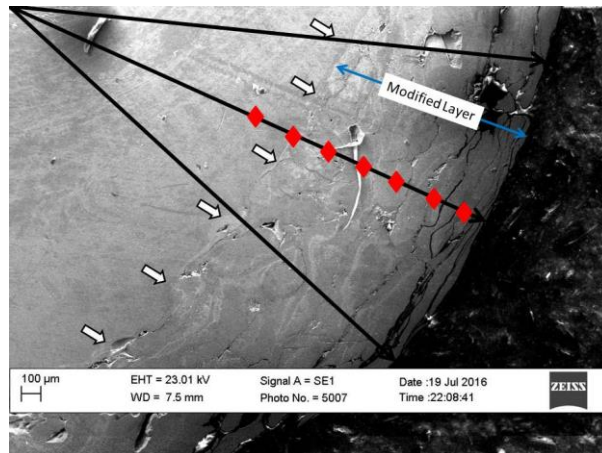
An as-received sample and four processed samples no. 8, 9, 10 and 15 corresponding to Table 4-8 were tested for the chemical and phase change which might be caused by the laser process. The following Figure 4-22 shows the points of analysis on the as-received sample and sample no. 10 for example. The points were located close to the sample surface and at the modified layer in order to find an accurate assessment of any effects that might be resulted due to the grit peening during the surface roughening and after the laser processing.



**Figure 4-22** SEM micrographs showing the test points where the EDAX analysis carried out on (a) as-received and (b) laser processed samples.

#### 4.11 Measuring the meltpool depth

The following Figure 4-23 shows a cross section image for sample no. 9 as an example to explain the technique used in measuring the melt-pool depth and the altered hardness of the modified layer. The white arrows indicate the melt pool boundary. Eight measures were taken and averaged for each sample and plotted versus the main laser processing parameters. A correlation graph for the resulting melt-pool versus the residence time and the power irradiance was obtained.



**Figure 4-23** SEM image of sample no. 9 showing the melt-pool depth.

#### **4.12 Measuring the micro-hardness**

Vickers micro-hardness was measured starting from the sample surface and moving toward the centre on three radial lines separated by 500  $\mu\text{m}$  with 50 micron between each measurement as indicated by the black arrows and the red diamond respectively, see Figure 4-23. The hardness measurement continued until the bulk material hardness of <300 HV was reached.

#### **4.13 Residual stresses investigation**

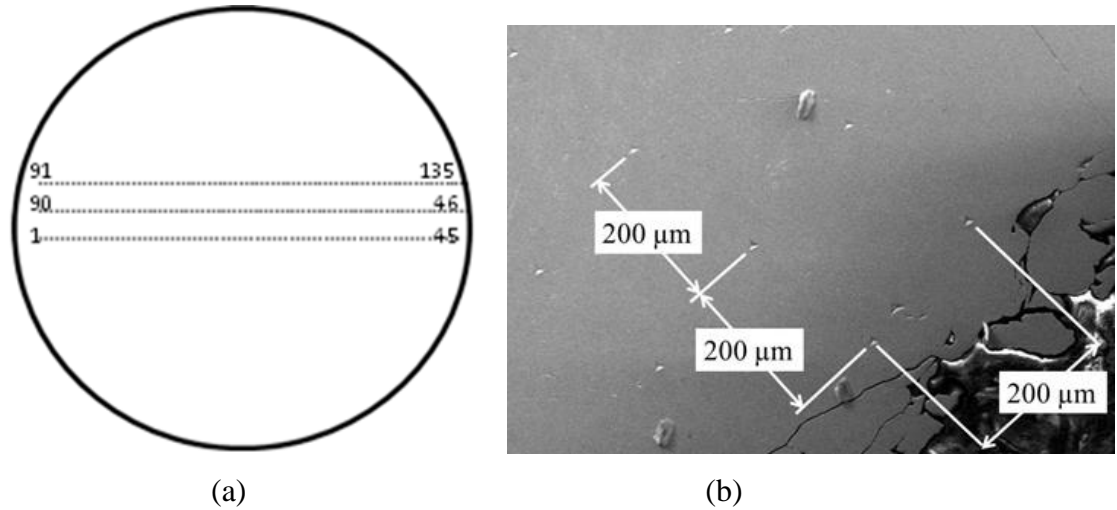
Residual stresses are usually created on the part surface after the surface modification treatment due to the ultra-high thermal gradients [176]. They could be induced due to the thermal expansion-contraction and/or whenever there is a phase change, e.g. from austenite to martensite which would result in compressive stresses because of the increase in volume of the martensite. Predominantly, residual stresses resulted in mechanical parts during manufacturing are neglected because they are self-equilibrium but in fact they could be harmful or beneficial and must be treated as external stresses [177]. They could significantly reduce the strength of a part and initiate a premature crack that leads to failure. Compressive residual stresses are beneficial for some applications subjected to cyclic loads due to the improvement in fatigue life and conversely, the detrimental tensile residual stresses can reduce fatigue limit and help the crack initiation [7,48,49].

##### **4.13.1 Elastic modulus and hardness investigation**

It is important to test and evaluate the residual stresses and understand their existing effect on the interference fit application and the influence of the processing parameters on them. A selection of 17 samples was performed based on a Box Bejnken design to carry out the test. The test was performed using a nano-indenter from Agilent G200 based on the Continuous Stiffness Measurement (CSM). Indentation were carried out in three lines on the cross section of each sample starting from one side to the other through the centre, see Figure 4-24 (a) and (b).

Each indentation line was comprised of 45 indents with 200 micron spacing between each indent and the same distance from the next line. A total number of 135 indents

were made on each sample. A Berkovich indenter of three sides with a sides angle of  $142.5^\circ$  was used to produce indents of a triangular impression.



**Figure 4-24** (a) The methodology used in nano-indentation and  
(b) SEM micrograph for the indents.

The system is embedded with a software programmed to carry out a load-displacement data record and was programmed to perform individual indents with an indent depth of  $2\ \mu\text{m}$  from the surface and a rate of  $10\ \text{nm/sec}$ , the corresponding load is recorded. A holding time of  $10\ \text{sec}$  is applied once the maximum depth was reached. The same rate of  $10\ \text{nm/sec}$  is applied during unloading with a holding time of  $100\ \text{sec}$  when the load is  $10\%$  of the maximum load reached. An average value of the elastic modulus and hardness was found from the data collected from each indent for the depth of  $800$  to  $1800\ \text{nm}$ . This arrangement was used in order to avoid any error which might be resulted from the vibration associated when the indenter approaches the surface.

The investigated elastic modulus and the hardness are reported and plotted with reference to each indent and its position on the cross sectional area.

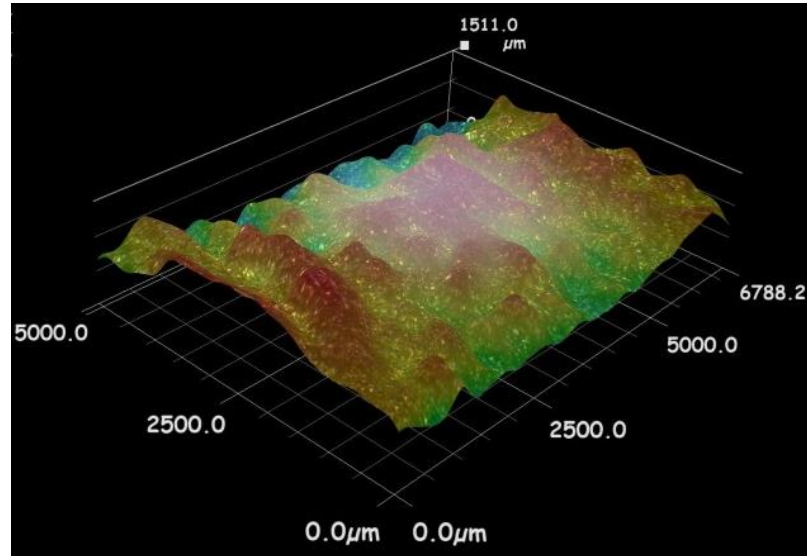


#### 4.14 Roughness measurements

Due to the high range of the produced surface roughness which is out the range of a surface contact traditional profilometers and the damage might be caused to the contact probe, the surface roughness profile was calculated by using 3D microscope. The texture profile was investigated by Keyence VHX2000E 3D digital microscope. At least five surface roughness profiles were obtained for each sample in the DoE on the axial direction for approximately 7 mm length and the average surface roughness with the 95% CI's were calculated. ISO 4288-4287 standard was used to calculate the surface roughness according to the following equation:

$$R_a = \frac{1}{N} \sum_{n=1}^N |r_n| \quad (4-7)$$

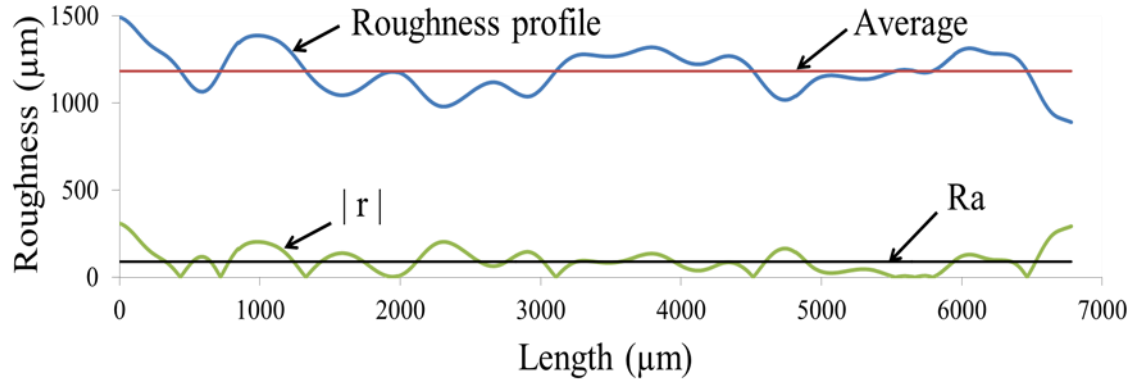
where N is the total number of data taken and r is the roughness value at each data point. Figure 4-25 shows the surface roughness profile for sample no. 9 corresponds to Table 4-8 as an example.



**Figure 4-25** 3D image of the surface roughness profile for Surface roughness profile.

The scale bar in Figure 4-25 indicates the surface roughness in addition to the curvature of the cylindrical sample geometry. In order to calculate the average surface roughness,

$R_a$ , using equation (4-7), a 2D profile was obtained parallel to the main axis of the sample as indicated by the blue (top) plot in Figure 4-26.



**Figure 4-26** 2D surface roughness profile oriented in the axial direction.

Since  $R_a$  equals the average of the deviation from the centre line ( $|r|$ ), a modified profile plot was created by inverting the (negative) regions as indicated in the lower (green) plot. Equation 4-7 was then applied on the  $r$  values below the new curve.

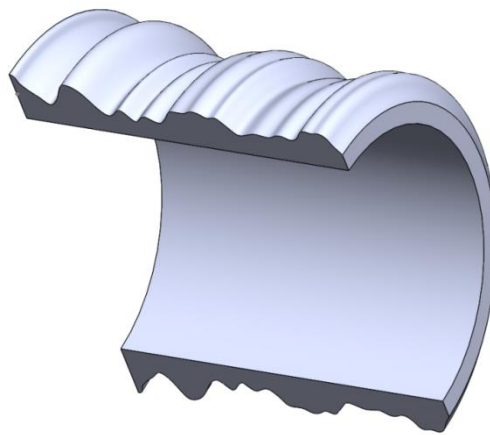
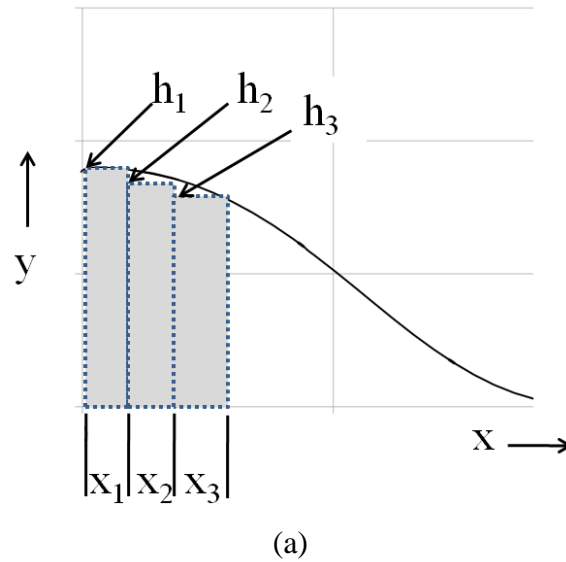
#### 4.15 Interfering volume calculation

The textured surface profile found in the previous section can be used to calculate the interfering metal volume between the insertion and the hub ring. Figure 4-27 (a) shows the specimens used to calculate the area under the texture profile and then the interfering volume by using eq. (4-8). Figure 4-27 (b) shows a cross section of this volume which is established as follows:

- Matching the maximum peak from the surface roughness profile in Figure 4-26 with the higher measured diameter for each sample.
- Revolving the area under the curve around the center of the cylindrical pin.
- Deducting the hole diameter of 10.05 mm.
- The net volume is the factor of the area under the curve multiplied by the ring hole circumference:

$$\text{Volume} = (\pi \cdot D) \times \sum_{n=1}^N \left( \frac{h_n + h_{n-1}}{2} \cdot (X_n - X_{n-1}) \right) \quad (4-8)$$

where,  $h$  and  $X$  are a specimen height and width under the curve gained from the 3D microscope output data,  $N$  is the number of data and  $D$  is the ring hole diameter.

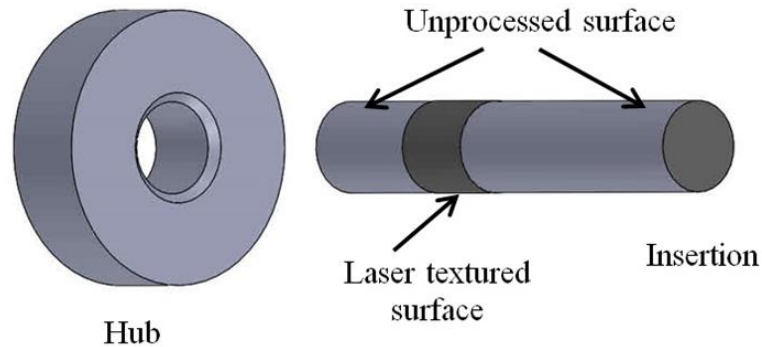


**Figure 4-27** (a) The area specimens under the roughness curve and (b) cross section of the interfering volume between the pin insertion and the hub ring.

Calculating the texture volume can provide a better understanding of the bond strength and might be correlated with the main laser processing parameters.

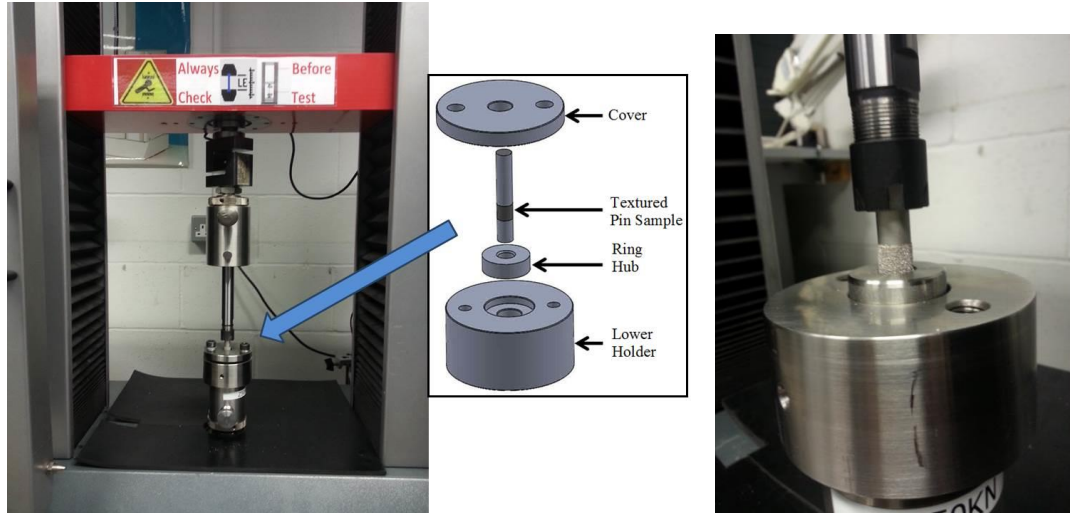
#### 4.16 Insertion and pull-out tests

The following Figure 4-28 shows a schematic diagram for the resulting textured pin sample and the hub ring. The hub rings were manufactured to the final dimension using high precision CNC lathe machines, and the hole was reamed to the required diameter of  $10.05 \pm 0.003$  mm. The hole was chamfered on one end at  $45^\circ$  for the ease of pin insertion and to reduce the destruction of the textured material by shear during insertion. The hub thickness and the chamfer angle were adjusted to keep the full engagement length between the two mating part always as 10 mm.



**Figure 4-28** Shows a laser textured insertion pin and the corresponding hub.

The test is a continuous insertion-removal and was carried out by using a Zwick Z-50 testing machine with the Zwick TestXpert simulation software. Both insertion and removal tests were carried out using speed of 5 mm/min. The two mating parts were vertically aligned by means of two holders along the main axis of the testing machine. The lower steel holder was used to hold the ring hub, while the insertion pin was rigidly held by means of a collet holder assembly mounted on the upper moving head, see Figure 4-36. The model was set to carry out the insertion and the removal tests subsequently using the same speeds with 30 seconds of full insertion holding time.



**Figure 4-29** Picture of the insertion and removal test arrangement on the Zwick Z-50.

More detailed drawings for this arrangement and assembly is in *Appendix C*.

#### **4.16.1 Commercial samples test**

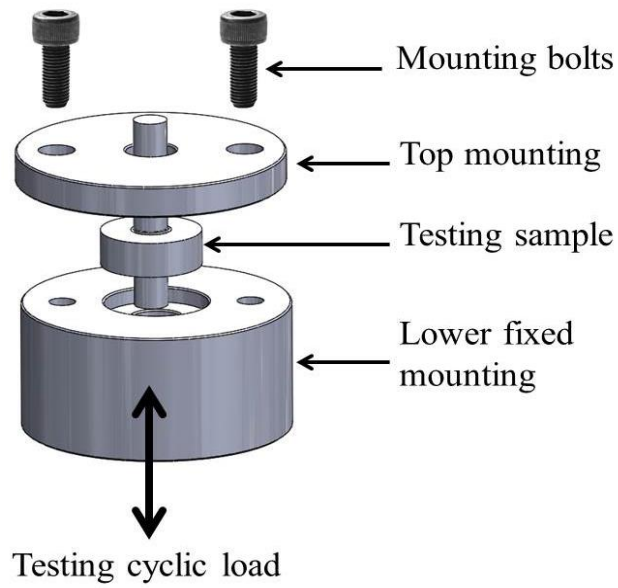
Commercial pin insertion samples of similar dimensions from Radionics were also tested for comparison. The samples are made from plain steel with carbon content of less than 2% and negligible amounts of other residual elements. The samples are surface hardened and polished to the final diameter of 10 mm from the origin, see Figure 4-30. The test was conducted according to the rule of thousandths explained in section 3.1, by inserting in a 9.99 mm hole diameter hubs and using the procedure explained formerly in this section. In addition, hubs with different hole diameter were also tested for the insertion and pull-out force investigations, more details are given in *Appendix C*.



**Figure 4-30** Commercial plain steel pin insertions.

#### **4.17 Fatigue test**

The axial force fatigue test was carried out to determine the fatigue strength of the joint for a large number of cycles. The test was conducted with accordance to the ASTM E466 standard [179] except that the specimen in this test represents the fit-joint. Sample no. 9 was used to carry out the proposed test using ESH 100 kN axial fatigue test machine controlled by servo-hydraulic associated with a PC and ESH software which calculates the stroke, strain and the load with reference to the time or the number of cycles achieved. The sample was mounted in the hydraulic clamp of the testing machine by using similar arrangement to that used in the insertion test, see section 4.16. The load values selection was based on the static loads found from the insertion test and was alternating in a constant amplitude at frequency of 10 Hz to obtain the joint behaviour to use in fatigue design. According to ASTM standards [180], in the frequency test range of 0.01 to 100 Hz were most results are found, the fatigue strength is unaffected for most engineering materials. The axial load was generated by the hydraulic actuator and was fully reversed during the entire test. The fatigue test was conducted under load and displacement control. During this test, the loading force and frequency were applied and the resulting strain was recorded. The test will be terminated when the recorded force ceased or dropped to 25% of the set load indicating the loss of bond and/or when the stroke reached 1000% of the initial stroke indicating joint failure by separation. The following Figure 4-31 shows the test set up.



(a)



(b)

**Figure 4-31** Fatigue test (a) sample assembly sketch and (b) experimental set up.

In this set up:

- The lower mounting is rigidly connected to the hydraulic cylinder of the testing machine. This cylinder is responsible for the cyclic load applied and controlled by a hydraulic servo valve and the ESH operating software.

- The lower mounting is machine to allow for an easy and flat engagement with the sample under testing.
- The top mounting is to be assembled and locked by means of two M12 hard steel bolts.
- The top jaw which is mounted on the fixed axis of the testing machine is lowered and gripped with the pin insertion.

#### 4.18 Laser nitriding

In this study, laser nitriding of 316L SST pins of 10 mm diameter and flat carbon steel samples were carried out. A 316L stainless steel pin material similar to that listed in section 4.2 was used in this experiment and processed by using the same laser processing parameters. A full set of 17 samples were selected from the previous  $3^3$  full factorial based on Box Behnken design. The test was carried out using the same procedure explained in section 4.5.1 except for the assist gas. The argon gas used in the first study was replaced by a gas mixture composition of 20% Ar-80% N<sub>2</sub>. The gas matrix was prepared and supplied in a standard type gas cylinder by BOC gases Ireland ltd. The dilution of nitrogen with an inert gas such as argon must render the liquidity of the molten metal allowing for higher penetration and diffusion of the nitrogen and eliminates the presence of cracking but at the expense of surface hardness [125,131,137,181,182].

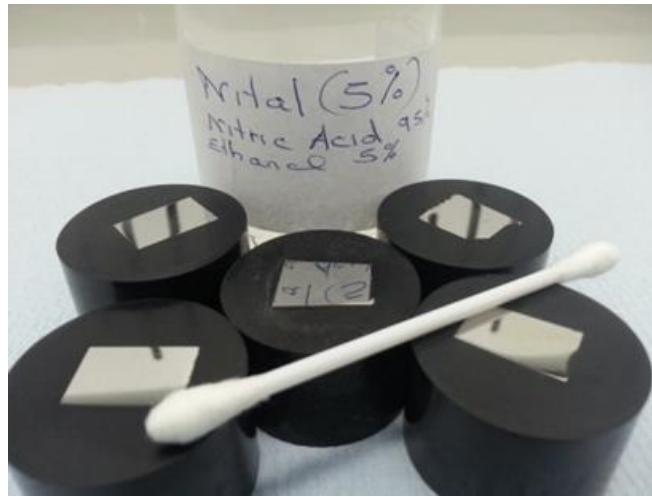
**The carbon steel sample:** The following Table 4-9 lists the mass percentage for the chemical composition of the carbon steel revealed by using Spark Spectroscopy. The aim of the experiment was the enhancement of the surface hardness, wear resistance and the investigation of the alteration in the microstructure due to the new nitrogen atmosphere.

**Table 4-9** Chemical composition of the carbon steel samples used in laser nitriding.

C%	Mn%	Cr%	Si%	Ni%	W%	Cu%	Co%	Ce%	Ta%	Mg%	V%	Fe%
0.2	1.5	0.02	0.05	0.03	1.2	0.55	3.0	0.64	0.9	0.12	0.11	97.5



A similar procedure to that described in section 4.8 was used for the samples preparation regarding the metallographic study. In order to facilitate a good phase change investigation and clear micrographs for the grain size and orientation, a 5% nital chemical etchant was used. The etchant is made up of 95% nitric acid and 5% ethanol and was applied on the cross sectional area for 3-5 seconds by swabbing the surface using a cotton cloth [183], see Figure 4-32.



**Figure 4-32** Sample preparation for the metallographic study.

#### **4.19 Wear test**

ASTM G-99 [184] pin-on-disc (POD) standard was used for testing the modified surface tribology and wear resistance. Due to the difficulties in accessing the inspection tools, a flat sample was necessary to be used in carrying out this test. The rotational speed of the sample was converted into linear speed as shown in Figure 4-16. In order to maintain a similar irradiation exposure time on the edge, the beam movement was set to pass the edges of the flat sample on both side with a distance equal to half the circumference of the cylindrical sample. In this case for the laser beam to move out and back in, the same time is to be consumed compared to that in case of the cylindrical sample.

The flat samples produced in this experiment were tested for the surface roughness and cross-section micro-hardness and were found to agree well with those obtained from the

cylindrical samples. This comparison indicates that the wear test can be performed on the flat sample confidentially.

The following Figure 4-33 shows the cylindrical geometry for sample no 9 with the equivalent flat sample produced.



**Figure 4-33** Flat sample produced to facilitate the pin on disc wear test.

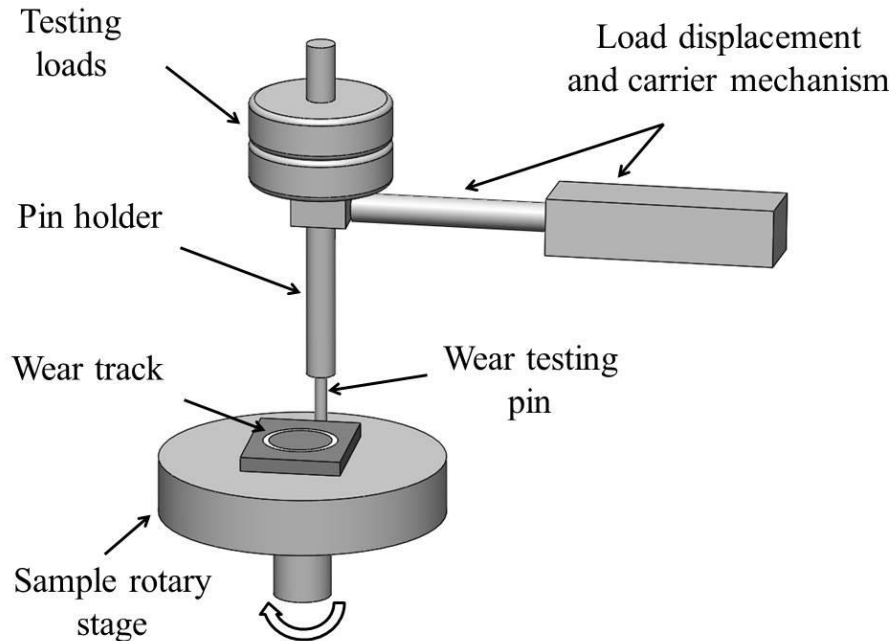
The specific wear rate can be calculated using the following equations (4-9) and (4-10)

$$\text{Volume loss, } \Delta V = \frac{\text{Mass loss}}{\text{Density}} \quad (4-9)$$

$$\text{Specific wear rate} = \frac{\text{Volume loss}}{\text{Total sliding distance} \times \text{Normal load}} \quad (4-10)$$

The mass loss was obtained using weighing scale from (Sartorius CP124S) with a resolution of 0.0001g. The parameters used in this test were applied load 25 N, rotational speed 200 rpm, wear track radius 4 mm, testing time 120 minutes. The wear testing pin used during the test was a tungsten carbide punch pin from Link-Tooling

with hardness of 63-65 HRC (775-834 HV) and a diameter of 5 mm. Figure 4-34 shows a schematic diagram for the wear testing instrument explaining the main parts and the sample under test.



**Figure 4-34** Schematic of the wear testing instrument.

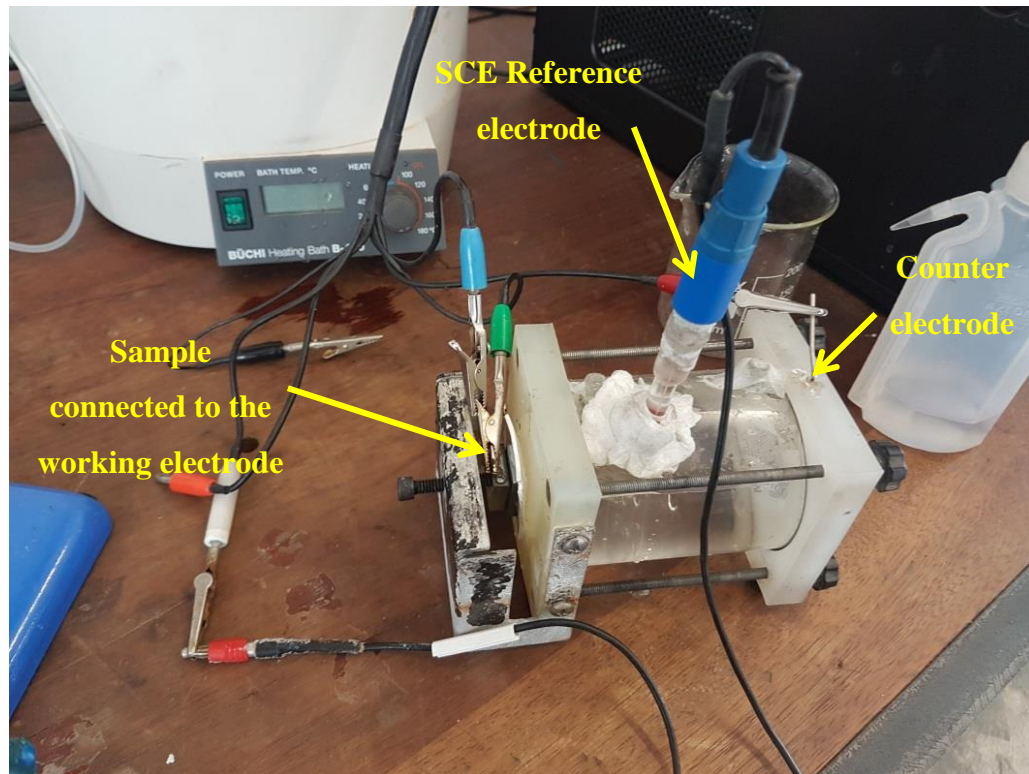
The test was carried out on three samples for comparison, one as-received and two laser processed samples, the first one was processed with argon and the other one with nitrogen as assist gas. Each sample was repeated for three times. The test results would be compared for the laser treated versus the un-treated samples in order to investigate the tribological effect of the laser processing on stainless steel surface.

The advantage from this test, as explained, is to investigate the effect of the laser processing on the surface hardness which is a function of the wear resistance. At the macroscopic level, interference-fit joints transmit loads from one part to another by means of the geometric interfering material. At the microscopic level, it is the peaks and the valleys that interfere, interlock and prevent the loss and failure of the assembly. Therefore, improving the wear resistance of a thin layer would prevent or reduce galling

of these peaks and enhance the joint strength. Although, making the part from a hard and wear resistant material would compromise the joint toughness and may result in a sudden failure under impact loads [157].

#### 4.20 Corrosion test

The effect of the laser processing on the corrosion resistance and corrosion rate of the material was investigated by using electrochemical testing in a NaCl solution of 0.6% concentration at room temperature. The linear polarization resistance test was used. It is a non-destructive testing method which is used to identify the corrosion resistance in metals. In this test, the sample was polarised by using a potentiostat polarisation unit from GAMRY Interference 1000 set to a scanning rate of 0.3 mV/sec. The sample was connected to the mounted working electrode (green and blue posts), the platinum counter electrode is connected to the (red post) and the reference electrode type used was silver chloride AgCl (white post). The experiment set up and arrangement can be seen in Figure 4-35.



**Figure 4-35** Polarisation electrolyte cell set up used for the corrosion tests.

The test is based on two electrochemical reactions. The first reaction is anodic in which an electron is released into the metal and the second is a cathodic reaction in which the electron is removed due to the reduced solution. When the two reactions reach an equilibrium status and the flow of electron from both reactions are equal, no net electric current supplied from the potentiostat occurs. This equilibrium status determines the corrosion potential ( $E_{cor}$ ), and the corrosion current ( $i_{cor}$ ) of a metal. The higher the corrosion potential the higher the corrosion resistance. The open circuit potential  $E_{oc}$  test was run until stabilisation and measured before commencing the potentiodynamic test. The actual test starts from -300 mV below the  $E_{oc}$  value.

An as-received sample and two other samples processed by CO<sub>2</sub> laser in argon and nitrogen atmosphere were tested for comparison. The samples were ultrasonically cleaned prior to the test in diluted citric acid for 90 seconds and 50 °C, rinsed in deionised water and dried by hot air gun. An area of 0.785 cm<sup>2</sup> from the textured surface was exposed to the electrolyte NaCl solution.

#### 4.20.1 Calculation of the corrosion rate

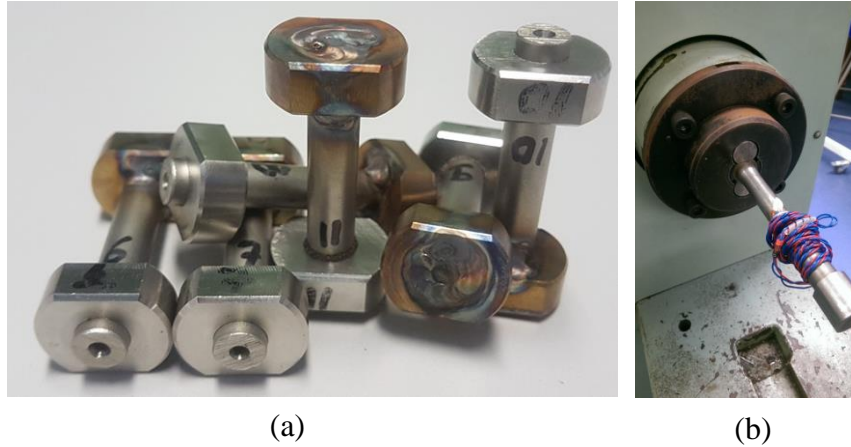
The corrosion rate, CR, of the metal in (mm/year) can be found by using the Tafel slope extrapolation analysis and the ASTM G102 standard, which is based on Faraday's law as follows:

$$CR = K_1 \cdot \frac{i_{cor}}{\rho} \cdot EW \quad (4-11)$$

where:  $K_1 = 3.27 \times 10^{-3}$  (mm.g/ $\mu$ A.cm.yr),  $\rho$  is the metal density = 8 g/cm<sup>3</sup> and EW is the equivalent weight of 316L stainless steel = 25.5 g/equivalent,  $i_{cor}$  is the corrosion current density ( $\mu$ A/cm<sup>2</sup>) =  $I_{cor}$ /localised exposed area of the specimen.  $I_{cor}$  can be found at the intersection point of the Tafel slopes on the potentiodynamic polarization plot. Note that the equivalent weight is the mass of a substance especially in grams that combines with or is chemically equivalent to eight grams of oxygen or one gram of hydrogen : the atomic or molecular weight divided by the valence.

#### 4.21 Torsion test

The torsion test was carried out on ten replicates of sample no. 9. The hub rings were machined into two opposite flat sections as shown in Figure 4-36 (a) in order to be held on the testing machine.

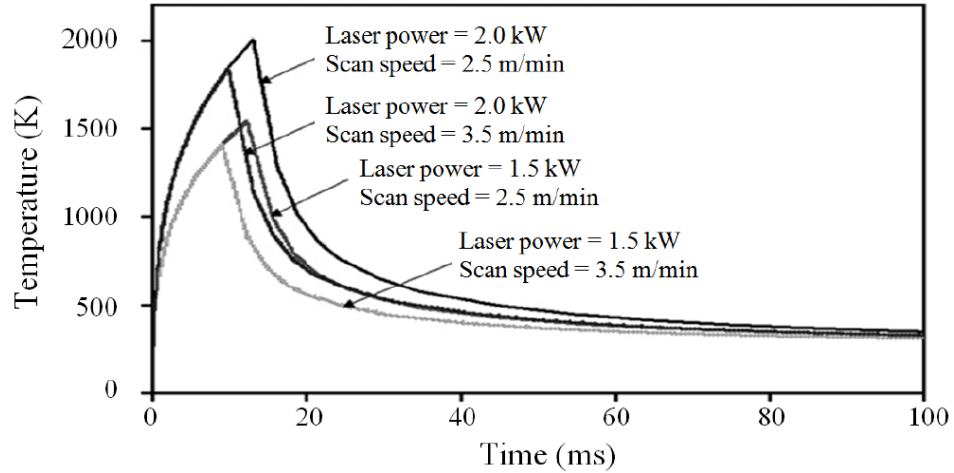


**Figure 4-36** (a) Samples preparation for torsion test (b) testing machine.

A similar hub rings were manufactured to be easy-fitted on the other end of the test samples. The two clamping jaws of the testing machine apply no force on the samples in order to avoid any interfere with the force created by the textured insertion, instead, the samples are only slide into the jaws and hold by means of the two flat sections. The testing machine is an analog testing and torque monitoring from Avery Birmingham. The test was carried out by apply fixed angular displacement of 30 degrees per minute and measuring the resisting torque created until failure and sliding of the insertion with respect to the hub.

#### 4.22 Thermal modelling

A thermal model has been implemented to investigate the surface temperature and temperature profile and their relationship with the laser processing parameters. This is important because the thermal history determines the resulting mechanical properties of the modified surface and its microstructure [185–189]. Basu et. al. [188] reported the correlation between the laser beam power and scanning speed with the resulting surface temperature for AISI 4140 steel, see Figure 4-37.



**Figure 4-37** Surface temperature plotted for different laser power and scanning speed as a function of time [188].

#### 4.22.1 Energy calculations:

The thermal energy deposited by the laser beam is converted to heat on a shorter time than the pulse duration or the laser-material interaction time [13,190]. The resulting temperature is a function of the deposited energy and the material thermal diffusivity ( $\alpha$ ). The thermal diffusivity can be calculated from:  $\alpha = k/\rho \cdot C_p$  where  $k$  is the thermal conductivity,  $\rho$  is the material density and  $C_p$  is the specific heat. The heat affected depth ( $z$ ) can be calculated as  $z = \sqrt{2 \cdot \alpha \cdot t_p}$  [13] where  $t_p$  is the pulse duration.

In this study, it was found that it is convenient to quantify one parameter which concludes the most significant factors for a better understanding and comparison of the applied parameters, their values and their effect on the resulting responses. The energy density,  $E$ , is useful to be implemented in this case because it is attributed to the laser beam power, scanning speed and the spot diameter.

$$E = \frac{\text{Average Laser Power}}{\text{Scanning Speed} \times \text{Spot Diameter}} \quad (\text{J/m}^2) \quad \dots\dots(4-11)$$

The maximum and minimum energy density used for the set of samples listed in the DoE Table 4-8 can be calculated from equation (4-2):

To find  $E_{\min}$ :

$$\omega_{\max} = \frac{\text{PRF}_{\max} \times 60 \times d}{\pi \times D \times (1 + \text{OV}_{\min})} = \frac{300 \times 60 \times 0.22}{\pi \times 10 \times 0.8} = 157.56 \text{ rpm}$$

$$U = 4950 \text{ mm/min} = 82.5 \text{ mm/sec}$$

Hence, 
$$E_{\min} = \frac{300 \times 0.5}{82.5 \times 0.2} = 9.9 \text{ J/mm}^2$$

Similarly, the maximum Specific Energy value is:

$$\omega_{\min} = \frac{\text{PRF}_{\min} \times 60 \times d}{\pi \times D \times (1 + \text{OV}_{\max})} = \frac{100 \times 60 \times 0.22}{\pi \times 10 \times 1.2} = 35 \text{ rpm}$$

$$U = 1100 \text{ mm/min} = 18.3 \text{ mm/sec}$$

$$E_{\max} = \frac{500 \times 0.5}{18.3 \times 0.2} = 68.30 \text{ J/mm}^2$$

This range of energy density is also shown in the excel sheet for the input and the calculated laser processing parameters in *Appendix B*. The calculated energy density values were advantageous during translating the laser processing parameters used on the cylindrical sample geometry to produce equivalent flat samples adopted in the wear and corrosion tests as explained in sections 4-19 and 4-20.

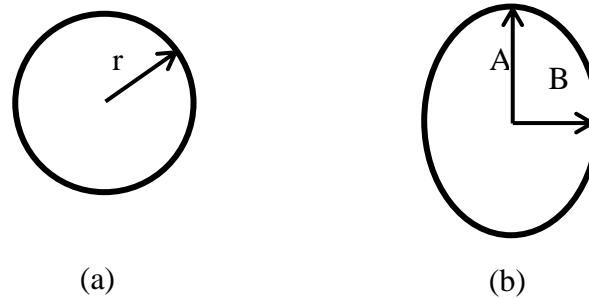
#### 4.22.2 Absorption factor calculations

From section 4.3, since the threshold amount of heat needed for melting the surface is 24.64 mJ for the particular set of parameters applied and the pulse energy deposited was 1000 mJ, then the absorption factor A is calculated from

$$A = \frac{\text{Heat Needed for melting}}{\text{Total Pulse Energy supplied}} = \frac{24.64}{1000} = 0.024$$



This value was calculated based on the assumption of a circular cross-section laser beam of 200  $\mu\text{m}$  spot size. As explained in section 4.3.1 and as can be seen in Figures 4-8 (b) and 4-38 below, the melted zone form an ellipse shape with the dimensions of  $A=360/2 \mu\text{m}$  and  $B=200/2 \mu\text{m}$ . Moreover, the estimation of the thermal energy needed for melting which was carried out in section 4.3.1, was based on using the calculated diffusion length as the full melt-pool depth. The actual melt-pool depth was found to be 70  $\mu\text{m}$  as shown in Figure 4-9.



**Figure 4-38** (a) The theoretical propagating laser beam cross-section and  
(b) the incident laser beam track and melt-pool form.

Considering the new dimensions and recalculating gives the actual melted mass would be  $3.18 \times 10^{-8} \text{ kg}$  and the thermal energy absorbed 22.5 mJ.

The main assumption here is that the thermal energy absorbed from the laser pulse is converted to heat and was all used to utilized the metal surface melting and that there is no heat loss to surrounding, see section 4.3.

#### 4.22.3 The mathematical model

A mathematical model was used to simulate the laser thermal processing and the temperature distribution. It is important to investigate the effect of the laser processing parameters on the heating and cooling rates in order to compare their effect on the resulting mechanical properties of the processed surface and the performance of the produced samples. The model had previously been developed at DCU [38] and was implemented by several researchers [38,53,185]. The model is using the LabView software to solve the space and time dependent temperature equation 4-12. The model is

based on a moving point heat source solution which is described by Dowden [191] and assuming that no heat is generated inside the processed substrate. The temperature distribution on a space and time dimensions  $T(x,y,z,t)$  is:

$$T(x,y,z,t) = T_0 + \frac{P(t)}{2\pi kr} \exp \left[ i\omega t + \frac{U}{2\alpha} \left( x - r \sqrt{1 + \frac{4\alpha\omega i}{U^2}} \right) \right] \dots\dots (4-12)$$

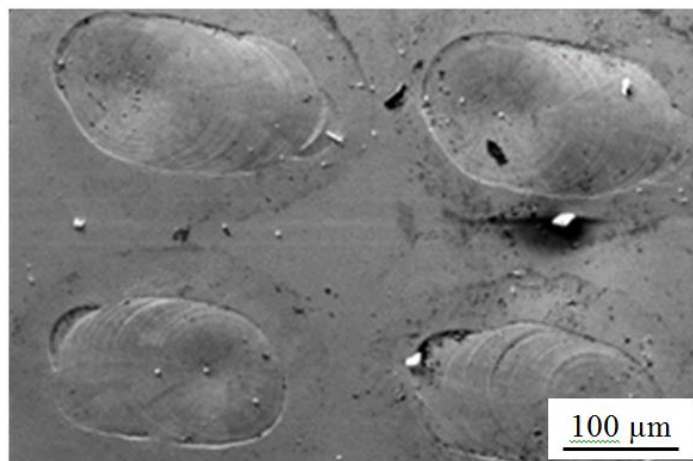
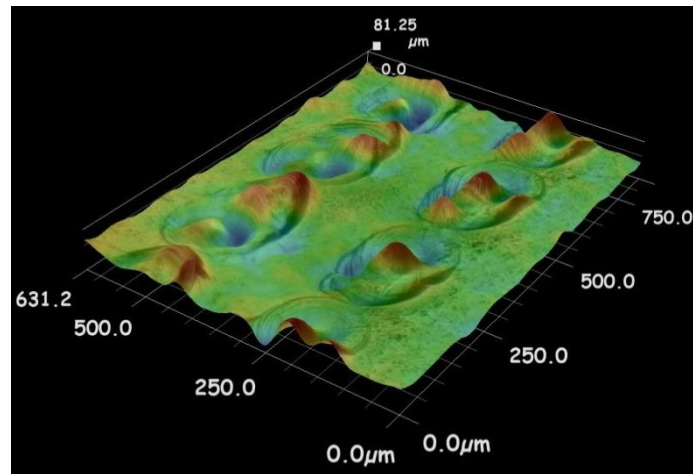
where  $P(t)$  is the time dependent laser power input (W),  $U$  is the scanning speed,  $r$  is the radial distance from the power source  $=\sqrt{x^2 + y^2 + z^2}$ ,  $\omega$  is the fundamental frequency  $= 2\pi PRF$ ,

This solution is based on the following assumption:

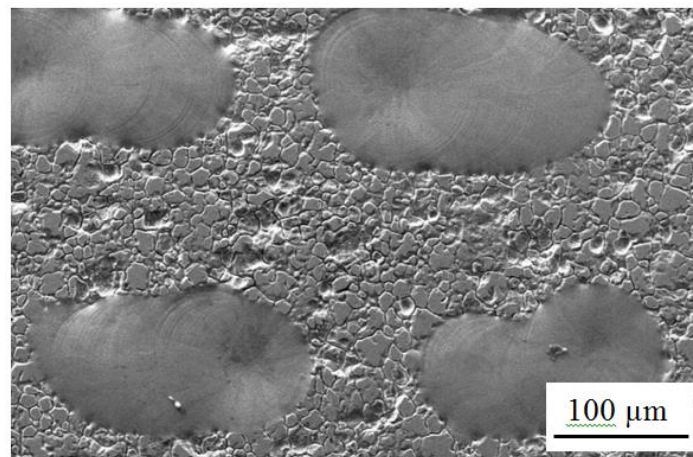
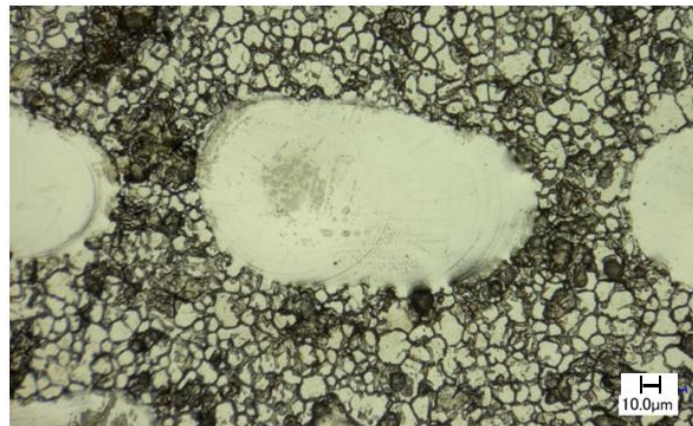
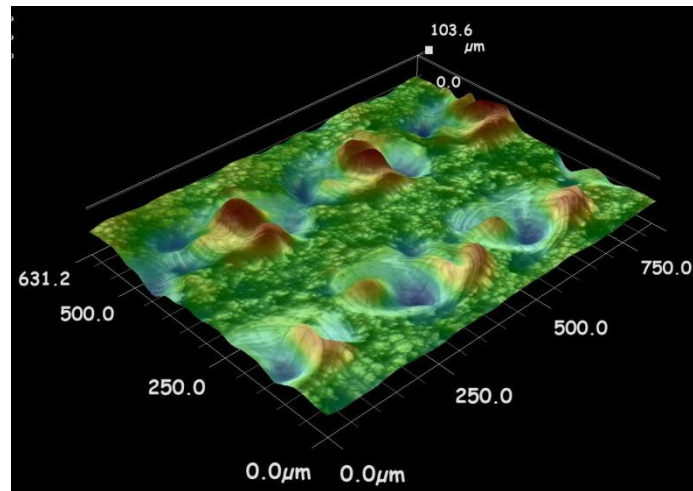
- Material initial temperature is equal to the room temperature.
- The problem is a pure heat conduction problem. And that all the input power is converted into heat.
- There is no heat loss to surrounding or from the metal surface opposite to the heat source, i.e.  $\frac{\partial T}{\partial z} = 0$ .
- No phase change results in the entire process.

### **5.1 Effect of surface roughness on absorption of thermal energy**

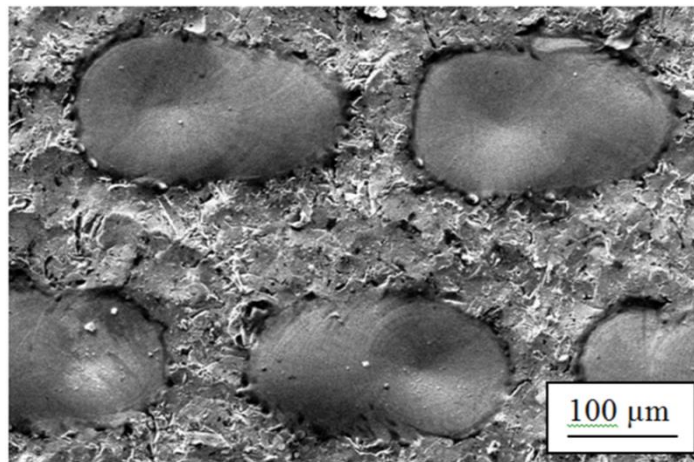
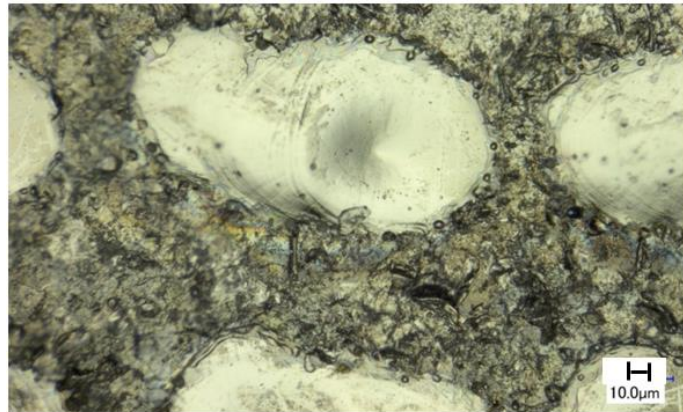
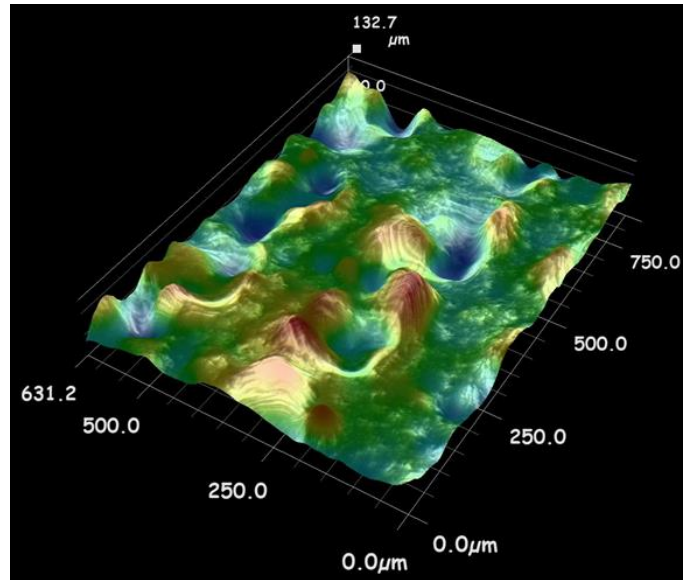
As explained in section 4.2.3, three flat samples with surface roughness of 0.01, 0.8 and 2.3  $\mu\text{m}$ , respectively, were processed by using PW mode as explained in section 4.3.2. The laser processing parameters applied were 200 W, 100 Hz and scanning speed of 2380 mm/min. The produced samples show a clear variation in the melt pool dimensions as listed in Table 5-1, indicating the variation in the amount of thermal energy absorbed by the metal surface. The following Figure 5-1 shows SEM and 3D optical microscope images for the melt pool of the three samples.



(a)



(b)



(c)

**Figure 5-1** Optical and SEM images for the melt crater on 316L SST flat samples using similar processing parameters with different average surface roughness Ra of (a) 0.01  $\mu\text{m}$  (b) 0.8  $\mu\text{m}$  and (c) 2.3  $\mu\text{m}$ .

**Table 5-1** The melt pool (MP) dimension corresponding to the samples in section 4.2.3

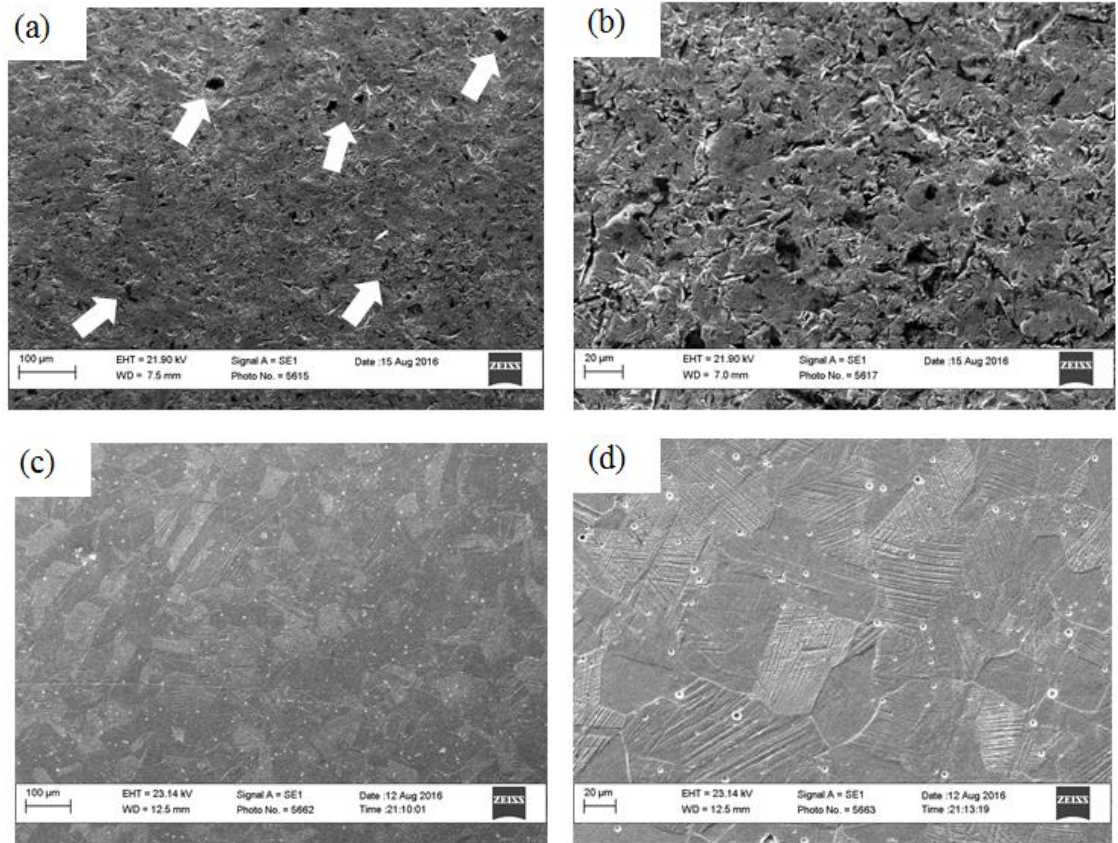
Sample surface roughness (Ra)	MP length ( $\mu\text{m}$ )	MP diameter ( $\mu\text{m}$ )	MP depth ( $\mu\text{m}$ )
0.01	240	110	81
0.8	350	185	103
2.3	385	205	132

The increase in the melt pool size can be explained by the increase in surface roughness and undulation waving leading to multi reflections for the laser beam. The rougher topography increase the possibility of a stimulated absorption caused by the beam interference with the sideways reflected beams. These results agree well with the results reported in the literature and explained in Section 1.5. More results images are shown in *Appendix D*.

## 5.2 Morphology and metallography investigations

**As-received samples:** Figures 5-2 (a) and (b) show SEM images for the surface morphology, Figures 5-2 (c) and (d) show the cross-sectional grain structure view for the as-received sample prior to laser processing. The dark spots indicated by the white arrows in Figures (a) and (b) show the martensite formed by cold working during manufacturing due to the non-stable austenite microstructure [183].





**Figure 5-2** SEM images of the as-received samples (a) and (b) surface,(c) and (d) cross section microstructure revealed by glyceresia etchant.

The pores and dots noted in Figures 5-2 (c) and (d) might be explained by the inclusions and impurities that been removed during the preparation of the sample. The preparation for the metallographic study include cross sectioning, grinding, polishing and chemical etching as explained in section 4.8. The grain structure in Figure 5-2 (c) and (d) were revealed using glyceresia.

### **5.3 Effect of the laser processing**

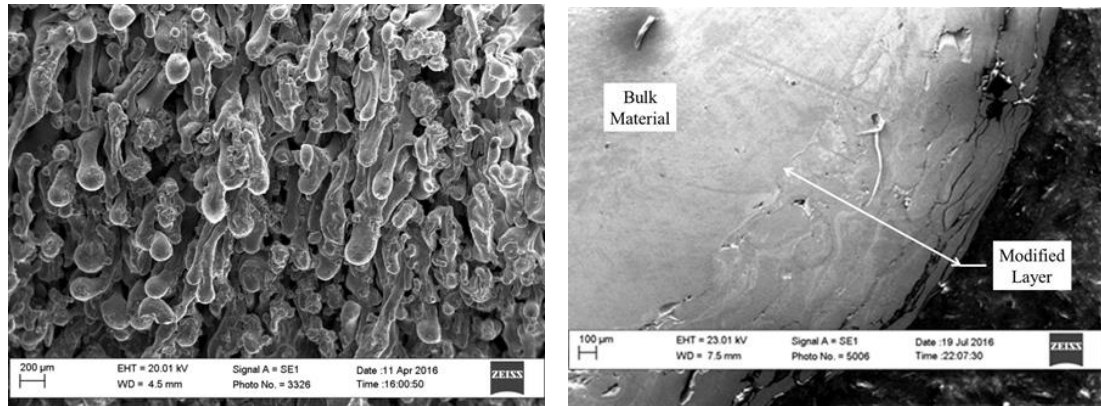
#### **5.3.1 Surface morphology and cross-sectional microstructure**

As detailed in Chapter 4, Sections 4.8 and 4.9, the laser processing parameters were selected based on the results from the preliminary test. To demonstrate the effect of the main laser processing parameters on the surface morphology and the cross sectional microstructure of the produced samples, two samples were selected to be inspected in details. These two samples were chosen for comparison because they exhibit the

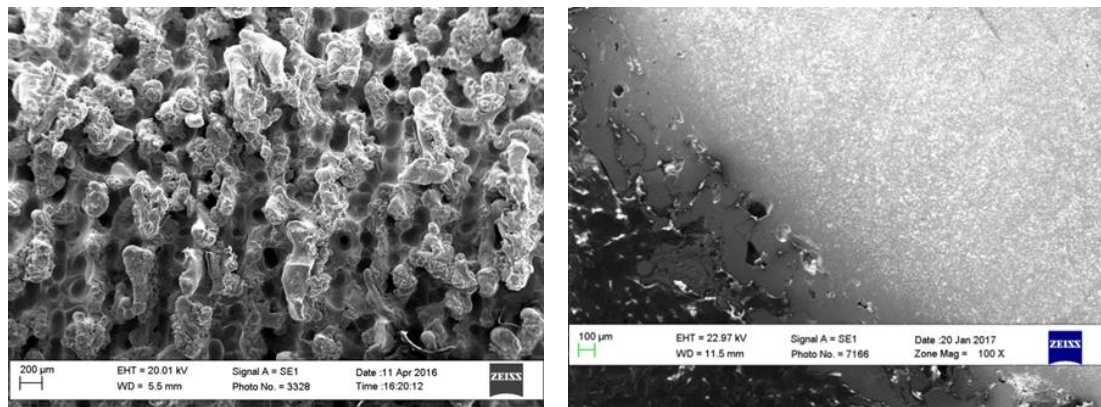


maximum and minimum pull-out forces of 6 kN for sample no. 9 and 0.17 kN for sample no.15. Sample no. 9 was processed with 400 W, 100 Hz, and -20% overlap, the resulting residence time is 4 ms, and the power density is 826 kW/cm<sup>2</sup>. Sample no. 15 was processed with 500 W, 300 Hz and -20% OV and a resulting residence time of 1.33 ms and power density of 1033 kW/cm<sup>2</sup>. Furthermore, there is more SEM micrographs for the processed samples in *Appendix D* and a table of the processing parameters, the related calculated parameters and the mechanical tests results are listed in excel sheet and shown in *Appendix B*.

The following Figures 5-3 and 5-4 illustrate the produced surface morphology and the cross sectional microstructure of the modified layer for samples no. 9 and 15 respectively.

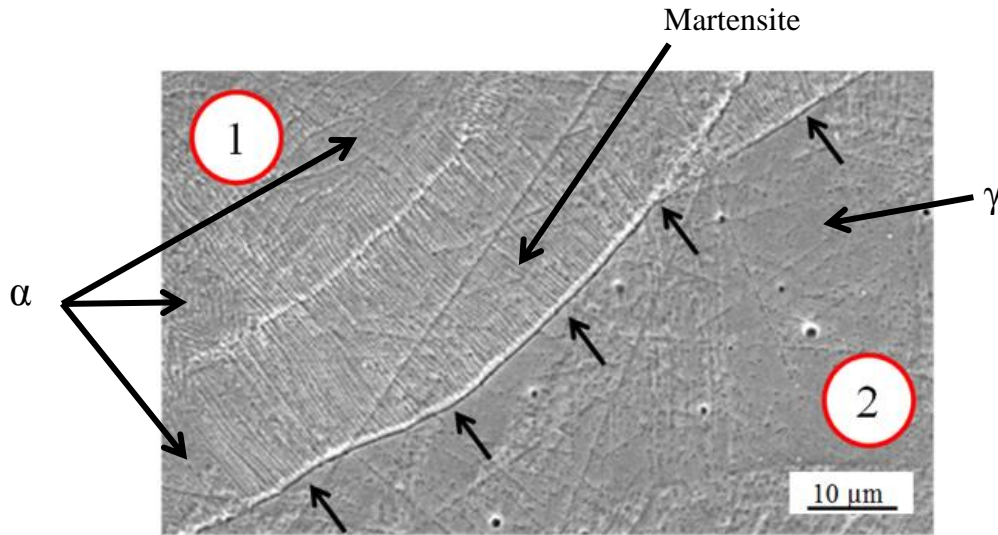


**Figures 5-3** Sample 9 surface morphology (left) and cross sectional microstructure (right).



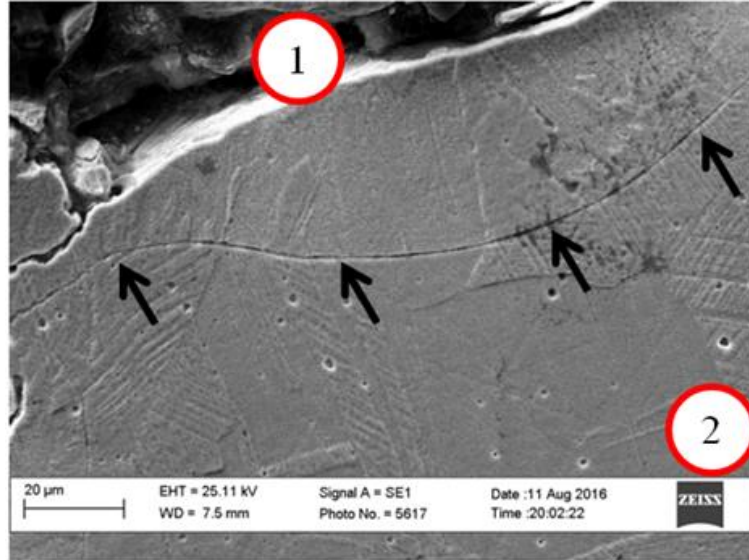
**Figure 5-4** Sample 15 surface morphology (left) and cross sectional microstructure (right).

A wide range of variation in the surface morphology, surface roughness and the melted layer depth was observed which can be related to the processing parameters as will be illustrated in the next chapter. The melted and re-solidified zone and its boundaries for samples no. 9 and 15 are presented in Figures 5-5 and 5-6, and indicated by area (1) and black arrows. Sample no. 9 shows a clear phase transform from the soft austenite ( $\gamma$ ) to the hard dendrites of martensite surrounded by islands of ferrite ( $\alpha$ ). The untreated bulk material is indicated by area (2).



**Figure 5-5** Micrograph of the cross section microstructure for sample no. 9 revealed by glyceresia etchant.

Due to the shorter processing time of (1/3) in case of S-15 compared to S-9, sample-15 exhibits no phase change except for the grain re-orientation, see Figure 5-6.



**Figure 5-6** Micrograph of the cross section microstructure for sample no. 15.

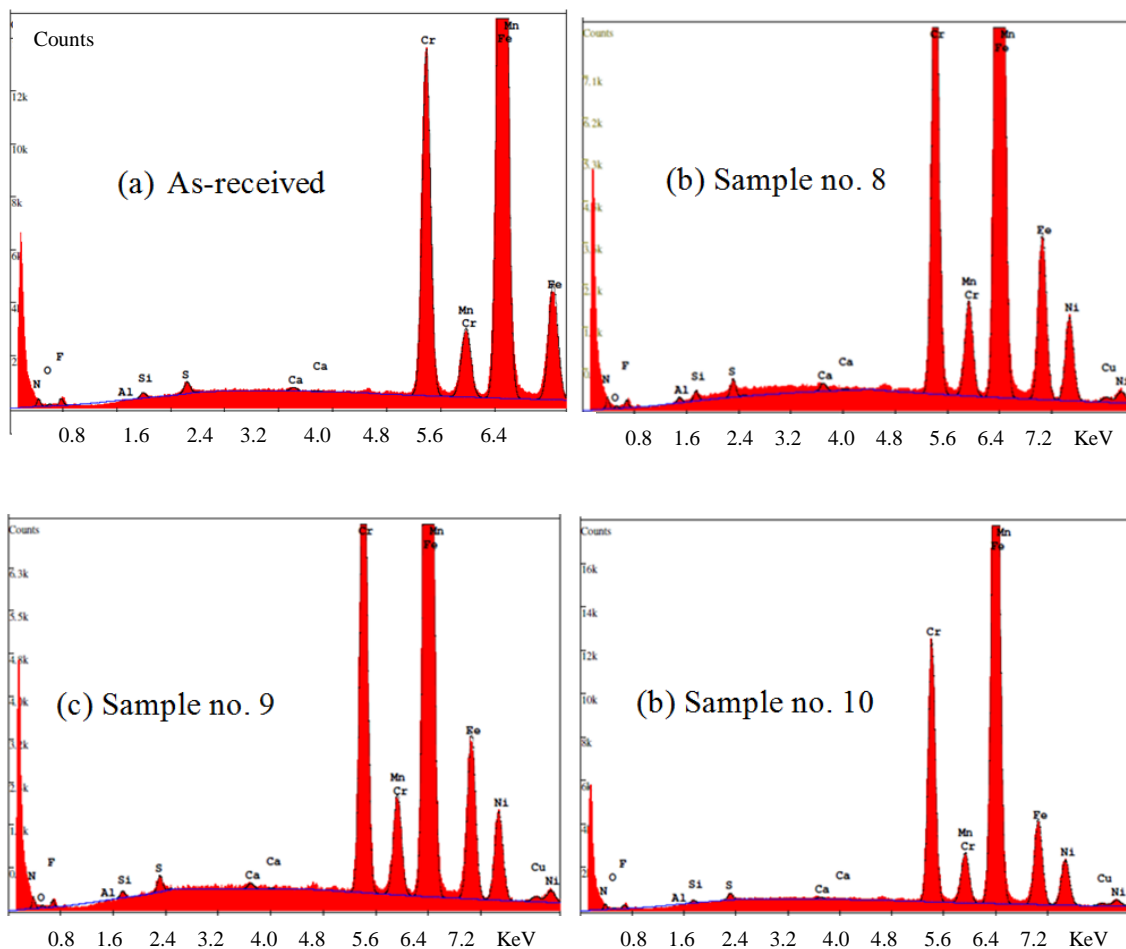
The surface morphology and the melt-pool depth exhibited in Figures 5-3 and 5-4, and the resulted surface roughness for sample no. 9 and 15 were found to be 102  $\mu\text{m}$  and 46  $\mu\text{m}$  respectively. This is due to the higher exposure time resulting from the larger pulse width for sample no. 9.

In addition, Figures 5-5 and 5-6 show the elimination of the pores and dots in the laser treated region as was noted on the cross-section view of all the samples in the DoE set. These dots could be impurities and inclusions, which might be removed during sectioning and polishing process as, explained earlier. Producing a chemically uniform surface and free of impurities can improve the wear resistance [170].

### 5.3.2 The chemical composition and EDAX test results

From section 4.10, the chemical composition for the as-received sample and samples no. 8, 9, 10 and 15 were analysed by using the energy dispersive analysis x-ray spectroscopy (EDAX). Figures 5-7 (a)-(d) show the EDAX spectrum for each sample carried out according to the method explained in section 4.10 and with respect to Figure 4-22. Table 5-2 lists the weight percentage of each element for the individual samples. As can be seen from this table, no significant changes were noted in the chemical

composition of the various elements as an indication of no phase change in the produced samples.



**Figure 5-7** EDAX spectrum of the (a) as-received and (b,c,d) processed samples.

**Table 5-2** The chemical composition of the as-received and processed samples.

Element weight %	Sample No.				
	As- received	8	9	10	15
Fe	68.99	69.58	68.63	69.06	69.44
Cr	17.27	17.22	17.52	17.61	17.24
Ni	7.8	7.68	8.01	8.0	7.89
Mn	1.99	1.37	1.95	1.79	1.90
Cu	0.61	0.49	0.56	0.48	0.52
S	0.54	0.34	0.52	0.41	0.39
Si	0.37	0.42	0.35	0.42	0.32

## 5.4 Resulting surface texture

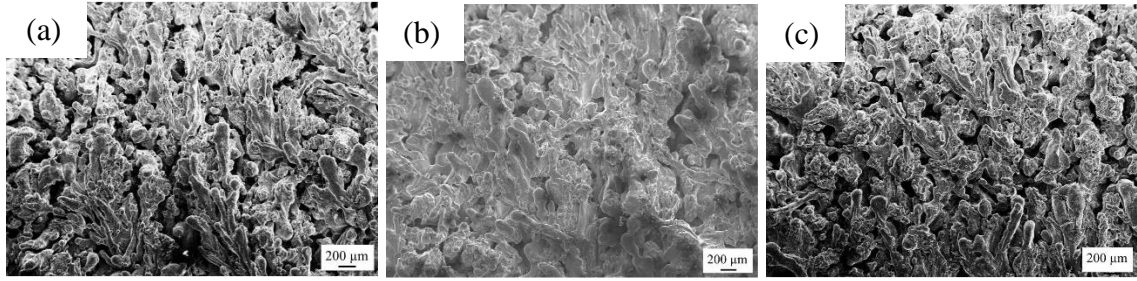
### 5.4.1 Texture pattern angle

The resulted surface texture was characterized by using SEM, see Figures 5-8 and 5-9. Figure 5-8 shows the produced textures for samples no. (a) 19, (b) 20, and (c) 11, listed in Table 5-3. Some samples show a clear texture pattern lines with an angle of 45° as indicated in Figure 5-9 which is due to the similar overlap used in the circumferential and axial direction.

**Table 5-3** The laser processing parameters applied to determine the effect of using different overlaps on the pattern angle

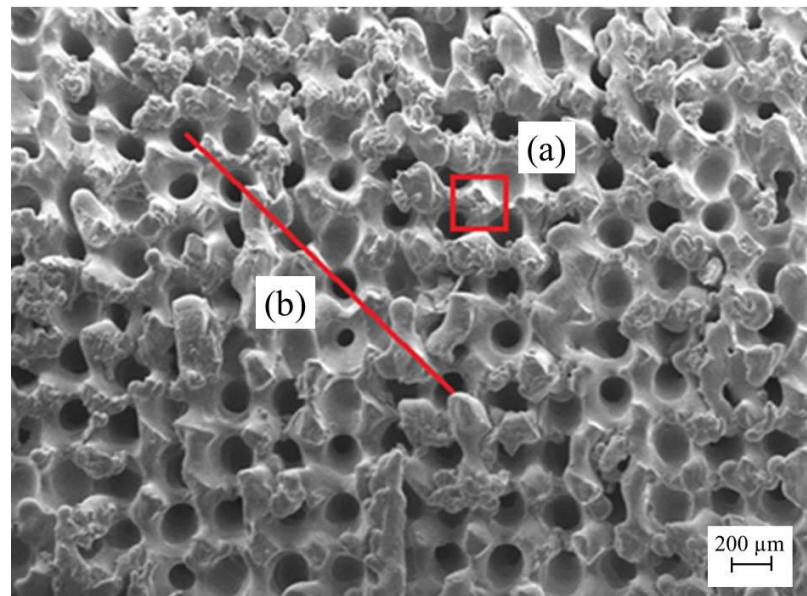
Sample No.	Power (W)	PRF (Hz)	Overlap (%OV)
19	500	300	0
20	500	300	20
11	500	300	-20





**Figure 5-8** SEM images of surfaces for sample no. (a) 19, (b) 20 and (c) 11.

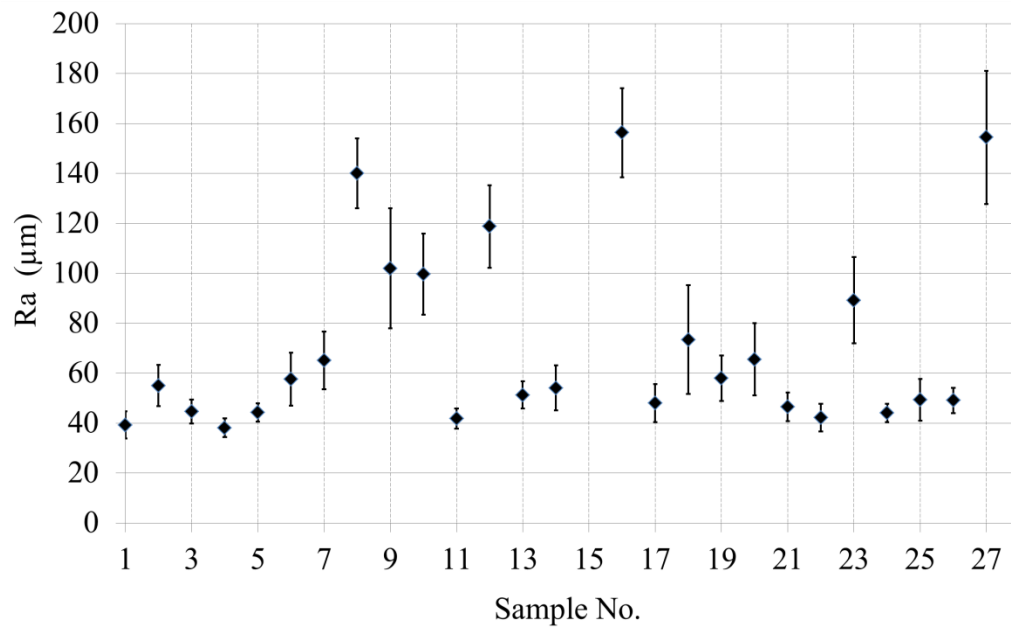
The square body (a) shown in Figure 5-9 indicates the equal distance between the centres of two consecutive pulses in the circumferential and axial directions and was calculated using image (J) software. From microstructural and macroscopic examination, no cracking was observed in the whole DoE set of samples.



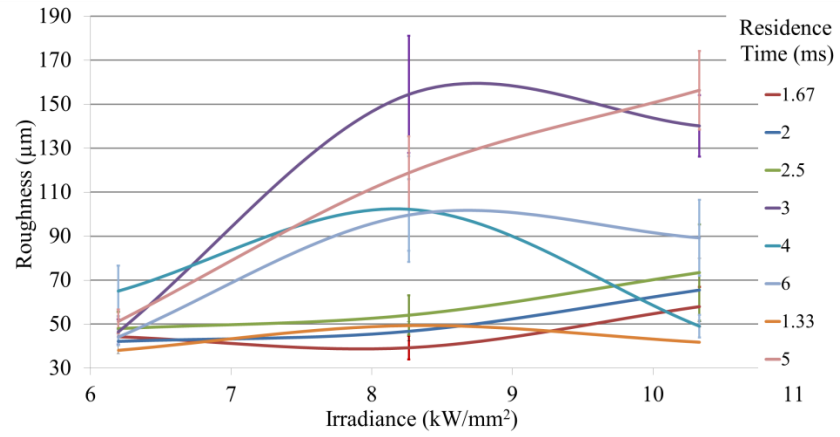
**Figure 5-9** (a) Shows the symmetrical percentage overlap -20% in both directions and (b) the pulses line angle for sample no. 4 correspond to table 4-8.

### 5.4.2 Surface roughness measurement

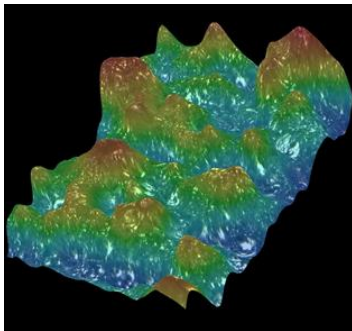
Using the method in section 4.14, the resulting average surface roughness of the produced samples was measured using the Keyence VHX2000E 3D digital microscope as explained in section 4.14. The data obtained from five measurements for each sample were averaged and plotted with the 95% CI's error bars, see Figure 5-10. Also the resulting surface roughness was plotted for the different levels of irradiance and residence time, see Figure 5-11. The 3D images of the surface roughness for the 27 samples of the full DoE model are presented in Figure 5-12.



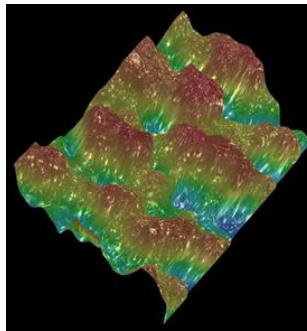
**Figure 5-10** Graph of the surface roughness recorded for each sample in the DoE, n=5.



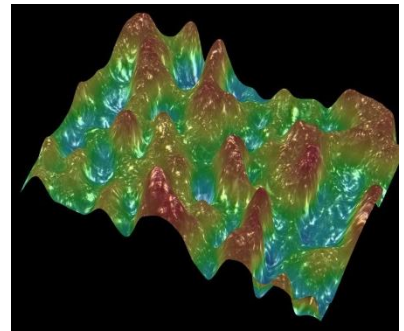
**Figure 5-11** The correlation between the surface roughness and the laser power irradiance for different residence time, n=5.



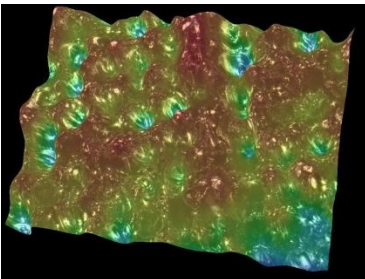
Sample-1, Ra=39.2  $\mu\text{m}$



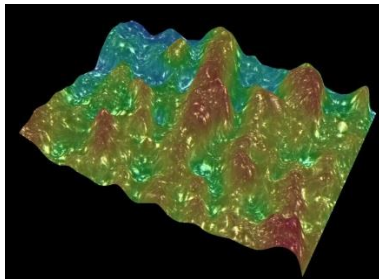
Sample 2, Ra=55.0  $\mu\text{m}$



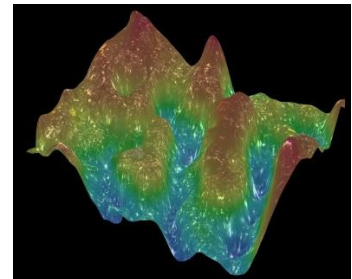
Sample 3, Ra=44.7  $\mu\text{m}$



Sample 4 Ra=38.1  $\mu\text{m}$

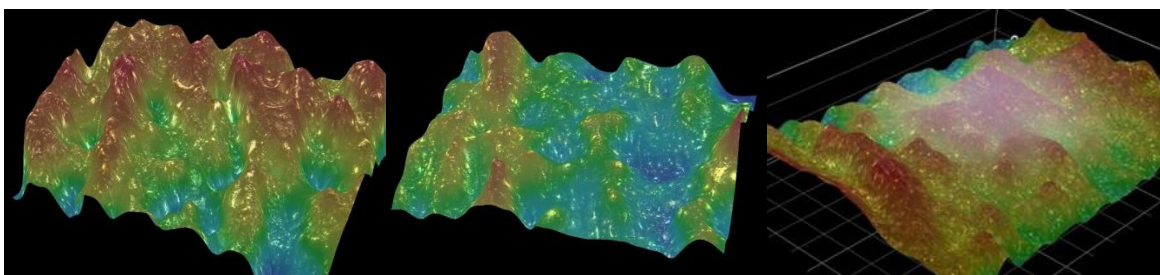


Sample 5, Ra=44.3  $\mu\text{m}$



Sample 6, Ra=57.6  $\mu\text{m}$

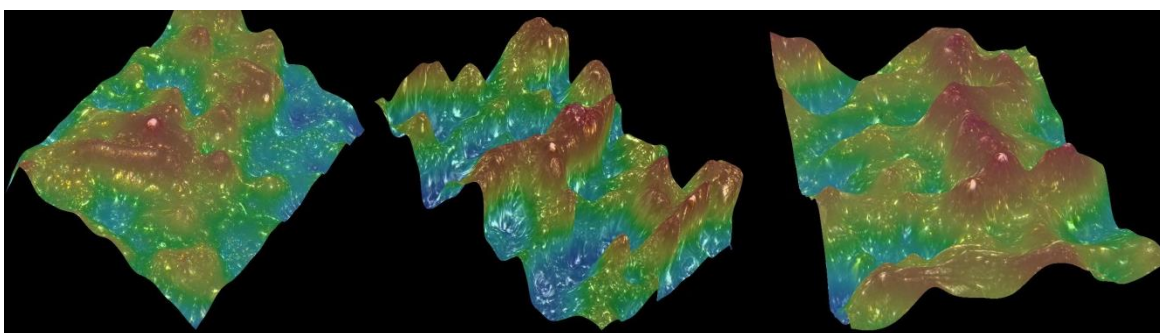




Sample 7 Ra=65.0  $\mu\text{m}$

Sample 8, Ra=140.0  $\mu\text{m}$

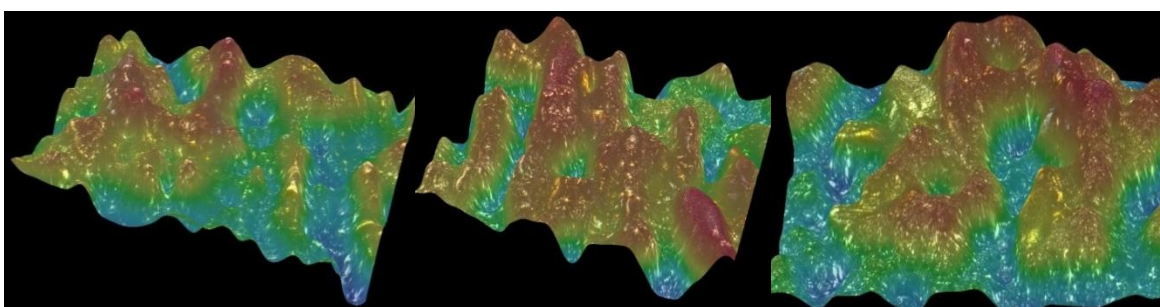
Sample 9, Ra=102  $\mu\text{m}$



Sample 10, Ra=99.6  $\mu\text{m}$

Sample 11, Ra=41.8  $\mu\text{m}$

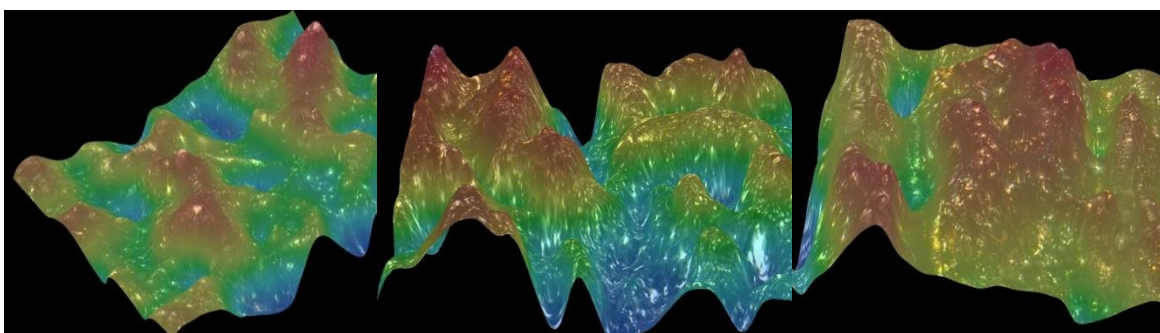
Sample 12, Ra=118.8  $\mu\text{m}$



Sample 13, Ra=51.2  $\mu\text{m}$

Sample 14, Ra=54.1  $\mu\text{m}$

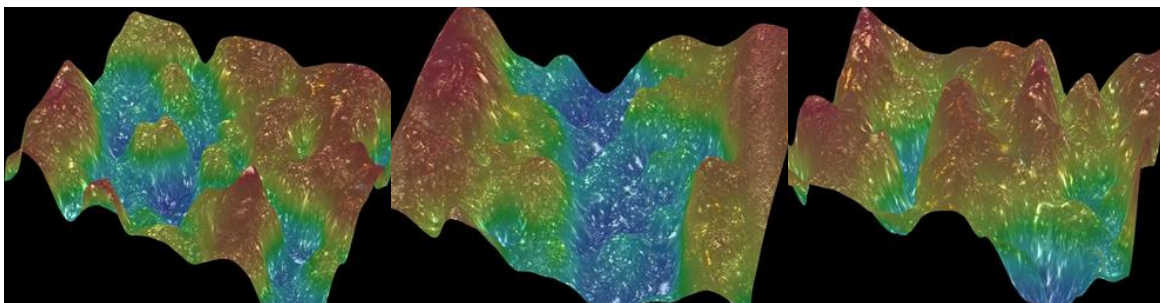
Sample 15, Ra=46.7  $\mu\text{m}$



Sample 16, Ra=156.3  $\mu\text{m}$

Sample 17, Ra=48.0  $\mu\text{m}$

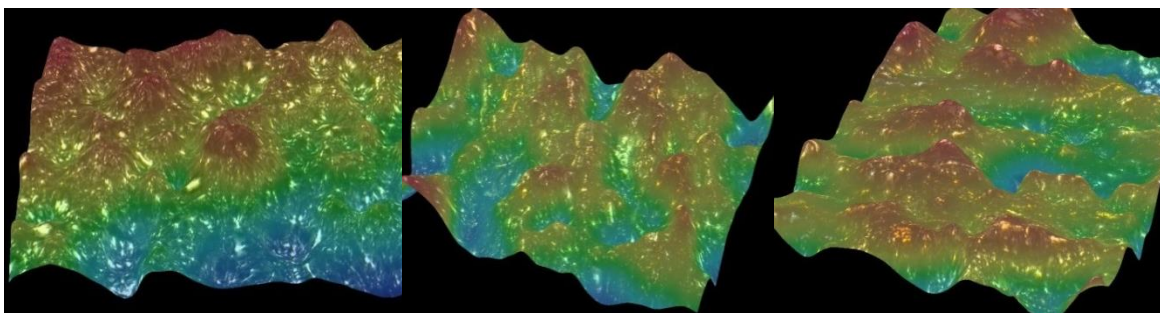
Sample 18, Ra=73.5  $\mu\text{m}$



Sample 19,  $R_a=58.0\ \mu\text{m}$

Sample 20,  $R_a=65.5\ \mu\text{m}$

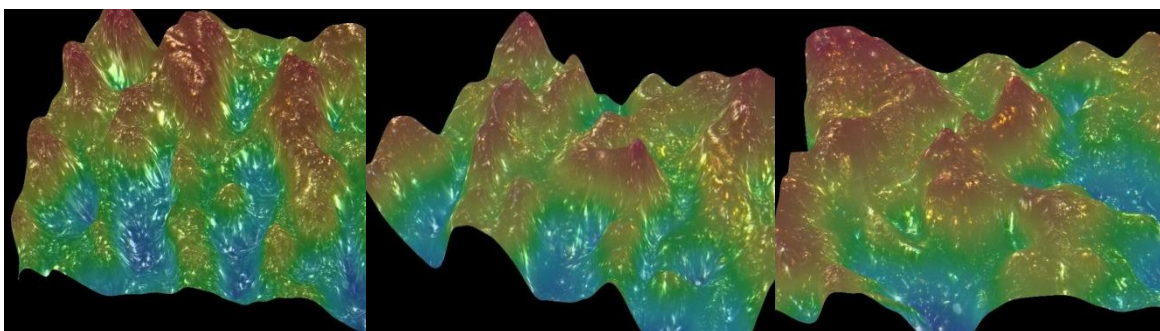
Sample 21,  $R_a=46.5\ \mu\text{m}$



Sample 22,  $R_a=42.2\ \mu\text{m}$

Sample 23,  $R_a=89.2\ \mu\text{m}$

Sample 24,  $R_a=44.1\ \mu\text{m}$



Sample 25,  $R_a=49.4\ \mu\text{m}$

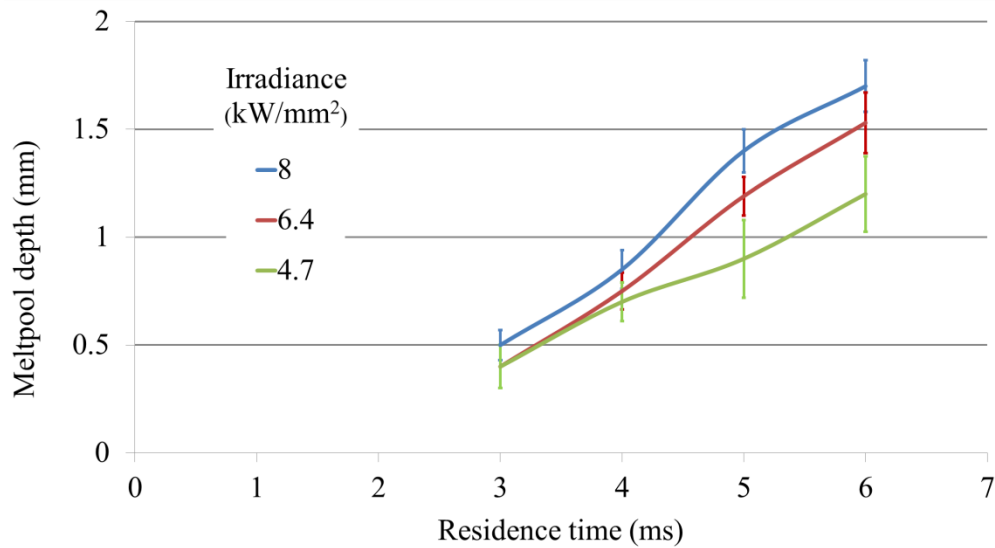
Sample 26,  $R_a=49.0\ \mu\text{m}$

Sample 27,  $R_a=514.4\ \mu\text{m}$

**Figure 5-12** 3D images for the surface roughness of the processed samples

### 5.5 The melt-pool depth

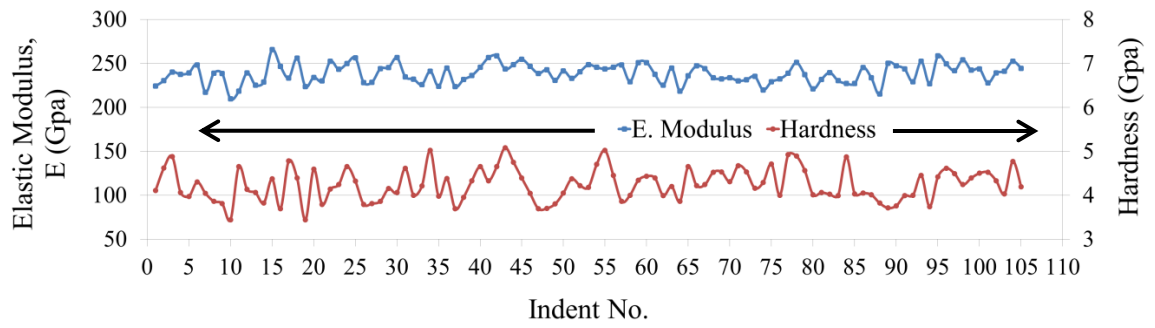
From section 4.11, the melt-pool depth was also investigated for the full set of the samples. SEM images were taken for the processed samples showing the re-solidified zone and the modified layer depth, see Figure 5-3 (right). Eight measures for the melt pool depth were taken on each sample, averaged and plotted versus the residence time with the 95% CI error bars as shown in Figure 5-13.



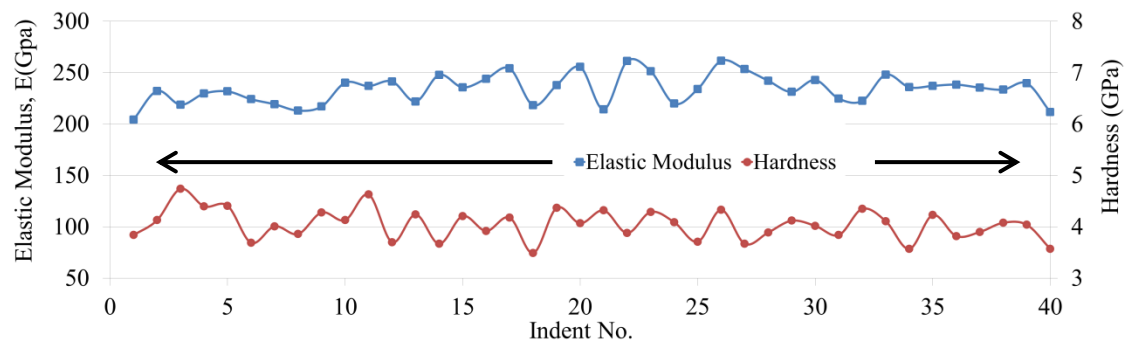
**Figure 5-13** Shows the effect of the residence time and Irradiance on the melt pool depth, n=8.

### 5.6 Elastic modulus and nano-hardness results

Using the method detailed in section 4.13, no significant changes in the elastic modulus or the hardness were found in the modified layer compared to the untreated bulk material for all the samples in the DoE, see Figure 5-14 as an example. The data in this figure were recorded for each indent using the method detailed in section 4.13. Table 5-4 lists the averages of the elastic modulus and the nano-hardness with their 95% CI's for the set of samples from the Box Behnken model. The data exhibit no significant change in the surface mechanical properties indicating no significant residual stresses were resulted (also see *Appendix E*).



(a)



(b)

**Figure 5-14** The average elastic modulus and hardness for  
(a) all the indents in sample no. 9 and (b) one line of  
indent in sample no. 15.

**Table 5-4** Averages of the elastic modulus and surface hardness

Sample No.	E(GPa) / 95% CI	Hardness (GPa) / 95% CI
3	232.7 / 2.23	4.29 / 0.061
5	234.9 / 2.02	4.36 / 0.066
6	233.9 / 2.67	4.28 / 0.062
8	237.3 / 2.02	4.24 / 0.061
9	237.8 / 2.26	4.24 / 0.072
10	231.4 / 2.91	4.20 / 0.058
13	234.5 / 2.52	4.22 / 0.074
14	236.3 / 2.09	4.29 / 0.057
15	232.9 / 2.8	4.14 / 0.060
16	231.4 / 2.65	4.31 / 0.064
19	232.1 / 2.07	4.43 / 0.060
21	243.2 / 2.23	4.04 / 0.067
25	232.7 / 1.94	4.24 0.054

### 5.7 The measured diameter increase, peak-valley and peak-peak distances

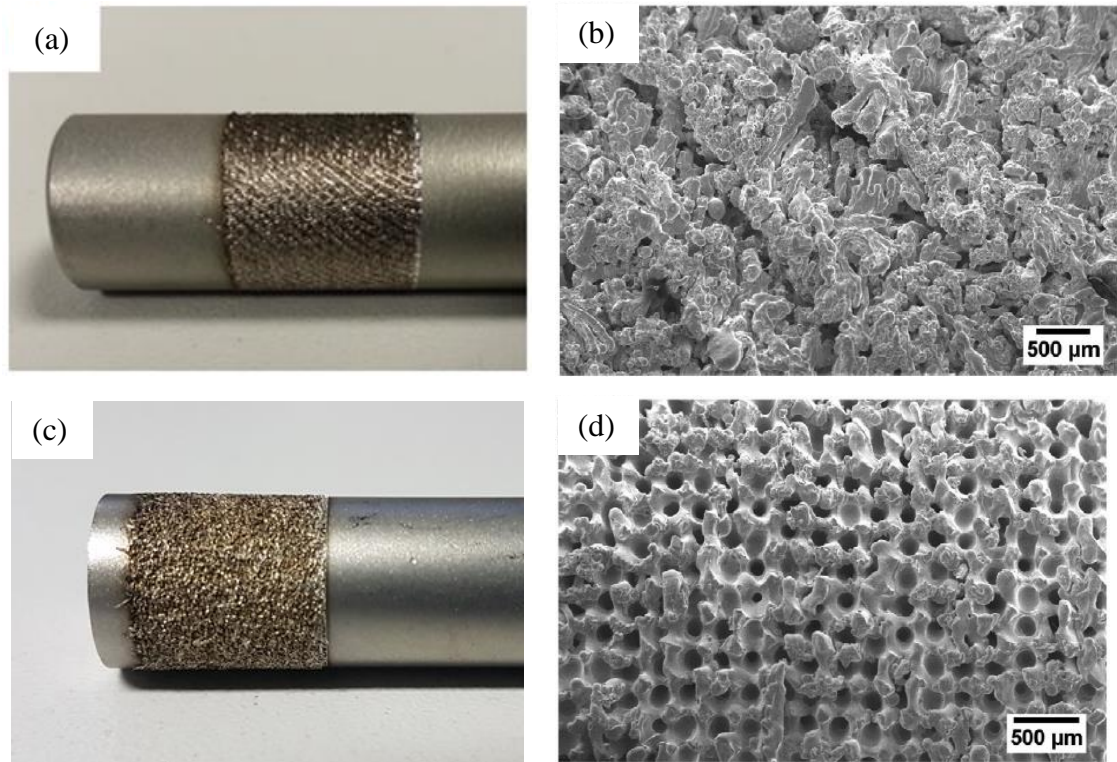
The increase in pin sample diameter, peak-valley and peak-peak distances were measured as explained in the previous Chapter 4 and are listed in the following Table 5-5.

**Table 5-5** Lists the textured surface geometry and type.

Sample No.	Diameter Increase (mm)	Peak-Peak ( $\mu\text{m}$ )	Peak-Valley ( $\mu\text{m}$ )	Pattern Angle ( $^{\circ}$ )	Profile type
1	$0.9 \pm 0.070$	$408 \pm 53$	$310 \pm 75$	45.2	Ridged
2	$1.1 \pm 0.082$	$610 \pm 105$	$540 \pm 95$	45.8	Ridged
3	$0.9 \pm 0.043$	-	$538 \pm 85$	-	Textured
4	$0.4 \pm 0.063$	-	$275 \pm 65$	-	Textured
5	$0.6 \pm 0.054$	$353 \pm 27$	$203 \pm 17$	45.4	Ridged
6	$0.9 \pm 0.061$	$583 \pm 16$	$600 \pm 50$	46.4	Ridged
7	$1.1 \pm 0.087$	-	$250 \pm 46$	-	Textured
8	$1.05 \pm 0.071$	-	$310 \pm 45$	-	Textured
9	$1.1 \pm 0.067$	-	$282 \pm 47$	-	Textured
10	$0.80 \pm 0.045$	-	$347 \pm 46$	-	Textured
11	$0.85 \pm 0.043$	$1100 \pm 57$	$599 \pm 57$	46	Ridged
12	$0.9 \pm 0.045$	-	$406 \pm 43$	-	Textured
13	$1.1 \pm 0.057$	$340 \pm 108$	$200 \pm 95$	46	Ridged
14	$0.9 \pm 0.054$	-	$574 \pm 51$	-	Textured
15	$0.85 \pm 0.144$	-	$541 \pm 75$	-	Textured
16	$0.75 \pm 0.050$	-	$459 \pm 17$	-	Textured
17	$0.95 \pm 0.059$	-	$501 \pm 19$	-	Textured
18	$0.94 \pm 0.043$	-	$406 \pm 48$	-	Textured
19	$0.75 \pm 0.059$	$1500 \pm 132$	$165 \pm 29$	45	Ridged
20	$0.75 \pm 0.077$	$1400 \pm 17$	$180 \pm 18$	46.2	Ridged
21	$0.85 \pm 0.032$	-	$632 \pm 26$	-	Textured
22	$0.50 \pm 0.063$	-	$383 \pm 14$	-	Textured
23	$0.75 \pm 0.069$	$502 \pm 13$	$135 \pm 15$	46.6	Ridged
24	$0.8 \pm 0.059$	-	$234 \pm 9$	-	Textured
25	$0.75 \pm 0.077$	-	$525 \pm 26$	-	Textured
26	$0.8 \pm 0.074$	-	$390 \pm 42$	-	Textured
27	$0.95 \pm 0.074$	-	$325 \pm 31$	-	Textured

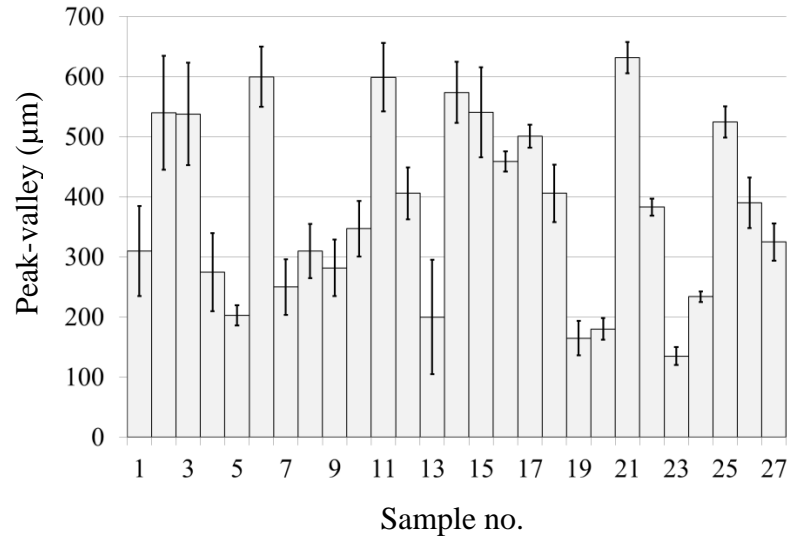


The produced samples are divided into two profile types: Ridged, where a clear and regular helical pattern of ridges is visible, see Figure 5-15 (a) and (b). The second type is the Textured, where there is a repeating texture but no clear ridged pattern see Figure 5-15 (c) and (d). A Keyence VHX2000E 3D digital microscope was used to determine the average peak-to-peak widths and peak-to-valley heights.

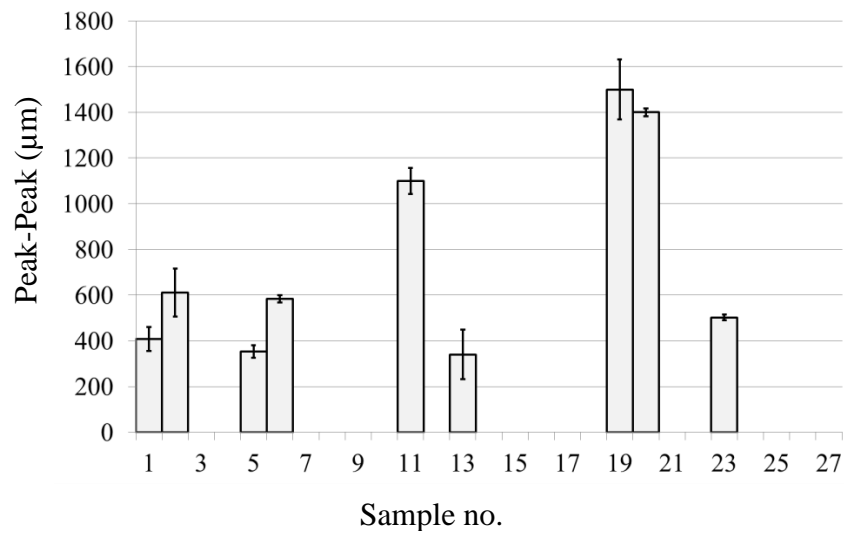


**Figure 5-15** (a) picture and (b) SEM image showing ridged pattern processed with 500 W, 300 Hz and 20% overlap (sample 20), (c) and (d) non-ridged textured sample processed with 300W, 300 Hz and -20% overlap (sample 4).

Figures 5-16, 5-17 and 5-18 show graphs of the average peak-valley and peak-peak distances and the diameter increase values with the corresponding DoE input conditions listed in Table 4-8 and they were measured as described in Section 4.7.2, see Figure 4-17 (section 4.7.2). For the textured samples, the average peak to valley height was measured as the distance between the maximum and minimum surface heights locally around the laser impact positions.

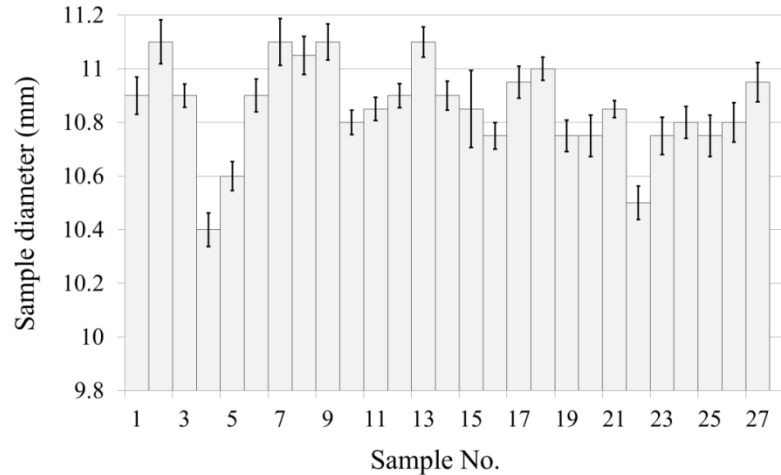


**Figure 5-16** Graph of the peak-valley values of the processed samples, n=8



**Figure 5-17** Graph of the peak-peak values of the processed samples with clear pattern, n=8.





**Figure 5-18** Graph of the average diameter increase, n= 8.

The produced samples showed an increase in pin diameter of 0.4 to 1.1 mm with short error bars indicating the high control on the processing parameters and the repeatability of the process. There was a wide range of peak to valley values recorded from the interactions between the different levels of the processing parameters.

Two DoE and RSM models were carried out, one for the increase in the pin diameter and another one is for the insertion and removal forces. In both models, the response is plotted versus the laser processing parameters for the three percentage overlapping scenarios.

As mentioned earlier, a full three level factorial design  $3^3$  was used in this study because it presents more comprehensive and detailed analysis of all parameters and their influence on the response. An (ANOVA) table was obtained from the model to test the adequacy of the model and the influence of each term. The F-value is an indication of the influence of the related factor. The higher the F-value the higher influence on the response. The p-values of less than 0.05 is an indication of the significance of the model/factor and indicates that the effect is of 95% confidence in the results. The R-square refers to the variation around the mean value, so the closer its value to a unity, the less the variation around the mean. The adjusted and predicted R-square values must be within 0.2 with respect to each other. Otherwise, there must be an error in the input data or the model settings. Finally, the adequacy precision must be greater than 4 to assure the adequacy of the design [192].

***The diameter increase model:***

The stepwise regression method was used because this method can eliminate the aliased terms indicated by the model automatically. In this model, the cubic term was aliased for the calculated range of data. The following Table 5-6 lists the calculated ANOVA results with the variance for the diameter increase as a response and the parametric terms in the model.

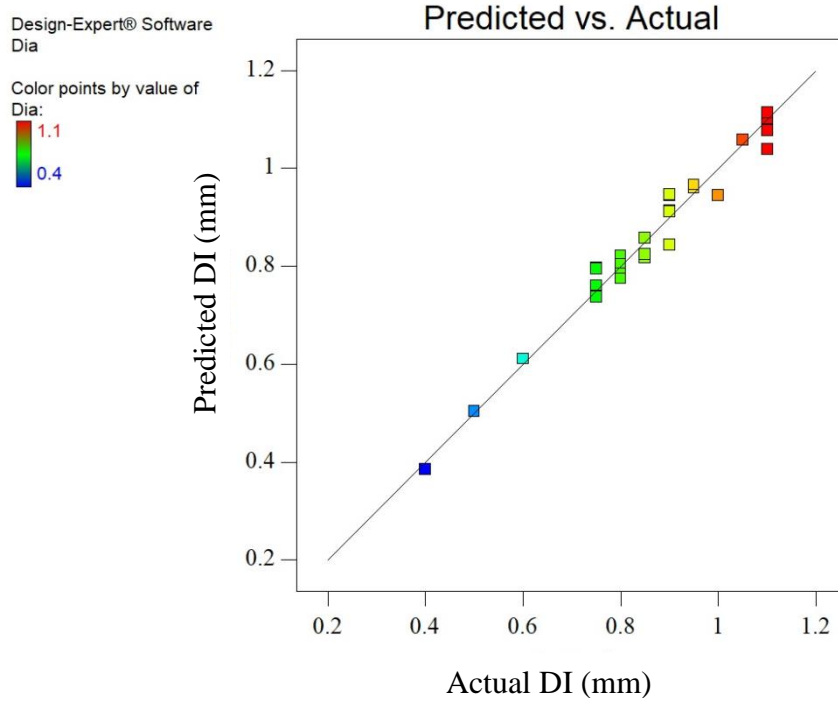
<b>Table 5-6</b> ANOVA results for the diameter increase model.						
Source	Sum of Squares	df	Mean Square	F Value	p-value Prob > F	
Model	0.49	16	0.031	13.14	0.0001	significant
A-Power	$2.53 \times 10^{-4}$	1	$2.53 \times 10^{-4}$	0.11	0.7486	
B-PRF	$7.77 \times 10^{-5}$	1	$7.77 \times 10^{-5}$	0.033	0.8588	
C-OV	$1.03 \times 10^{-4}$	1	$1.03 \times 10^{-4}$	0.044	0.8376	
AB	0.13	1	0.13	56.59	< 0.0001	significant
AC	$1.10 \times 10^{-4}$	1	$1.10 \times 10^{-4}$	0.047	0.8323	
BC	0.021	1	0.021	8.80	0.0141	significant
A <sup>2</sup>	$9.05 \times 10^{-4}$	1	$9.05 \times 10^{-4}$	0.39	0.5471	
B <sup>2</sup>	$9.37 \times 10^{-4}$	1	$9.37 \times 10^{-4}$	0.40	0.5403	
C <sup>2</sup>	$7.95 \times 10^{-6}$	1	$7.95 \times 10^{-6}$	$3.41 \times 10^{-3}$	0.9546	
ABC	0.020	1	0.020	8.65	0.0148	significant
A <sup>2</sup> B	0.024	1	0.024	10.28	0.0094	significant
AC <sup>2</sup>	0.017	1	0.017	7.22	0.0229	significant
B <sup>2</sup> C	$3.51 \times 10^{-4}$	1	$3.51 \times 10^{-4}$	0.15	0.7060	
BC <sup>2</sup>	$4.89 \times 10^{-3}$	1	$4.89 \times 10^{-3}$	2.10	0.1778	
A <sup>2</sup> B <sup>2</sup>	$9.31 \times 10^{-3}$	1	$9.31 \times 10^{-3}$	3.99	0.0736	
B <sup>2</sup> C <sup>2</sup>	$2.83 \times 10^{-3}$	1	$2.83 \times 10^{-3}$	1.21	0.2962	
R-Squared	0.9546	Adj R-Squared		0.8820		
Adeq Precision	16.363	Pred R-Squared		0.6369		

From Table 5-6, the p-value of 0.0001 for the model indicates that the model is significant. Moreover, there is no significant effect for the individual factors on the output response but only the combined effect noted from the interactions between the processing parameters. Also, the R-square value of 0.9546 means that 92% of the variability of the data is explained in this model. Finally, the adequacy precision of 16.36 indicates adequate model discrimination. Since this ratio is >4, this means that the current design can be used to navigate the design space.

The following equation (5-1) was obtained from the model for the investigated range of the laser processing parameters and can be used to predict the diameter increase, DI, on the stainless steel cylindrical samples within this range.

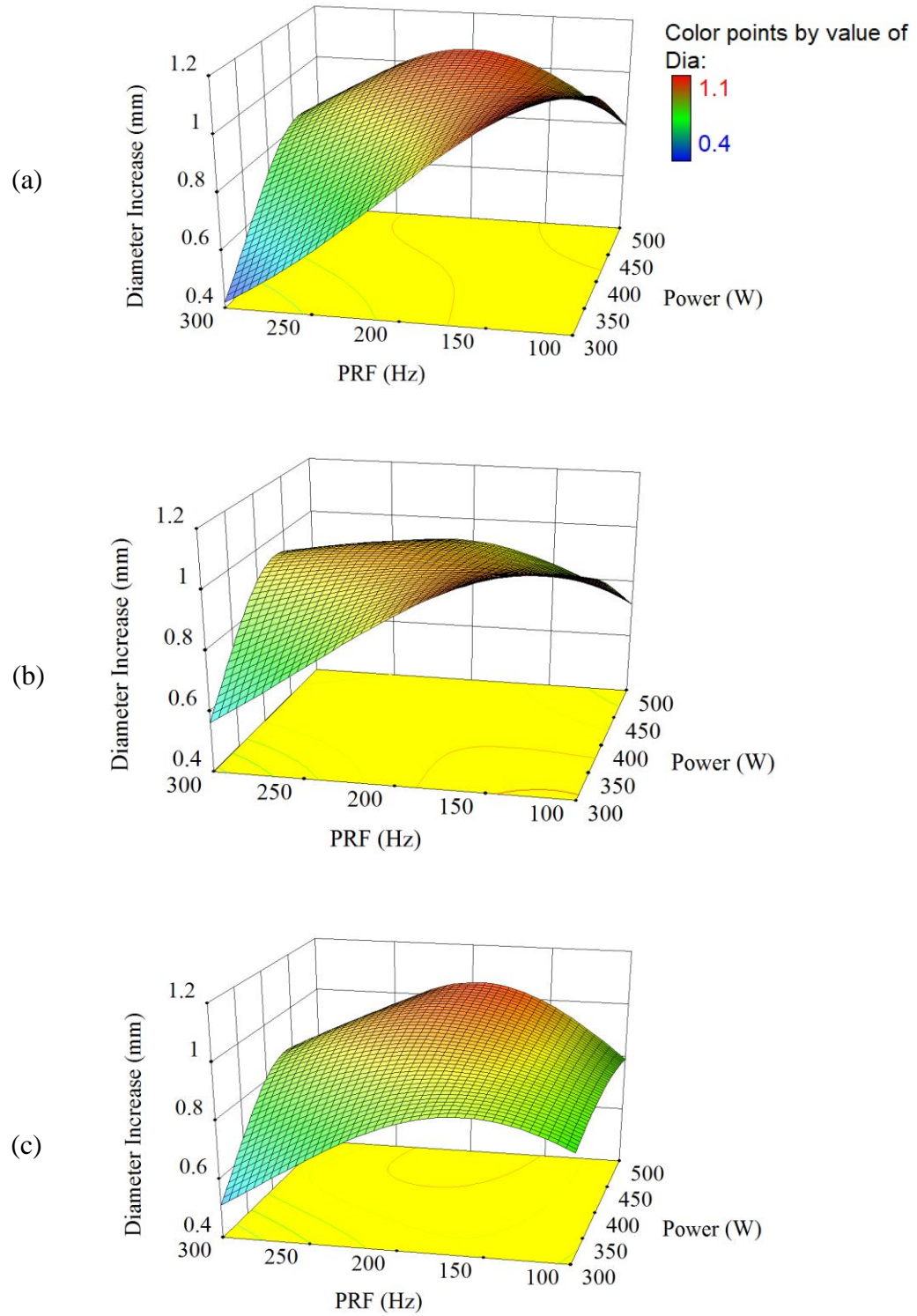
$$\frac{1}{\sqrt{DI}} = -0.68561 + 8.39 \times 10^{-3} \times \text{Power} + 0.0118 \times \text{PRF} + 0.027 \times \text{OV} - 7.24 \times 10^{-5} \times \text{Power} \times \text{PRF} - 5.17 \times 10^{-5} \times \text{Power} \times \text{OV} - 1.4 \times 10^{-4} \times \text{PRF} \times \text{OV} - 8.5 \times 10^{-6} \times \text{Power}^2 + 1.2 \times 10^{-5} \times \text{PRF}^2 + 9.3 \times 10^{-4} \times \text{OV}^2 + 2.5 \times 10^{-7} \times \text{Power} \times \text{PRF} \times \text{OV} + 8.63 \times 10^{-8} \times \text{Power}^2 \times \text{PRF} - 1.62 \times 10^{-6} \times \text{Power} \times \text{OV}^2 + 4.68 \times 10^{-8} \times \text{PRF}^2 \times \text{OV} - 3.73 \times 10^{-6} \times \text{PRF} \times \text{OV}^2 - 2.23 \times 10^{-11} \times \text{Power}^2 \times \text{PRF}^2 + 1.15 \times 10^{-8} \times \text{PRF}^2 \times \text{OV}^2 \quad (5-1)$$

In order to investigate the fitness of the model equation (5-1), the following Figure 5-19 shows the predicted diameter increase DI, plotted versus the actual data. Using this equation provides the predicted DI values for the investigated range of the laser processing parameters. The distribution of the data equally on both sides of the 45 degree trend line observes an acceptable fitness values for the model.



**Figure 5-19** Actual versus predicted diameter increase.

Figure 5-20 shows the 3D plots of the response surface method, RSM, for the increase in samples diameter. In this figure, the effect of two factors on the response was examined while the third factor remains constant. Both the laser beam power and frequency were changing at the time the percentage overlap was fixed.

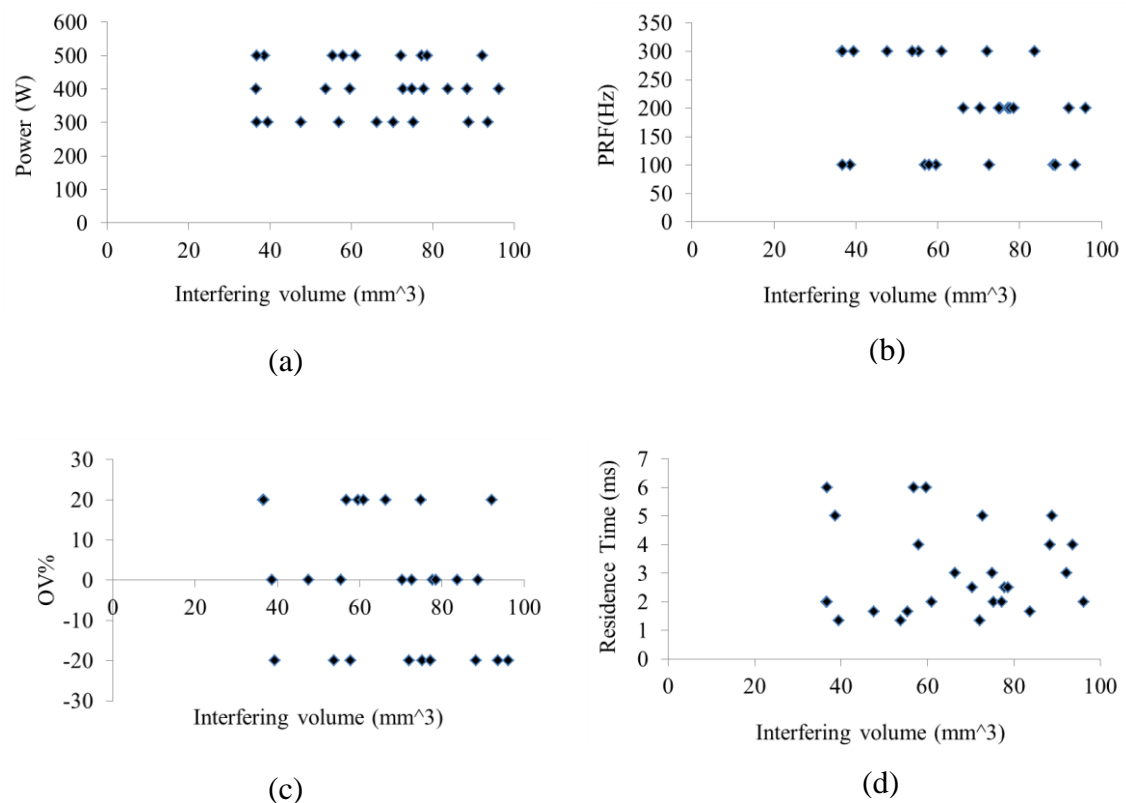


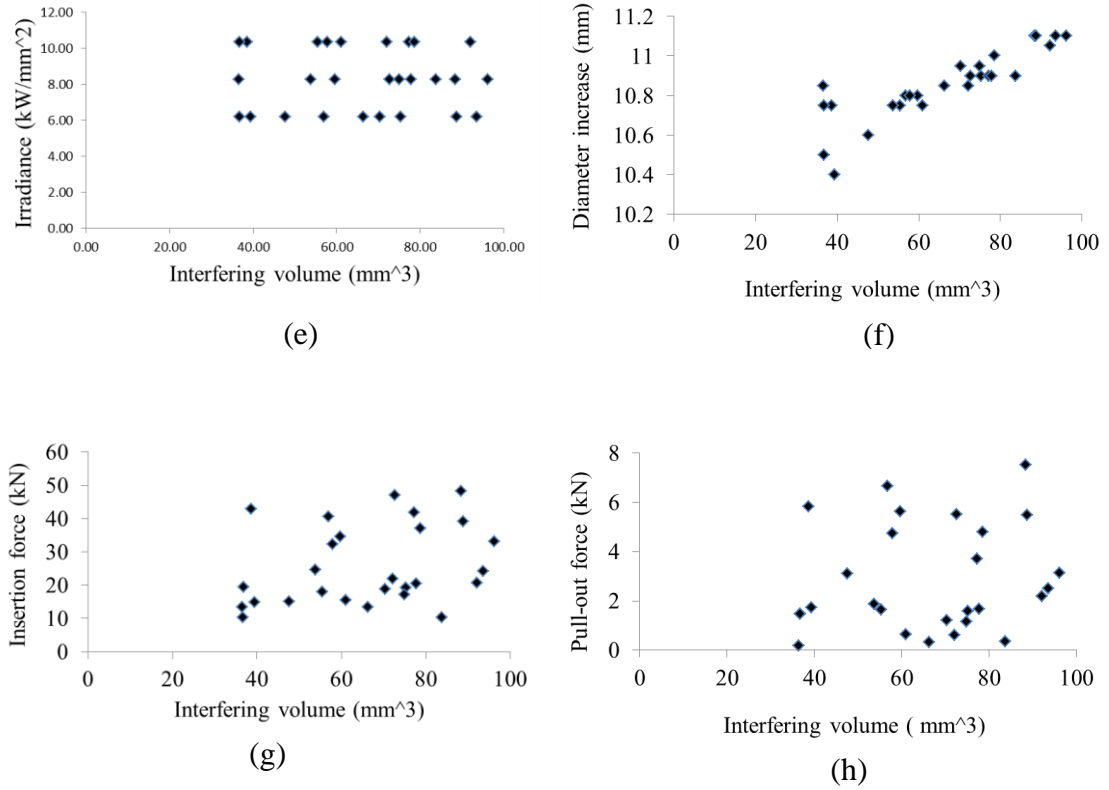
**Figure 5-20** RSM graphs of the interactive effect of P and the PRF on DI at OV of (a) -20, (b) 0 and (c) 20%.

As it can be seen, the power has direct proportional effect while the frequency has inverse proportional effect on the diameter increase. The advantage from presenting the 3D plots is that a digital, direct and visual comparison between the response can be found with respect to the samples and the laser processing parameters.

## 5.8 Interfering volume

Figure 5-21 shows graphs for the interfering volume of the textured surface calculated as explained in section 4.15 versus the processing parameters and the measured insertion and pull out forces. A clear direct proportional relationship was obtained with the diameter increase but no correlation can be extracted with respect to the measured forces. This means that not only the amount of interfering material that controls the mechanical forces but also the mechanical properties of the modified surface.



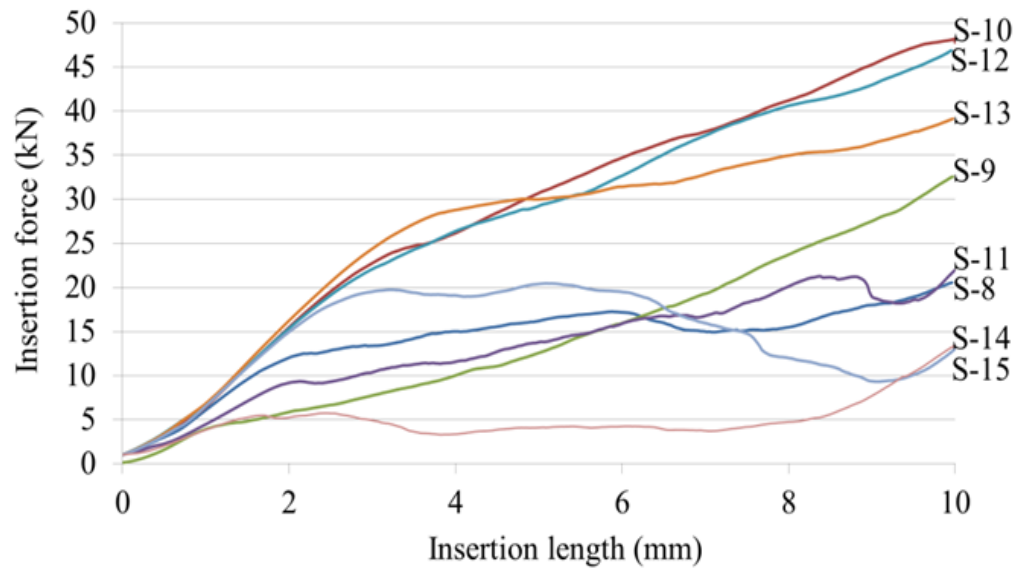


**Figure 5-21** The relationship between the interfering material volume and  
(a) Power, (b) PRF, (c) OV%, (d) Res. Time, (e) Irradiance, (f) DI,  
(g) Insertion force and (h) Pull out force.

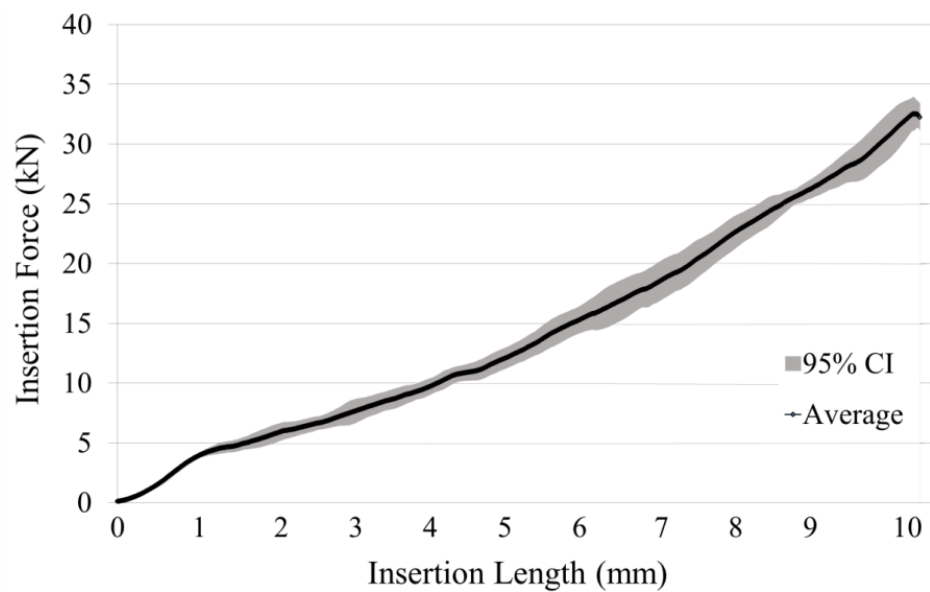
## 5.9 Insertion and pull-out test

### 5.9.1 Insertion test results

The relationships between the insertion forces and the insertion length were obtained and plotted for the full DoE set of samples. Figures 5-22 (a) shows the average of these relations plotted for samples 8 through 15 as an example. Each sample was repeated for three times at least. For a better visual consideration, the insertion force plot for sample no. 9 is shown in Figures 5-22 (b) individually. The DoE results for the full set of samples are presented in *Appendix C*. Figures 5-23 and 5-26 show the RSM plots of the insertion and pull-out forces respectively.



(a)



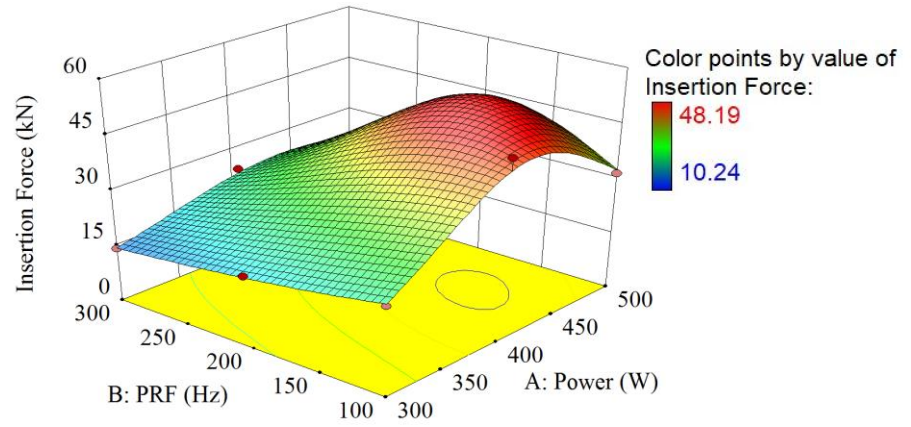
(b)

**Figure 5-22** Graphs of the insertion force against insertion length of (a) eight samples and (b) for sample no. 9 with the 95% CI,  $n=8$ .

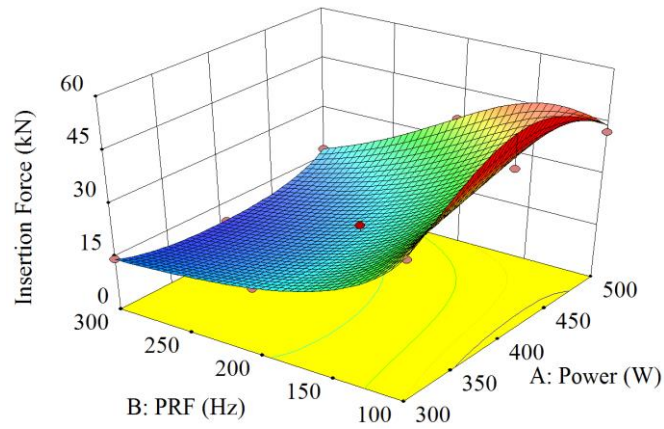


**Table 5-7** ANOVA results for the insertion force model.

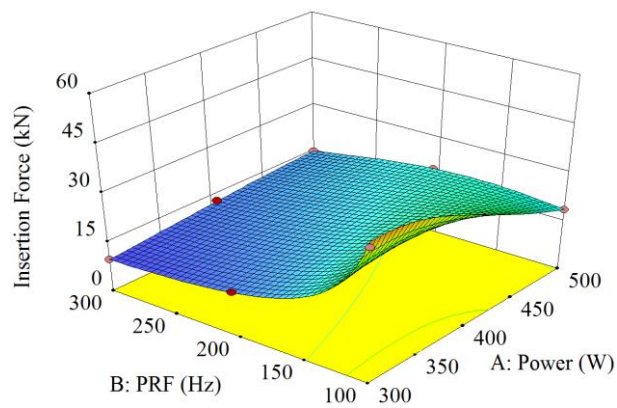
Source Model	Sum of Squares	df	Mean Square	F Value	p-value Prob > F	
	0.013	21	6.021E-04	34.52	0.0005	significant
A-Power	5.693E-4	1	5.693E-04	32.64	0.0023	significant
B-PRF	2.891E-3	1	2.891E-03	165.76	< 0.0001	significant
C-OV	7.712E-4	1	7.712E-04	44.21	0.0012	significant
AB	1.897E-5	1	1.897E-05	1.09	0.3448	
AC	1.392E-6	1	1.392E-06	0.080	0.7889	
BC	1.678E-4	1	1.678E-04	9.62	0.0268	significant
A2	3.890E-4	1	3.890E-04	22.30	0.0052	significant
B2	4.027E-5	1	4.027E-05	2.31	0.1891	
C2	3.709E-4	1	3.709E-04	21.26	0.0058	significant
ABC	2.871E-4	1	2.871E-04	16.46	0.0098	significant
A2B	5.178E-4	1	5.178E-04	29.68	0.0028	significant
A2C	4.432E-5	1	4.432E-05	2.54	0.1718	
AB2	3.290E-4	1	3.290E-04	18.86	0.0074	significant
AC2	5.214E-6	1	5.214E-06	0.30	0.6081	
B2C	7.912E-5	1	7.912E-05	4.54	0.0864	
BC2	6.256E-4	1	6.256E-04	35.86	0.0019	significant
A2BC	1.782E-6	1	1.782E-06	0.10	0.7622	
A2C2	7.476E-4	1	7.476E-04	42.86	0.0012	significant
AB2C	2.007E-5	1	2.007E-05	1.15	0.3325	
ABC2	1.214E-4	1	1.214E-04	6.96	0.0461	significant
A2BC2	3.293E-4	1	3.293E-04	18.88	0.0074	significant
R-Squared	0.9931		Adj R-Squared		0.9644	
Adeq Precision	20.899		Pred R-Squared		0.8227	



(a) -20% OV.



(b) 0% OV.

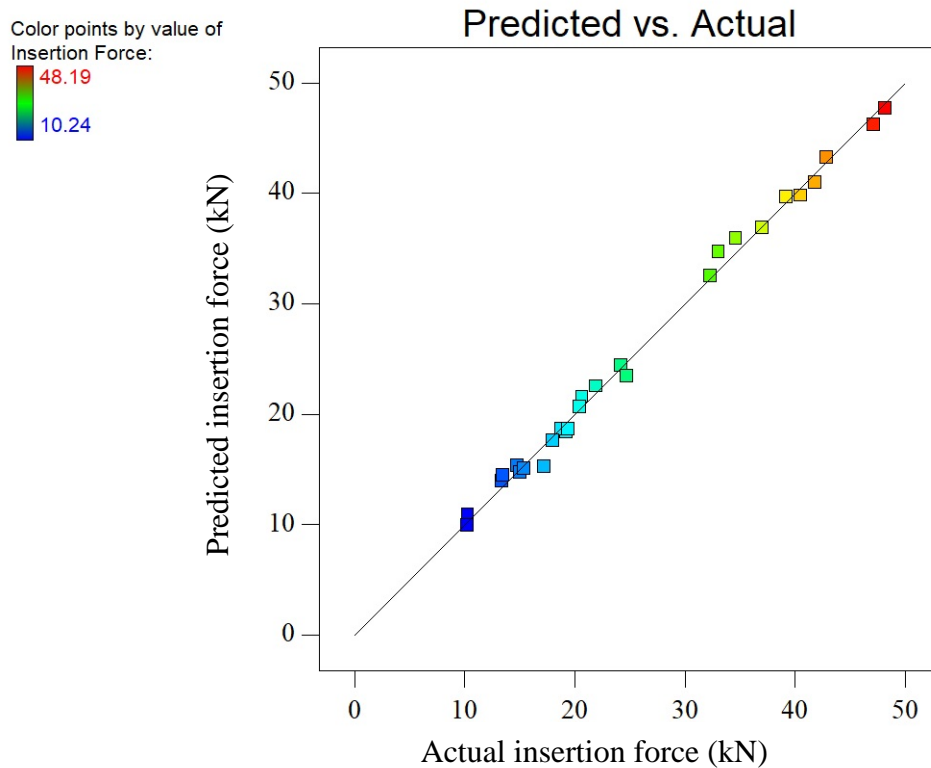


(c) 20% OV

**Figure 5-23** RSM plots for the insertion force showing the effect of PRF and laser power on the insertion force for different overlap.

The R-squared value of 99.31% indicated in Table 5-7 means that the model is significantly fit to the design data and that the insertion force can be predicted from the following equation (5-2). This equation was used to plot the predicted versus the actual data and show an acceptable agreement as shown in Figure 5-24.

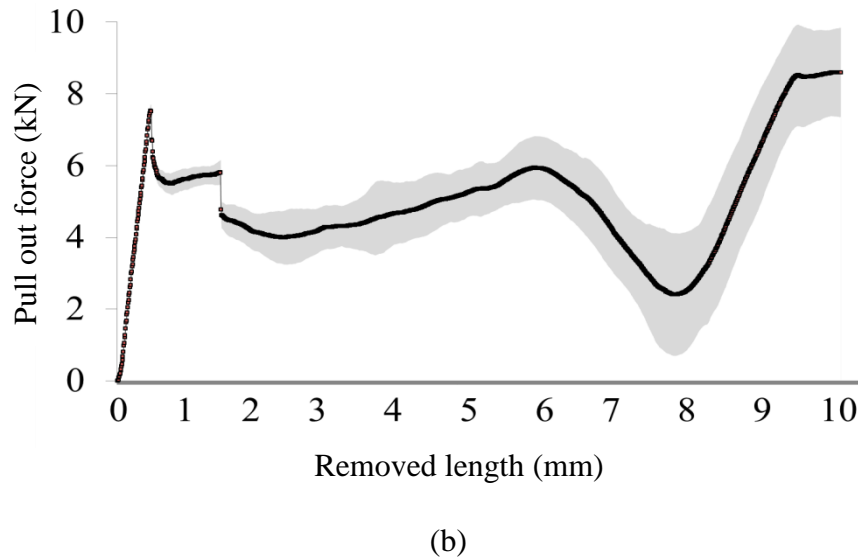
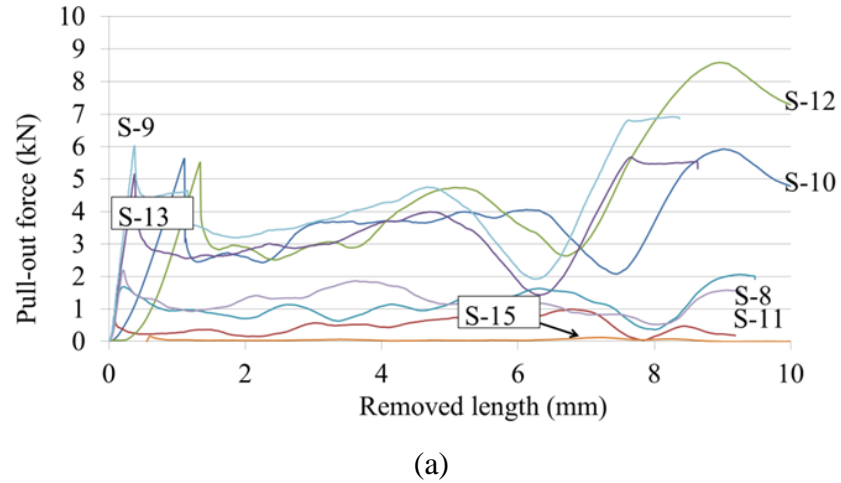
$$\frac{1}{\text{Insertion force (kN)}} = 0.28 - 1.76 \times 10^{-3} \times \text{Power} - 1.33 \times 10^{-3} \times \text{PRF} - 6.87 \times 10^{-3} \times \text{OV} + 1.2 \times 10^{-5} \times \text{Power} \times \text{PRF} + 1.85 \times 10^{-5} \times \text{Power} \times \text{OV} + 3.95 \times 10^{-5} \times \text{PRF} \times \text{OV} + 2.5 \times 10^{-6} \times \text{Power}^2 - 3.3 \times 10^{-6} \times \text{PRF}^2 - 6.4 \times 10^{-4} \times \text{OV}^2 - 5.2 \times 10^{-8} \times \text{Power} \times \text{PRF} \times \text{OV} - 1.97 \times 10^{-8} \times \text{Power}^2 \times \text{PRF} - 8.46 \times 10^{-9} \times \text{Power}^2 \times \text{OV} + 9 \times 10^{-9} \times \text{Power} \times \text{PRF}^2 + 3.2 \times 10^{-6} \times \text{Power} \times \text{OV}^2 - 7.7 \times 10^{-8} \times \text{PRF}^2 \times \text{OV} + 7.83 \times 10^{-6} \times \text{PRF} \times \text{OV}^2 - 4.09 \times 10^{-11} \times \text{Power}^2 \times \text{PRF} \times \text{OV} - 3.7 \times 10^{-9} \times \text{Power}^2 \times \text{OV}^2 + 1.37 \times 10^{10} \times \text{Power} \times \text{PRF}^2 \times \text{OV}^4 \times 10^{-8} \times \text{Power} \times \text{PRF} \times \text{OV}^2 + 4.8 \times 10^{-11} \times \text{Power}^2 \times \text{PRF} \times \text{OV}^2 \quad (5-2)$$



**Figure 5-24** The actual versus predicted values of the insertion force.

### 5.9.2 Pull-out test results

Figures 5-25 (a) shows the average of these forces plotted for samples 8 through 15 as an example. The pull-out force plot for sample no. 9 is shown in Figures 5-25 (b) individually.



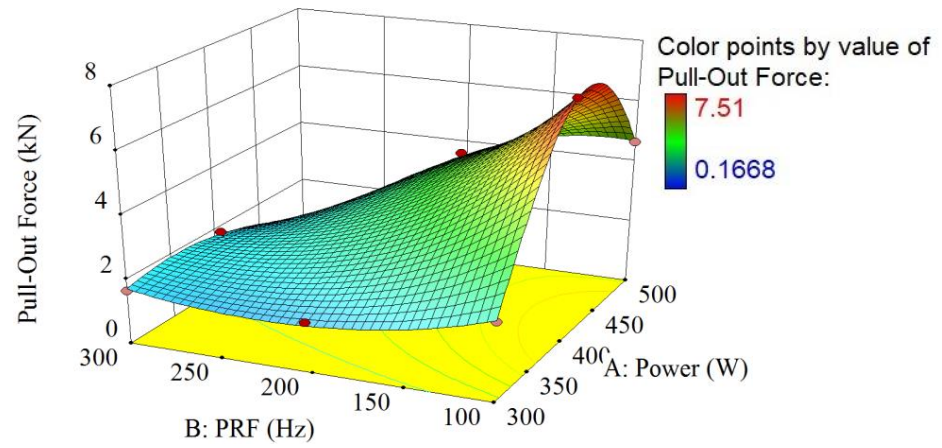
**Figure 5-25** Graphs of the pull-out force against removal length of  
(a) eight samples, and (b) for sample no. 9,  $n=8$ .

Similar to the previous two RSM models, the step-wise regression was used to analyse the pull-out force test results with all the possible combinations except for the cubic combinations. This was due to the software evaluation of the results which indicate that

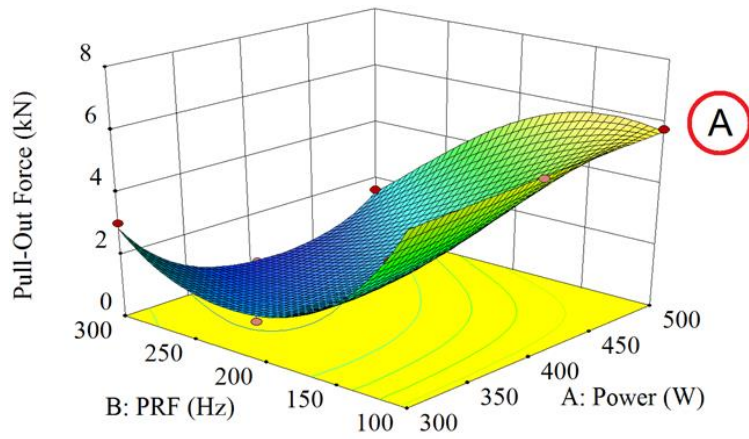
the cubical terms were aliased. The variation of this model and the ANOVA results are listed in the following Table 5-8.

**Table 5-8** ANOVA results for the pull-out force model.

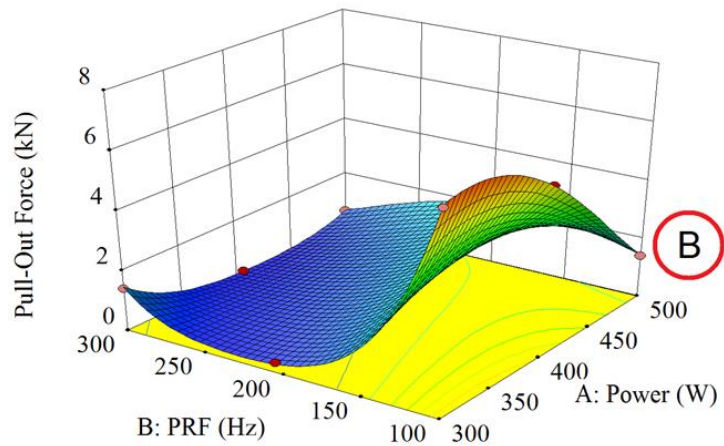
Source Model	Sum of Squares	df	Mean Square	F Value	p-value Prob > F	
	11.46	22	0.52	70.55	0.0004	significant
A-Power	1.00	1	1.00	135.31	0.0003	significant
B-PRF	2.64	1	2.64	357.47	< 0.0001	significant
C-OV	0.24	1	0.24	33.14	0.0045	significant
AB	0.076	1	0.076	10.35	0.0324	significant
AC	0.015	1	0.015	1.98	0.2323	
BC	0.087	1	0.087	11.84	0.0263	significant
A <sup>2</sup>	0.27	1	0.27	36.30	0.0038	significant
B <sup>2</sup>	0.14	1	0.14	18.33	0.0128	significant
C <sup>2</sup>	0.085	1	0.085	11.49	0.0276	significant
ABC	0.54	1	0.54	73.23	0.0010	significant
A <sup>2</sup> B	0.70	1	0.70	94.37	0.0006	significant
A <sup>2</sup> C	6.390E-003	1	6.390E-003	0.87	0.4049	
AB <sup>2</sup>	1.54	1	1.54	209.04	0.0001	significant
AC <sup>2</sup>	0.060	1	0.060	8.19	0.0459	significant
B <sup>2</sup> C	4.381E-004	1	4.381E-004	0.059	0.8196	
BC <sup>2</sup>	7.391E-004	1	7.391E-004	0.10	0.7675	
A <sup>2</sup> B <sup>2</sup>	4.668E-003	1	4.668E-003	0.63	0.4711	
A <sup>2</sup> BC	0.047	1	0.047	6.34	0.0655	
A <sup>2</sup> C <sup>2</sup>	0.56	1	0.56	75.74	0.0010	significant
AB <sup>2</sup> C	0.23	1	0.23	30.80	0.0052	significant
ABC <sup>2</sup>	0.037	1	0.037	5.02	0.0887	
A <sup>2</sup> B <sup>2</sup> C	0.059	1	0.059	7.93	0.0480	significant
R-Squared	0.9974	Adj R-Sq		0.9832		
Adeq Precision	29.61	Pred R-Sq		0.7911		



(a)



(b)

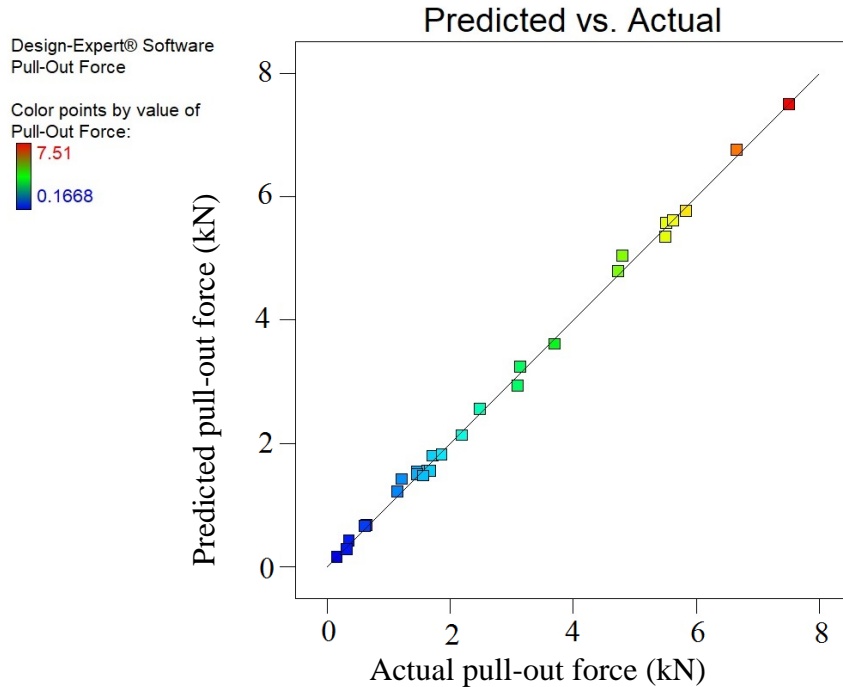


(c)

**Figure 5-26** RSM plots for the pull-out force for the laser processing parameters at (a) -20%, (b) 0%, and (c) 20% overlap.

From Table 5-8, the R squared for this model is 99.74% indicating the value of the data explained by the model and the high significance of fit to the design data range. In addition, the insertion force can be predicted from the following equation (5-3). This equation was also used to plot the predicted data versus the actual data, see Figure 5-27. The scattering of the predicted data and the actual data along the trend line confirm that the model has an excellent fitness values.

$$\begin{aligned} \text{Pull-out force (kN)} = \{ & 1.14 + 0.031 \times \text{Power} - 8.18 \times 10^{-3} \times \text{PRF} + 0.9918 \times \text{OV} - \\ & 2.88 \times 10^{-4} \times \text{Power} \times \text{PRF} - 4.13 \times 10^{-3} \times \text{Power} \times \text{OV} - 0.01 \times \text{PRF} \times \text{OV} - 6 \times 10^{-5} \times \\ & \text{Power}^2 + 1.8 \times 10^{-4} \times \text{PRF}^2 - 0.021 \times \text{OV}^2 + 4.29 \times 10^{-5} \times \text{Power} \times \text{PRF} \times \text{OV} + 6.54 \times \\ & 10^{-7} \times \text{Power}^2 \times \text{PRF} + 4.155 \times 10^{-6} \times \text{Power}^2 \times \text{OV} - 1.478 \times 10^{-7} \times \text{Power} \times \\ & \text{PRF}^2 + 1.2 \times 10^{-4} \times \text{Power} \times \text{OV}^2 + 2.646 \times 10^{-5} \times \text{PRF}^2 \times \text{OV} - 1.14 \times 10^{-5} \times \\ & \text{PRF} \times \text{OV}^2 - 5.91 \times 10^{-10} \times \text{Power}^2 \times \text{PRF}^2 - 4.47 \times 10^{-8} \times \text{Power}^2 \times \text{PRF} \times \text{OV} - \\ & 1.62 \times 10^{-7} \times \text{Power}^2 \times \text{OV}^2 - 1.172 \times 10^{-7} \times \text{Power} \times \text{PRF}^2 \times \text{OV} + 2.946 \times 10^{-8} \times \\ & \text{Power} \times \text{PRF} \times \text{OV}^2 + 1.283 \times 10^{-10} \times \text{Power}^2 \times \text{PRF}^2 \times \text{OV} \}^2 \end{aligned} \quad (5-3)$$

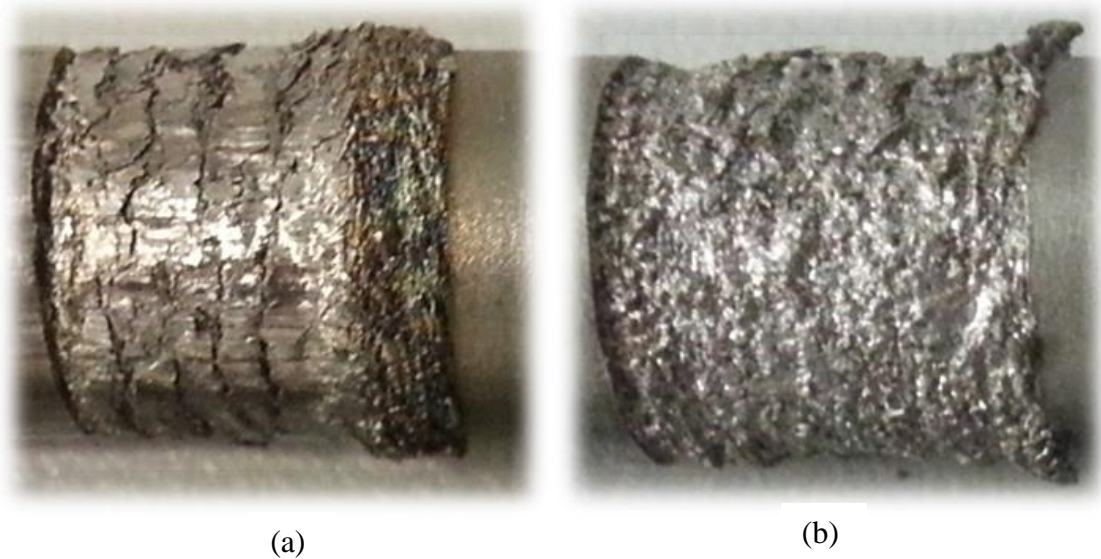


**Figure 5-27** Actual and predicted values of the pull-out force.

Figures 5-26 (a), (b) and (c) show a wide range of variation in the pull-out force. This variation could be explained by the alteration in the resulting mechanical properties of the processed surface and not only the increase in the diameter as will be explained in the next chapter. For example, points A and B in Figures 5-26 (b) and (c) belong to samples no. 16 (500 W, 100 Hz, 0% OV) and 23 (500 W, 100 Hz, 20%) and they both exhibit similar diameter increase of 0.75 and 0.8 mm, respectively. It was noted that sample no. 16 exhibits a removal force of 5.7 kN before failure while sample no. 23 fails at 1.4 kN.

### 5.10 Tested samples

The following Figure 5-28 shows samples no. 9 and 15 after the insertion pull-out test. Some of the brittle textured surface material has been removed from sample 15, Figure 5-28 (b), while the hard martensite in sample no. 9 was compressed against the bulk lower strength austenite bulk material and maintain a better bond strength, Figure 5-28 (a).

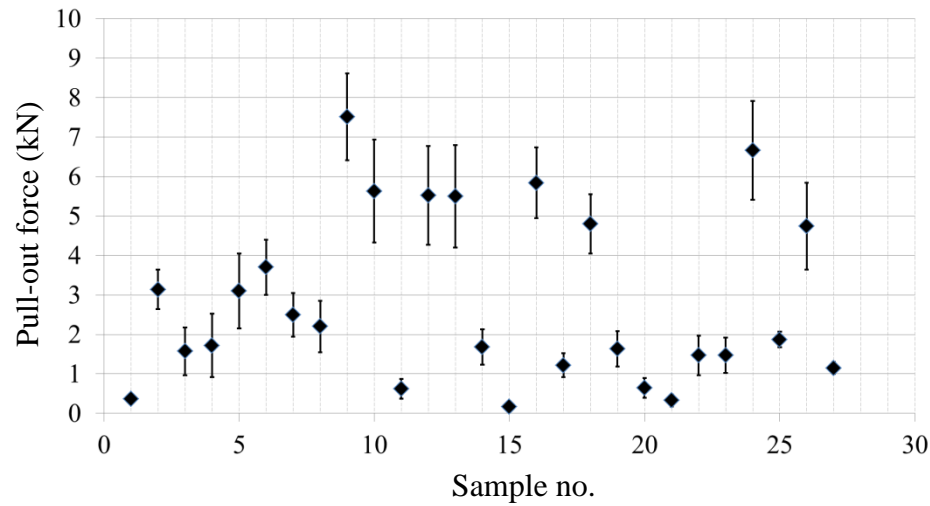


**Figure 5-28** Pictures of 316L cylindrical samples after the insertion and removal test

- (a) sample 9 processed with 400 W, 100 Hz, -20%, 4 ms residence time, and
- (b) sample 15 processed with 500 W, 300 Hz, -20%, 1.33 ms residence time.



The following Figure 5-29 shows the pull out force for each sample in the DoE model.



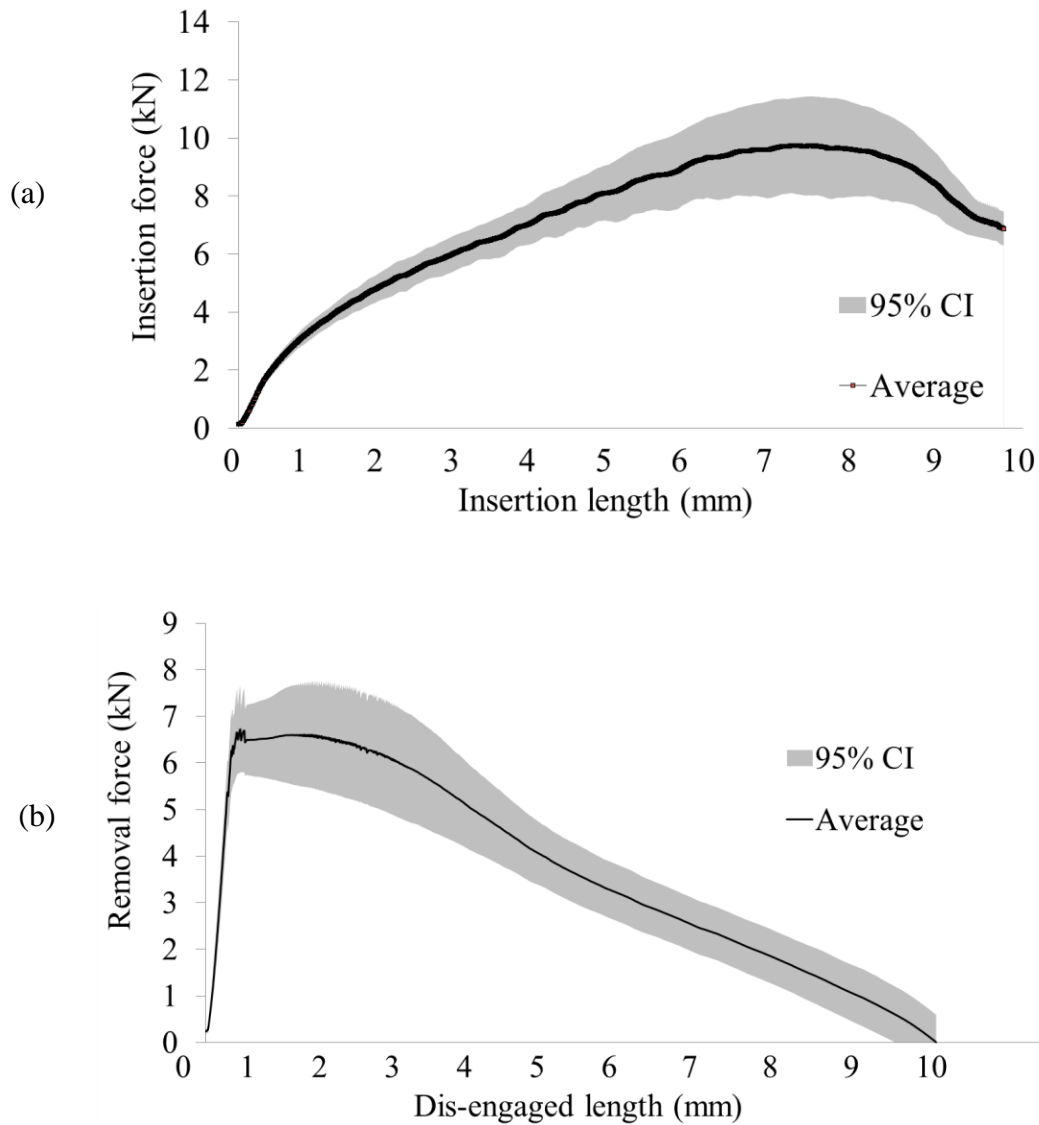
**Figure 5-29** The pull out force test result for the full set of samples in the DoE.

The figure shows that the higher pull-out force values were observed for samples no. 9 and 24 while samples no. 1 and 15 were the lowest. The increases in the samples diameter are listed in Table 5-5 and shown in Figure 5-18, these are 1.1, 0.8, 0.9 and 1.1 mm respectively. This result agrees with the result detailed in Section 5.8 that the mechanical properties of the modified surface texture controls the bond strength of the joint more significantly than the increase in diameter.

### 5.11 Insertion and pull-out test of the commercial samples

During the insertion and pull-out test of seven commercial samples, it was found that the maximum insertion force required was less than that for the laser textured samples due to the less friction generated by the polished surface of the commercial pins. It was also noted that the variation of the force around the mean is wider in the commercial pins compared to the textured indicating a better control of the laser processing parameters on the modified surface mechanical properties and good prediction of the joint strength.

The pull-out force plot show a similar stiffness (N/mm) to that of the laser texture sample shown in Figure 5-25 (b) but a sudden failure of the assembly was obtained, see Figure 5-30 (b). This result was not observed on the laser textured insertion, instead a significant grip was noted during the entire removal process.



**Figure 5-30** (a) Insertion and (b) pull-out forces plots for the commercial samples tested in a 9.99 mm diameter hubs, n=7.

Also, these samples were tested for the insertion and removal force analysis by using hub rings with hole diameters of 9.75, 9.90 and 9.95 mm, see *Appendix C*.

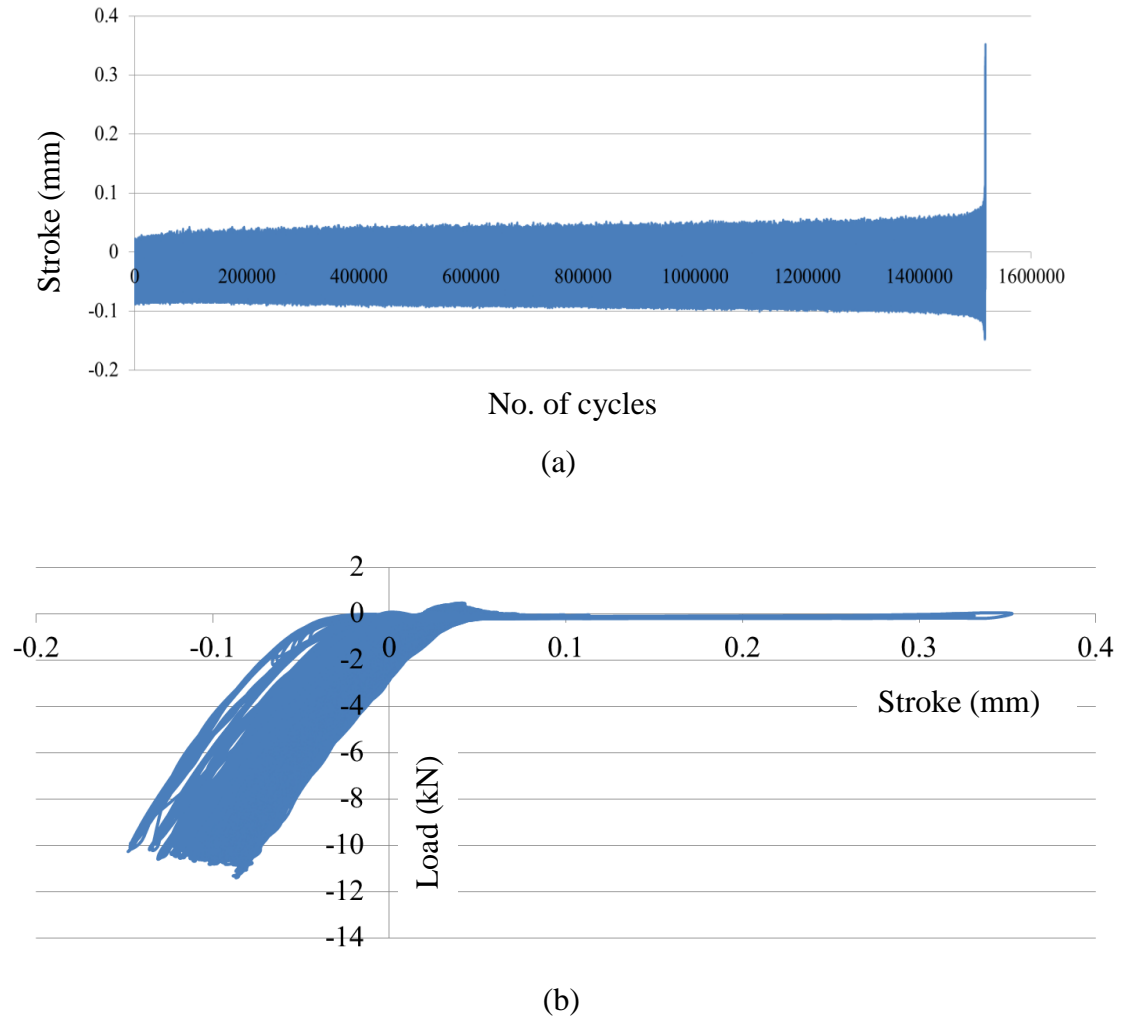
### 5.12 Fatigue test

The fatigue test of the joint assembly exhibits different behaviour and results compared to that of a single specimen fatigue test when considering the load (stress)-life (no. of cycles) relationship. This is due to the microstructure of the hard texture bonding material explained in Sections 5.3 and 5.10. The hard lamellar shielding provides high fretting strength, and when they deform against the softer bulk material; they can damp and absorb the dynamic loads. It was found that for high cyclic loading near the maximum pull-out failure loads, the joint fail in  $19 \times 10^4$  cycles by exceeding high strain with a significant reduction in strength, i.e. no or small force value was recorded. When investigating lower load values, a significant improvement in fatigue strength was noted when loading with 5 kN for three replicates on fresh samples no. 9. No failure was noted when the load was reduced to 3 kN as listed in the following Table 5-9 for the corresponding load value.

**Table 5-9** The fatigue test results for samples produced under sample setting conditions no. 9, 400 W, 100 Hz, -20%OV, and at a fatigue test frequency of 10 Hz.

Testing load (kN)	6.5	5	3	2	1
No. of cycles	190,000	Fail at (1) $1.50 \times 10^6$ (2) $1.15 \times 10^6$ (3) $1.60 \times 10^6$	No failure (1) $12 \times 10^6$ (2) $10 \times 10^6$	No failure for $10 \times 10^6$	No failure for $10 \times 10^6$

The bonding stroke-number of cycles and stroke-load data for the sample loaded with 5 kN is presented in the following Figure 5-31 (a) and (b) respectively.



**Figure 5-31** Fatigue test (a) stroke displacement vs no. of cycles and (a) stroke displacement vs load.

### 5.13 Wear test results

The test was carried out to distinguish between the wear resistance for the as received material and the laser processed material surface in (1) argon and (2) nitrogen environment. The following Table 5-10 lists the test results and the reduction in wear. It was found that the laser processing of stainless steel surface always enhanced the wear resistance due to the high cooling rates and improved the surface hardness. The test was carried out on a flat sample equivalent to the cylindrical sample no.9 as explained in section 4.19. The specific wear rate in ( $\text{mm}^3/\text{N.m}$ ) listed in this table was found using equations (4-8) and (4-9).

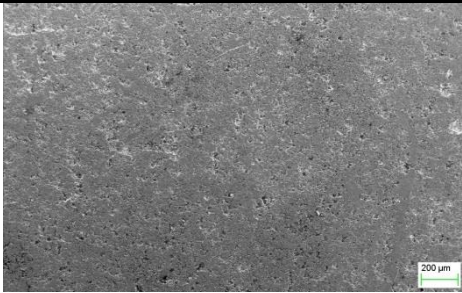
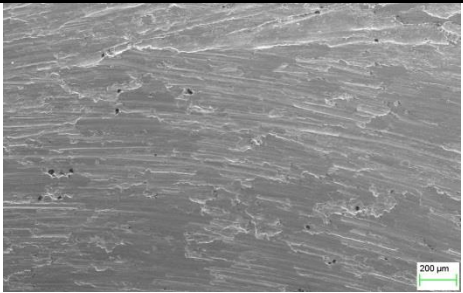
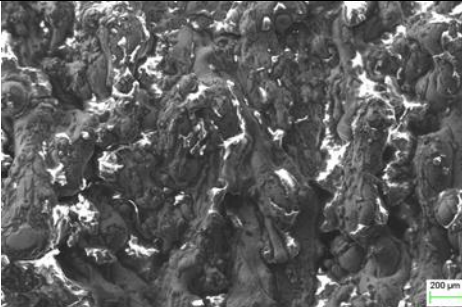
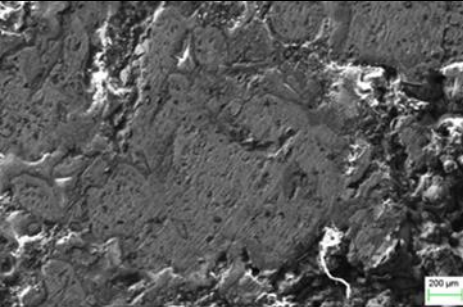

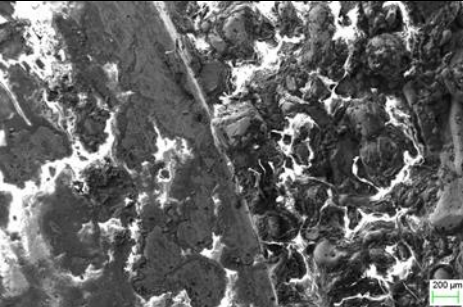
**Table 5-10** Wear resistance of 316L SST before and after CO<sub>2</sub> laser treatment.

Process surrounding conditions	Mass Loss (g)	Specific wear rate (mm <sup>3</sup> /N.m)	Reduction in Wear (%)
As-received	0.0203	$3.365 \times 10^{-7}$	-
Argon gas	0.0089	$1.475 \times 10^{-7}$	56.15
Nitrogen gas	0.0007	$1.160 \times 10^{-8}$	96.55

This result can be explained by

- 1) The increase in the hard martensite portion in the modified layer.
- 2) That the formation of the soft ferrite is suppressed by the addition of nitrogen.

Figure 5-32 shows the effect of laser processing with argon and argon-nitrogen gas mixture shielding on the surface structure and the wear resistance.

Shielding gas	Surface micrograph	Wear test track
As-received		
Argon	 (a)	 (b)
20% Ar- 80% N <sub>2</sub>	 (c)	 (d)

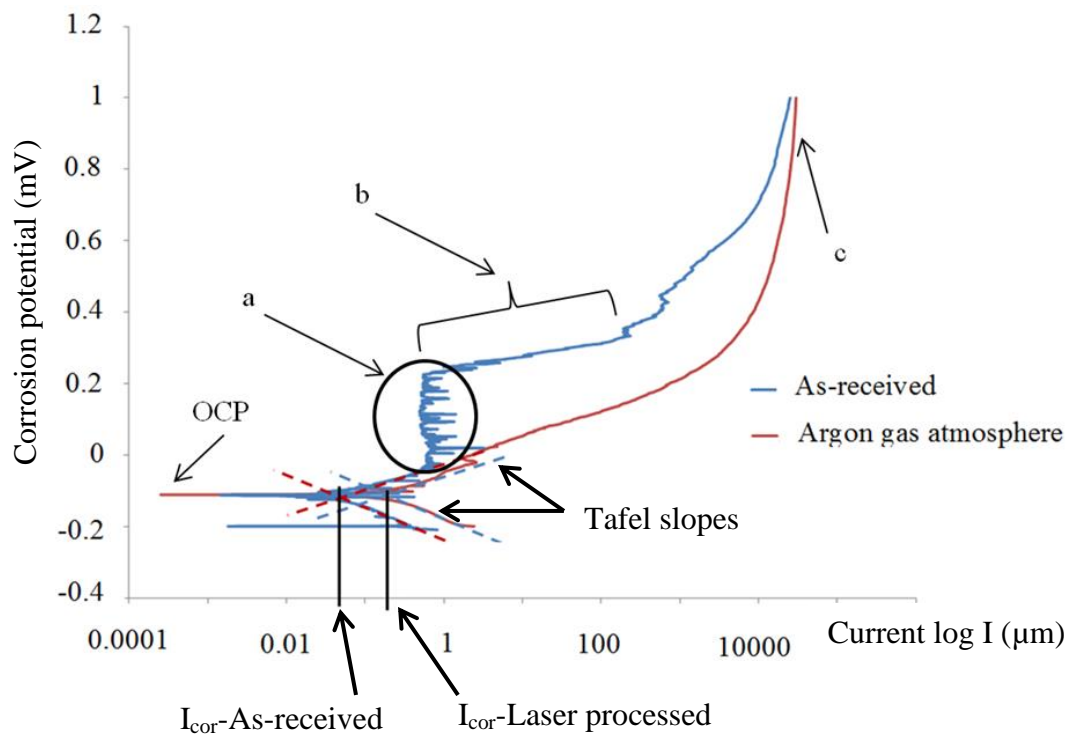
**Figure 5-32** The surface structure of 316L SST flat samples processed in (a) and (b) argon, (c) and (d) argon-nitrogen gas shielding.

The surface microstructure of the untreated sample composed of the soft austenite and the wear track suggest an abrasive and adhesive wear mechanism in which the removed material smears the sample surface. In contrast, the hard martensite, represented by the bright material in the laser processed samples enhance the wear resistance and invert the wear into an abrasive mechanism. The dark portion in the two laser processed samples

is the soft ferrite. The increase in the hard phase explains the improved wear resistance shown in Table 5-10. The laser nitriding processing is discussed in more details with their applications in the following chapters.

#### 5.14 Corrosion test

The electric potential plot versus the absolute current on a log scale is shown in the following Figure 5-33 for the as-received sample and the sample processed in argon gas atmosphere.



**Figure 5-33** Potentiodynamic polarization curves of an as-received and laser processed samples in argon atmosphere.

From this figure, the as-received sample shows passivity in the anodic reaction zone (a) which can be explained by the formation of an oxide layer. Portion (b) indicates a reversion to the normal corrosion as a sign of the penetration of the oxide layer. The top portion (c) indicates a stable current density against the potential. The two samples show similar open circuit potential (OCP) while a noticeable increase in the corrosion

current from  $1.38 \times 10^{-2} \mu\text{A}$  for the as-received to  $1.09 \times 10^{-1} \mu\text{A}$  for the laser processed sample. By applying eq. 4-11, the resulting corrosion rates for the as-received and the laser processed samples were found to be  $1.832 \times 10^{-4}$  and  $1.447 \times 10^{-3}$  mm/year, respectively.

### **5.15 Correlation strength investigation**

The correlation strength ( $r$ ) between the diameter increase, insertion and the pull out forces as the resulting responses with the main laser processing parameters were calculated using the Pearson correlation coefficient standard. On a range of -1 to 1, the higher the absolute value of ( $r$ ) the stronger the correlation with the direction of proportionality indicated by the (-/+) sign. Table 5-11 lists these correlations with the significance of each correlation measured by the p-value. The strongest and the most significant correlations were indicated by absolute  $r$ -values of greater than 0.35 and p-values of less than 0.05; these are highlighted in Table 5-11.

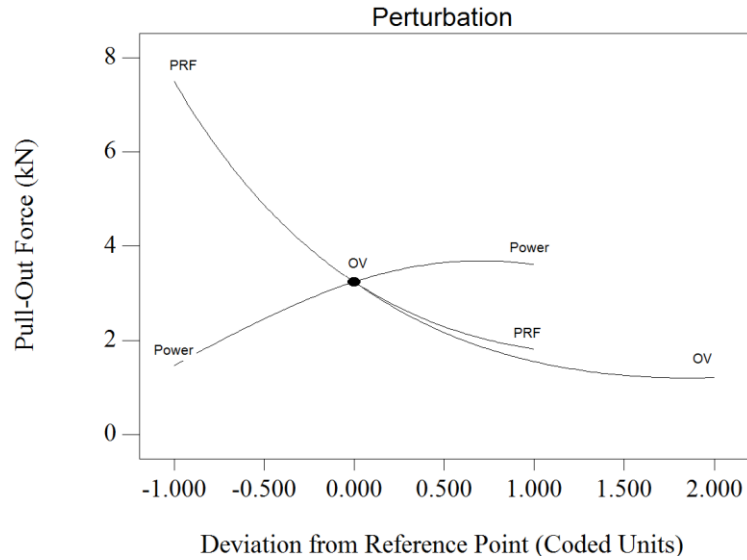


**Table 5-11** The correlation strength (r) and the significance of correlation (p) of the process parameters and resulting profile and force measurements.

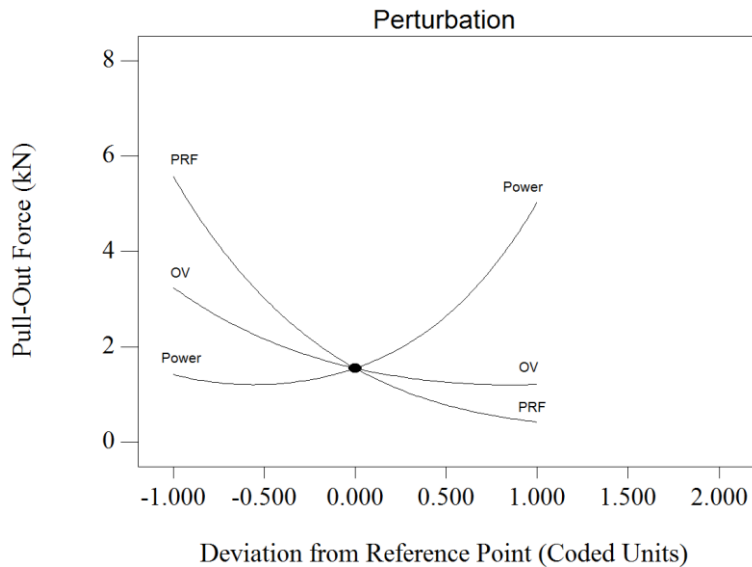
	Diameter Increase	Insertion Force	Pull-Out Force
Power	r = 0.11	0.21	0.03
	P = 0.598	0.294	0.866
PRF	-0.46 0.0147	-0.72 $2.4 \times 10^{-5}$	-0.72 $2.1 \times 10^{-5}$
OV%	-0.16 0.427	-0.29 0.138	-0.16 0.415
Pulse Energy	0.25 0.216	0.69 $7.7 \times 10^{-5}$	0.68 $1 \times 10^{-4}$
Energy Density	0.16 0.431	0.55 $2.7 \times 10^{-3}$	0.58 $1.6 \times 10^{-3}$
Fluence	0.25 0.21	0.69 $7.7 \times 10^{-5}$	0.67 $1 \times 10^{-4}$
Diameter Increase		0.42 0.03	0.24 0.22
Insertion Force	0.42 0.03		0.91 $4.7 \times 10^{-11}$
Pull-Out Force	0.42 0.22	0.91 $4.7 \times 10^{-11}$	
Interfering volume	0.847 $8.9 \times 10^{-9}$	0.29 0.069	0.155 0.44
Surface Hardness	0.86 $8.98 \times 10^{-9}$	-0.2 0.32	-0.3 0.13

From Table 5-11, it can be seen that the pulse repetition frequency always has the strongest effect on all the results. This conclusion can be represented by the following perturbation graphs, see Figure 5-34. The perturbation graph is a very important tool to compare the effect of all the processing parameters on the respond at a specific point. The plots are presented on a coded scale from -1 to 1 for the two factors under

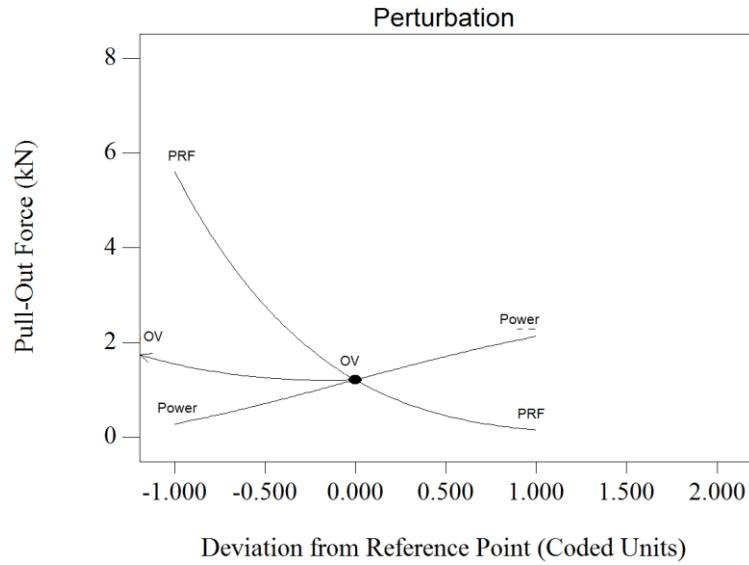
investigation, P and PRF for a specific value of OV% at the central intersection point =0. The slope of any curve at this point represents the effect of the corresponding parameter on the response. In this figure, only the correlation between the laser processing parameters and the pull-out force is presented at the three percentage overlap as an example.



(a)



(b)



(c)

**Figure 5-34** The perturbation graphs shows the relationship between the processing parameters and the pull-out force at overlaps of (a) -20%, (b) 0% and (c) 20%

The figure shows that at these point locations, the PRF always has an inverse proportional with the pull-out force while the laser beam power has a direct proportion. The percentage overlap exhibits strong negative relationship when a spread scanning tracks are applied, i.e. negative overlap. This relationship reduces when approaching zero overlap and disappears at the maximum applied overlap of 20%.

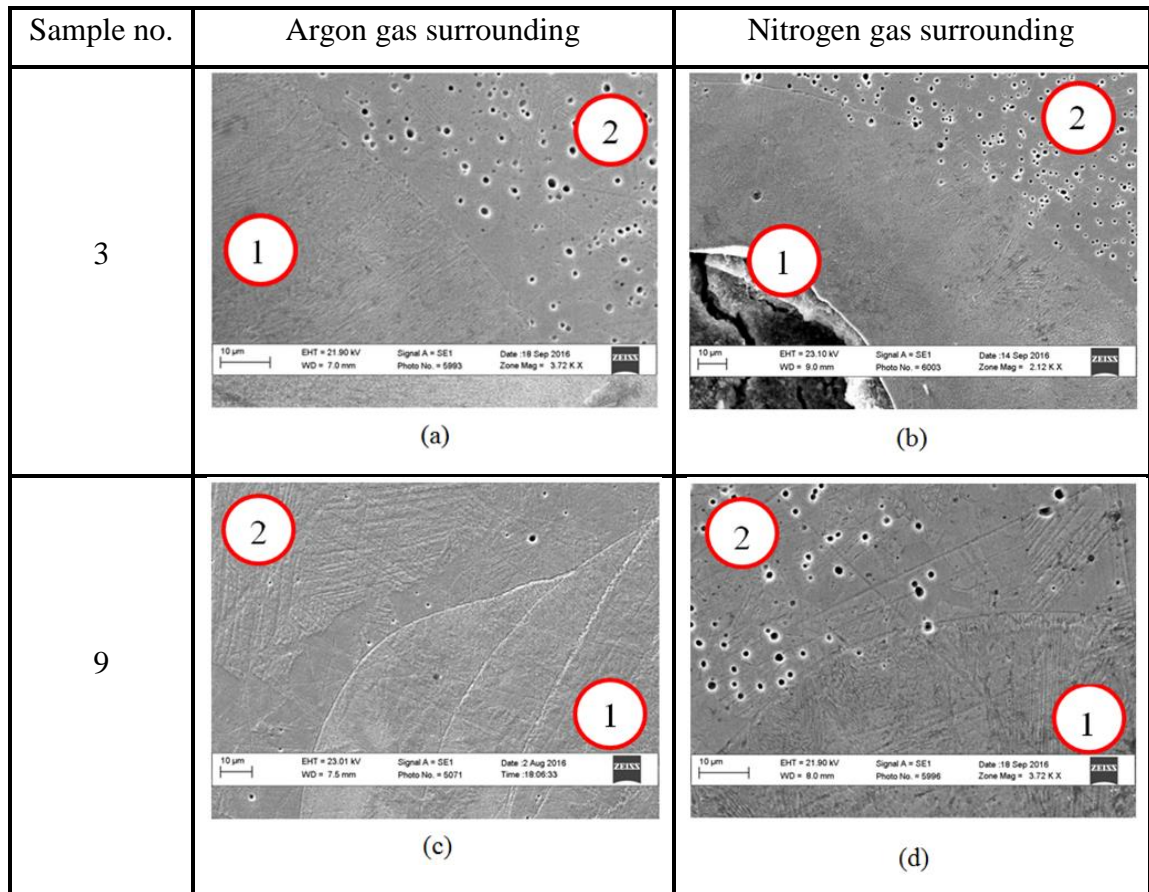
### 5.16 Laser nitriding results

In order to investigate the alteration in the mechanical properties caused by the application of the nitrogen gas atmosphere, both micro-hardness and insertion-removal tests were measured for the set of samples and compared with the results from the samples processed with argon gas. Seventeen samples were selected from the full DoE and re-produced by processing in nitrogen gas atmosphere. The selection of the samples was conducted based on a Box Behnken design and was repeated for three times for the reproducibility assurance.

### 5.16.1 Microstructure:

#### *316L Stainless steel pin samples:*

The following Figure 5-35 shows a comparison between the microstructure of 316L stainless steel pin samples no. 3 and 9 processed by using the argon and nitrogen gas mixture atmosphere. The modified area is indicated by no. (1) and the bulk substrate material is marked with no (2).

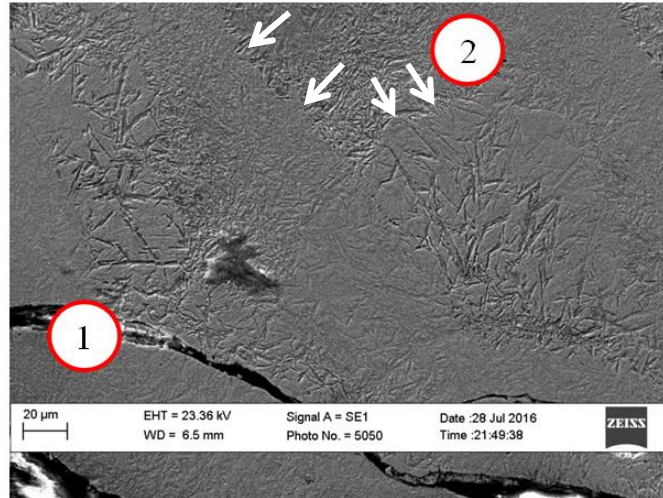


**Figure 5-35** SEM cross section micrographs of samples no. 3 and 9 processed with (a), (c) argon and (b), (d) nitrogen gas.

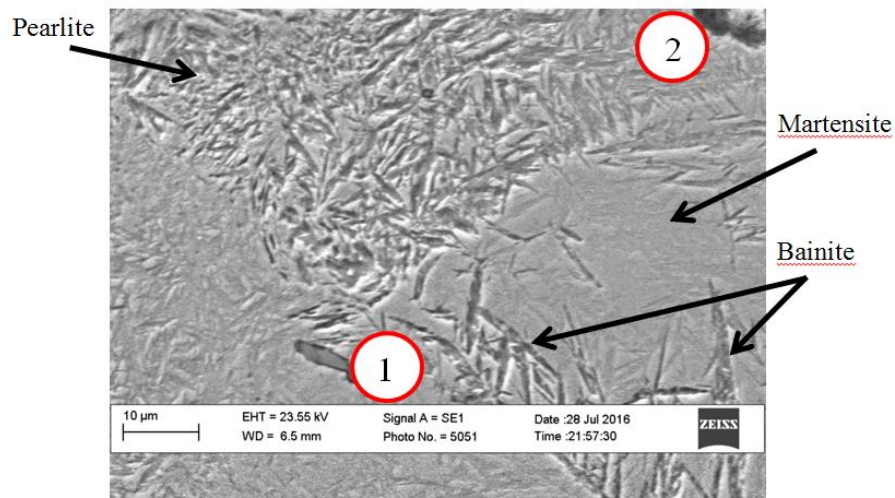
No significant change in the microstructure and grain size was noted when processing with nitrogen gas compared to that of argon gas. The major change found was the enhancement in the modified layer hardness of stainless steel as will be explained later.

### ***Carbon Steel:***

Similarly, Figure 5-36 shows micrographs of the cross section microstructure for the carbon steel samples processed with argon and nitrogen gas. The microstructure of the un-processed material (area 2) shows a predominant pearlite phase with an average hardness of (400-480 HV). After the laser processing, the modified layer (area 1) shows a bainite microstructure which is composed of plates of alternating layers of the hard cementite and soft ferrite residing in large islands of the hard martensite.



(a)

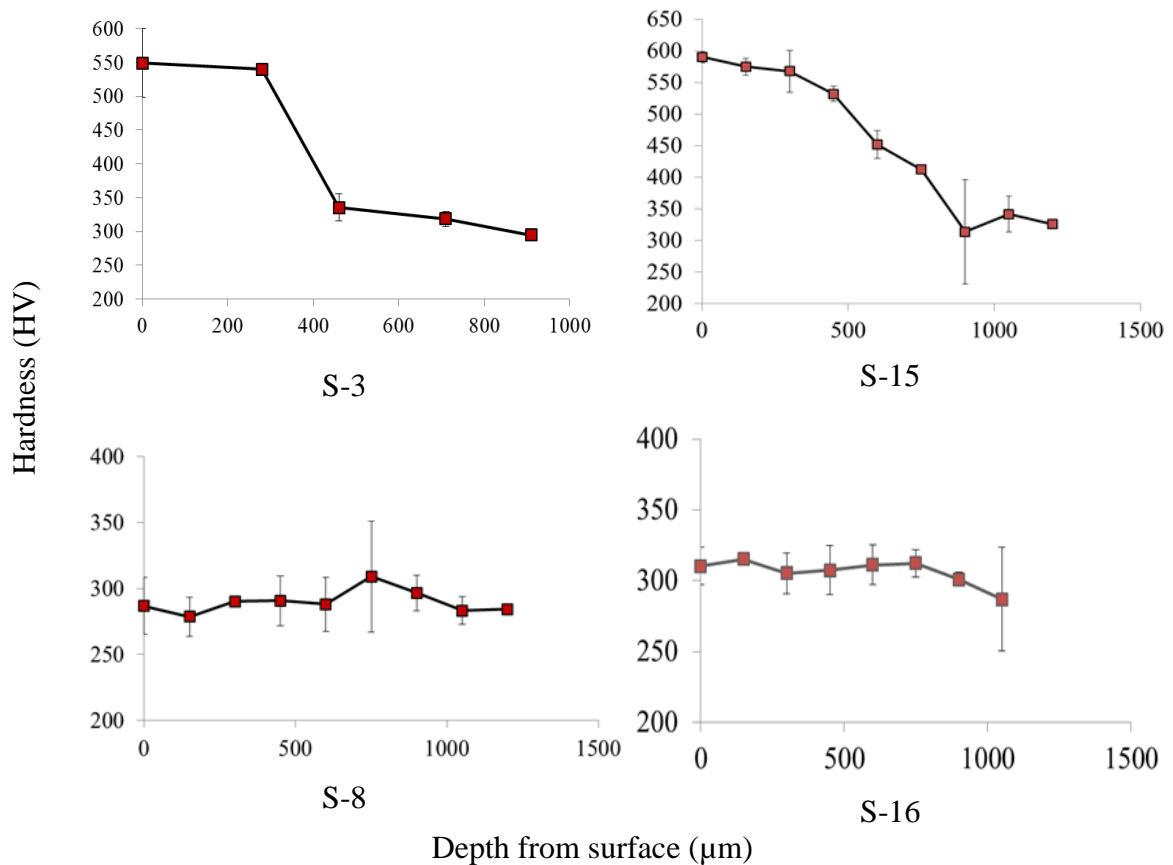


(b)

**Figure 5-36** (a) SEM micrographs of cross-section of carbon steel processed with  $\text{CO}_2$  laser of 325 W and 800 Hz revealed by nital 5% etchant, (b) high magnification of (a), (1) processed and (2) un-processed area.

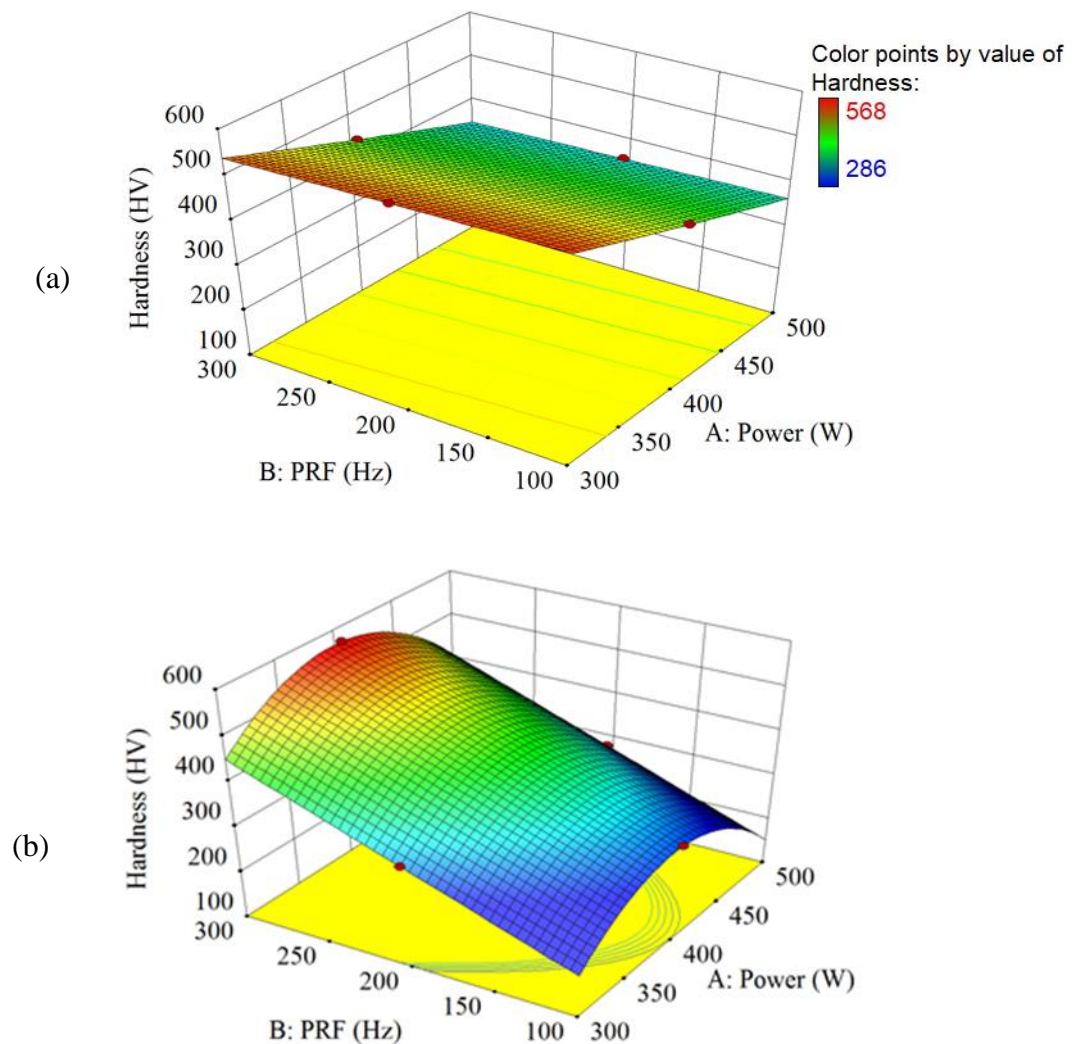
### 5.16.2 Alteration in surface hardness - *Stainless steel*:

The average hardness of the untreated stainless steel cylindrical samples was found to be (250-280) HV. After laser nitriding, a significant enhancement in the surface hardness was observed on some samples. Figure 5-37 shows the resulting micro-hardness measured from the surface toward the bulk material. From the figure, it can be seen that some samples exhibit a clear improvement in hardness and for depth of 400-500 micron as shown in samples 3 and 15 below. The processed samples did not show a significant improvement in the surface hardness in predominant as in samples 8 and 16. The measured surface hardness for the full set of samples processed with argon-nitrogen gas atmosphere is shown in *Appendix E*. As explained in previous chapter that hardening of metals is difficult when the processing time is short and when the carbon content is small [10,164]. In the case of stainless steel, both these situations are presented.



**Figure 5-37** Effect of laser nitriding on surface micro-hardness for samples 3, 15, 8 and 16

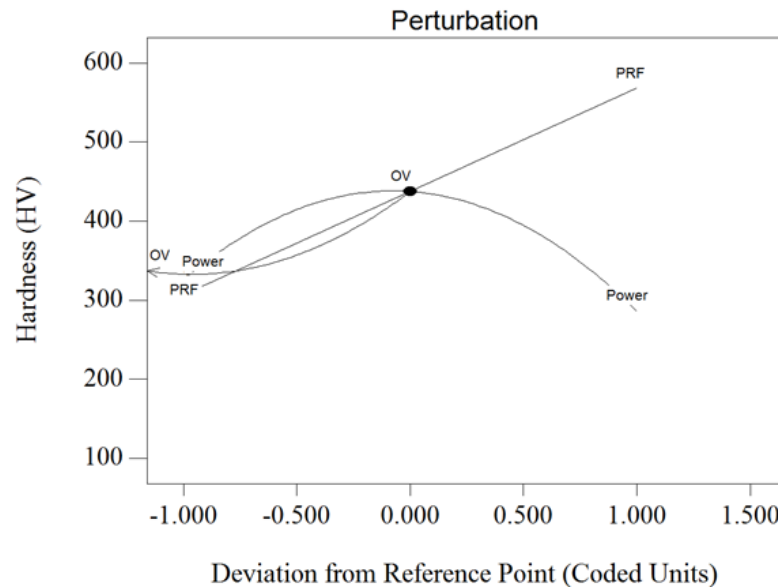
The following 3D RSM plots explain the effect of the laser processing parameters in a nitriding containing atmosphere on the micro-hardness of the 316L stainless steel cylindrical samples. The figure indicates that the PRF has the strongest and direct proportional effect on the hardness while the laser beam power has an inverse proportion, see Figure 5-38. These trends are in agreement with the literature results for example, Schaaf [109]. This effect can be explained by the shorter time associated with the high frequency which can lead to a strong take-up of nitrogen by the molten metal and the formation of the nitrided and hard layer.



**Figure 5-38** 3D RSM plots for the hardness of the laser nitriding for (a) -20% and (b) 20% OV.



The formerly mentioned correlation also can be seen in the perturbation plot in Figure 5-39 which is taken at 400 W, 200 Hz and 20% OV. The figure shows that at this point location, the percentage overlap has a strong direct proportional effect on the micro-hardness.

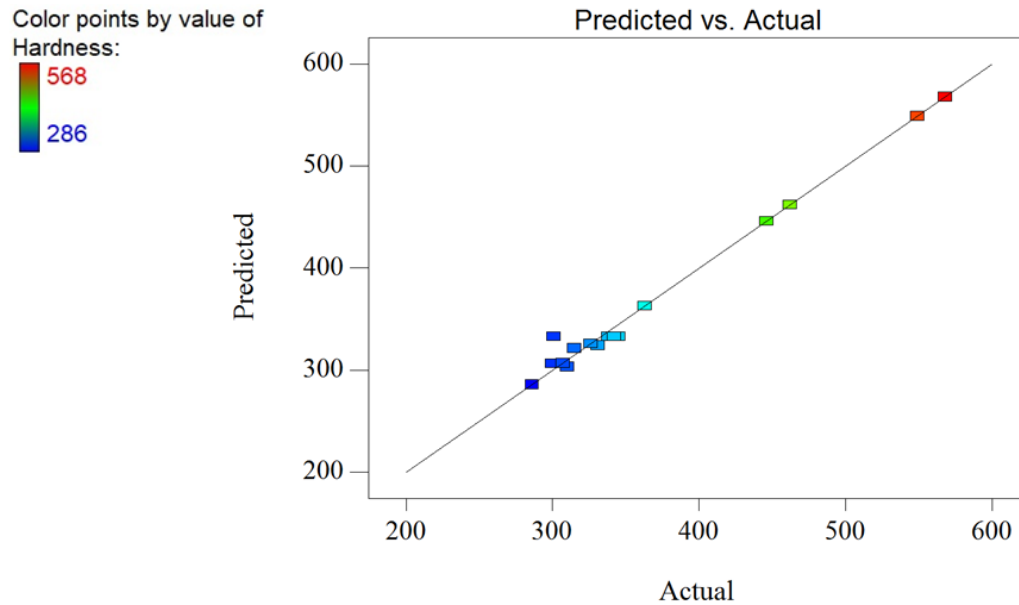


**Figure 5-39** The perturbation plot of the processing parameters and the hardness relationship.

The combination of the power and frequency (P/PRF) is equal to the pulse energy, which in turn indicates the amount of thermal energy delivered to the material. From Figure 5-38, it can be concluded that the lower pulse energy and fluence the higher the surface hardness. This fact was also achieved by Schaaf [138].

For the validation of the Box-Behnken design model, Figure 5-40 shows the scattering of the collected predicted and actual data along the trend line, which indicate that the model has a significant fitness value.

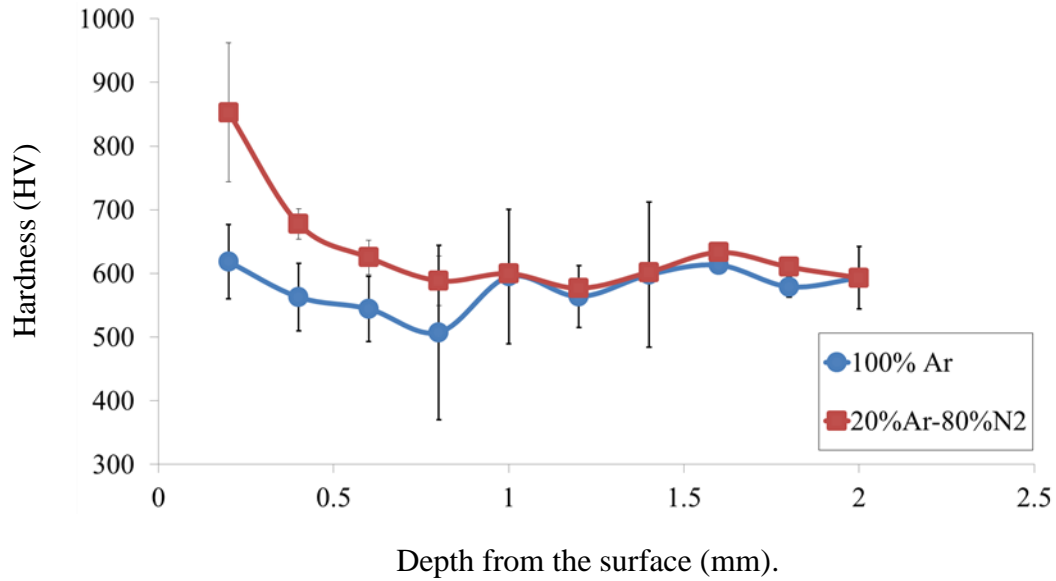




**Figure 5-40** Graph of the actual and predicted data.

#### ***Carbon steel:***

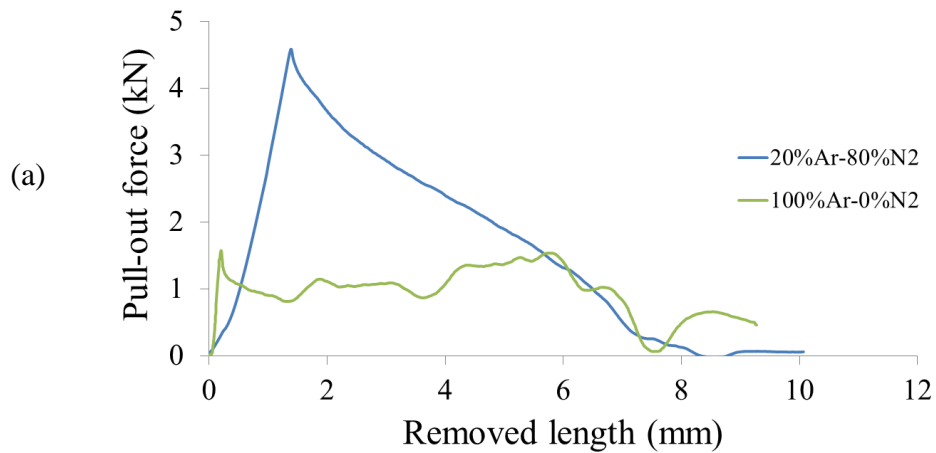
The carbon content in addition to the other alloying elements improves the heat treatment, case hardening and nitriding of steel. The influence of the experimental parameters, like operating mode (pulse or continuous) and scanning speed have a greater effect on the micro-hardness compared to that of stainless steel samples. It was found that the surface hardness improved up to more than 600 HV for the sample processed in pure argon gas and up to 850 HV for the sample processed in (80% N<sub>2</sub> - 20% Ar) atmosphere. The modified layer thickness observed was approximately 2mm as can be seen in Figure 5-41.

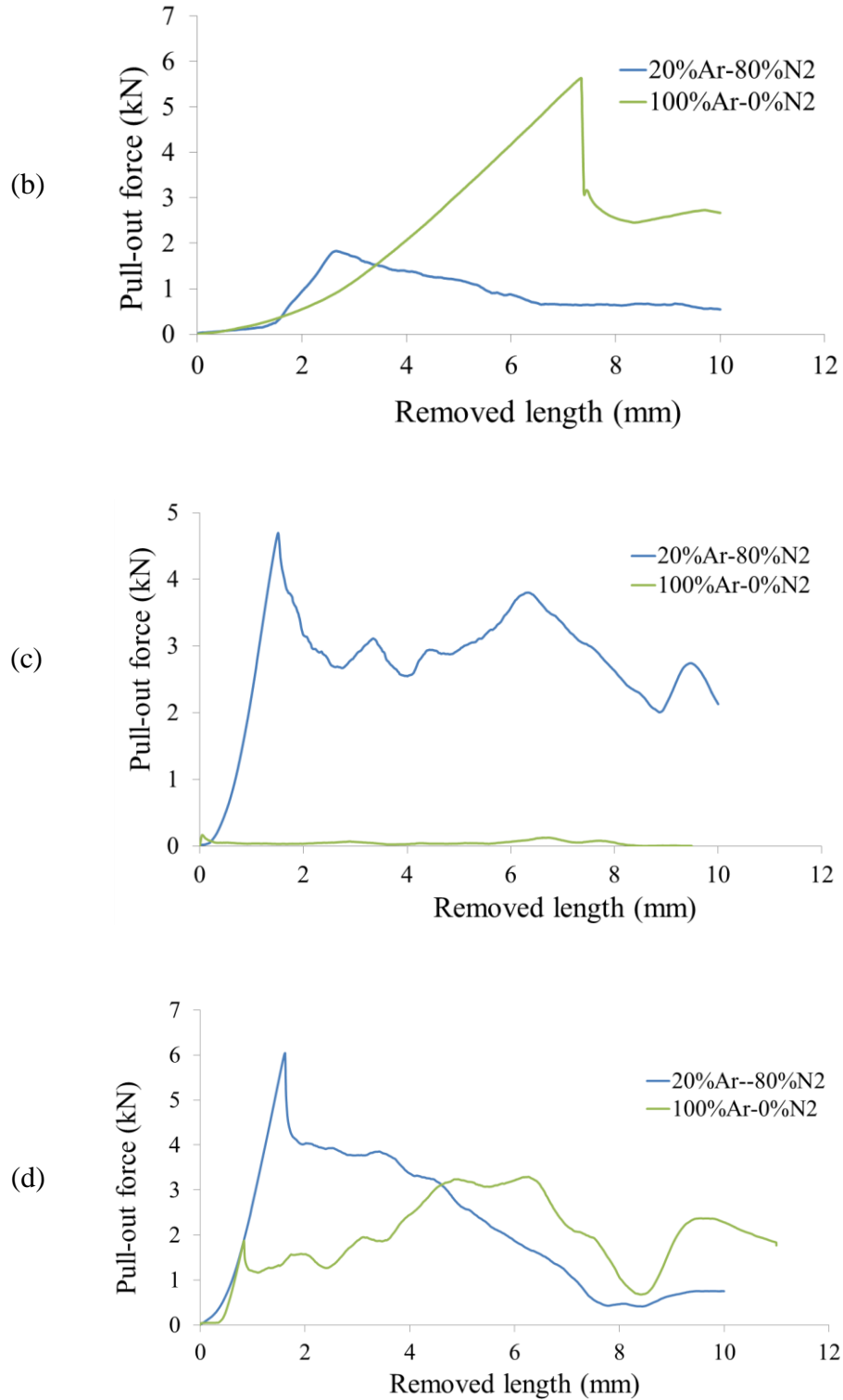


**Figure 5-41** Surface hardness of carbon steel scanned by CO<sub>2</sub> pulsed laser in argon and nitrogen gas atmosphere, n=3.

### 5.16.3 The insertion and pull-out tests of the nitrided samples

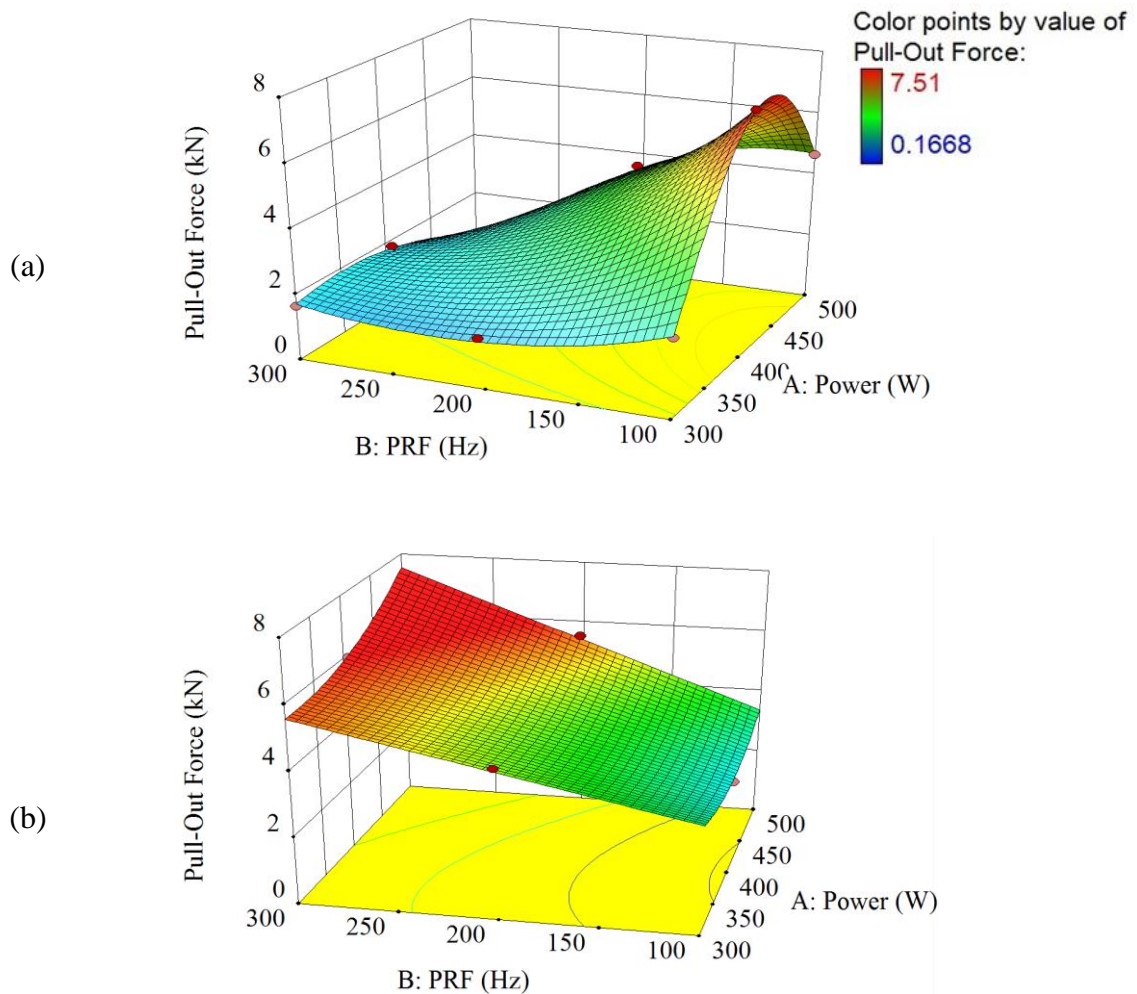
A noticeable alteration in the insertion and removal forces was found after laser nitriding process. The following Figure 5-42 shows a comparison plots of the pull-out forces for samples no. 3, 10, 15 and 25 for example.





**Figure 5-42** Shows a comparison between the pull-out forces for the nitride and non-nitrided samples no. (a) 3, (b) 10, (c) 15 and (d) 25.

It can be seen that laser nitriding enhances the fretting resistance of the textured surface by improving the surface hardness when short laser pulses are applied as in samples no. 3 and 15 processed with 200 and 300 Hz respectively. Opposite result was found for samples no. 10 when a PRF value of 100 Hz was applied. These trends are in agreement with the literature results for example Schaaf [73]. For convenience reasons, the following Figure 5-43 shows a comparison between the pull-out forces of the same set of samples processed with argon gas shown previously in Figure 5-26 (a) and the samples processed in nitrogen gas atmosphere.

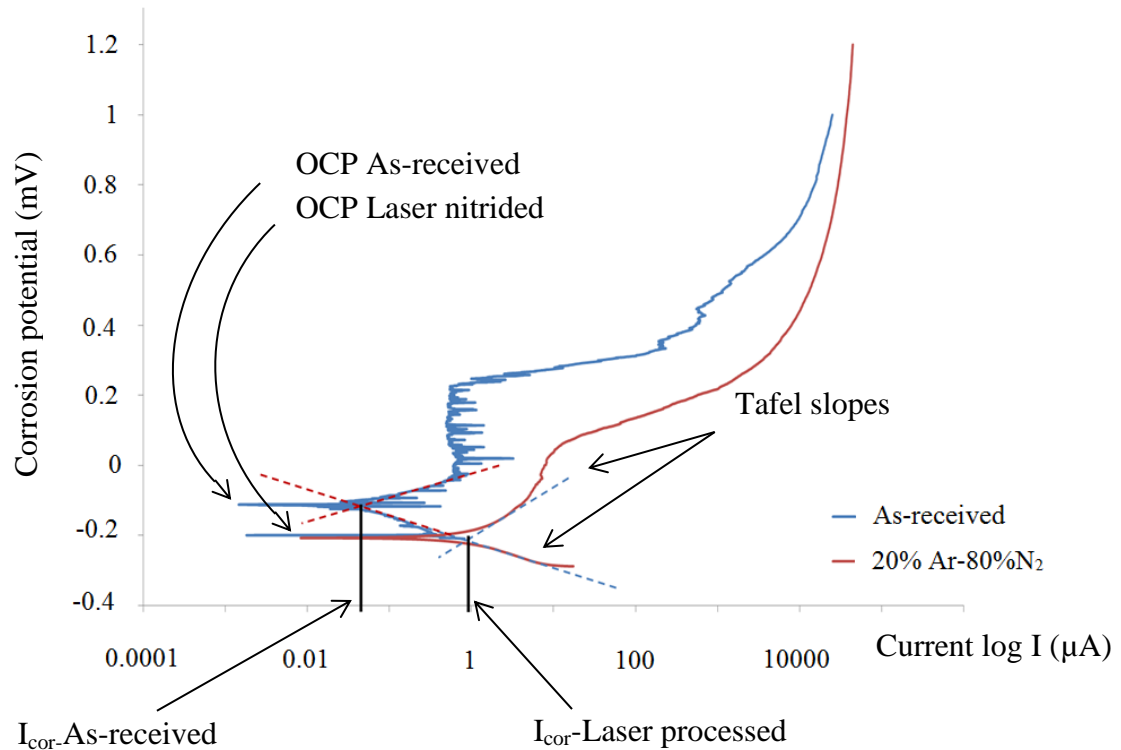


**Figure 5-43** RSM graph for the relationship between the laser processing parameters and the pull-out force for samples processed in (a) argon and (b) nitrogen gas atmosphere at(-20%) pulse overlap.

The figure indicates a significant enhancement in the pull-out forces on the high frequency level of 300 Hz on the left hand side of Figure 5-43 (b). For example, sample no. 15 and 25 were processed with (300 W-200 Hz) and (400 W-300 Hz) exhibit force improvements of (0.1 to 4.8) and (1.9 to 6.2) kN respectively. This improvement can be explained by the reduction in fretting the surface texture lamellas during insertion due to the increase in surface hardness after laser nitriding. The harder surface of samples no. 3 and 15 explained in Figure 5-37 contribute in maintaining a significant bonding between the mating parts.

#### 5.16.4 Corrosion test results

The following Figure 5-44 shows the potentiodynamic polarization plot of the as-received sample and the laser nitrided sample. A noticeable degradation in corrosion resistance for the nitride sample can be seen in both the increase in  $I_{cor}$  and the decrease in the open current potential (OCP).



**Figure 5-44** Potentiodynamic polarization curves of an as-received and laser processed samples in argon-nitrogen gas atmosphere.

### 5.17 Torsion test

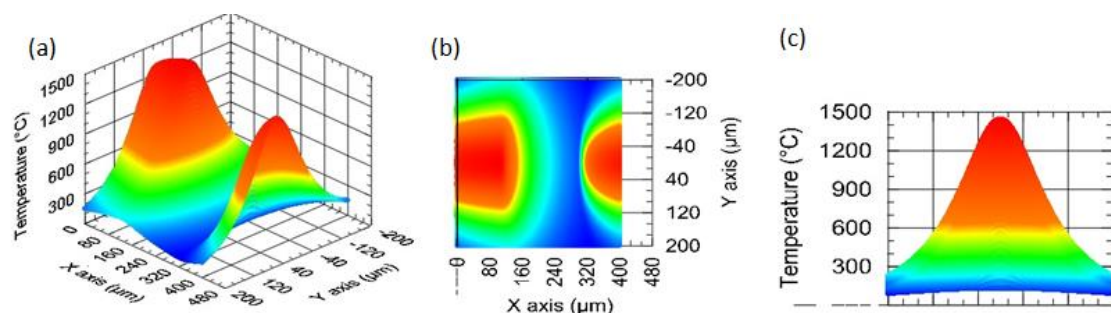
The samples fail at an average torque of 23.13 N.m with a standard deviation of 5.7, see table 5-12. The failure mechanism of the tested samples was very similar to the removal and fatigue test in which the samples observe an efficient strength after failure by fluctuating in a range of 5-7 N.m below the maximum failure torque. This phenomena indicates a safer performance.

**Table 5-12** Torque test results for sample no. 9

Sample No. 9	1	2	3	4	5	6	7	8	9	10
Torque (N.m)	26	25.5	20	24	21	25	26	33	21.5	23

### 5.18 Thermal profile

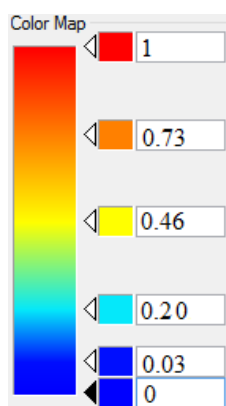
Figure 5-45 shows the temperature profile for a single laser pulse at 78 $\mu$ m depth from the surface. This sample was produced during the preliminary test for the calculation of the thermal energy required; an SEM micrograph and optical image are shown in Figures 4-8, 4-9 and 4-21. This result was generated from simulation with the model presented in equation 4-12 and input parameters of 200 W, 100 Hz, 50% duty cycle and scanning speed of 39.8 mm/sec. The temperatures here show that at this depth there is only a small region in which the temperature is above the melt temperature, 1445 °C. This agrees well with the corresponding micrograph in Figure 4-9 (b).



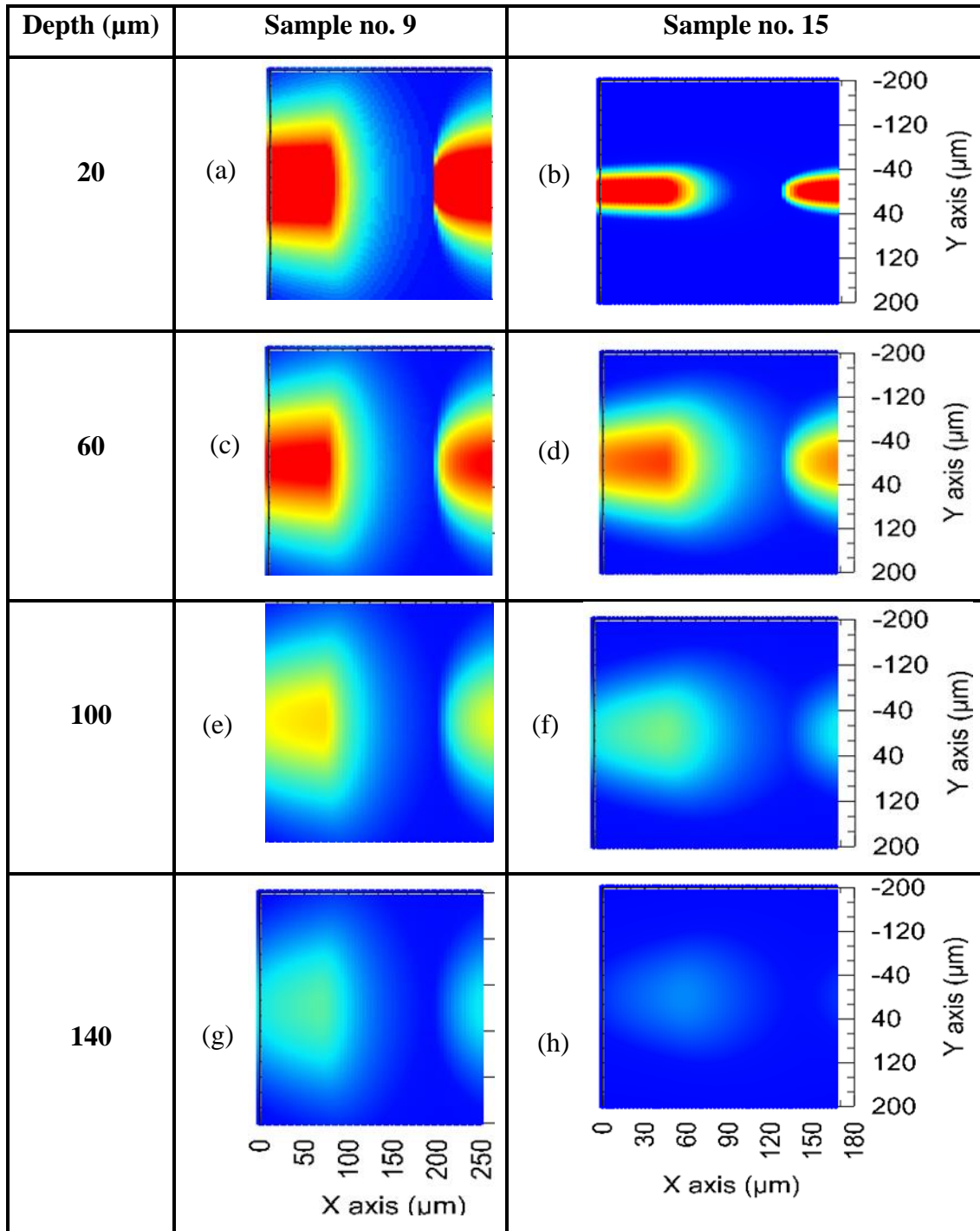
**Figure 5-45** (a) Perspective, (b) top, and (c) side view for the temperature profile at 78  $\mu\text{m}$  depth for 316L resulting from 200W, 100 Hz, 2.5ms residence time, and 50% duty cycle, conditions for sample no. 7-1 (Table A-1, *Appendix A*).

### 5.18.1 The temperature profile and thermal history

The temperature gradient profiles for samples no. 9 and 15 were calculated for four depths in the  $z$ -direction as shown in the following Figure 5-44. The temperature legend used in this figure is shown in a separate figure below and for a normalized scale from 0 to 1:



As listed in Table 4-8, sample no. 9 was processed with 400 W and 100 Hz, 5 ms pulse width and scanning speed of 25 mm/sec while sample no. 15 was processed with 400 W and 300 Hz, 1.6 ms and scanning speed of 50 mm/sec. The effect of the pulse width, which is a function of the frequency, and the residence time which is a function of the scanning speed, can be seen clearly in Figure 5-46.



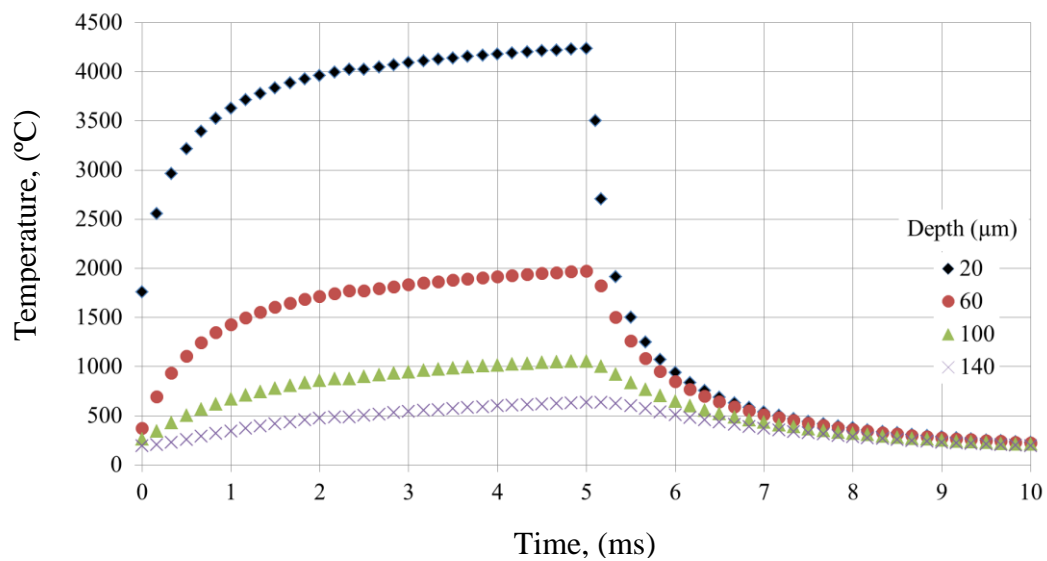
**Figure 5-46** Shows the normalized temperature distribution for samples no. 9 and 15 in planes at 20, 60, 100 and 140  $\mu\text{m}$  beneath the surface.



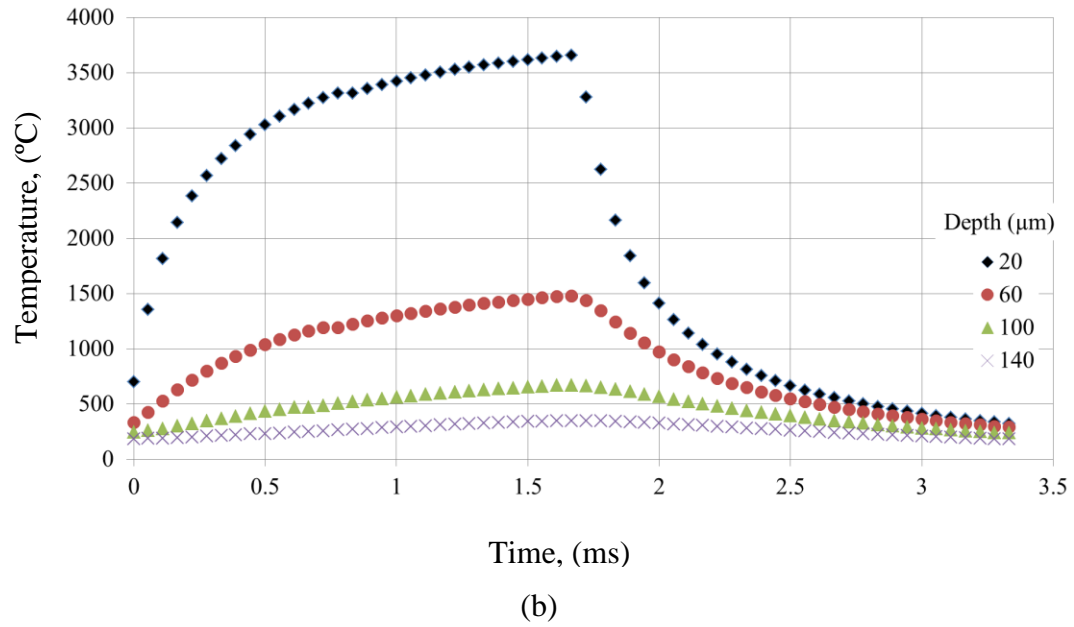
For example, at 20  $\mu\text{m}$  depth, Figure 5-46 (a), the heat has sufficient time to transfer and diffuse in the metal in both  $x$  and  $y$  directions in the case of sample no.9. Sample no. 15, shows a narrower temperature diffusion profile in the same  $z$ -plane of 20  $\mu\text{m}$  depth due to the shorter pulse and the higher scanning speed. In the following  $z$ -plane of 60  $\mu\text{m}$  depth, sample no. 9 shows a cooling behaviour and heat loss to the cold surround material with almost no significant change in the  $x$  and  $y$  dimensions. In contrast, sample no. 15 shows in addition to the temperature reduction, there was noticeable heat dissipation and expansion in the HAZ. Both temperature level and HAZ are smaller compared to sample no. 9 where the heating time (pulse width) is higher and it can also be seen in the resulting melt depth of the two samples. This result also agrees well with the results from the literature. Many researchers stated that the pulse width effect the shape of the melted zone [48,170,188,190,191,193–195] and that when the pulse width decreases, the melt pool decreases as well and may not be formed [49] which is due to the lower time scale [196].

### 5.18.2 Heating and cooling rates

The temperature history profile was also calculated at a distance of 30  $\mu\text{m}$  from the laser spot centre in the  $y$ -direction and for the same depths explained in the previous section, see Figure 5-47.

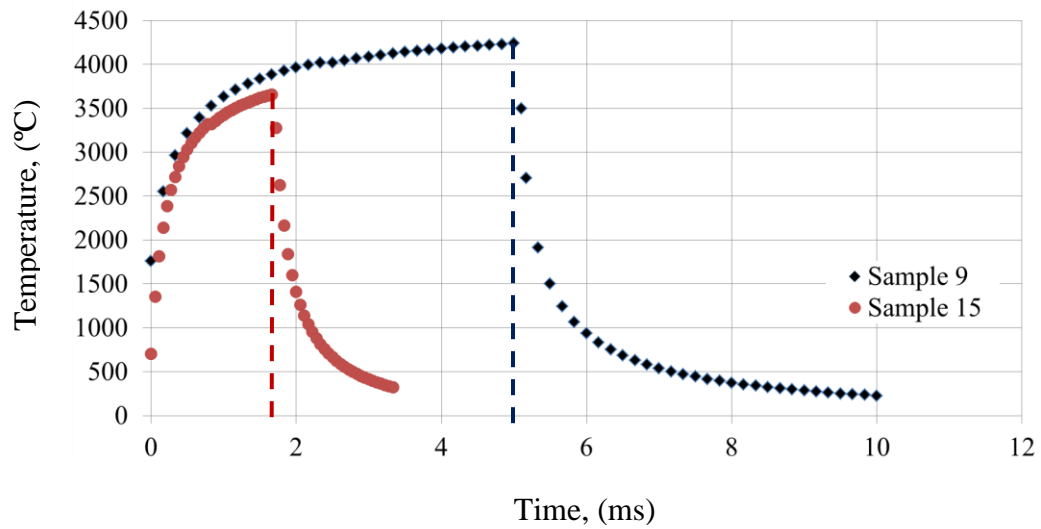


(a)



**Figure 5-47** Temperature history for (a) sample no. 9 and  
(b) sample no. 15 at four depths.

Figure 5-48 below shows the temperature-time profile for the two samples at  $z = 20 \mu\text{m}$  plotted on one platform for convenient comparison.



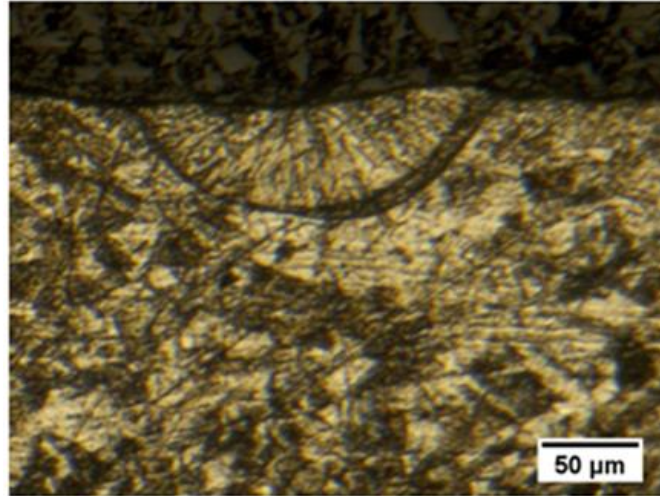
**Figure 5-48** Temperature-time history profile for samples no. 9 and 15  
at depth =  $20 \mu\text{m}$ .

Sample no 9 (blue coloured) reached the maximum temperature of 4250 °C in a time of 5 ms equals to the pulse width ( $\tau$ ) and 5 ms for cooling and sample no. 15 (red coloured) reached its maximum temperature of 3660 °C in a time,  $\tau = 1.6$  ms and 1.7 ms for cooling down. The maximum heating and cooling rates were extracted from this figure and found to be  $5 \times 10^5$  and  $8 \times 10^5$  °C/s for sample no. 9 and  $2 \times 10^6$  and  $2 \times 10^6$  °C/s respectively.

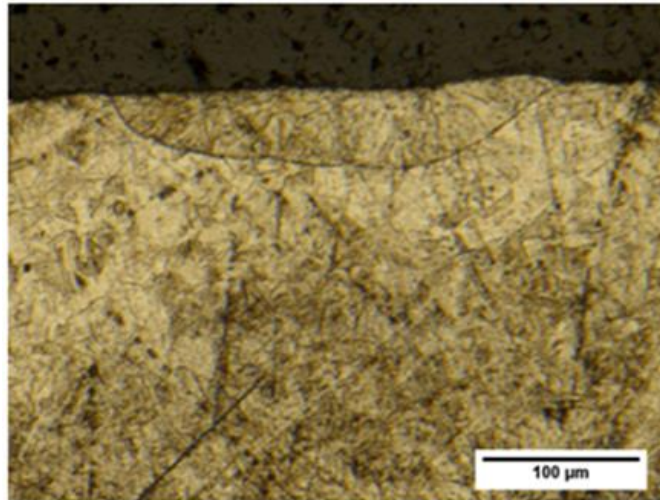
### 6.1 Thermal energy and absorption factor

The processing parameters applied on the sample presented in Figure 4-7 where the surface was locally melted with negative overlap, correspond to each laser pulse delivering an energy of 1000 mJ. Since most metals and alloy surfaces are reasonably reflective to the longer-wavelength infrared light beams, such as CO<sub>2</sub> laser [6,51,171], the energy supplied must be several times the calculated one based solely on consideration of heat capacity, latent heat of fusion, and latent heat of vaporisation. Quintino et al. [51] noted for example that iron absorbs about 5% of the energy from the CO<sub>2</sub> laser radiation, while steel absorb 12%. As noted in Section 4.4.2221 the corresponding energy required for melting a cylindrical shape at the surface, of a diameter equals to the laser spot and depth equals to the heat affected depth  $z$ , was approximated as 24.64 mJ. This indicates that approximately 2.46% of the heat energy delivered was utilized to initiate the surface melting. Other laser energy delivered to the surface is known to be lost due to reflection, radiation, conduction, and convection. Figure 4-8 (b) and Figure 4-21 suggest that the re-solidified melt pool shape shows that it resembles an ellipse rather than a circle, even though the beam is TEM<sub>00</sub> Gaussian which should be circular. The elliptical shape can be understood to be due to the moving of the sample during laser firing. This means that the HAZ must be corrected. Moreover, the mass affected by the laser energy also need to be recalculated to the exact melt depth of 70  $\mu\text{m}$  found experimentally, see Figure 6-1 (a). Considering this and recalculating, the actual amount of energy absorbed was 2.25% of the input laser beam thermal energy.

(a)



(b)

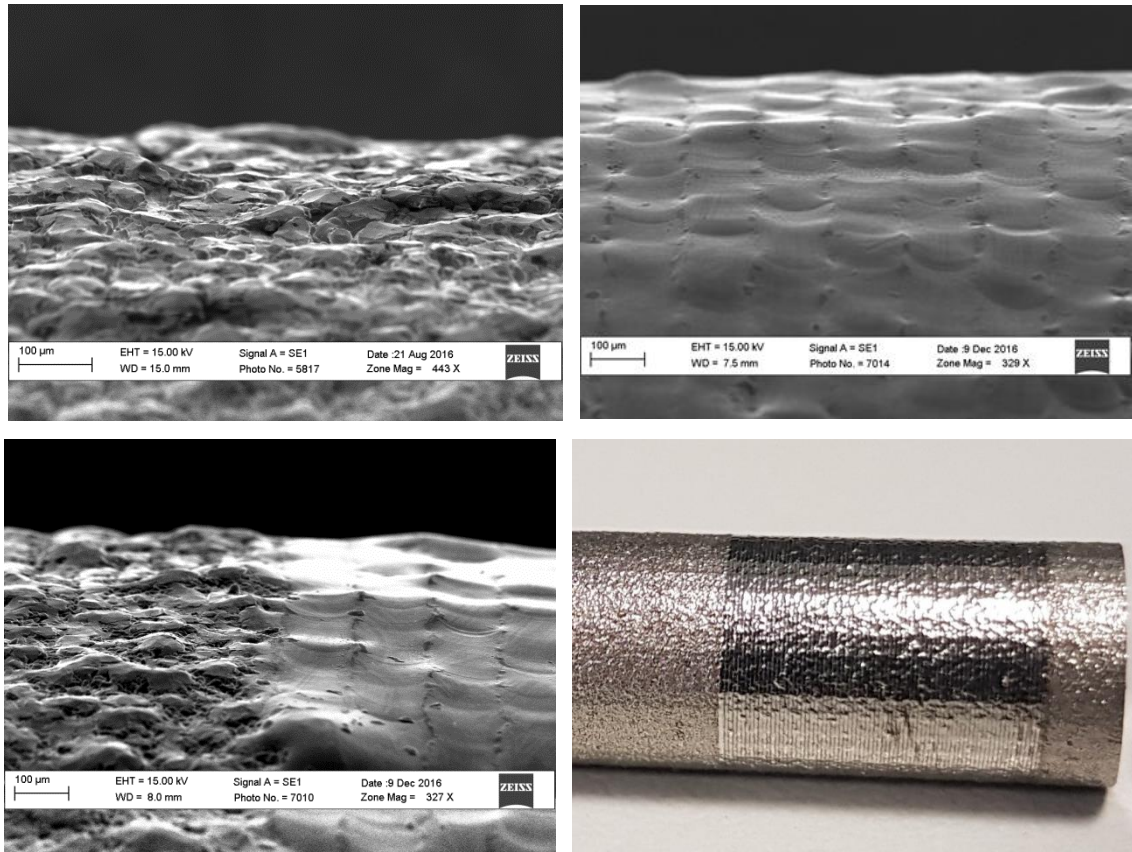


**Figure 6-1** Optical micrographs of the melt pool (a) width and depth in the longitudinal section and (b) length in the transvers section (see Figure 4-18), revealed by Adler etchant.

These absorption factor values are still lower than expected, compared to those reported by Quintino, for iron (5%) and steel (12%). This could be explained by the stainless steel, as an alloy, is more reflective than other types of steel at the same wavelength, and it would therefore be expected to reflect a larger percentage of the incident visible and IR radiation than pure steel. An assumption adopted in this consideration is that the heat loss to the surrounding by convection and radiation is negligible, and that all the absorbed pulse energy is converted into heat energy. This assumption is reasonable because the melting process is carried out in such a short time, equal to one pulse width

of 5 ms. Moreover, the PRF value of 100 Hz is the minimum value applied in this study, see Table 4-13. The PRF of 200 and 300 Hz would result in pulse widths of 2.5, and 1.6 ms respectively, thus reducing the process time and not allowing sufficient time for significant heat loss to the surroundings, which supports the assumption adopted here.

The extensive control over the laser processing parameters harnessed the high control on the melt layer thickness. This was advantageous to be adopted for the laser polishing experiment of a 316L SST cylindrical samples based on the principles explained in section 2.4.6. the samples were produced by using the additive manufacturing method (AM). The (AM) manufacturing is widely employed in biomedical implants, aerospace, automotive and many other types of industry. The produced parts exhibit high surface roughness attributed to the initial particle size of the metal powder used. For some applications or on customer demand, the parts must be polished to some level on the whole surface or in some certain portions. Figure 6-2 below shows the side view for the cylindrical pin sample of 8 mm diameter before and after polishing. The laser processing parameters used during polishing were 110 W of CO<sub>2</sub> laser beam in continuous wave mode (CW), spot size of 0.2 mm focused on the surface, 5 ms residence time and 3.5 kW/mm<sup>2</sup> irradiance. The resulting surface roughness achieved was 0.8 µm down from 3-4 µm for the as-received sample roughness.



**Figure 6-2** Laser micro-polishing of a cylindrical SST sample produced by additive manufacturing (AM) before (top left) and after (top right).

## 6.2 Measured micro texture longitudinal and circumferential dimensions

The gaps between the molten pools seen in Figure 4-8, in both the circumferential and the axial directions, were found to be 100 µm. This value is half of the laser beam spot diameter of 0.2mm, which is consistent with the controlled overlap value of -50%. These gaps were consistent during the entire scanning process. The melt pool circumferential spot length, expanded to 360 µm in the beam propagation direction due to the high circumferential speed of 2400 mm/min. The distance scanned by each pulse can be calculated as the pulse width times the scanning speed =  $0.005 \text{ s} \times (2400 / 60) \text{ mm/s} = 200 \text{ µm}$ .

For the 200 µm diameter laser spot to translate 200 µm, the total processed surface length would be 400 µm. The measured melt pool is 40 µm shorter than this which could be considered to be due to the time needed for heat energy to build up before

melting is initiated. This explanation is supported by the melt pool longitudinal length, see Figure 4-8 (b), which is narrower where the laser shot begins than where it finishes. It is considered that energy accumulation is required before being sufficient for melting. The dimensions discussed are taken from both optical microscope and SEM, the results were consistent with each other. As discussed, the dimensions observed agree well with what is expected from the laser parameters, which supports the ability to predict and produce a pre-determined texture with this technique.

The maximum melt depth measured experimentally for the sample shown in Figure 4-9, matched reasonably well with the thermal model prediction, both of which indicated similar melt depth of 70  $\mu\text{m}$  and 78  $\mu\text{m}$  respectively. The 8  $\mu\text{m}$  difference between the experimental and the modelled melt depth might be due to the assumption of no heat loss to surrounding which was adopted in the mathematical model.

### **6.3 The effect of the laser processing**

Many researchers [44,197–199] have reported the effect of the pulse repetition frequency (PRF) on the surface morphology, microstructure and ablation of the laser processed material. Schaffer et al. [44] stated that heat builds up from the pulsed laser thermal energy only when the time intervals between successive pulses is shorter than the thermal diffusivity of the material. Taking this into account and assuming the thermal diffusivity of 316L SST,  $\alpha = 3.8 \times 10^{-6} \text{ m}^2/\text{s}$  and laser beam focus size of 200  $\mu\text{m}$ , would result in a diffusion time of 8 ms. Since the full DoE test was performed in a range of pulse width of 1.6 – 5 ms, no extreme melting or material ablation resulted.

Also, from the insertion-removal test for samples no. 15 and 24, which show the same surface roughness of 46  $\mu\text{m}$ , the removal forces found were 0.17 and 6.66 kN respectively. This can be explained by the differences in the frequency, which produced a hard surface layer on sample no. 24, compared to a brittle lamella surface on sample 15 which can be removed during the insertion, see Figure 6-3.



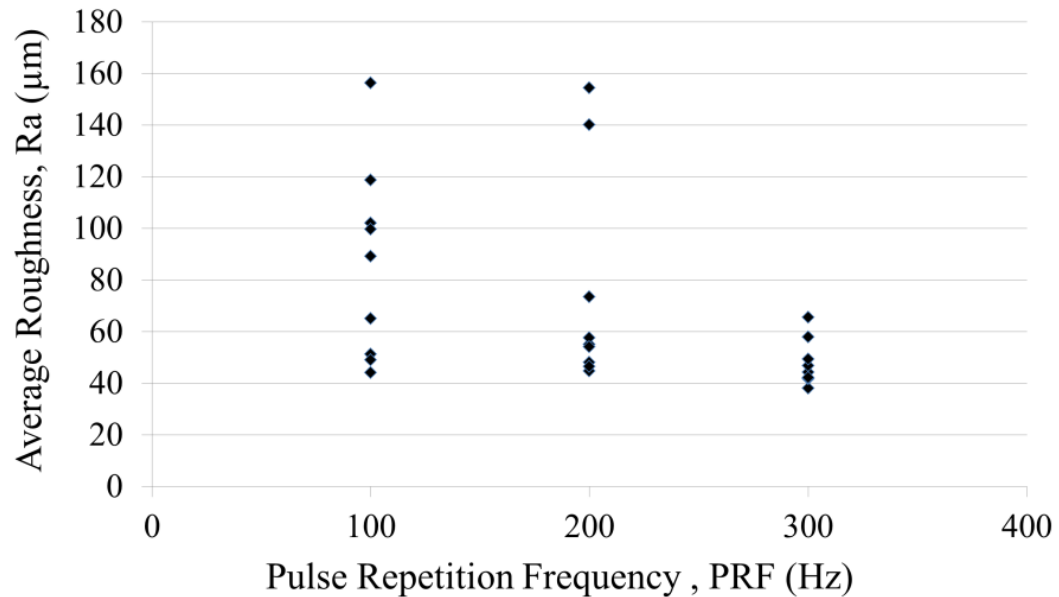


**Figure 6-3** Samples no. 15 (left) and 24 (right) after insertion.

From the insertion and pull-out forces plotted in Figures 5-22 and 5-25, and the RSM plots shown in Figures 5-23 and 5-26, the processed samples exhibited a range of 10 to 47 kN for the insertion force and 0.1 to 7.5 kN for the pull out force respectively. This variation could be explained by the alteration in the resulting mechanical properties of the processed surface and not only the increase in the diameter. For example, points A and B in Figure 5-26 (b) and (c) belong to samples no. 16 (500 W, 100 Hz, and 0% OV) and 23 (500 W, 100 Hz, 20%) and they both have similar diameter increases of 0.75 and 0.8 mm, and surface hardness of 341 and 376 HV respectively. It was noted that sample no. 16 exhibits a removal force of 5.7 kN before failure while sample no. 23 fails at 1.4 kN. The reduction in the pull out force in sample no. 23 is caused by the positive overlapping scans, in which the laser beam re-melts the surface material which already been processed during the previous scan resulting in a higher surface temperature. The subsequent high cooling rate results in a brittle lamellar surface microstructure, which tends to break and destroyed during insertion. Moreover, the lower roughness of  $89\text{ }\mu\text{m}$  in sample 23 would contribute to a reduction of the friction force. The failure mechanism for all the samples indicates high joint bond strength between the insertion and the hub which persists and even strengthens further during pull-out, as can be seen in Figure 5-24. Rather than a complete, immediate failure of the joint this is effectively a re-gripping of the joint before total failure. This is beneficial for providing a safer

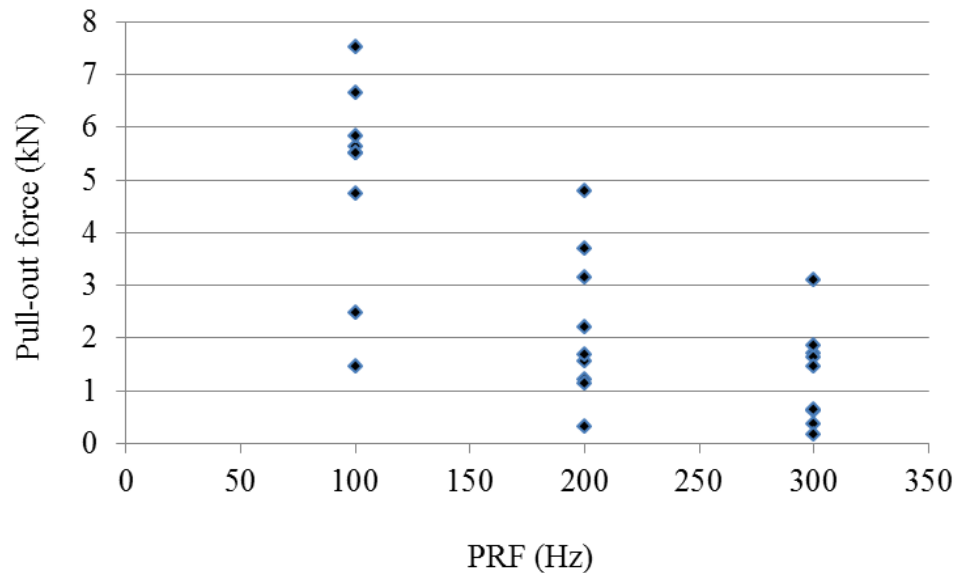
joint compared to conventional joints. An additional safety factor is evident due to the extended displacement provided from these joints before joint failure.

The inverse relationship between the frequency and the measured responses; the increase in diameter, the insertion and pull-out forces, has a strong and significant correlation as can be seen from the (r) and (p) values listed in Table 5-10. It was particularly noted that increasing pulse frequency results in a reduction in the bonding forces. The higher frequency of 300 Hz resulted in smaller increase in the samples diameter, and lower level of surface roughness, due to the short heating time. Also, a similar correlation was found between the frequency and the resulting surface roughness, see Figure 6-4. The lower the frequency the longer the heating time and the larger the melt pool size, which produces a higher surface roughness. The increased melt liquid, with the aid of the assist gas jet and the centrifugal force generated from the high rotational speed combine in this case to create more rough and variable surface profile. This conclusion also agrees with the results plotted in Figure 5-12. The maximum Ra was reached at the residence time of 3 ms and the irradiance of 8.26 kW/mm<sup>2</sup>. A steep degradation in the surface roughness was noted when exceeding these values due to the over melting and resulting flow of the liquid melt.



**Figure 6-4** Graph of the average surface roughness, Ra, versus the PRF for all test conditions.

A similar effect for the frequency on the pull-out force were noticed as can be seen from the following Figure 6-5. The increase in heating time (low frequency) allow for larger areas of the hard martensite to be formed in the account of the soft ferrite. Both these phases are significantly bonded on the yield austenite of the bulk material. The larger portions of the hard martensite improve the fretting and wear resistance of the insertion surface and contribute in maintaining high joint strength compared to the ultra-high hardness and brittleness of the texture produced with shorter pulses.



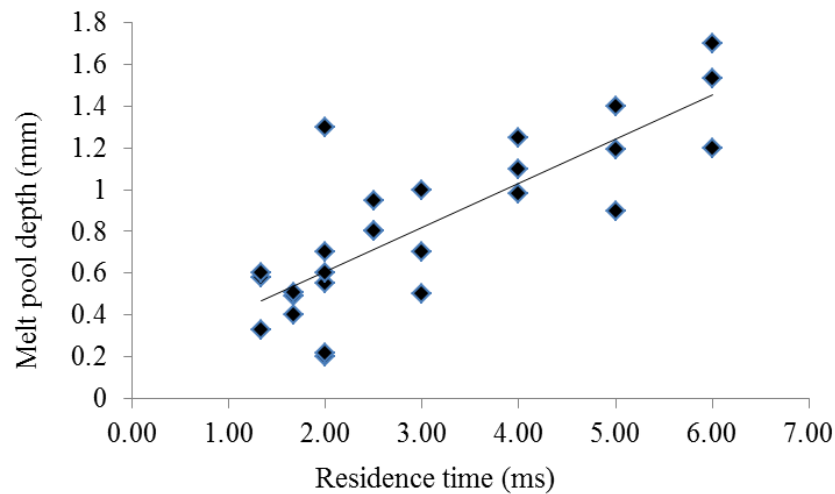
**Figure 6-5** Shows the PRF and pull-out force data scattering.

During the preliminary test, it was observed that when using the CW mode, an over melting and none consistent surface texture results due to the accumulative thermal energy and heat build-up. The samples produced using the CW mode show more melting and material removal at the end of the process compared to the start in addition to the darker colour, hence only the PW mode was used. Moreover, the laser focus position was also investigated during the preliminary scanning test. It was found that no clear surface texture can be produced. Compared to samples processed using similar parameters, a clear texture pattern lines were produced. This could be explained by the higher thermal energy absorbed when adjusting the laser focus below the metal surface. This effect was also reported by several researchers [57,60,61].

#### 6.4 The melt-pool depth

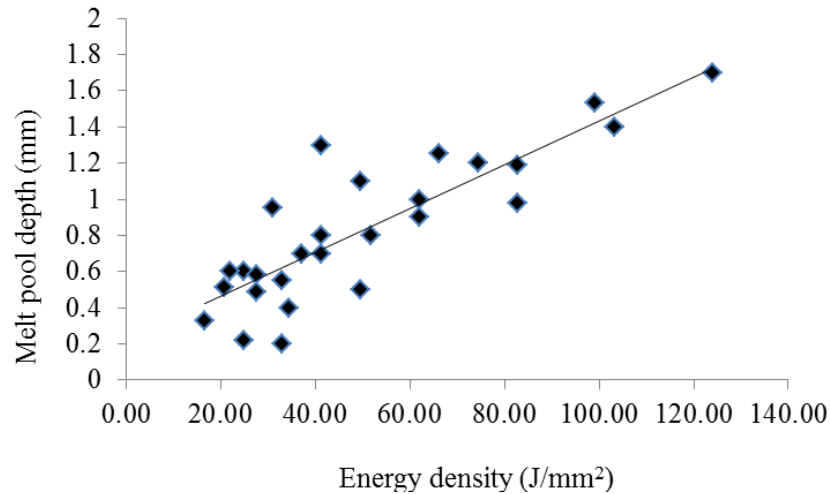
The modified layer thickness can influence the mechanical part's lifetime, and as such it is essential to control this. An average treated layer thickness of 40 to 60  $\mu\text{m}$  is regarded to be ideal [200,201]. The new modified layer will have altered mechanical properties due to the phase transformation from austenite to martensite, which is caused by the high cooling rates of between  $10^3$  and  $10^6$  K/s [13,156,163]. Typically, this change will result in increased hardness and wear resistance, due to the presence of the martensite, though this should be confirmed for specific operational conditions.

The melt pool depth increases by increasing both irradiance and residence time. This result could be explained by the reduction in the scanning speed and the increase in the laser beam-metal surface interaction and exposure time and thermal energy applied as can be seen from the following Figures 6-6 and 6-7. This result also agree well with the results from the literature [201,203]. At lower levels of residence time of up to 3 ms, all the three levels of irradiance applied show low and interfering melt pool depths. The maximum depth was found to be 1.7 mm at 6 ms and  $10.33 \text{ kW/mm}^2$ .



**Figure 6-6** Shows the relationship between the residence time and the melt pool depth.

The data presented in Figure 6-6 are plotted for different values of irradiance and hence the large variation in the melt pool for the same level of residence time.



**Figure 6-7** Shows the relationship between the energy density and the melt pool depth.

The highly controlled laser processing parameters affirm the homogenous melt depth, which is important to most engineering applications as this, would indicate the mechanical properties of the modified layer.

### 6.5 The chemical composition and phase change

The EDX test results of the chemical composition show no major change in the modified layer compared to the bulk material. This is due to the short processing time and the effect of the high cooling rates which does not allow a sufficient time for the diffusion of the alloying elements.

For the samples processed with nitrogen gas atmosphere, and from the analysis of the surface hardness, EDX results and the surface BSE images, it can be concluded that the laser processing in nitrogen gas atmosphere boosts the formation of the hard martensite (the bright portion in the BSE image) compared to the soft ferrite (dark), Figure 5-32. The absorption of nitrogen by the metal surface is very small to be shown in the EDX pattern when irradiated with CO<sub>2</sub> laser because of the low energy delivered. The CO<sub>2</sub> laser photon energy is 0.12 eV, which is too small compared to 15.6 eV required to ionise the N<sub>2</sub> gas and 9.8 eV required for the dissociation and that the power density applied in this experiment was ( $1.2 \times 10^6$  kW/cm<sup>2</sup>) is also small compared to the irradiation of ( $3 \times 10^{10}$  kW/cm<sup>2</sup>) needed for the gas breakdown.

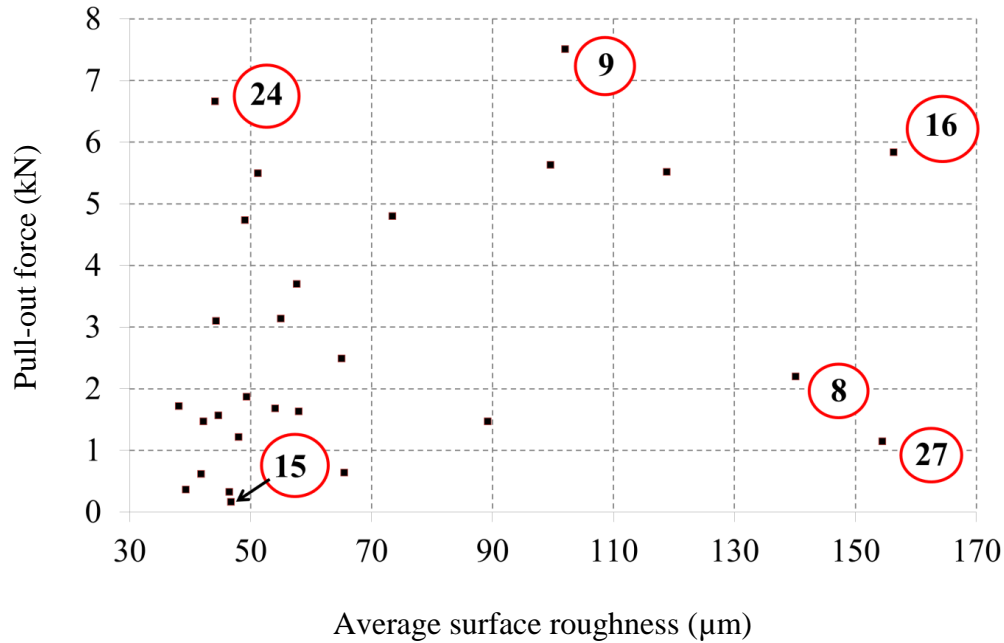
## **6.6 The elastic modulus and nano-hardness**

The cold-drawn, austenitic 316L SST has an (FCC) microstructure at room temperature and hence is ductile and low strength alloy, with large variation in the hardness and elastic modulus. This variation can result from the cold work during manufacturing. Compared to other types of steel, the thermal processing and hardening of austenitic stainless steel and undergoing phase transformation does not always result in residual surface stresses, and only small or negligible change in the surface micro-hardness can be measured. When the localized molten material re-solidifies and the surrounding (HAZ) that reached the phase transformation temperature cools and transform to martensite, the softer austenite in the bulk material plastically deforms and compensates the expansion and the volume change associated with the formation of martensite [63]. Due to the aforementioned effects, there was no sign of surface residual stresses noted and the fluctuation in the nano-hardness and the elastic modulus was symmetrical around the average values when measured both at the surface and near the untreated centre, see Figure 5-14.

## **6.7 The surface roughness measurements**

The resulting average surface roughness shows a large variation of values which can be explained with reference to the calculated laser processing parameters, see Figure 5-12. This graph highlights the high surface roughness at high levels of irradiance and residence time due to the longer exposure time. This result was also shown by Pinkerton and Li [20]. The measured surface roughness data with the 95% CI's error bars are shown in Figure 5-10 and the correlation between the surface roughness and laser processing parameters is shown in, Figure 5-12. It is clear from Figure 5-11 that there is a wide range of control over surface roughness. Figure 5-11 indicates that lower roughness levels occurred at lower levels of irradiance. The high levels of irradiance and residence time exhibited wider ranges of roughness, due to the resulting larger melt pool sizes and the gas jet effect in spreading the molten material. In this study, the higher surface roughness noted was  $156\text{ }\mu\text{m}$  at a residence time of  $>3\text{ ms}$  and irradiance of  $>8.26\text{ kW/mm}^2$  was applied. Exceeding these levels would be resulted in over-melting and material loss causing degradation in surface roughness. The variances in

the surface roughness and the melt depth for samples 9 and 15 for example can be seen in the surface morphology and the cross section SEM micrographs listed in Figure 5-4, respectively. The following Figure 6-8 shows the data scattering for the pull-out force versus the surface roughness.



**Figure 6-8** Distribution of the full DoE set of samples showing the surface roughness versus the pull-out force.

While the pin removal force is not solely reliant on surface roughness, the distribution of the samples in this graph indicates that the majority of the samples produced with low surface roughness exhibited low removal force.

Samples no. 9 and 15 presented an average surface roughness of 102 and 46  $\mu\text{m}$ , melt depth of 1.25 and 0.2 mm, and exhibit a removal force of 7.51 and 0.17 kN respectively. This could be explained by the low frequency used in sample no. 9 which leads to a longer heating time. The longer residence time in turn leads to larger heat affected zone (HAZ), and the formation of the hard lattice martensite residing on the soft and low strength austenite, see Figure 5-5. Table 6 lists the related processing parameters with

the resulting surface roughness and pull-out force for the samples highlighted in Figure 6-8.

**Table 6-1** Calculated laser processing parameters with the resulting Melt-pool depth, average surface roughness and the pull-out force for selected samples.

<b>Sample No.</b>	<b>Irradiance (kW/mm<sup>2</sup>)</b>	<b>Residence time (ms)</b>	<b>Melt-pool depth (μm)</b>	<b>Av. surface roughness (μm)</b>	<b>Pull-out force (kN)</b>
<b>8</b>	10.33	3.0	650	140.1	2.2
<b>9</b>	8.26	4	990	102	7.51
<b>15</b>	8.26	2	580	46.74	0.17
<b>16</b>	10.33	5	1250	156.3	5.84
<b>24</b>	6.2	6	1200	44.13	6.66
<b>27</b>	8.26	3	680	154.4	1.15

### 6.8 The diameter increase

The diameter increase is most notably inversely proportional to the pulse repetition frequency due to the corresponding increase in heating time and pulse period which leads to a larger melt pool size. This effect was also observed by Kumar [201]. Moreover, positive correlation strength was noted for the fluence and the pulse energy, see Table 5-10. A lower correlation was noted between the diameter increase and the energy density (e), laser power (a) and percentage overlap (c). The low correlation of the energy density can be understood as the energy density is a function of the scanning speed and that the processed depth decreases as the scanning rate increases [201,202]. From the presentation of the experimental data in RSM graphs, Figure 5-20, the interaction effect of the laser beam power and the frequency for different percentage overlaps, it can be concluded that the higher increase in diameter were achieved when lower levels of PRF values was used with moderate or higher power levels. The application of a high laser power in conjunction with low PRF value would result in a



larger amount of molten material, due to the higher average power and pulse energy. Moreover, the negative overlaps produced more re-solidification build-up and overall diameter increase, in comparison with the positive overlap processing. This may be due to a smoothing of the previous molten scanned layer by the subsequent scan. From Figure 5-20 (c), at a power level of 400W and PRF of 100 Hz, the melt pool could be expected to be large, for both the current and the previous scans. However, the diameter increase was only 0.8 mm, sample no. 10 in Figure 5-18. When the frequency was increased to 200 Hz, the pulse energy would be reduced from 2 to 1 J, and similarly the pulse width reduced from 5 to 2.5 ms. A reduction in the melt pool size resulted, and less material removal by the gas jet, thus an increase in the micro texture thickness of up to 0.95 mm was noted, see sample no. 27 in Figure 5-18. The same scenario is repeated when moving to the highest frequency value, 300 Hz, the reduction in the pulse energy and the melt pool size is continued. A reduction in micro-texture thickness of 0.85 mm would be resulted this time due to the smaller melt pool size, not material jetting, which is caused by the smaller amount of thermal energy delivered, see sample no. 15.

Figure 4-13 show samples produced with the same laser power and PRF, but with differing percentage overlap as in the corresponding Table 4-7. The 0% and 20% overlap samples exhibit a spiral patterning, visible to the naked eye, which can be seen in the photographic, SEM, and 3d microscope images, while no such pattern is seen for the negative overlap value. From the 3d microscope data the average peak-to-peak widths and peak-to-valley heights can be determined. For the 0% overlap, an average width and height of 1.6 mm and 165  $\mu\text{m}$ , respectively was found. For the 20% overlap, an average width and height of 1.3 mm and 180  $\mu\text{m}$ , respectively was found.

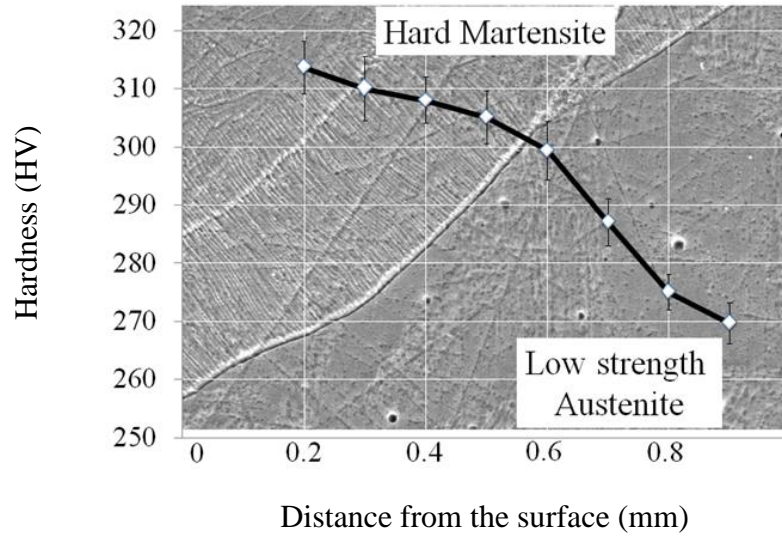
## **6.9 Metallographic test results**

The micrograph images in Figure 6-4 show acceptable results that agree with the modelled data. Figures 4-7 (a) and (b) shows an almost same scale reduction in all dimensions compared to the modelled data and the results in Figure 4-8 as well. This could be explained by the location of the section cut which passes through the first portion of the melted zone where the material is still under heating, and the temperature

is building up. In Figure 4-8 (c), the maximum captured melt depth was found to be 70  $\mu\text{m}$  where the gap width is 100  $\mu\text{m}$ . Compared to the modelled melt depth value of 78  $\mu\text{m}$ , both results are confidentially matches and acceptable. The 8  $\mu\text{m}$  difference between the experimental and the modelled melt depth could be neglected and may be explained by the assumption of ignoring the heat loss to the surrounding which is adopted in the mathematical model.

#### **6.10 The insertion and pull-out test**

It was shown in the results chapter that the joint bond and the pull-out force is mainly a function of the resulting mechanical properties of the modified surface more than that of the diameter increase or the material interfering volume. The modified surface hardness has the most significant effect on the insertion and pull-out forces due to the reduction in the fretting of the surface texture occurring during the insertion of the pin. It was also noted that the samples exhibit higher levels of surface hardness ( $>370$  HV) have small joint bond and fail in small values of removal force due to the brittle surface texture. In contrast, the higher grip and joint bond was found to be in the samples with high interfering volume but also small improvement in the surface hardness as can be seen in the following Table 6-2. For example, samples no. 9, 10, 16 and 24 show high joint strength which is related to the larger areas of the hard martensite ( $<340$  HV) compared to the soft ferrite ( $\alpha$ ), see Figure 5-5 and Figure 6-9 below.



**Figure 6-9** Shows the surface hardness profile and the hard martensite of sample no. 9

Table 6-2 lists the samples from Table 4-12 with the calculated insertion, pull-out forces, the material interfering volume and the surface micro-hardness. The samples in this table are listed according to the pull-out force in an ascendant manner for convenient comparison.

**Table 6-2** Lists the processed samples with their related forces, interfering volume and surface hardness.

Sample No.	Insertion force (kN)	Pull-out force (kN)	Material interfering volume (mm <sup>3</sup> )	Average surface hardness (HV)
15	13.41	0.17	36.54	347.33
21	13.48	0.33	66.32	343.33
1	10.28	0.36	83.74	344.66
11	21.94	0.62	72.11	349.67
20	15.40	0.64	61.02	344.67
27	17.21	1.15	74.95	332.00
17	18.81	1.22	70.3	347.33
22	10.24	1.47	36.72	344.67
23	19.36	1.47	36.76	343.67
3	19.22	1.57	75.28	342.26
19	17.98	1.64	55.42	346.67
14	20.45	1.68	77.78	334.00
4	14.78	1.72	39.42	258.00
25	24.68	1.87	53.76	338.67
8	20.65	2.20	92.11	243.67
7	24.21	2.49	93.6	324.67
5	15.04	3.10	47.64	344.33
2	33.03	3.14	96.2	343.67
6	41.82	3.70	77.25	324.33
26	32.30	4.74	57.87	323.67
18	37.01	4.80	78.62	314.00
13	39.21	5.50	88.8	333.00
12	47.10	5.52	72.67	297.33
10	34.61	5.63	59.69	313.33
16	42.84	5.84	38.65	306.67
24	40.49	6.66	56.88	322.33
9	48.19	7.51	88.38	313.67

As explained in the previous chapters, the surface hardness is a function of the amount of the thermal energy delivered and the time this energy was applied. These two terms control the heating/cooling rates as shown in section 5.17.2. The following Table 6-3 lists the related processing parameters, the calculated heating/cooling rates, and the resulting surface hardness.

**Table 6-3** Lists the surface hardness and the corresponding heating and cooling rates for sample no. 9 and 15.

Sample No.	Pulse energy (J)	Fluence ( $\text{J}/\text{mm}^2$ )	Residence time (ms)	Pulse width (ms)	Heating rate ( $^{\circ}\text{C}/\text{s}$ )	Cooling rate ( $^{\circ}\text{C}/\text{s}$ )	Surfaces Hardness (HV)
9	2.0	56.66	4.0	5	$8.5 \times 10^5$	$8 \times 10^5$	313.67
15	0.67	18.89	2.0	1.6	$2.2 \times 10^6$	$2 \times 10^6$	347.33

### 6.11 Corrosion test

The reduction in corrosion resistance is caused by the formation of the chromium carbide  $\text{Cr}_{23}\text{C}_6$  and chromium nitride, which precipitate on the grain boundaries and act as electrolytic cells [9]. This phenomenon is known as sensitization and it occurs when heating the ferritic and austenitic stainless steels to elevated temperature more than  $800^{\circ}\text{C}$ , i.e. welding. The reaction happens at around  $650^{\circ}\text{C}$  when the carbon rapidly tends to react with chromium. Due to this reaction and the formation of the chromium carbide, the material loses corrosion resistance along the grain boundaries because of the reduction in the free chromium.

## 6.12 Conclusions

In this study, a high-speed CO<sub>2</sub> laser surface treatment was successfully carried out on 316L SST cylindrical samples to produce highly controlled surface texture with pre-defined texture pattern, diameter increase, microstructure and mechanical properties. The study is suggesting that the produced samples can fit the application of the interference fit (press-fit) which is widely used in machinery, aerospace and automotive industry. A comprehensive preliminary test was performed in order to identify the most significant laser processing parameters and their useful ranges. From this test, it was found that three parameters have a direct effect on the outcome responses; these parameters are the main laser beam power (W), the pulse repetition frequency (PRF) (Hz) and the percentage overlapping scanning tracks. Other parameters which show less significance were kept constants on the values that show the best effect on the results gained from this test. Such parameters like the laser beam focal position and the assist gas pressure. A full 3<sup>3</sup> DoE model was built and repeated in three experiments in order to optimize the process factors and results value.

The produced samples were tested and characterized as in the following categories:

- **Surface morphology:** measurements of the surface roughness, surface texture pattern and the increase in diameter.
- **Microstructure:** samples were sectioned and prepared for the SEM, and EDX tests in order to investigate the modified layer properties phase and grain size and orientation changes in addition to the chemical composition investigation.
- **Residual stresses and surface micro-hardness:** the cross sectioned samples were also tested for these terms in order to understand the effect of the laser process and correlate these measurements and parameters with the following insertion and pull-out tests as the end point application.
- **Corrosion test:** this test was carried out by using a polarization electrolyte cell and the test was performed using NaCl solution. The test results specified that the metal surface exhibits degradation in the corrosion resistance due to the melting and re-solidification process which disrupts the distribution of the free chromium.

- ***Insertion and pull-out test:*** the force values were calculated and explained with reference to the laser processing parameters. It was found that the force value is directly affected by the frequency, which in turn effect the resulting surface hardness. Despite the fact that austenitic stainless steels are difficult to be hardened by heat treatment and that the only way to increase surface hardness is by cold work but the small increase in hardness make the textured surface very brittle.
- ***The interfering volume:*** is not always an indication of good bonding but the small increase in the surface hardness reduces the fretting of the texture and maintain good friction and bond between the mating parts.
- ***The fatigue test:*** The bond joint was found to re-grip at high force levels after initial failure, providing more secure joint and increased safety.

This is an open topic of research and the results explored and shown in the previous chapters represent the basis of the technique. The interference fit joint strengths were related to the processing parameters used. Different and improved results can be obtained for more specific application by altering the process parameters. For example, changing the laser beam focus size to find different levels of power irradiance or a better control on the melt pool dimensions. Another suggestion for improvement is the machining of the hub ring hole to a higher finishing and diameter accuracy, for example, grinding and polishing the inner diameter to the final dimension. This will reduce the error of  $\pm 1.5$  micron on the hole radius produce after the reamer machining. The later operation will of course add more cost and time but it will provide a better understanding on the joint strength and control on the interfering volume. Although, the small error bars on the insertion force graph of sample no. 9 suggest an acceptable error at this stage, see Figure 5-22 (b), reducing the tolerance on the hole diameter would be expected to reduce the pull-out force error bars even further. The differences in interfering volume for sample no. 9 due to this error was calculated and found to be approximately 0.3% of the average interfering volume for either of the two error limits. The author repeated this test; the DoE set of samples were repeated three times and the samples with interesting and important results were repeated several times in order to

investigate the other mechanical and metallurgy tests. A high level of result reproducibility always resulted.

This joining method allows for the possibility of joining different materials. Also, the new technique can be applied on parts with different sections and geometry and must efficiently save material and labour when the bearing is set on specific sections. This method avoids manufacturing the mechanical parts in bigger diameters and then machining them into different sections. Moreover, the application of other types of assist gas may improve the mechanical and chemical properties of the product. In this study, although the employment of nitrogen gas enhanced the surface hardness on some samples, a decrease in the corrosion resistance was also suggested in one case. This reduction might not be an essential obstacle when working in a non-corrosive environment or an anti-corrosion sealant can be used to cover the exposed area. Also, stainless steel with lower carbon content can be used to reduce the formation of the chromium carbide.

The cost of manufacturing is competitive to commercial and conventional methods. Table 6-4 lists the cost of the main factors affecting the manufacture per piece with a comparison to the cost of a commercial insertion available on shelf. An arrangement for mass production must positively affect the total cost.

**Table 6-4** Manufacturing cost estimate for the laser surface textured interference fit pin.

Item	QTY/Units	Cost estimate (€)
Material (Stainless Steel 316L $\Phi$ 10 mm bars)	30 grams	0.08
CO <sub>2</sub> Laser Gas Consumption	< 0.15 l/hr	0.002
Labour (Cutting + Lasing + Preparation)	-	0.5
Total (cost/pin insertion)	1	< 0.6
Cost for a similar commercial pin insertion = 8 €/pin (in a 100 pc container)		



## References

---

- [1] M. v. Allmen, A. Blatter, Laser-beam interactions with materials: physical principles and applications, Springer Science & Business Media, 2013.
- [2] J. Hecht, The laser guidebook, McGraw-Hill Professional, 1986.
- [3] W. Ryba-Romanowski, R. Lisiecki, H. Jelinková, J. Šulc, Thulium-doped vanadate crystals: Growth, spectroscopy and laser performance, Prog. Quantum Electron. 35 (2011) 109–157.
- [4] M. Kalyon, B.S. Yilbas, Laser pulse heating: A formulation of desired temperature at the surface, Opt. Lasers Eng. 39 (2003) 109–119. doi:10.1016/S0143-8166(02)00088-X.
- [5] E.K. Jr, MATERIALS PROCESSING PRINCIPLES OF LASER, n.d.
- [6] W.M. Steen, J. Mazumdar, Laser Material Processing, 4th ed., Springer-Verlag London Ltd, London, 2010.
- [7] E. Chryssolouris, Laser machining: theory and practice, Springer Science & Business Media, 2013.
- [8] N.B. Dahotre, S. Harimkar, Laser fabrication and machining of materials, Springer Science & Business Media, 2008.
- [9] E. Kannatey-Asibu, Principles of Laser Materials Processing, 2009. <http://www3.interscience.wiley.com/cgi-bin/bookhome/121427953/>.
- [10] J. Elijah Kannatey-Asibu, Materials Processing Principles of Laser, 2009.
- [11] W. Duley, CO<sub>2</sub> lasers effects and applications, Elsevier, 2012.
- [12] I. Coherent, Lasers Operation, Equipment, Application and Design, (1980).
- [13] J. Dutta Majumdar, I. Manna, Laser processing of materials, Sadhana. 28 (2003) 495–562. doi:10.1007/BF02706446.
- [14] A.J. Pinkerton, L. Li, An investigation of the effect of pulse frequency in laser multiple-layer cladding of stainless steel, Appl. Surf. Sci. 208–209 (2003) 405–410. doi:10.1016/S0169-4332(02)01420-4.
- [15] A. Hamasaiid, G. Dour, T. Loulou, M.S. Dargusch, A predictive model for the evolution of the thermal conductance at the casting–die interfaces in high pressure die casting, Int. J. Therm. Sci. 49 (2010) 365–372.

- [16] T. Nagai, Relationship between the Cooling Rate and the Formation of Chilled Microstructure for Laser Melting of Cast Iron-Laser Surface Modification of Case Iron Aimed at Refining the Wear Resistance (Report1), *Quar.J.JWS.* 21 (2003) 466–473.
- [17] H.L. Tsai, P.C. Tsai, Performance of laser-glazed plasma-sprayed (ZrO<sub>2</sub>-12wt.% Y<sub>2</sub>O<sub>3</sub>)/(Ni-22wt.% Cr-10wt.% Al-1wt.% Y) thermal barrier coatings in cyclic oxidation tests, *Surf. Coatings Technol.* 71 (1995) 53–59.
- [18] J.F. Ready, *Industrial Applications of Lasers*, 1997. doi:10.1016/B978-012583961-7/50016-8.
- [19] B.S. Yilbas, S.Z. Shuja, M. Sami, Pulsed laser heating of steel surfaces—Fourier and electron kinetic theory approaches, *Int. Commun. Heat Mass Transf.* 25 (1998) 843–852.
- [20] J.S. Selvan, K. Subramanian, A.K. Nath, Effect of laser surface hardening on En18 (AISI 5135) steel, *J. Mater. Process. Technol.* 91 (1999) 29–36.
- [21] W.M. Steen, *Laser Material processing*, 3rd ed., Ed. Springer Verlag, 2003.
- [22] P.A.A. Khan, T. Debroy, Absorption of CO<sub>2</sub> laser beam by AISI 4340 steel, *Metall. Mater. Trans. B.* 16 (1985) 853–856.
- [23] C.-P. Fung, K.-P. Peng, J.-L. Doong, Study of surface temperature on laser cutting and welding power absorption, *Int. Commun. Heat Mass Transf.* 17 (1990) 147–154.
- [24] H.A. Eltawahni, A.G. Olabi, K.Y. Benyounis, Investigating the CO<sub>2</sub> laser cutting parameters of MDF wood composite material, *Opt. Laser Technol.* 43 (2011) 648–659. doi:10.1016/j.optlastec.2010.09.006.
- [25] T. Mahank, *Laser Glazing of Metals and Metallic and Ceramic Coatings*, Pennsylvania State University, 2004.
- [26] D. Bergström, J. Powell, A.F.H. Kaplan, The absorptance of steels to Nd: YLF and Nd: YAG laser light at room temperature, *Appl. Surf. Sci.* 253 (2007) 5017–5028.
- [27] Y.-C. Chuang, S.-C. Lee, H.-C. Lin, Effect of temperature on the sliding wear behavior of laser surface alloyed Ni-base on Al–Mg–Si alloy, *Appl. Surf. Sci.* 253 (2006) 1404–1410.

- [28] D. Kuo, S.D. Vierk, G. Rauch, S.R. Media, Laser Zone Texturing, 33 (1997) 944–949.
- [29] T.D. Bennett, D.J. Krajnovich, L. Li, D. Wan, Mechanism of topography formation during CO<sub>2</sub> laser texturing of silicate glasses, J. Appl. Phys. 84 (1998) 2897–2905.
- [30] M. Watanabe, Y. Kuroiwa, S. Ito, Study of femtosecond laser ablation of multicomponent glass, Reports Res. Lab. Asahi Glas. 55 (2005) 27–31.
- [31] B.S. Yilbas, M. Kalyon, Analytical solution for multilayer assembly including heating and cooling cycles with laser pulse parameter variation, Opt. Lasers Eng. 44 (2006) 1219–1234.
- [32] S. Safdar, L. Li, M.A. Sheikh, Numerical analysis of the effects of non-conventional laser beam geometries during laser melting of metallic materials, J. Phys. D. Appl. Phys. 40 (2007) 593.
- [33] A.N. Samant, N.B. Dahotre, Computational prediction of grain size during rapid laser surface modification of Al–O ceramic, Phys. Status Solidi (RRL)-Rapid Res. Lett. 1 (2007) R4–R6.
- [34] A.S.M.H. Volume, 16: Machining (1995), ASM Int. Met. Park. Ohio, USA. (n.d.).
- [35] J.T. Black, “Machining” in ASM Handbook, 9th Edition, ASM-International, Ohio, USA, 1997.
- [36] J. Ion, Laser processing of engineering materials: principles, procedure and industrial application, Butterworth-Heinemann, 2005.
- [37] J.R. Davis, ASM specialty handbook: heat-resistant materials, Asm International, 1997.
- [38] A. Issa, COMPUTATIONAL CONTROL OF LASER SYSTEMS FOR MICRO-MACHINING, Dublin City University, 2007.
- [39] W.J. Suder, S.W. Williams, Investigation of the effects of basic laser material interaction parameters in laser welding, J. Laser Appl. 24 (2012) 32009.
- [40] A. Stournaras, P. Stavropoulos, K. Salonitis, G. Chryssolouris, An investigation of quality in CO<sub>2</sub> laser cutting of aluminum, CIRP J. Manuf. Sci. Technol. 2 (2009) 61–69. doi:10.1016/j.cirpj.2009.08.005.

- [41] I.A. Choudhury, S. Shirley, Laser cutting of polymeric materials: An experimental investigation, *Opt. Laser Technol.* 42 (2010) 503–508. doi:10.1016/j.optlastec.2009.09.006.
- [42] H.A. Eltawahni, M. Hagino, K.Y. Benyounis, T. Inoue, A.G. Olabi, Effect of CO<sub>2</sub> laser cutting process parameters on edge quality and operating cost of AISI316L, *Opt. Laser Technol.* 44 (2012) 1068–1082. doi:10.1016/j.optlastec.2011.10.008.
- [43] P.R. Herman, H. Higaki, E. Rouillon, R.S. Marjoribanks, Ponderomotive-driven “acceleration” of etch rates for short-pulse laser micromachining of transparent glasses, in: *Lasers Electro-Optics, 1998. CLEO 98. Tech. Dig. Summ. Pap. Present. Conf., IEEE, 1998*: pp. 524–525.
- [44] C.B. Schaffer, A. Brodeur, E. Mazur, Laser-induced breakdown and damage in bulk transparent materials induced by tightly focused femtosecond laser pulses, *Meas. Sci. Technol.* 12 (2001) 1784.
- [45] C.B. Schaffer, J.F. García, E. Mazur, Bulk heating of transparent materials using a high-repetition-rate femtosecond laser, *Appl. Phys. A* 76 (2003) 351–354.
- [46] L. Li, R. Eghlio, S. Marimuthu, Laser net shape welding, *CIRP Ann. - Manuf. Technol.* 60 (2011) 223–226. doi:10.1016/j.cirp.2011.03.066.
- [47] P.R. Herman, K.P. Chen, P. Corkum, A. Naumov, S. Ng, J. Zhang, Advanced lasers for photonic device microfabrication, *RIKEN Rev.* (2001) 31–35.
- [48] D. V Tran, H.Y. Zheng, Y.C. Lam, V.M. Murukeshan, Femtosecond laser-induced damage morphologies of crystalline silicon by sub-threshold pulses, 43 (2005) 977–986. doi:10.1016/j.optlaseng.2004.10.006.
- [49] X. Liu, D. Du, G. Mourou, Laser Ablation and Micromachining with Ultrashort Laser Pulses, 33 (1997) 1706–1716.
- [50] D. Homoelle, S. Wielandy, A.L. Gaeta, N.F. Borrelli, C. Smith, Infrared photosensitivity in silica glasses exposed to femtosecond laser pulses, *Opt. Lett.* 24 (1999) 1311–1313.
- [51] L. Quintino, A. Costa, R. Miranda, D. Yapp, V. Kumar, C.J. Kong, Welding with high power fiber lasers—a preliminary study, *Mater. Des.* 28 (2007) 1231–1237.
- [52] E. Brandl, F. Palm, V. Michailov, B. Viehweger, C. Leyens, Mechanical

- properties of additive manufactured titanium (Ti–6Al–4V) blocks deposited by a solid-state laser and wire, *Mater. Des.* 32 (2011) 4665–4675.
- [53] S.N. Aqida, S. Ahmad, *Laser Surface Modification of Steel*, DUBLIN CITY UNIVERSITY Dr, 2011.
  - [54] A. Basu, J. Chakraborty, S.M. Shariff, G. Padmanabham, S. V Joshi, G. Sundararajan, J.D. Majumdar, I. Manna, Laser surface hardening of austempered (bainitic) ball bearing steel, *Scr. Mater.* 56 (2007) 887–890.
  - [55] C. Batista, A. Portinha, R.M. Ribeiro, V. Teixeira, M.F. Costa, C.R. Oliveira, Surface laser-glazing of plasma-sprayed thermal barrier coatings, *Appl. Surf. Sci.* 247 (2005) 313–319.
  - [56] H.J. Shin, Y.T. Yoo, Microstructural and hardness investigation of hot-work tool steels by laser surface treatment, *J. Mater. Process. Technol.* 201 (2008) 342–347.
  - [57] D. Du, Y.F. He, B. Sui, L.J. Xiong, H. Zhang, Laser texturing of rollers by pulsed Nd: YAG laser, *J. Mater. Process. Technol.* 161 (2005) 456–461.
  - [58] E. V Bordatchev, S.K. Nikumb, Effect of focus position on informational properties of acoustic emission generated by laser–material interactions, *Appl. Surf. Sci.* 253 (2006) 1122–1129.
  - [59] L.E.E. Jae-Ho, J. Jeong-Hwan, J.O.O. Byeong-Don, S.O.N. Young-Myung, M. Young-Hoon, Laser surface hardening of AISI H13 tool steel, *Trans. Nonferrous Met. Soc. China.* 19 (2009) 917–920.
  - [60] J.F. Ready, *Effects of high-power laser radiation*, Academic press, INC (London) Ltd, New York, London, 1971.
  - [61] R. Singh, A. Kurella, N.B. Dahotre, Laser surface modification of Ti–6Al–4V: wear and corrosion characterization in simulated biofluid, *J. Biomater. Appl.* 21 (2006) 49–73. doi:0885328206055998 [pii].
  - [62] F. Audebert, R. Colaco, R. Vilar, H. Sirkin, Production of glassy metallic layers by laser surface treatment, *Scr. Mater.* 48 (2003) 281–286.
  - [63] T.M. Yue, T.M. Cheung, H.C. Man, The effects of laser surface treatment on the corrosion properties of Ti-6Al-4V alloy in Hank’s solution, *J. Mater. Sci. Lett.* 19 (2000) 205–208.

- [64] N. Zaveri, M. Mahapatra, A. Deceuster, Y. Peng, L. Li, A. Zhou, Corrosion resistance of pulsed laser-treated Ti–6Al–4V implant in simulated biofluids, *Electrochim. Acta.* 53 (2008) 5022–5032.
- [65] Z. Sun, I. Annergren, D. Pan, T.A. Mai, Effect of laser surface remelting on the corrosion behavior of commercially pure titanium sheet, *Mater. Sci. Eng. A.* 345 (2003) 293–300.
- [66] E. Teoman, D.L. Church, *General Laser MicroMachining Principles*, (2003).
- [67] A. Astarita, S. Genna, C. Leone, F.M.C. Minutolo, A. Squillace, C. Velotti, Study of the laser marking process of cold sprayed titanium coatings on aluminium substrates, *Opt. Laser Technol.* 83 (2016) 168–176.
- [68] S. Dadbin, Surface modification of LDPE film by CO<sub>2</sub> pulsed laser irradiation, *Eur. Polym. J.* 38 (2002) 2489–2495.
- [69] C.N. Panagopoulos, A.E. Markaki, P.E. Agathocleous, Excimer laser treatment of nickel-coated cast iron, *Mater. Sci. Eng. A.* 241 (1998) 226–232.
- [70] S. Steel, *The Pocket Guide To Stainless Steel*, (n.d.).
- [71] Outokumpu, *Handbook of Stainless Steel*, (2013) 1–89.
- [72] AK Steel Corporation, Product Data Sheet: Stainless Steel 316/316L, AK Steel. (2007) 2. doi:10.1016/B978-0-444-89875-3.50030-2.
- [73] Euro Inox, Technical table stainless steel type 304L, 5 (2010).
- [74] E. December, *Carbon Steel Handbook*, 3 (2006).
- [75] W.D. Callister, D.G. Rethwisch, *Materials science and engineering: an introduction*, Wiley New York, 2007.
- [76] D.R. Lesuer, C.K. Syn, O.D. Sherby, Nano-scale strengthening from grains, subgrains, and particles in Fe-based alloys, *J. Mater. Sci.* 45 (2010) 4889–4894.
- [77] Y.Y. Lim, M.M. Chaudhri, The influence of grain size on the indentation hardness of high-purity copper and aluminium, *Philos. Mag. A.* 82 (2002) 2071–2080.
- [78] M.Y. Liu, B. Shi, C. Wang, S.K. Ji, X. Cai, H.W. Song, Normal Hall–Petch behavior of mild steel with submicron grains, *Mater. Lett.* 57 (2003) 2798–2802.
- [79] K. Hiroshi, T. Makoto, I. Kenji, Nanoindentation Hardness Test for Estimation of Vickers Hardness  $H_V$ , 35 (2006) 57–61.

- [80] J.D. Bronzino, Biomedical engineering handbook, CRC press, 1999.
- [81] M. William, Laser Material Processing.pdf, Springer-Verlag, Berlin, 1991.
- [82] W. Jiang, P. Molian, Nanocrystalline TiC powder alloying and glazing of H13 steel using a CO<sub>2</sub> laser for improved life of die-casting dies, *Surf. Coatings Technol.* 135 (2001) 139–149.
- [83] L.M. Cabalin, D. Romero, J.M. Baena, J.J. Laserna, Effect of surface topography in the characterization of stainless steel using laser-induced breakdown spectrometry, *Surf. Interface Anal.* 27 (1999) 805–810.
- [84] T. Li, Q. Lou, J. Dong, Y. Wei, J. Liu, Modified surface morphology in surface ablation of cobalt-cemented tungsten carbide with pulsed UV laser radiation, *Appl. Surf. Sci.* 172 (2001) 331–344.
- [85] A.J. Pinkerton, L. Li, The effect of laser pulse width on multiple-layer 316L steel clad microstructure and surface finish, *Appl. Surf. Sci.* 208 (2003) 411–416.
- [86] S. V Joshi, G. Sundararajan, Lasers for metallic and intermetallic coatings, ASM Int. Member/Customer Serv. Center, Mater. Park. OH 44073-0002, USA, 1998. (1998) 121–177.
- [87] R.F. Duhamel, C.M. Banas, R.L. Kosenski, Production laser hardfacing of jet engine turbine blades, in: OE/LASE'86 Symp (January 1986, Los Angeles), International Society for Optics and Photonics, 1986: pp. 31–39.
- [88] Y. Wang, H.M. Wang, Wear resistance of laser clad Ti-2Ni-3Si reinforced intermetallic composite coatings on titanium alloy, *Appl. Surf. Sci.* 229 (2004) 81–86.
- [89] D. Hosson, D.T.A. Matthews, V. Ocel, Tribological and mechanical properties of high power laser surface-treated metallic glasses, *Mater. Sci. Eng.* (2007). doi:10.1016/j.msea.2007.02.119.
- [90] Y.S. Tian, C.Z. Chen, S.T. Li, Q.H. Huo, Research progress on laser surface modification of titanium alloys, *Appl. Surf. Sci.* 242 (2005) 177–184.
- [91] L. Jianglong, L. Qiquan, Z. Zhirong, Laser gas alloying of titanium alloy with nitrogen, *Surf. Coatings Technol.* 57 (1993) 191–195.
- [92] H. Chmelickova, L. Kucharicova, J. Grezl, Powder alloying of low-carbon steel by CO<sub>2</sub> laser, *Laser Phys.* 8 (1998) 349–351.

- [93] O. de O.D. Neto, R.M.S. Vilar, Interaction between the laser beam and the powder jet in blown powder laser alloying and cladding, in: Proc. Laser Mater. Process. Conf. ICALEO, 1998: pp. 180–189.
- [94] E. Eiholzer, C. Cusano, J. Mazumder, Wear properties of laser alloyed Fe–Cr–Mn–C alloys, ICALEO’85 Proc. (1985).
- [95] W.J. Gavigan, C.L. Snyder, F.J. Tufano, R.S. Miller, Laser nitriding of the surface layer of Ti6Al4V titanium alloy, Shaft Laser Nitride-Hardened Surf. Titan. (1994).
- [96] K. Zeng, D. Pal, B. Stucker, A review of thermal analysis methods in laser sintering and selective laser melting, 23rd Annu. Int. Solid Free. Fabr. Symp. - An Addit. Manuf. Conf. SFF 2012. (2012) 796–814.  
<http://www.scopus.com/inward/record.url?eid=2-s2.0-84893079154&partnerID=tZOtx3y1>.
- [97] W.J. Gavigan, C.L. Snyder, F.J. Tufano, R.S. Miller, Shaft of Laser Nitrided-Hardened Surface of Titanium., Shaft Laser Nitride-Hardened Surf. Titan. (1994).
- [98] W.J. Gavigan, C.L. Snyder, F.J. Tufano, R.S. Miller, Laser surface melting and alloying of titanium, Shaft Laser Nitride-Hardened Surf. Titan. (1994).
- [99] H.W. Bergmann, Laser surface melting of iron-base alloys, in: Springer, 1986: pp. 351–368.
- [100] J.D. Majumdar, I. Manna, Laser-assisted fabrication of materials, Springer Science & Business Media, 2012.
- [101] W.W. Duley, Excimer laser etching of organic polymers, Laser Adv. Manuf. Process. (LAMP’87), Osaka, Japan. High Temp. Soc. Japan, Pap. 7A02. (1987) 585–594.
- [102] W.W. Duley, UV Lasers: effects and applications in materials science, Cambridge University Press, 2005.
- [103] R. Poprawe, Tailored Light 2 Laser Application Technology, Aachen, 2011.
- [104] S. Marimuthu, A. Triantaphyllou, M. Antar, D. Wimpenny, H. Morton, M. Beard, Laser polishing of selective laser melted components, Int. J. Mach. Tools Manuf. 95 (2015) 97–104. doi:10.1016/j.ijmachtools.2015.05.002.



- [105] L. Giorleo, E. Ceretti, C. Giardini, Ti Surface Laser Polishing: Effect of Laser Path and Assist Gas, *Procedia CIRP*. 33 (2015) 446–451. doi:10.1016/j.procir.2015.06.102.
- [106] J. Kumstel, B. Kirsch, Polishing titanium- and nickel-based alloys using cw-laser radiation, *Phys. Procedia*. 41 (2013) 362–371. doi:10.1016/j.phpro.2013.03.089.
- [107] R. Ostholt, E. Willenborg, K. Wissenbach, Laser polishing of freeform surfaces, in: *Proc. 5th Int. WLT-Conference Lasers Manuf.*, 2009: pp. 397–402.
- [108] T. Kiedrowski, *Oberflächenstrukturbildung beim Laserstrahlpolieren von Stahlwerkstoffen*, Shaker, 2009.
- [109] P. Schaaf, Laser nitriding of metals, *Prog. Mater. Sci.* 47 (2002) 1–161. doi:10.1016/S0079-6425(00)00003-7.
- [110] S. Becker, *VDI-Lexikon Werkstofftechnik, berichtigter Nachdruck*, hrsg. von Hubert Gräfen, 1172 Seiten, 977 Bilder, 188 Tabellen, VDI-Verlag Düsseldorf 1993, 278,-DM, ISBN 3-18-400893-2, *Mater. Corros.* 46 (1995) 388.
- [111] R. Canh, P. Haasen, *Physical Metallurgy 3rd revised and enlarged edition*, (1983).
- [112] D. Pye, *Practical nitriding and ferritic nitrocarburizing*, ASM international, 2003.
- [113] D. Pye, *Practical NITRIDING and Ferritic Nitrocarburizing*, 2003.
- [114] A. Zhecheva, W. Sha, S. Malinov, A. Long, Enhancing the microstructure and properties of titanium alloys through nitriding and other surface engineering methods, *Surf. Coatings Technol.* 200 (2005) 2192–2207.
- [115] C.A. Keyser, *Basic engineering metallurgy: theories, principles, and applications*, Prentice-Hall, 1959.
- [116] S. Katayama, A. Matsunawa, Y. Arata, A. Morimoto, S. Ishimoto, Surface hardening of titanium by laser nitriding, in: *Metall. Soc. AIME, Annu. Meet. Los Angeles, CA*, 1984.
- [117] B.H. Amstead, P.F. Ostwald, M.L. Begeman, *Manufacturing Processes.*, John Wiley Sons, Xii 739, 24 X 17 C. Illus. 1977. (1977).
- [118] E.P. DeGarmo, J.T. Black, R.A. Kohser, B.E. Klamecki, *Materials and process in manufacturing*, Prentice Hall, 1997.
- [119] H. Lavvafi, M.E. Lewandowski, D. Schwam, J.J. Lewandowski, *Effects of*

- surface laser treatments on microstructure, tension, and fatigue behavior of AISI 316LVM biomedical wires, *Mater. Sci. Eng. A.* 688 (2017) 101–113.
- [120] *Laser Processing and Chemistry*, n.d.
- [121] P. Schaaf, Laser nitriding of metals, 47 (2002) 3–7.
- [122] M.S. Trtica, V.F. Tarasenko, B.M. Gaković, A. V. Fedenev, L.T. Petkovska, B.B. Radak, E.I. Lipatov, M.A. Shulepov, Surface modifications of TiN coating by pulsed TEA CO<sub>2</sub> and XeCl lasers, *Appl. Surf. Sci.* 252 (2005) 474–482. doi:10.1016/j.apsusc.2005.01.029.
- [123] P.P. Psyllaki, A. Griniari, D.I. Pantelis, Parametric study on laser nitriding of 1.5919 steel, *J. Mater. Process. Technol.* 195 (2008) 299–304. doi:10.1016/j.jmatprotec.2007.05.023.
- [124] E. Carpena, P. Schaaf, Laser nitriding of iron and aluminum, *Appl. Surf. Sci.* 186 (2002) 100–104. doi:10.1016/S0169-4332(01)00596-7.
- [125] F.M. Shuaib, K.Y. Benyounis, *Advances in Laser Nitriding Methods and Apparatus for Metals and Alloys*, *Ref. Modul. Mater. Sci. Mater. Eng.* (2016) 1–20. doi:10.1016/B978-0-12-803581-8.04021-2.
- [126] H. Yu, F. Sun, J. Zhang, Laser and plasma nitriding of titanium using CW-CO<sub>2</sub> laser in the atmosphere, *Curr. Appl. Phys.* 9 (2009) 227–233. doi:10.1016/j.cap.2008.01.013.
- [127] B.S. Yilbas, *Laser duplex treatment of surfaces for improved properties.*, Elsevier. 9 (2014).
- [128] P. Schaaf, *Laser gas-assisted nitriding of Ti alloys*, Elsevier. (2014).
- [129] M.G. Perez, N.. Harlan, F. Zapirain, F. Zubiri, Laser nitriding of an intermetallic Ti Alalloy with a diode laser., *Surf. Coat. Technol.* 200 (2006) 5152–55159.
- [130] P. Schaaf, F. Landry, K.-P. Lieb, Origin of nitrogen depth profiles after laser nitriding of iron, *Appl. Phys. Lett.* 74 (1999) 153–155.
- [131] S. Mridha, T.N. Baker, Crack-free hard surfaces produced by laser nitriding of commercial purity titanium, *Mater. Sci. Eng. A.* 188 (1994) 229–239.
- [132] F. Sun, J. Liu, Y. Yang, H. Yu, Nitridation of iron by CW-CO<sub>2</sub> laser nitriding technologies, *Mater. Sci. Eng. B Solid-State Mater. Adv. Technol.* 122 (2005) 29–33. doi:10.1016/j.mseb.2005.04.010.

- [133] B.L. Mordike, Laser gas alloying, in: Springer, 1986: pp. 389–412.
- [134] P.H. Morton, T. Bell, A. Weisheit, J. Kroll, B.L. Mordike, K. Sagoo, Laser gas nitriding of titanium and titanium alloys, *Surf. Modif. Technol.* (1991) 593–609.
- [135] T. Bell, H.W. Bergmann, J. Lanagan, P.H. Morton, A.M. Staines, Surface engineering of titanium with nitrogen, *Surf. Eng.* (2013).
- [136] M. Grenier, D. Dube, A. Adnot, M. Fiset, Microstructure and wear resistance of CP titanium laser alloyed with a mixture of reactive gases, *Wear*. 210 (1997) 127–135.
- [137] M.S. Selamat, T.N. Baker, L.M. Watson, Study of the surface layer formed by the laser processing of Ti–6Al–4V alloy in a dilute nitrogen environment, *J. Mater. Process. Technol.* 113 (2001) 509–515.
- [138] H. Xin, L.M. Watson, T.N. Baker, Surface analytical studies of a laser nitrided Ti–6Al–4V alloy: a comparison of spinning and stationary laser beam modes, *Acta Mater.* 46 (1998) 1949–1961.
- [139] W. J., C.D. Lundin, Surface Tension of 304 Stainless Steel under Welding Conditions, 7 (1986) 2226.
- [140] M. Le, F. Ville, X. Kleber, J. Cavoret, M.-C. Sainte-Catherine, L. Briancon, Influence of gas nitriding on rolling contact fatigue: application on alloyed steels for gears, *Tribol. Lubr. Technol.* 71 (2015) 20.
- [141] K.J.B. Ribeiro, R.R.M. de Sousa, F.O. De Araújo, R.A. de Brito, J.C.P. Barbosa, C. Alves, Industrial application of AISI 4340 steels treated in cathodic cage plasma nitriding technique, *Mater. Sci. Eng. A*. 479 (2008) 142–147.
- [142] K. Lin, X. Li, Y. Sun, X. Luo, H. Dong, Active screen plasma nitriding of 316 stainless steel for the application of bipolar plates in proton exchange membrane fuel cells, *Int. J. Hydrogen Energy*. 39 (2014) 21470–21479.
- [143] K.-L. Ou, H.-H. Chou, C.-M. Liu, P.-W. Peng, Surface modification of austenitic stainless steel with plasma nitriding for biomedical applications, *Surf. Coatings Technol.* 206 (2011) 1142–1145.
- [144] R.L. Norton, Machine Design An Integrated Approach No Title, 4th ed., Pearson Education, New Jersey, 2011.
- [145] R.O. Parmley, Standard handbook of fastening and joining, McGraw-Hill

Companies, 1989.

- [146] R.L. Mott, Machine Elements in Mechanical Design, 4th ed., Pearson Prentice Hall, 2004, New Jersey, 2004.
- [147] H. Huyuk, O. Music, A. Koç, C. Karadogan, Ç. Bayram, Analysis of elastic-plastic interference-fit joints, *Procedia Eng.* 81 (2014) 2030–2035.
- [148] J.A. Speck, No Title, n.d.
- [149] P.O.F. Materials, M. Operations, M. Processes, M. Elements, M. Units, Machinery ' s Handbook, n.d.
- [150] Y. Fu, E. Ge, H. Su, J. Xu, R. Li, Cold expansion technology of connection holes in aircraft structures: A review and prospect, *Chinese J. Aeronaut.* 28 (2015) 961–973. doi:10.1016/j.cja.2015.05.006.
- [151] W. Shizhen, L. Cuiyun, W. Ruolin, M. Chaoli, Effect of Cold Expansion on High Cycle Fatigue of 7A85 Aluminum Alloy Straight Lugs, *Rare Met. Mater. Eng.* 44 (2015) 2358–2362. doi:10.1016/S1875-5372(16)30020-0.
- [152] S. Barter, B. Dixon, Investigation using quantitative fractography of an unexpected failure in an F/A-18 centre fuselage bulkhead in the FINAL teardown program, *Eng. Fail. Anal.* 16 (2009) 833–848. doi:10.1016/j.engfailanal.2008.07.008.
- [153] N. Yasavol, a. Abdollah-zadeh, M. Ganjali, S. a. Alidokht, Microstructure and mechanical behavior of pulsed laser surface melted AISI D2 cold work tool steel, *Appl. Surf. Sci.* 265 (2013) 653–662. doi:10.1016/j.apsusc.2012.11.070.
- [154] A. Rosenkranz, L. Reinert, C. Gachot, F. Mücklich, Alignment and wear debris effects between laser-patterned steel surfaces under dry sliding conditions, *Wear.* 318 (2014) 49–61. doi:10.1016/j.wear.2014.06.016.
- [155] D.M. Mattox, Handbook of physical vapor deposition (PVD) processing, William Andrew, 2010.
- [156] D.G. Waugh, J. Lawrence, Laser Surface Engineering: Processes and Applications, (2015).
- [157] R.W. Messler, Joining of materials and structures: from pragmatic process to enabling technology, Butterworth-Heinemann, 2004.
- [158] V.M. Faires, Design of machine elements, Macmillan Coll Div, 1965.

- [159] E. Oberg, F.D. Jones, H.L. Horton, H.H. Ryffel, J.H. Geronimo, Machinery's handbook, Industrial Press New York, 2004.
- [160] K.H. Berdolt, Method of forming interference fits by heat treatment, Method Form. Interf. Fits by Heat Treat. (1971).
- [161] U.C. Jindal, Machine design, Pearson Education India, 2010.
- [162] D.A. Madsen, D.P. Madsen, Engineering drawing and design, Nelson Education, 2016.
- [163] Hilti X-BT Threaded Fastener Specification, (2010).
- [164] J.F. Ready, D.F. Farson, LIA handbook of laser materials processing, Laser Institute of America Orlando, 2001.
- [165] Synrad, (n.d.). <http://www.synrad.com/Products/marketing.htm> (accessed March 9, 2017).
- [166] Rofin-Sinar Laser, (n.d.). <http://www.rofin.com/en/applications/laser-cutting/stainless-steel> (accessed March 9, 2017).
- [167] P. Schmutz, N.-C. Quach-Vu, I. Gerber, Metallic medical implants: electrochemical characterization of corrosion processes, Electrochem. Soc. Interface. 17 (2008) 35.
- [168] E. Klar, P.K. Samal, Powder metallurgy stainless steels: processing, microstructures, and properties, ASM international, 2007.
- [169] A to Z of Material Website, Stainless Steel - Grade 316L - Properties, Fabrication and applications, (2008). <http://www.azom.com/details.asp?ArticleID=2382> (accessed April 28, 2017).
- [170] E. Chikarakara, LASER SURFACE MODIFICATION OF BIOMEDICAL ALLOYS, Dublin City University, 2012.
- [171] P.A. Dearnley, A review of metallic, ceramic and surface-treated metals used for bearing surfaces in human joint replacements, Proc. Inst. Mech. Eng. H, J. Eng. Med. 213 (1999) 107–135. doi:10.1243/0954411991534843 [doi].
- [172] L. Straka, I. Corny, J. Pitel, Properties Evaluation of Thin Microhardened Surface Layer of Tool Steel after Wire EDM, (2016). doi:10.3390/met6050095.
- [173] Pace Technologies, (n.d.). [http://www.metallographic.com/Etchants/Stainless steel etchants.htm](http://www.metallographic.com/Etchants/Stainless%20steel%20etchants.htm) (accessed March 13, 2017).

- [174] M.A. Obeidi, E. McCarthy, D. Brabazon, Methodology of laser processing for precise control of surface micro-topology, *Surf. Coatings Technol.* 307 (2016) 702–712.
- [175] A.S.M. Handbook, Vol. 9 Metallography and Microstructures, 1985, ASM International, Met. Park. OH. (n.d.).
- [176] T.N. Baker, Laser surface modification of Ti alloys, (2010).
- [177] G.S. Schajer, Practical Residual Stress Measurement Methods, 2013.
- [178] N. Huang, Y.X. Leng, P.D. Ding, Surface Engineering of Light Alloys - Al, Mg and Ti alloys, 2010. doi:10.1533/9781845699451.3.568.
- [179] C. ASTM, 143: "Standard Test Method for Slump of Hydraulic-Cement Concrete," Am. Soc. Test. Mater. Annu. B. ASTM Stand. 4 (2003).
- [180] A. Standard, E466: Standard Practice for Conduction Force Controlled Constant Amplitude Axial Fatigue Test of Metallic Materials, vol. 03.01, Annu. B. ASTM Stand. West Conshohocken. (2002).
- [181] T. Bell, H.W. Bergmann, J. Lanagan, P.H. Morton, A.M. Staines, Surface engineering of titanium with nitrogen, *Surf. Eng.* 2 (1986) 133–143.
- [182] L. Xue, M. Islam, A.K. Koul, M. Bibby, W. Wallace, Laser gas nitriding of Ti-6Al-4V part 1: Optimization of the process, *Adv. Perform. Mater.* 4 (1997) 25–47.
- [183] A.S.M. Handbook, Volume 9, Metallogr. Microstruct. (2004).
- [184] Astm, G 99: Standard Test Method for Wear Testing with a Pin-on-Disk Apparatus, Annu. B. ASTM Stand. G-99-95a. (2000) 1–5. doi:10.1520/G0099-05R10.2.
- [185] A. Issa, D. Brabazon, M.S.J. Hashmi, 3D transient thermal modelling of laser microchannel fabrication in lime-soda glass, *J. Mater. Process. Technol.* 207 (2008) 307–314.
- [186] M. Van Elsen, M. Baelmans, P. Mercelis, J.-P. Kruth, Solutions for modelling moving heat sources in a semi-infinite medium and applications to laser material processing, *Int. J. Heat Mass Transf.* 50 (2007) 4872–4882.
- [187] L. Orazi, A. Fortunato, G. Cuccolini, G. Tani, An efficient model for laser surface hardening of hypo-eutectoid steels, *Appl. Surf. Sci.* 256 (2010) 1913–

1919.

- [188] A. Basu, A.N. Samant, S.P. Harimkar, J.D. Majumdar, I. Manna, N.B. Dahotre, Laser surface coating of Fe–Cr–Mo–Y–B–C bulk metallic glass composition on AISI 4140 steel, *Surf. Coatings Technol.* 202 (2008) 2623–2631.
- [189] B.S. Yilbas, A.F.M. Arif, C. Karatas, M. Ahsan, Cemented carbide cutting tool: Laser processing and thermal stress analysis, *Appl. Surf. Sci.* 253 (2007) 5544–5552.
- [190] C.W. White, M.J. Aziz, L.E. Rehn, S.T. Picraux, W. Wiedersich, Surface Alloying by Ion, Electron and Laser Beams, *Am.Soc.Metals, Met. Park. Ohio.* (1987) 19.
- [191] J.M. Dowden, *The mathematics of thermal modeling: an introduction to the theory of laser material processing*, CRC Press, 2001.
- [192] Design-Expert software, “DX9, user’s guide, Technical manual”, Stat-Ease Inc., (2014).
- [193] D. V Tran, H.Y. Zheng, Y.C. Lam, V.M. Murukeshan, J.C. Chai, D.E. Hardt, Femtosecond laser-induced damage morphologies of crystalline silicon by sub-threshold pulses, *Opt. Lasers Eng.* 43 (2005) 977–986.
- [194] H.S. Carslaw, J.C. Jaeger, *Conduction of heat in solids*, Oxford Clarendon Press. 1959, 2nd Ed. (1959).
- [195] G. Allcock, P.E. Dyer, G. Elliner, H. V Snelling, Experimental observations and analysis of CO<sub>2</sub> laser-induced microcracking of glass, *J. Appl. Phys.* 78 (1995) 7295–7303.
- [196] K. Sokolowski-Tinten, J. Bialkowski, A. Cavalleri, D. von der Linde, A. Oparin, J. Meyer-ter-Vehn, S.I. Anisimov, Transient states of matter during short pulse laser ablation, *Phys. Rev. Lett.* 81 (1998) 224.
- [197] S. Zhang, X. Ouyang, J. Li, S. Gao, S. Han, L. Liu, H. Wei, Underwater drag-reducing effect of superhydrophobic submarine model, *Langmuir.* 31 (2014) 587–593.
- [198] H. Park, G. Sun, Superhydrophobic turbulent drag reduction as a function of surface grating parameters, *J. Fluid Mech.* 747 (2014) 722–734.
- [199] O.I. Vinogradova, A.L. Dubov, Superhydrophobic textures for microfluidics,


Mendelev Commun. 22 (2012) 229–236.

- [200] T.N. Baker, “Laser surface modification of Ti alloys” in Surface Engineering of Light Alloys - Aluminium, Magnesium and Titanium Alloys, 2009.
- [201] V.C. Kumar, Process parameters influencing melt profile and hardness of pulsed laser treated Ti–6Al–4V, Surf. Coatings Technol. 201 (2006) 3174–3180.
- [202] B. Basu, D.S. Katti, A. Kumar, Advanced biomaterials: fundamentals, processing, and applications, John Wiley & Sons, 2010.
- [203] P. Jiang, X.L. He, X.X. al Li, L.G. Yu, H.M. Wang, Wear resistance of a laser surface alloyed Ti–6Al–4V alloy, Surf. Coatings Technol. 130 (2000) 24–28.
- [204] E.K.-A. Jr, Principles of laser materials processing, John Wiley & Sons, 2009.
- [205] A. Gisario, A. Boschetto, F. Veniali, Surface transformation of AISI 304 stainless steel by high power diode laser, Opt. Lasers Eng. 49 (2011) 41–51. doi:10.1016/j.optlaseng.2010.09.001.





**A-2** The chemical composition of the grit particles used in the shot peening for roughening the samples prior to laser irradiation.

Manual Blast Systems	<h1>BLAST MEDIA DATA SHEET - GUYSON HONITE</h1> <p>(for use with all compressed air blast systems - dry and wet)</p>		<div></div> <p>where quality comes to the surface</p>																																									
Semi/Fully Automated Blast Systems	<h2>GENERAL</h2> <p>Guyson Honite is a premium quality soda-lime glass bead manufactured specifically for impact blast finishing applications.</p> <p>It is a chemically inert, iron-free product, available in a range of bead sizes and can be used for a wide variety of cleaning, finishing and peening operations.</p>																																											
	Robotic Blast Systems	<h2>TYPICAL APPLICATIONS</h2> <p>Cleaning, Peening, Sheen Surface Finishing, General cleaning of tarnished components, Inert cleaning of sensitive surfaces e.g. auto parts, moulds and dies, removing heat scale and discolouration, creating a none reflective finish, cosmetic blending and covering surface defects etc.</p>																																										
Ultrasonic Baths and Tanks		<table><tr><th>Chemical Composition</th><th>Sizes Available:</th><th>Nominal Size Range (microns)</th></tr><tr><td>Soda-lime glass beads</td><td></td><td></td></tr><tr><td>SiO<sub>2</sub> : &lt; 75%</td><td>Honite 7 : 600 - 850</td><td></td></tr><tr><td>Na<sub>2</sub>O : &lt; 15%</td><td>Honite 8 : 425 - 600</td><td></td></tr><tr><td>CaO : &lt; 10%</td><td>Honite 9 : 250 - 425</td><td></td></tr><tr><td>MgO : &lt; 5%</td><td>Honite 10 : 180 - 300</td><td></td></tr><tr><td>Free iron : 0.1% (max by weight)</td><td>Honite 12 : 150 - 250</td><td></td></tr><tr><td></td><td>Honite 13 : 106 - 212</td><td></td></tr><tr><td></td><td>Honite 14 : 75 - 150</td><td></td></tr><tr><td></td><td>Honite 16 : 53 - 106</td><td></td></tr><tr><td></td><td>Honite 18 : 45 - 90</td><td></td></tr><tr><td></td><td>Honite 22 : 4 - 45</td><td></td></tr><tr><td></td><td>Pack Size : 25 kg bag</td><td></td></tr><tr><td></td><td colspan="2">See Guyson MSDS reference 10 for all other details</td></tr></table>		Chemical Composition	Sizes Available:	Nominal Size Range (microns)	Soda-lime glass beads			SiO <sub>2</sub> : < 75%	Honite 7 : 600 - 850		Na <sub>2</sub> O : < 15%	Honite 8 : 425 - 600		CaO : < 10%	Honite 9 : 250 - 425		MgO : < 5%	Honite 10 : 180 - 300		Free iron : 0.1% (max by weight)	Honite 12 : 150 - 250			Honite 13 : 106 - 212			Honite 14 : 75 - 150			Honite 16 : 53 - 106			Honite 18 : 45 - 90			Honite 22 : 4 - 45			Pack Size : 25 kg bag			See Guyson MSDS reference 10 for all other details
	Chemical Composition	Sizes Available:	Nominal Size Range (microns)																																									
Soda-lime glass beads																																												
SiO <sub>2</sub> : < 75%	Honite 7 : 600 - 850																																											
Na <sub>2</sub> O : < 15%	Honite 8 : 425 - 600																																											
CaO : < 10%	Honite 9 : 250 - 425																																											
MgO : < 5%	Honite 10 : 180 - 300																																											
Free iron : 0.1% (max by weight)	Honite 12 : 150 - 250																																											
	Honite 13 : 106 - 212																																											
	Honite 14 : 75 - 150																																											
	Honite 16 : 53 - 106																																											
	Honite 18 : 45 - 90																																											
	Honite 22 : 4 - 45																																											
	Pack Size : 25 kg bag																																											
	See Guyson MSDS reference 10 for all other details																																											
Multi-Stage Aqueous Ultrasonic Systems	<h2>Physical Data</h2> <table><tr><td>Shape : Spherical and smooth</td><td rowspan="5"><p>All Guyson Honite can be supplied with certification to Rolls Royce CSS8 ae rosapace standard should this be required. This is one of the highest conformity standards in the world and many other aerospace standards follow its lead. To achieve compliance, Honite has to pass rigorous batch tests that ensure its physical and chemical properties remain consistent.</p><p>Honite is a non-toxic and non-hazardous product that contains no free silica. No special disposal precautions are required for the product once it has been used for blast finishing purposes. However, contamination from a specific application or process must also be considered prior to disposal.</p></td></tr><tr><td>Colour : White</td></tr><tr><td>Specific gravity : 2.4 – 2.6</td></tr><tr><td>Bulk density : 1.5 g/cc</td></tr><tr><td>Hardness : Mohs 5</td></tr></table>		Shape : Spherical and smooth	<p>All Guyson Honite can be supplied with certification to Rolls Royce CSS8 ae rosapace standard should this be required. This is one of the highest conformity standards in the world and many other aerospace standards follow its lead. To achieve compliance, Honite has to pass rigorous batch tests that ensure its physical and chemical properties remain consistent.</p> <p>Honite is a non-toxic and non-hazardous product that contains no free silica. No special disposal precautions are required for the product once it has been used for blast finishing purposes. However, contamination from a specific application or process must also be considered prior to disposal.</p>	Colour : White	Specific gravity : 2.4 – 2.6	Bulk density : 1.5 g/cc	Hardness : Mohs 5																																				
	Shape : Spherical and smooth	<p>All Guyson Honite can be supplied with certification to Rolls Royce CSS8 ae rosapace standard should this be required. This is one of the highest conformity standards in the world and many other aerospace standards follow its lead. To achieve compliance, Honite has to pass rigorous batch tests that ensure its physical and chemical properties remain consistent.</p> <p>Honite is a non-toxic and non-hazardous product that contains no free silica. No special disposal precautions are required for the product once it has been used for blast finishing purposes. However, contamination from a specific application or process must also be considered prior to disposal.</p>																																										
Colour : White																																												
Specific gravity : 2.4 – 2.6																																												
Bulk density : 1.5 g/cc																																												
Hardness : Mohs 5																																												
Mono and Co-Solvent Ultrasonic Cleaning Systems																																												
	Rotary Basket Spray Wash Systems																																											
Conveyorised Spray Wash Systems																																												

All Guyson Honite can be supplied with certification to Rolls Royce CSS8 aerospace standard should this be required. This is one of the highest conformity standards in the world and many other aerospace standards follow its lead. To achieve compliance, Honite has to pass rigorous batch tests that ensure its physical and chemical properties remain consistent.

Honite is a non-toxic and non-hazardous product that contains no free silica. No special disposal precautions are required for the product once it has been used for blast finishing purposes. However, contamination from a specific application or process must also be considered prior to disposal.

### A.3 The preliminary test results table

Before starting the actual laser processing testing, a preliminary test were carried out to investigate and estimate; (a) the most significant laser processing parameters and (b) their effective ranges. During this test, only a visual testing was done on the produced samples to investigate the increase in diameter, the consistency of the textured pattern, and avoiding the severe presence of oxide. Different sample diameters were used to investigate the process flexibility and reflectivity on different geometries.

**Table A-1** Samples treated with argon gas shielding

No.	Power (W)	PRF (Hz)	OV (%)	U (mm/min)	$\omega$ (rpm)	Diameter (mm)	Energy Density (J/mm <sup>2</sup> )
S1-1	500	750	-20	43	179	20.25	13.33
S1-2	500	750	0	28.64	143.24	20.15	16.66
S1-3	500	750	20	19.09	119.366	20.1	20.00
S1-4	700	1500	-10	85.94	385.098	20.1	8.68
S1-5	700	1500	0	57.29	286.47	20.05	11.67
S1-6	700	1500	20	38.19	238.73	20.1	14.00
S2-1	700	2250	-20	128.91	537.14	20.05	6.22
S2-2	700	2250	0	85.94	429.71	20.1	7.77
S2-3	700	2250	25	57.29	385.98	20.1	8.66
S2-4	1000	2250	-20	129	538.9	20.1	8.86
S2-5	1000	2250	0	85.94	429.7	20.1	11.11
S3-1	1000	2250	20	57.29	358	20	13.33
S3-2	1000	300	-20	17.2	71.62	20.6	66.66
S3-3	1000	300	20	7.64	47.75	Melt	99.99
S3-4	500	300	-20	17.2	71.62	20.5	33.33
S3-5	500	300	20	7.64	47.75	20.6	49.99
S4-1	700	1500	-20	85.94	119.37	20.1	27.99
S4-2	700	2250	25	57.29	79.58	20.1	41.99
S4-3	1000	500	-20	28.65	119.37	20.4	39.99
S4-4	1000	500	20	12.73	79.58	Melt	59.99
S4-5	500	500	-20	28.65	119.37	20.35	20.00
S4-6	500	500	20	12.73	79.58	20.4	30.00
S4-7	200	100	-50	11.5	38	20	25.13
S5-1	700	400	-20	23	95.5	20.4	34.99
S5-2	700	400	-50	45.8	153	20.5	21.84
S5-3	700	800	-20	45.8	190.9	20.25	17.51

S5-4	500	400	-50	45.8	152.7	20.6	15.63
S5-5	700	200	20	5	31.8	20.5	105.10

S	Power (W)	PRF (Hz)	OV (%)	U (mm/min)	W (rpm)	Diameter (mm)	Energy Density (J/mm <sup>2</sup> )
S6-1	500	100	-20	5.7	23.9	20.85	100
S6-2	700	750	-20	43	179	20.25	18.667
S6-3	500	1500	-20	85.94	358	20.15	6.667
S6-4	300	100	-20	5.7	23.9	20.80	60
S6-5	500	200	-20	11.43	47.75	20.65	50
S7-1	200	100	-20	5.7	23.9	Not Cons.	40
S7-2	400	100	-20	5.7	23.9	20.8	80
S7-3	300	300	-20	17	71.6	20.2	20
S7-4	300	100	-50	11.5	38	20.6	37.5
S7-5	300	750	-50	11.5	38	20.5	5
S7-6	300	100	0	3.8	19	20.75	75
S7-7	600	200	0	7.6	38	21.05	75
Assist Gas Pressure of <b>1 bar</b> (Repeated Scans)							
No.	P (W)	PRF (Hz)	OV%	U mm/min	w (rpm)	D (mm)	D(mm), 1 <sup>st</sup> Treat.
S8-1	300	100	-20	5.7	23.9	20.85	20.8
S8-2	300	100	0	3.8	19	20.75	20.75
S8-3	500	100	-20	5.7	23.9	21.05	20.85
S8-4	500	1500	-20	85.94	358	20.1	20.15
S8-5	700	400	-20	23	95.5	20.8	20.4
S8-6	700	400	-50	45.8	153	20.75	20.5
S8-7	500	500	20	12.7	79.57	20.4	20.4
Laser beam spot is <b>1 mm</b> below the surface (Repeated Scans)							

No.	P (W)	PRF (Hz)	OV%	U mm/min	w (rpm)	D (mm)	D(mm), 1 <sup>st</sup> Treat.
S9-1	500	100	-20	5.5	23.95.7	20.75	20.85
S9-2	700	750	-20	43	179	20.4	20.25
S9-3	500	750	0	28.6	143	20.25	20.15
S9-4	500	1500	-20	85.94	358	20.1	20.15
S9-5	500	300	20	7.6	47.6	20.75	20.6
S9-6	1000	300	-20	17.6	71.6	20.6	20.6
<b>Ø 10 mm Diameter, Focus 1mm below surface, 4 bars (Repeated Scans)</b>							
No.	P (W)	PRF (Hz)	OV%	U mm/min	w (rpm)	D (mm)	D(mm), 1 <sup>st</sup> Treat.
S10-1	500	100	-20	11.45	47.76	10.8	20.85
S10-2	700	750	-20	86	385	10.4	20.4
S10-3	500	750	0	57.3	286.4	10.2	20.25
S10-4	500	1500	-20	171.9	716.2	10.1	20.1
S10-5	500	300	20	15.2	95.5	10.75	20.75
S10-6	1000	300	-20	34.4	143.15	10.6	20.6
<b>Ø 10 mm Diameter, Focus 1mm below surface, 4 bars</b>							
S11-1	500	300	20	15.2	95.5	10.8	
S11-2	500	300	20	15.2	95.5	10.65	
S11-	400	300	20	15.2	95.5	10.45	

3							
S11-4	600	300	20	15.2	95.5	10.5	
S11-5	400	300	20	15.2	95.5	10.4	
S11-6	500	300	30	12.34	88	10.55	
S11-7	500	300	10	19	104	10.6	
Ø 16 mm, Focus 1 mm below surface, p= 4 bars							
S12-1	500	300	0	14	71.6	16.6	
S12-2	500	300	-10	17.5	79.5	16.5	
S12-3	500	300	-20	21	89.5	16.5	
S12-4	500	300	20	9.55	59.68	16.6	
S12-5	500	300	-20	21	89.5	16.4	
S12-6	500	300	20	9.55	59.68	16.6	
Ø 16 mm, Focus 1 mm below surface, p = 4 bars							
S13-1	300	300	-20	21.5	89.5	16.2	
S13-2	300	750	-20	53.7	223.8	16.1	
S13-3	600	200	0	9.5	47.74	16.7	
S13-	600	200	20	9.5	59.6	16.6	

4							
S13-5	300	300	20	9.5	59.6	16.25	
S13-6	300	300	50	4.7	47.74	16.2	
<b>Ø 16 mm, Focus 1 mm below surface, 0% OV, <math>p = 0.5 - 3</math> bars</b>							
S14-1	500	300	0	14	71.6	16.5	0.5 bar
S14-2	500	300	0	14	71.6	16.75	1 bar
S14-3	500	300	0	14	71.6	16.7	1.5 bar
S14-4	500	300	0	14	71.6	16.75	2 bar
S14-5	500	300	0	14	71.6	16.6	2.5 bar
S14-6	500	300	0	14	71.6	16.6	3 bar
S15-1	500	300	0	14	71.6	16.5	3.5 bar
S15-2	500	300	0	14	71.6	16.5	4 bar
S15-3	500	300	0	14	71.6	16.5	4.5 bar
S15-4	500	300	0	14	71.6	16.45	5 bar
S15-5	500	300	0	14	71.6	16.45	5.5 bar
S15-6	500	300	0	14	71.6	16.4	6 bar

<b>Ø 16 mm, Focus 1 mm below surface, -20% OV, <math>p = 0.5 - 4.5</math> bars</b>							
S16-1	500	300	-20	21.48	89.5	16.35	0.5 bar
S16-2	500	300	-20	21.48	89.5	16.6	1.5 bar
S16-3	500	300	-20	21.48	89.5	16.55	2.5 bar
S16-4	500	300	-20	21.48	89.5	16.4	3.5 bar
S16-5	500	300	-20	21.48	89.5	16.35	4.5 bar
<b>Ø 16 mm, Focus 1 mm below surface, 20% OV, <math>p = 0.5 - 5.5</math> bars</b>							
S17-1	500	300	20	9.5	59.68	16.45	0.5 bar
S17-2	500	300	20	9.5	59.68	16.6	1.5 bar
S17-3	500	300	20	9.5	59.68	16.4	2.5 bar
S17-4	500	300	20	9.5	59.68	16.35	3.5 bar
S17-5	500	300	20	9.5	59.68	16.35	4.5 bar
S17-6	500	300	20	9.5	59.68	16.4	5.5 bar
<b>Ø 16 mm, Focus 1 mm below surface, 0% OV, <math>p = 0.5 - 4.5</math> bars</b>							
S18-1	700	300	0	14	71.6	16.5	2.5 bar
S18-2	700	300	0	14	71.6	16.5	3.5 bar
S18-	700	300	0	14	71.6	16.6	4.5 bar



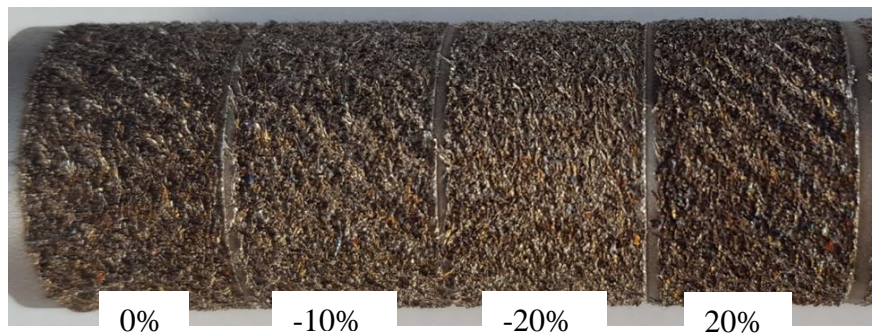
3							
S18-4	300	300	0	14	71.6	16.35	2.5 bar
S18-5	300	300	0	14	71.6	16.25	3.5 bar
S18-6	300	300	0	14	71.6	16.25	4.5 bar
<b>Ø 16 mm, Focus 1 mm below surface, 20% OV, <math>p = 0.5 - 4.5</math> bars</b>							
S19-1	500	500	0	23.8	119.36	16.45	2.5 bar
S19-2	500	500	0	23.8	119.36	16.3	3.5 bar
S19-3	500	500	0	23.8	119.36	16.3	4.5 bar
S19-4	500	700	0	33.4	167.1	16.25	2.5 bar
S19-5	500	700	0	33.4	167.1	16.25	3.5 bar
S19-6	500	700	0	33.4	167.1	16.3	4.5 bar
<b>Ø 16 mm, Focus 1 mm below surface, <math>p = 3</math> bars</b>							
S20-1	500	300	-30	26.6	102.3	16.4	3 bar
S20-2	500	300	-50	42.97	143.24	16.45	3 bar
S20-3	700	300	-50	42.97	143.24	16.6	3 bar
S20-4	600	300	-20	21.48	89.5	16.55	3 bar
S20-	500	300	0	14	71.1	16.35	3 bar,

5							30% DC
S20- 6	500	300	0	14	71.1	16.55	3 bar, 70% DC

The following Table A-2 lists the resulting increase in pin diameter due to the change in percentage overlap. Figure A-1 shows the produced texture pattern for the samples processed with the laser parameters listed in Table 4-7.

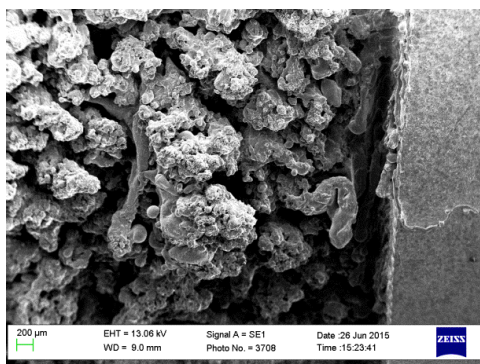
**Table A-2** Lists the results for processing with different Overlapping.

Power (W)	PRF (Hz)	OV (%)	Diameter increase (mm)
500	300	0	0.6
500	300	-10	0.5
500	300	-20	0.5
500	300	20	0.6



**Figure A-1** Sample textured with the parameters listed in Table A-2 showing the effect of the percentage overlap.

When processing with percentage overlap of higher than 20%, no significant increase in pins diameter was found. This can be explained by re-melting the same zone of the surface that already been treated in the previous track which would result in massive removal of the material, see Figure A-2



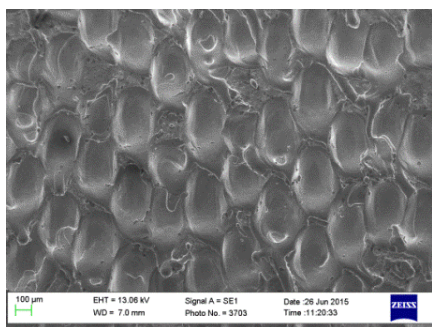
(a)



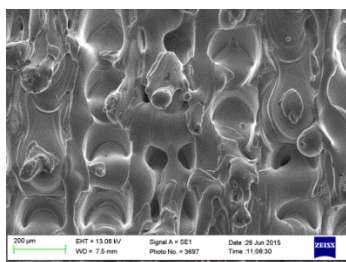
(b)

**Figure A-2** (a) SEM and (b) images for processing with: 500 W, 300 Hz and 30% overlap.

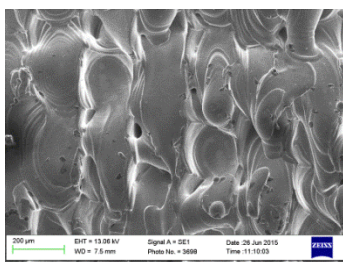
It was always observed that using the percentage overlap of -20%, 0% and 20% produces a significant improvement in pin samples diameter and that the presence of the weak, brown and brittle dendrites was reduced or disappeared, see Figures A-3 and A-4.



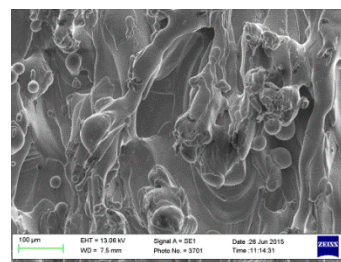
**Figure A-3** SEM and real image of sample processed with 700 W, 1500 Hz and -10% OV.



(a)



(b)



(c)

**Figure A-4** SEM images for SST 304 samples processed with CO<sub>2</sub> laser of 500 W/750 Hz; (a) -20% , (b) 0% and (c) 20% overlap.

#### A.4 The effect of the average power

The laser beam power is a very significant factor in laser processing of materials [24,42,205]. Various levels of power were tested while the other parameters were fixed at constant levels. The following Table A-3 lists five samples processed with power of 300, 400, 500, 600 and 1000 W while PRF, percentage overlap and assist gas pressure were kept constant at 300 Hz, 20% and 0.4 MPa respectively.

**Table A-3** The effect of various power levels on the diameter increase.

Power (W)	PRF (Hz)	OV (%)	Diameter increase (mm)
300	300	20	0.25
500	300	20	0.65
400	300	20	0.45
600	300	20	0.5
1000	300	20	Excessive melt



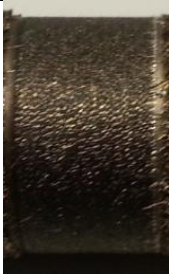



When the laser beam power of 300 W was applied, an increase of 0.25 mm on the sample diameter was observed. It was also noted that more increase in sample's diameter can be found with the increase in laser beam power which can be related to the increase of the melt pool size. Increasing the power for more than 600 W was resulted in extreme melting and ablation of the material. For this reason and in order to avoid changing the mechanical properties of the bulk material and presence of oxidation, these levels were not applied.

#### A.5 The effect of the assist gas pressure

The gas utilized in the preliminary test was argon, and the pressure applied was 0.4 MPa. The role of the assist gas was explained in section 4.2.1. Argon, as an inert gas was implemented in this test to reduce the oxidation of the processed surface caused by the interaction of the melted zone with the surrounding air. The effect of the assist gas pressure was reported by several researchers and for various processes like laser drilling and laser cutting [24,30,41].

In this study, an investigation of the effect of the assist gas pressure on the diameter increase and surface morphology was carried out. A selection of samples were re-

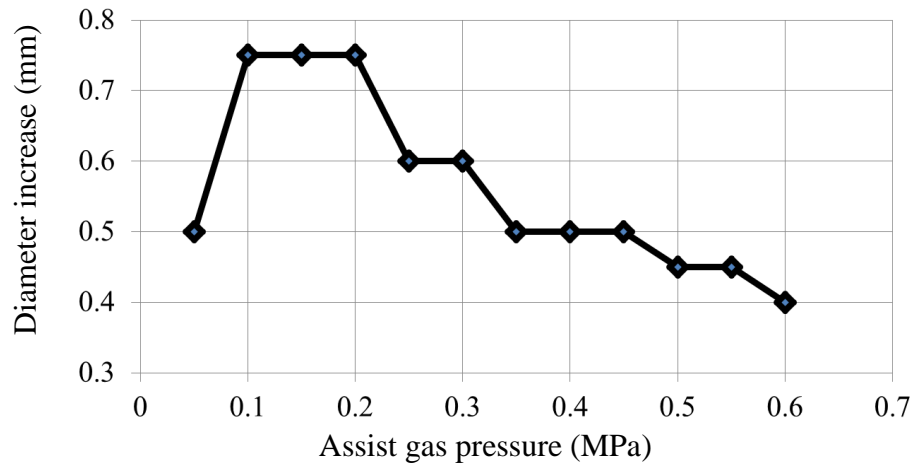
produced by fixing the laser processing parameters values and increasing the gas pressure from 0.1 to 0.6 MPa with 0.5 MPa graduation each time. A clear surface oxidation was resulted on the samples processed with low gas pressure. Figure A-5 shows the dark oxide surface resulted on the samples processed with 0.1 MPa (left) compared to the light coloured samples processed with 0.4 MPa. This can be explained by the reduction in the inert shroud size surrounding the molten portion when the gas pressure was reduced to 0.1 MPa which expose the heated material to the atmosphere.

Processing parameters	p = 0.1 MPa	p = 0.4 MPa
500 W 500 Hz 20% Overlap		
500 W 1500 Hz -20% Overlap.		
300 W 100 Hz 0% Overlap.		

**Figure A-5** Shows samples processed with similar laser processing Parameters with different assist gas pressure.

The alteration in surface roughness, topography and the increase in diameter were always the investigated responses for changing the assist gas pressure by successive increments of 0.5 bar each time while keeping the laser parameters values unchanged.

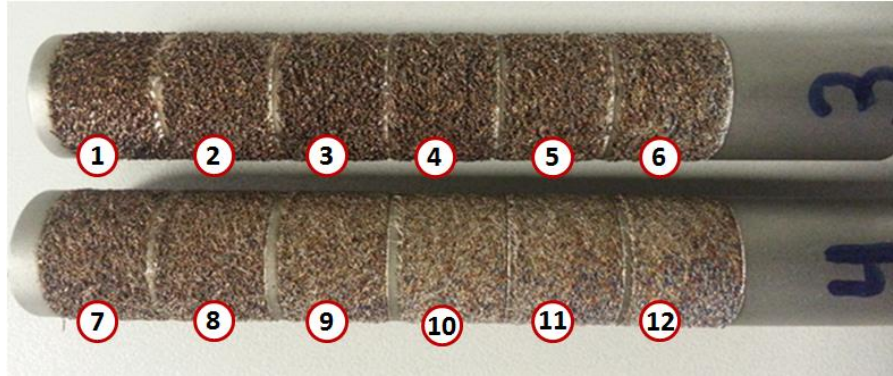
The increase in samples' diameter was recorded and plotted against the associated gas pressure in the following Figure A-6. This sample was processed with 500 W, 300 Hz and 0% overlap.



**Figure A-6** Plot of the effect of the increase in assist gas pressure on the increase in sample's diameter.

The minimum amount of pressure needed to produce the sufficient protection of the lens, see section 4.2.1, is 0.5 bar. Starting with this pressure, a diameter increase of 0.5 mm was noted with clear excessive surface roughness and oxide presence, see Figure A-7. The second and third samples were scanned with 1 and 1.5 bars respectively and showed a greater growth of material and rougher surface. Samples 4 to 8 were processed with 2 to 4 bars and show lesser material build up of 0.5 to 0.75 mm caused by the removal of material. A reduction in pins' diameter was found on the samples processed with a gas pressure of 5 bars and higher as a result of the blow of the molten material.





**Figure A-7** Images of laser scans with 500 W, 300 Hz, 0% OV and assist gas pressure of 0.5-6 bars.

From Figure A-7 and the surface topography of the processed samples, it was decided that the best range for the assist gas pressure is between 2 and 3 bars.

#### **A.6 The effect of the beam focus position**

Samples with significant increase in diameter and various laser processing parameters were re-produced by adjusting the focal position at 1 mm below the sample surface. A noticeable improvement was found in the diameter in addition to the clear and homogeneous surface texture and roughness.

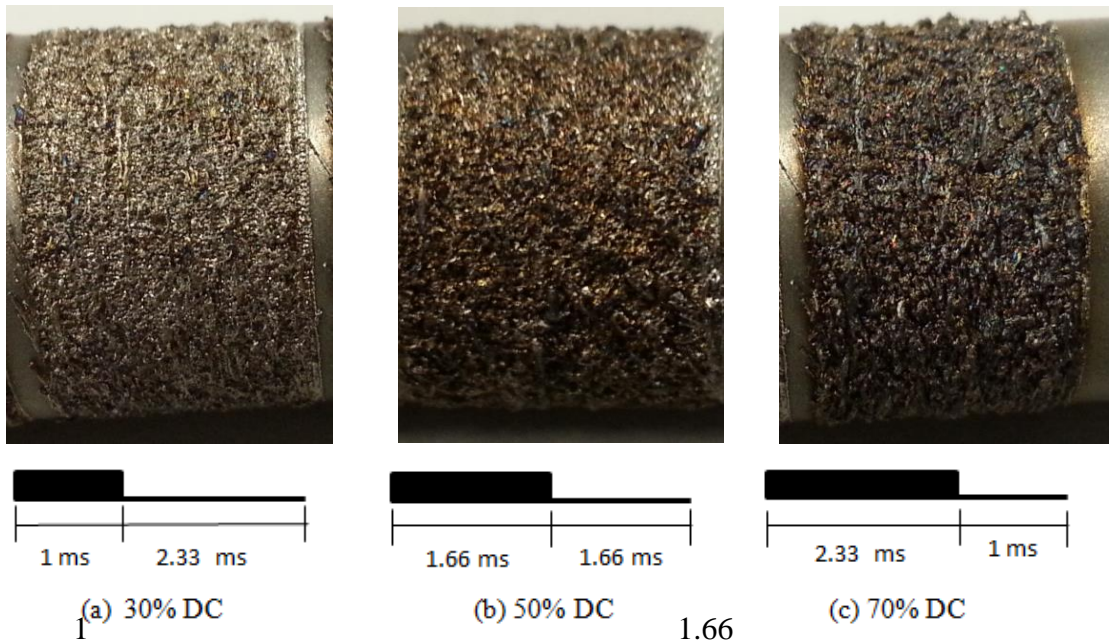
**Table A-4** Shows a comparison between the increase in samples diameter processed with focal position on the surface ( $D_1$ ) and 1 mm below the surface ( $D_2$ )

P (W)	PRF (Hz)	OV%	$D_1$ (mm)	$D_2$ (mm)
500	100	-20	0.85	0.75
700	750	-20	0.25	0.4
500	750	0	0.15	0.25
500	1500	-20	0.15	0.1
500	300	20	0.6	0.75
1000	300	-20	0.6	0.6

From the results listed in Table A-4 and the consistency of the surface texture, it was decided to process the set of samples by setting the focal position to 1 mm below the sample surface.

#### A.7 The effect of varying the duty cycle

The change in Duty Cycle was also investigated. Sample S14-6 was processed the first time with P=500 W, PRF=300 Hz, DC=50%, OV=0% and assist gas pressure = 3 bar. This sample was repeated by using two different Duty Cycles of 30% and 70%. See Figure A-8 and Table A-5.



**Figure A-8** Laser processing with different duty cycles.

**Table A-5** Laser processing with different duty cycles p=3 bar.

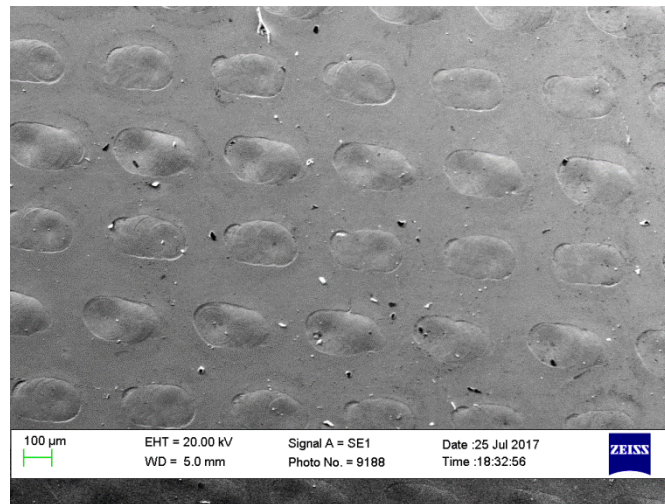
Power (W)	PRF (Hz)	OV (%)	DC %	Diameter (mm)
500	300	0	30	0.35
500	300	0	50	0.6
500	300	0	70	0.55



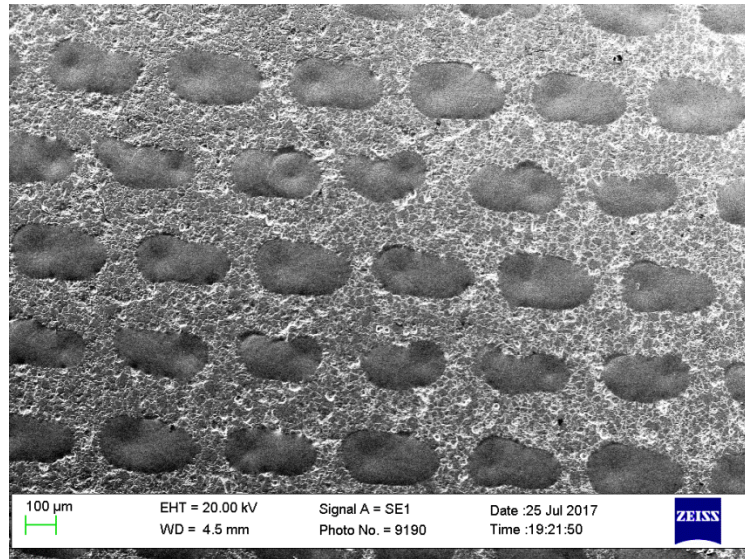
It could be concluded from Figure A-8 and Table A-5 that the reduction in duty cycle to 30% leads to the reduction in sample's diameter from 0.6 to 0.35 mm due to the reduction in residence (heating) time with non-consistent surface texture. The application of higher duty cycle value of 70% leads to excessive oxidation and high roughness and knurl surface due to the high residence time. Similar surface properties were found when the continuous wave mode was used. A fixed duty cycle value of 50% was used during the entire DoE test.

#### **A.8 The effect of the surface roughness on the absorption of the radiation**

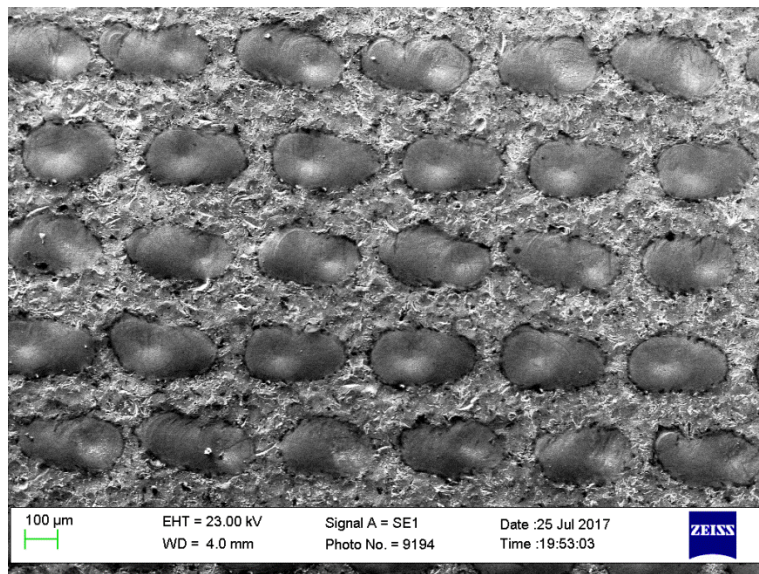
This effect was explained in details in section 1.5 and the results found in this study were listed in section 5.1. The following Figure A-9 shows more SEM image for the SST samples with different surface roughness. All of these samples were processed with 200 W, 100 Hz, 50% DC, -50% OV and 2378 mm/min scanning speed.



(a) High polished surface,  $R_a = 0.01 \mu\text{m}$



(b) As-received sample surface,  $R_a = 0.8 \mu\text{m}$



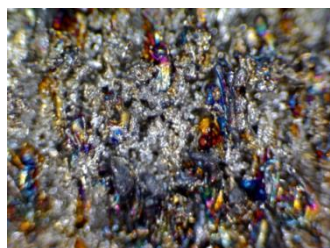
(c) Roughened surface,  $R_a = 2.3$

**Figure A-9** 316L sample surface polished to different roughness before  $\text{CO}_2$  laser irradiation.

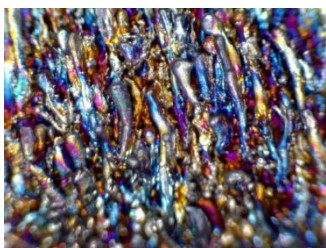


**Figure A-10** Shows some of the produced samples.

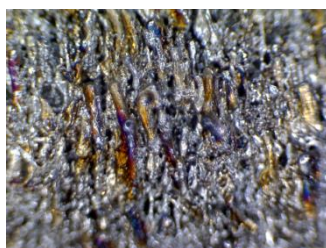




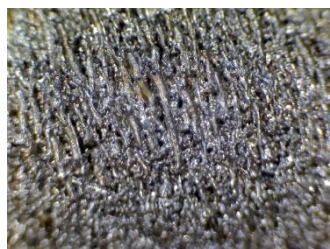
(1)



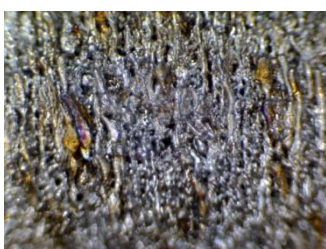
(2)



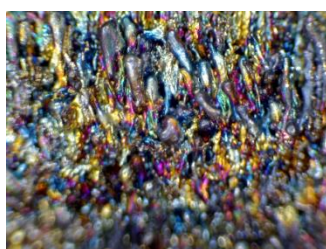
(3)



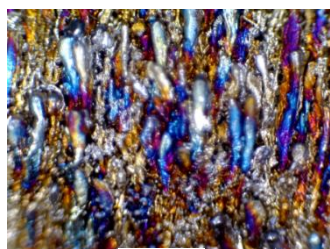
(4)



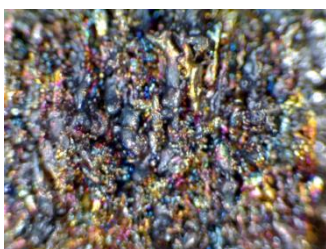
(5)



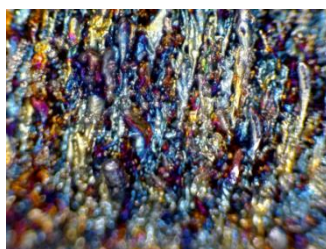
(6)



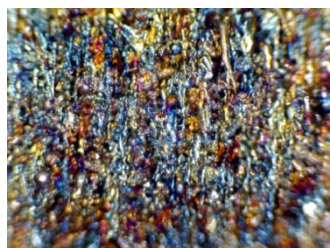
(7)



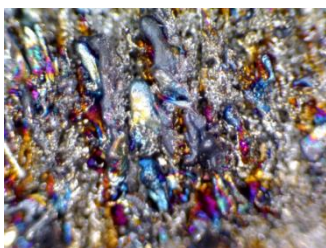
(8)



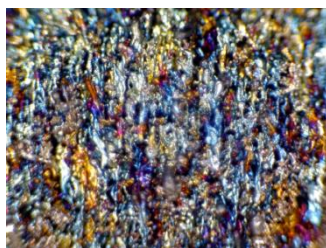
(9)



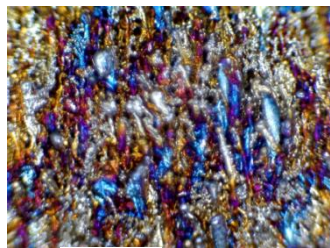
(10)



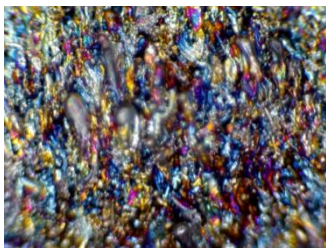
(11)



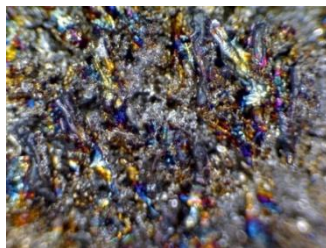
(12)



(13)

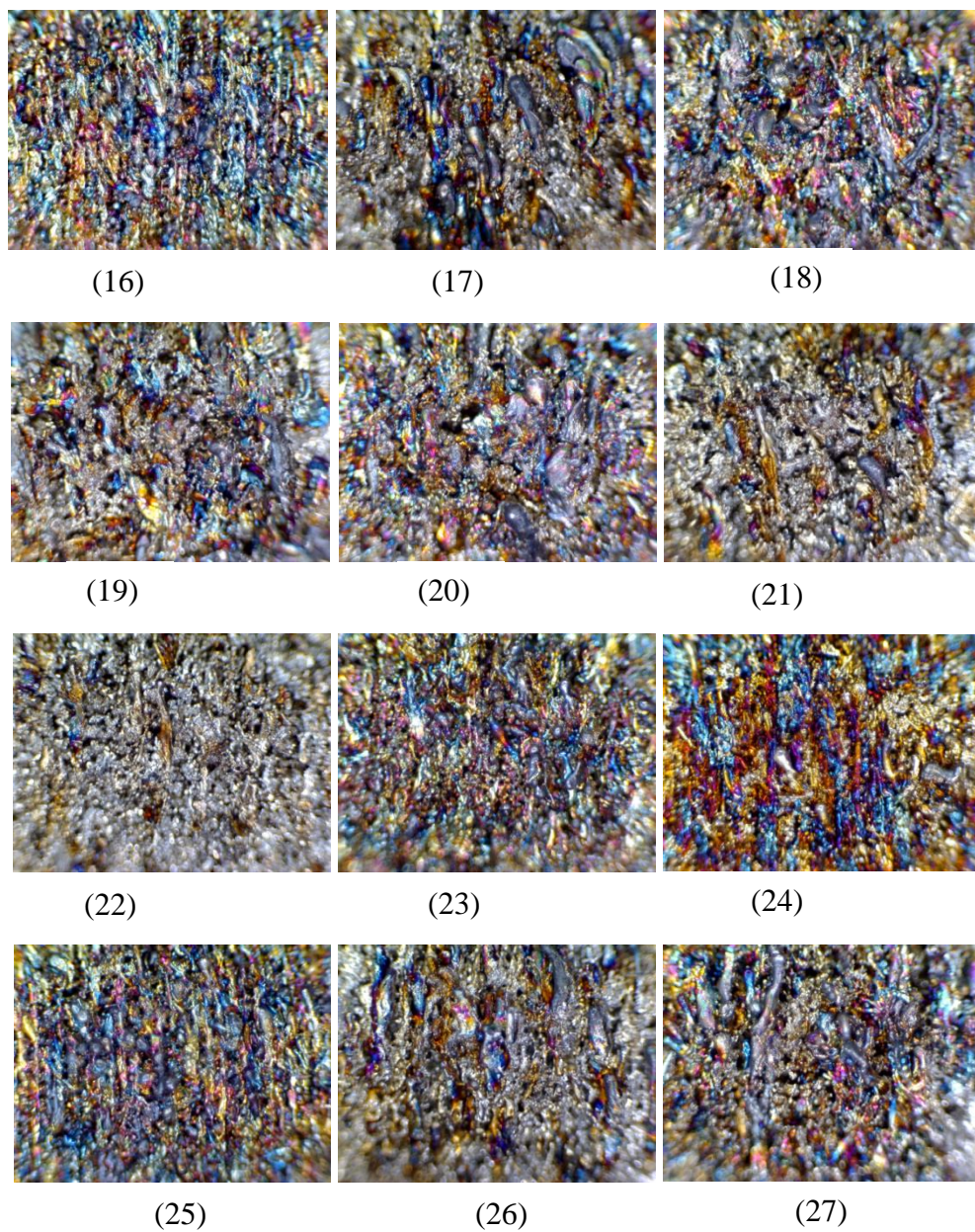


(14)



(15)





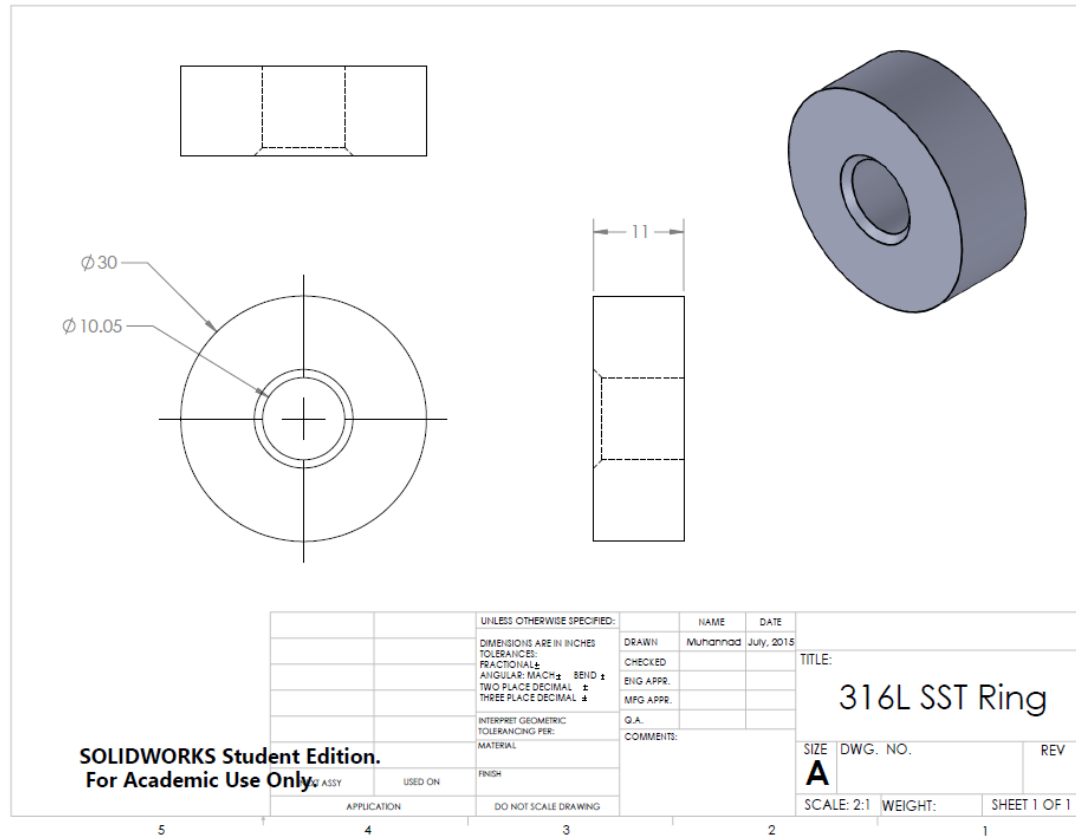
**Figure A-11** Shows low magnification images for the samples listed in Table 4-8. The figure shows the versatile surface roughness and oxide after the laser irradiation.

## Appendix B Input laser processing parameters and out-put measures

S	INPUT Parameters				Related Parameters		OUTPUT Resp.	Calculated Terms					Ins.F. Pull F.		Ra	fzltDepth	Int. volume	Hardness	
	P (W)	PRF (Hz)	OV (%)	w (rpm)	U (mm/min)	Diameter (mm)		Ur (mm/sec)	En.Den. (J/mm²)	Pulse En (J)	Fluence (J/mm²)	R Time (ms)	Ir. (kW/mm²)	kN					kN
No.	1	400	300	0	126.05	27.73	10.9	66.00	27.55	0.67	18.89	1.67	8.26	10.28	0.36	39.27	0.49	83.74	344.66
2	2	400	200	-20	105.04	27.73	11.1	55.00	33.06	1.00	28.33	2.00	8.26	33.03	3.14	55	0.55	96.2	343.67
3	3	300	200	-20	105.04	27.73	10.9	55.00	24.79	0.75	21.25	2.00	6.20	19.22	1.57	44.68	0.6	75.28	342.26
4	4	300	300	-20	157.56	41.60	10.4	82.50	16.53	0.50	14.16	1.33	6.20	14.78	1.72	38.11	0.33	39.42	258.00
5	5	300	300	0	126.05	27.73	10.6	66.00	20.66	0.50	14.16	1.67	6.20	15.04	3.10	44.28	0.51	47.64	344.33
6	6	500	200	-20	105.04	27.73	10.9	55.00	41.32	1.25	35.41	2.00	10.33	41.82	3.70	57.61	0.7	77.25	324.33
7	7	300	100	-20	52.52	13.87	11.1	27.50	49.59	1.50	42.49	4.00	6.20	24.21	2.49	65.05	1.1	93.6	324.67
8	8	500	200	20	70.03	12.32	11.05	36.67	61.98	1.25	35.41	3.00	10.33	20.65	2.20	140.11	1	92.11	243.67
9	9	400	100	-20	52.52	13.87	11.1	27.50	66.11	2.00	56.66	4.00	8.26	48.19	7.51	102	1.25	88.38	313.67
10	10	400	100	20	35.01	6.16	10.8	18.33	99.17	2.00	56.66	6.00	8.26	34.61	5.63	99.6	1.53	59.69	313.33
11	11	500	300	-20	157.56	41.60	10.85	82.50	27.55	0.83	23.61	1.33	10.33	21.94	0.62	41.79	0.58	72.11	349.67
12	12	400	100	0	42.02	9.24	10.9	22.00	82.64	2.00	56.66	5.00	8.26	47.10	5.52	118.78	1.19	72.67	297.33
13	13	300	100	0	42.02	9.24	11.1	22.00	61.98	1.50	42.49	5.00	6.20	39.21	5.50	51.23	0.9	88.8	333.00
14	14	400	200	0	84.03	18.49	10.9	44.00	41.32	1.00	28.33	2.50	8.26	20.45	1.68	54.08	0.8	77.78	334.00
15	15	400	300	20	105.04	18.49	10.85	55.00	33.06	0.67	18.89	2.00	8.26	13.41	0.17	46.74	0.2	36.54	347.33
16	16	500	100	0	42.02	9.24	10.75	22.00	103.30	2.50	70.82	5.00	10.33	42.84	5.84	156.33	1.4	38.65	316.67
17	17	300	200	0	84.03	18.49	10.95	44.00	30.99	0.75	21.25	2.50	6.20	18.81	1.22	48	0.95	70.3	339.33
18	18	500	200	0	84.03	18.49	11	44.00	51.65	1.25	35.41	2.50	10.33	37.01	4.80	73.45	0.8	78.62	314.00
19	19	500	300	0	126.05	27.73	10.75	66.00	34.43	0.83	23.61	1.67	10.33	17.98	1.64	57.97	0.4	55.42	346.67
20	20	500	300	20	105.04	18.49	10.75	55.00	41.32	0.83	23.61	2.00	10.33	15.40	0.64	65.5	1.3	61.02	344.67
21	21	300	200	20	70.03	12.32	10.85	36.67	37.19	0.75	21.25	3.00	6.20	13.48	0.33	46.48	0.7	66.32	343.33
22	22	300	300	20	105.04	18.49	10.5	55.00	24.79	0.50	14.16	2.00	6.20	10.24	1.47	42.19	0.22	36.72	301.67
23	23	500	100	20	35.01	6.16	10.75	18.33	123.96	2.50	70.82	6.00	10.33	19.36	1.47	89.23	1.7	36.76	341.67
24	24	300	100	20	35.01	6.16	10.8	18.33	74.38	1.50	42.49	6.00	6.20	40.49	6.66	44.13	1.2	56.88	322.33
25	25	400	300	-20	157.56	41.60	10.75	82.50	22.04	0.67	18.89	1.33	8.26	24.68	1.87	49.36	0.6	53.76	338.67
26	26	500	100	-20	52.52	13.87	10.8	27.50	82.64	2.50	70.82	4.00	10.33	32.30	4.74	49.07	0.98	57.87	323.67
27	27	400	200	20	70.03	12.32	10.95	36.67	49.59	1.00	28.33	3.00	8.26	17.21	1.15	154.44	0.5	74.95	332.00

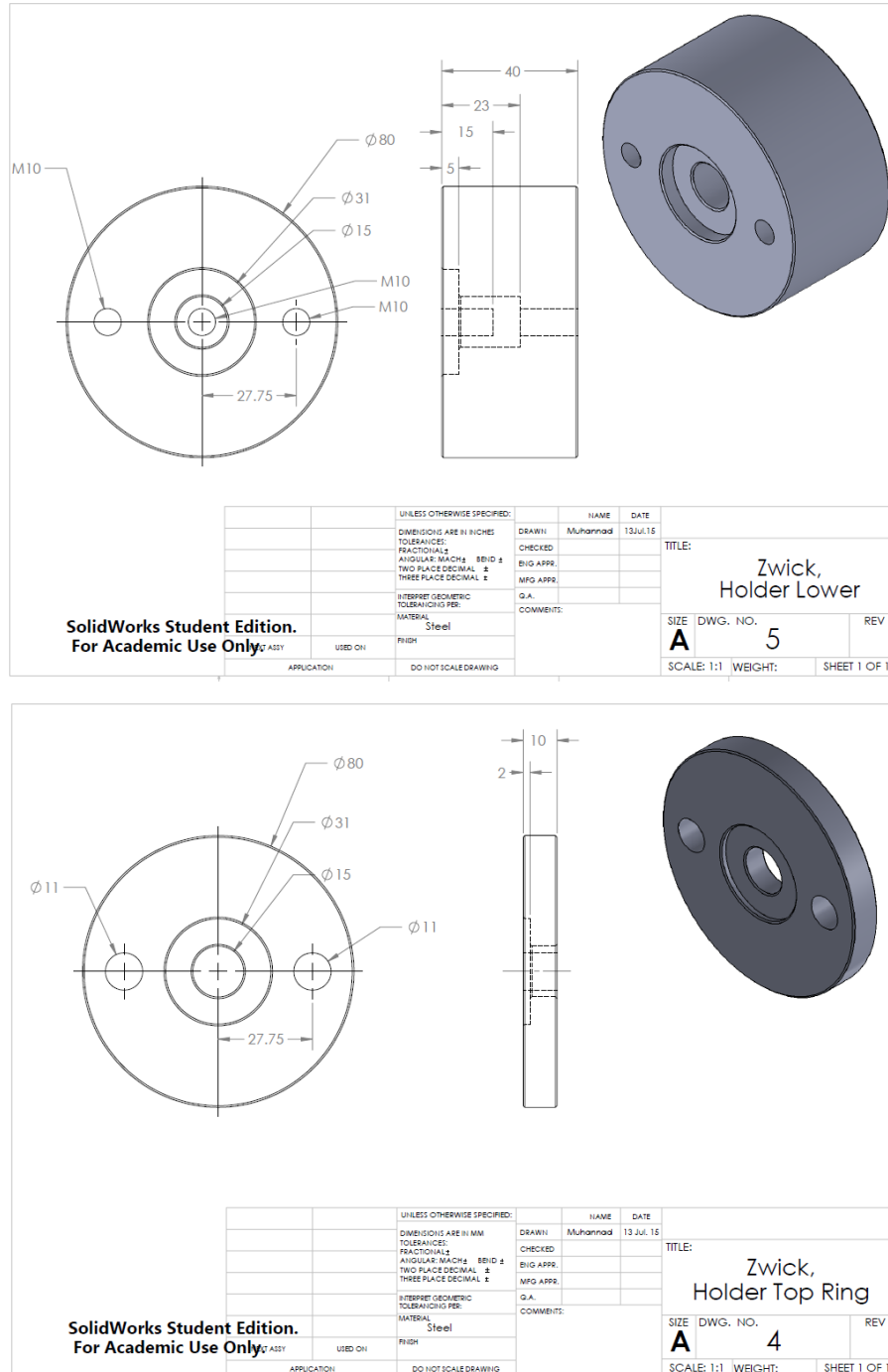
## Appendix C- Metallographic arrangements

### C-1 CAD drawings for the parts manufactured in DCU workshop to support this study:



**Figure- C-1** The 316L SST hub rings used in the insertion-removal test

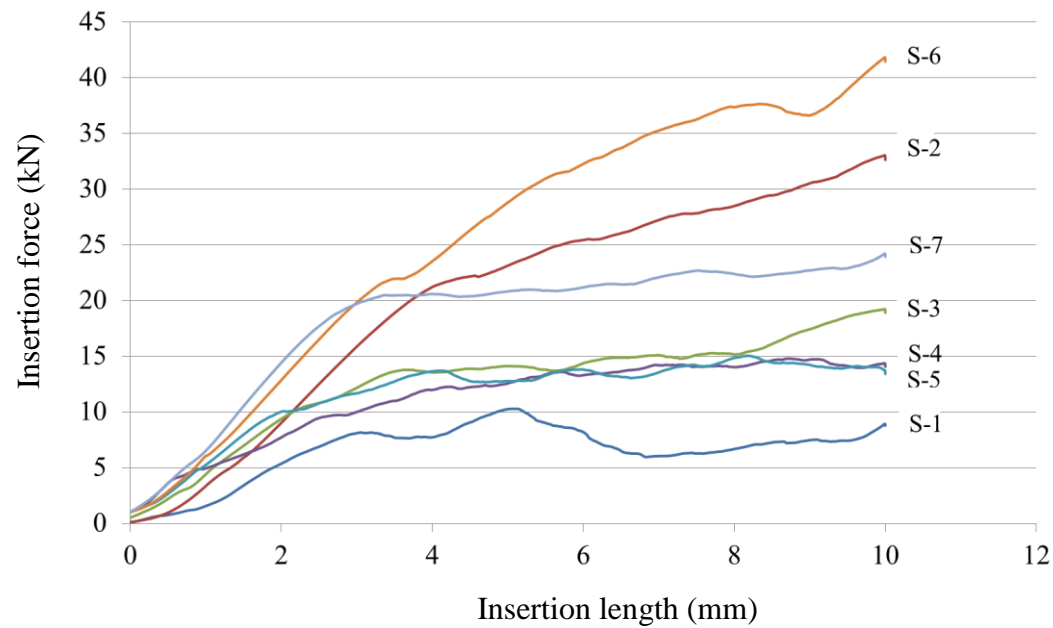




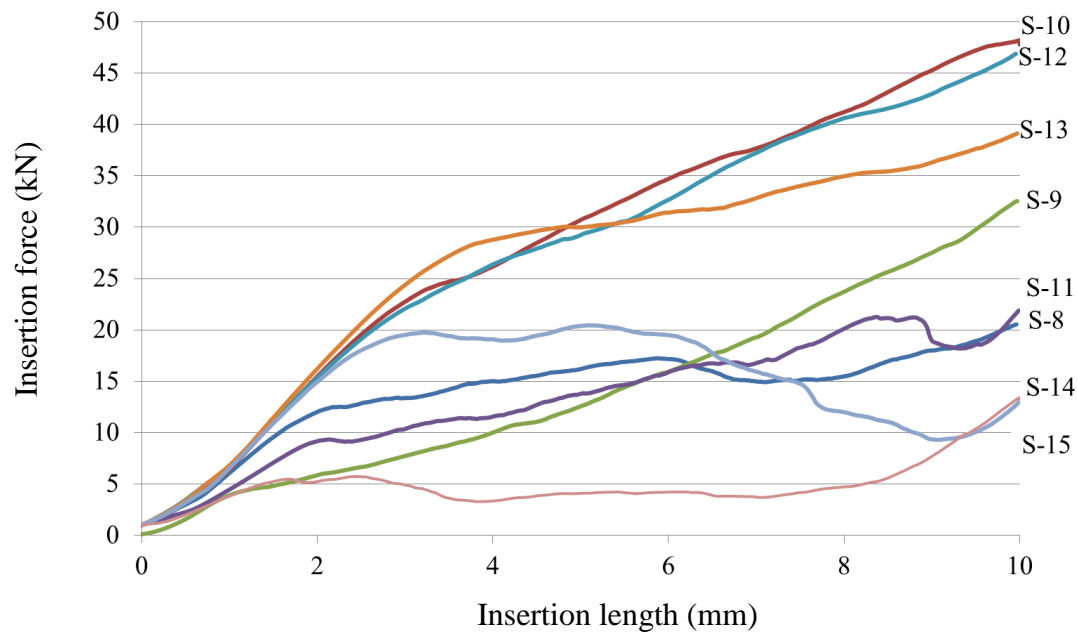
**Figure C-2** The upper and lower parts of the capsule used to hold the joint assembly during the insertion-removal and fatigue tests. Both parts were manufactured in DCU workshop



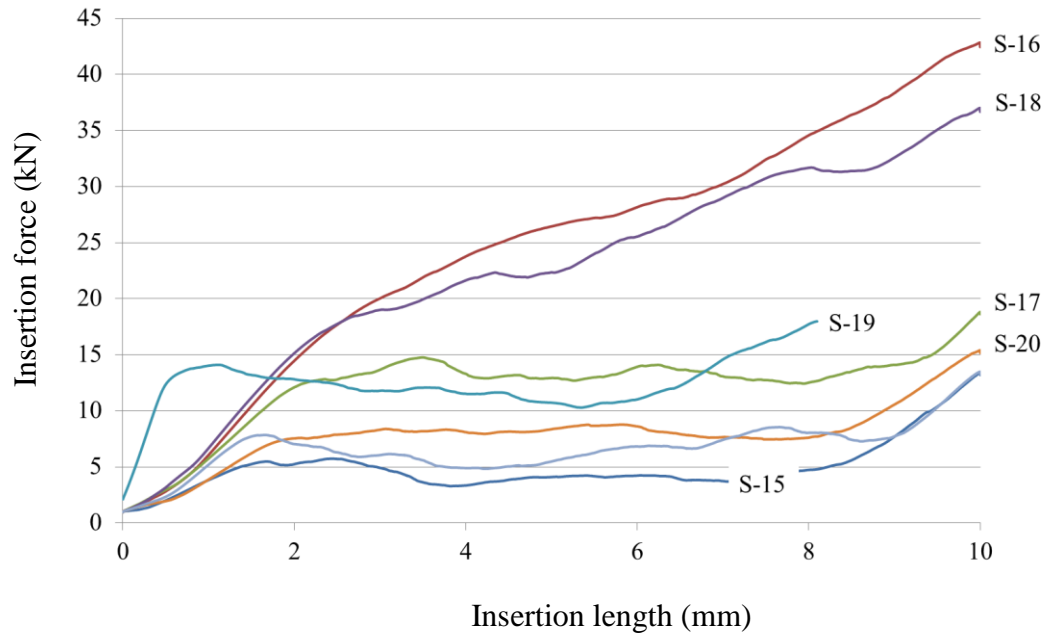
**C-2 Insertion force:**



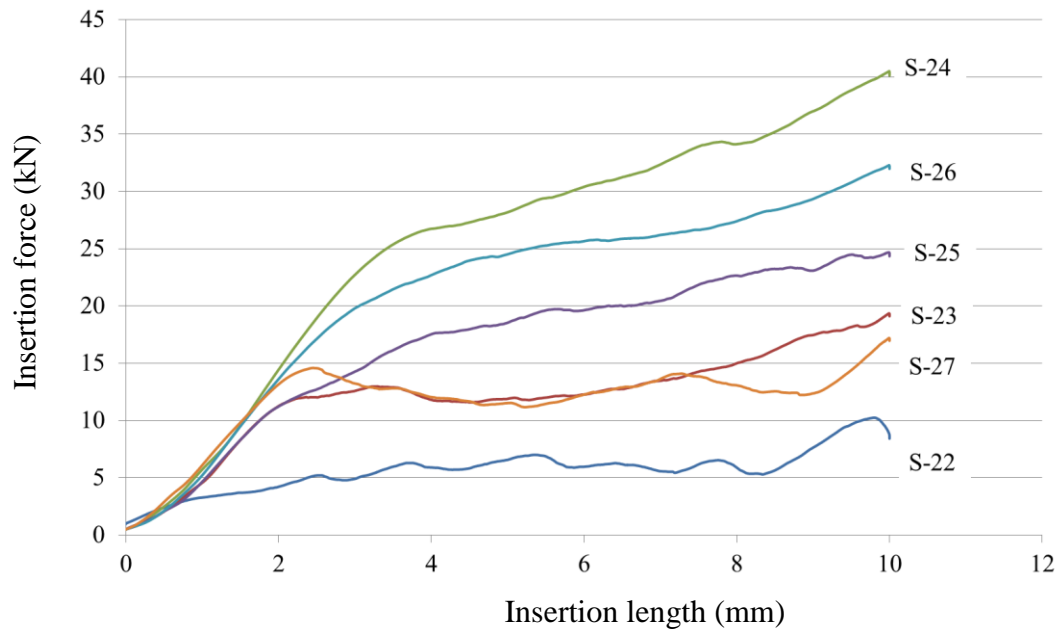
(a) Samples 1-7



(b) Samples 8-14



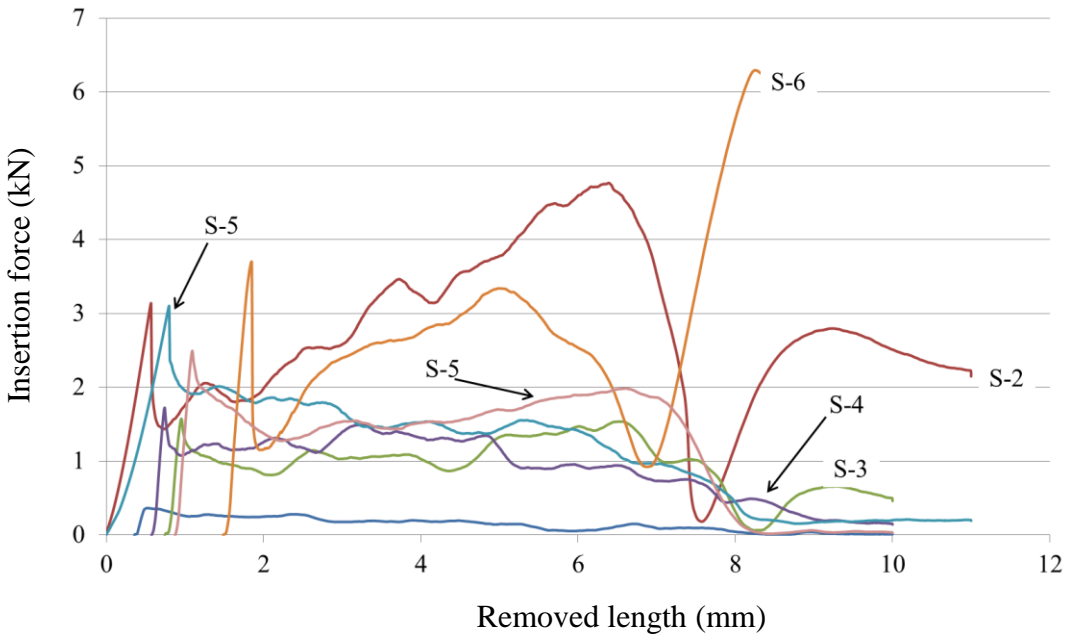
(c) Samples 15-21



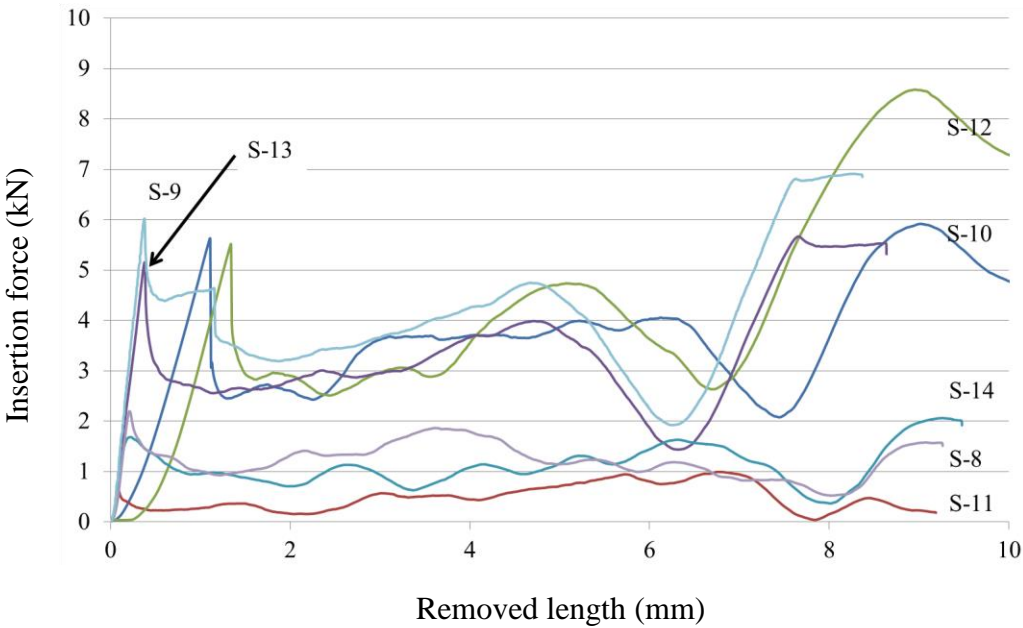
(d) Samples 22-

**Figure C-3** The insertion force plots for the full set of samples in the DoE.

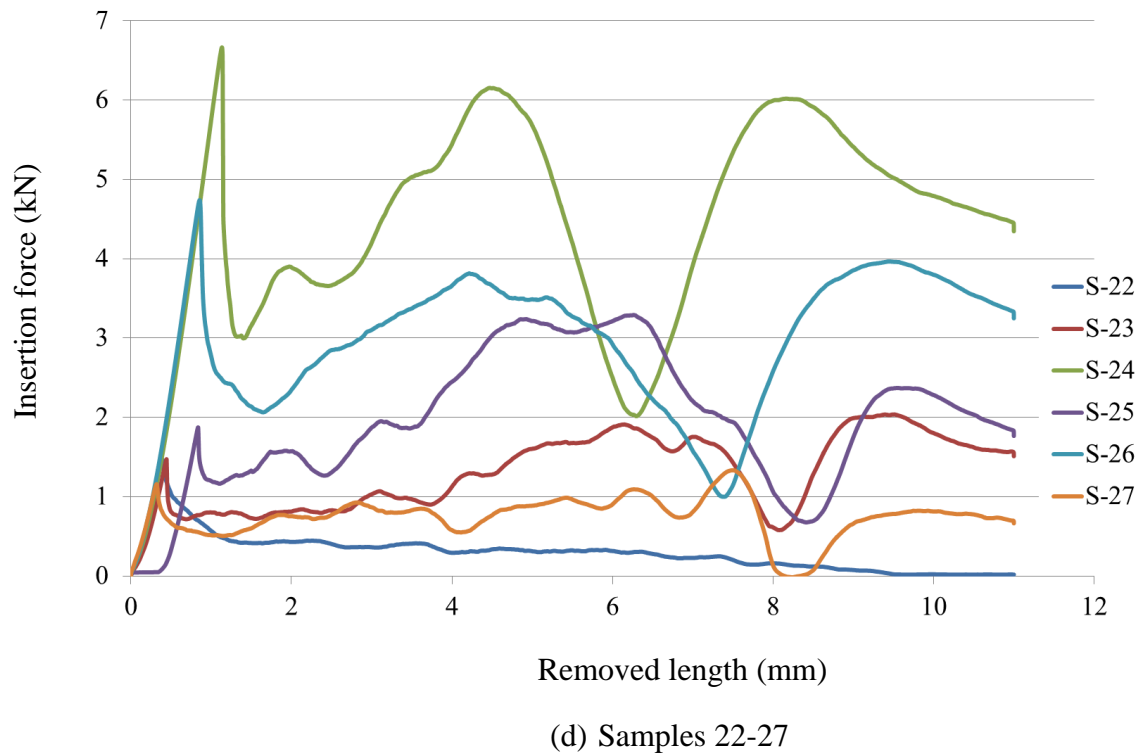
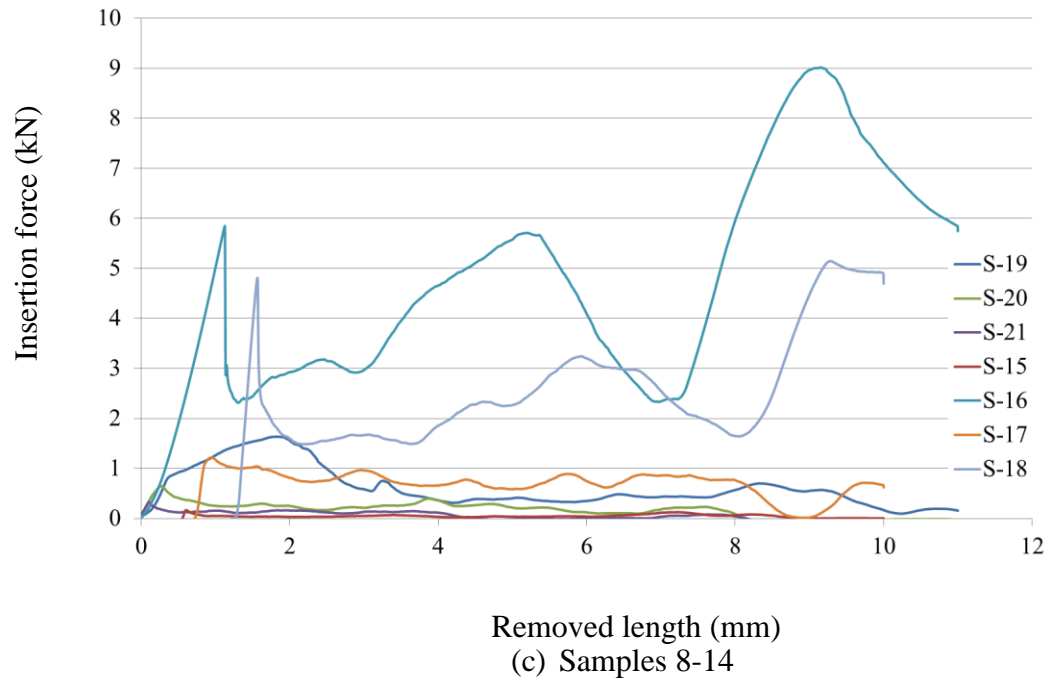
**C-3 The pull-out test results**



(a) Samples 1-7



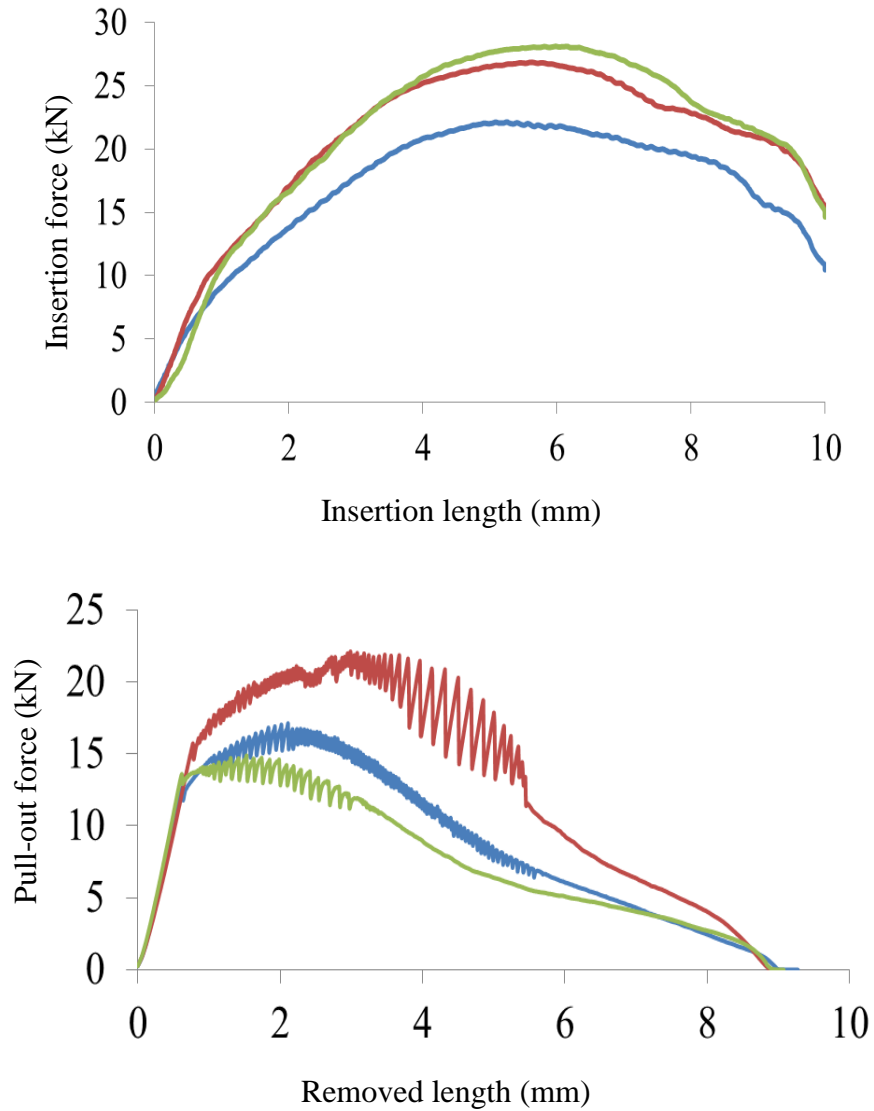
(b) Samples 8-14



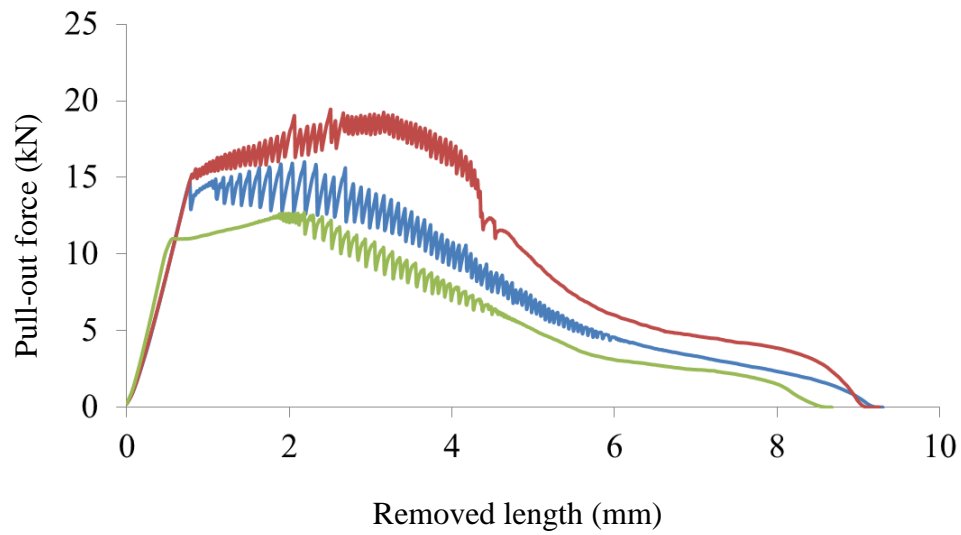
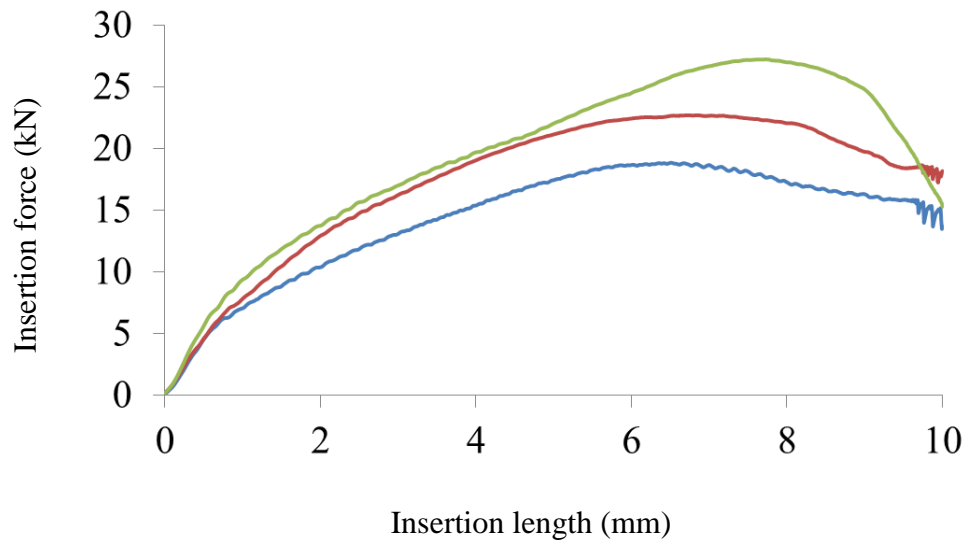
**Figure C-4** The pull-out force plots for the full set of samples in the DoE.

#### C-4 Commercial pins

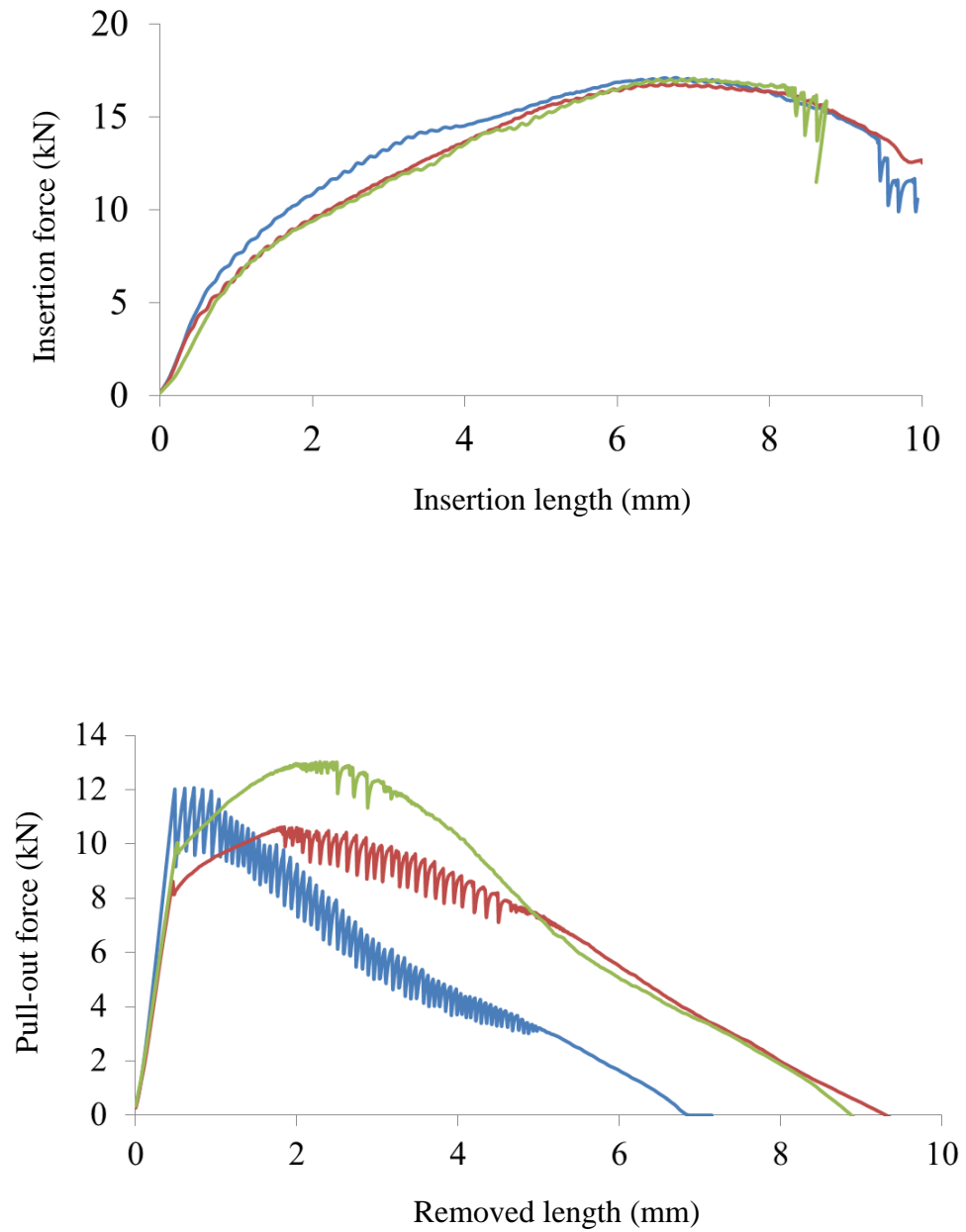
Insertion and pull-out forces plots:



**Figure C-5** Shows the insertion and pull-out forces for the 10 mm diameter Commercial pin samples inserted in 9.75 mm diameter hole rings.



**Figure C-6** Shows the insertion and pull-out forces for the 10 mm diameter Commercial pin samples inserted in 9.90 mm diameter hole rings.



**Figure C-7** Shows the insertion and pull-out forces for the 10 mm diameter Commercial pin samples inserted in 9.95 mm diameter hole rings.

From these figures, it is clear that the commercial samples require less insertion force compared to the textured samples due to the reduction in the friction as the sample surface is much smoother. Also, the rougher plot lines, especially after the failure point in the case of the removal test indicate the fast sliding of the insertion during the removal. Moreover, this is an indication of the elastic-plastic deformation in the hub and the re-gripping periodically. A diametric plastic deformation of ~100 micron was noted on the rings with hole diameter of 9.95 and 9.99 mm and 200 micron on the 9.75 mm hole diameter. This result means that these insertions are not feasible when the need for a scheduled disassembly and maintenance is essential taking in account that the hub represents the actuator and cannot be replaced or plastically deformed. The novelty of the laser texturing technique offers insertions that plastically deform, maintain good grip and cause no damage or deformation in the mechanical part.



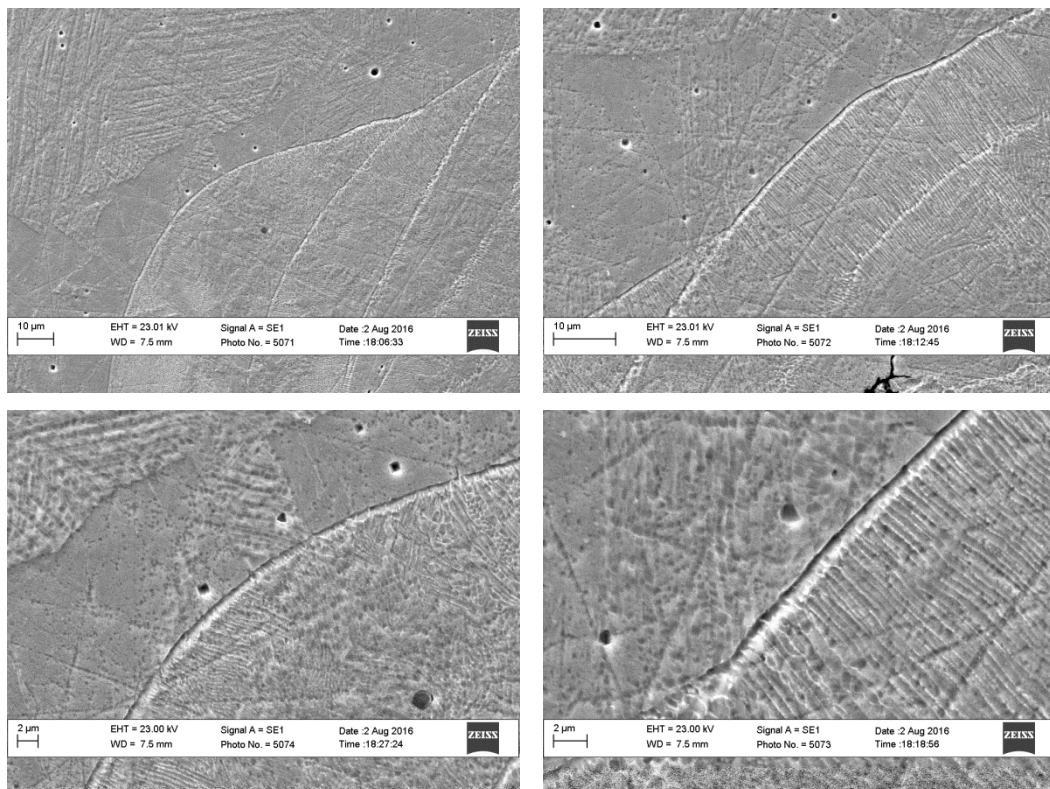
## Appendix D

### D-1 Chemical etchant:



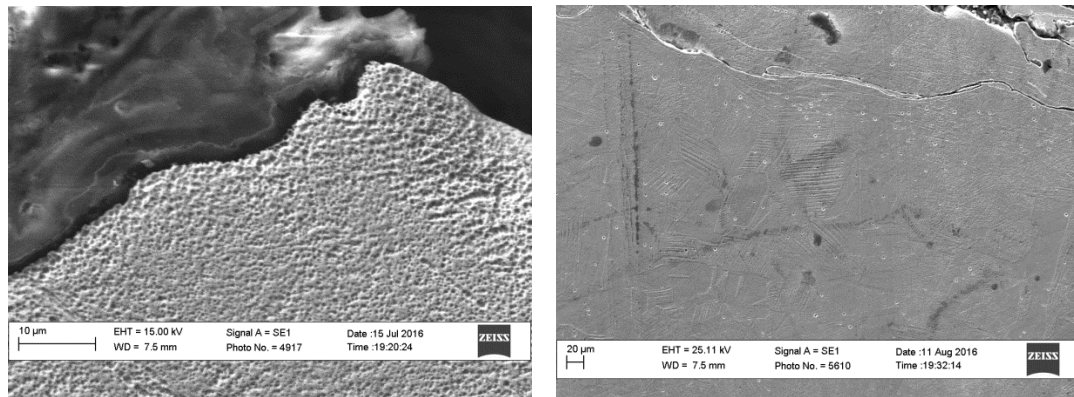
**Figure D-1** Glyceregia, Adlers and natal chemical etchants used during the metallographic study to investigate the modified layer depth and the new microstructure and phase change.

### D-2 SEM micrographs:



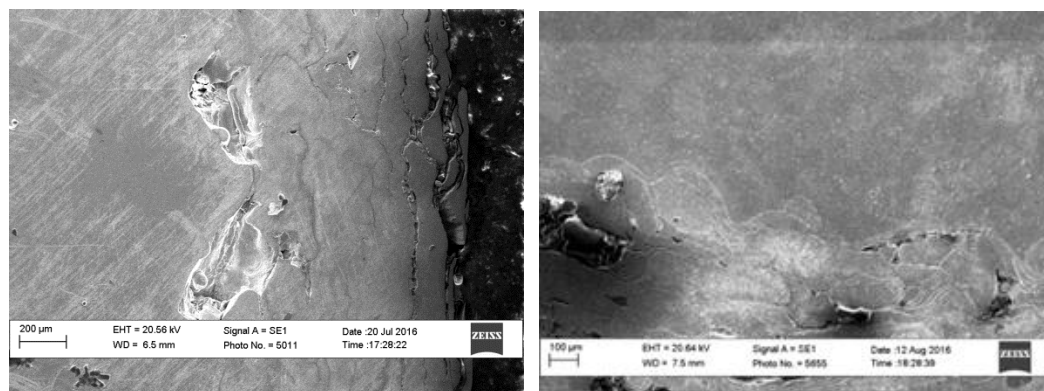
**Figure D-2** Sample-9

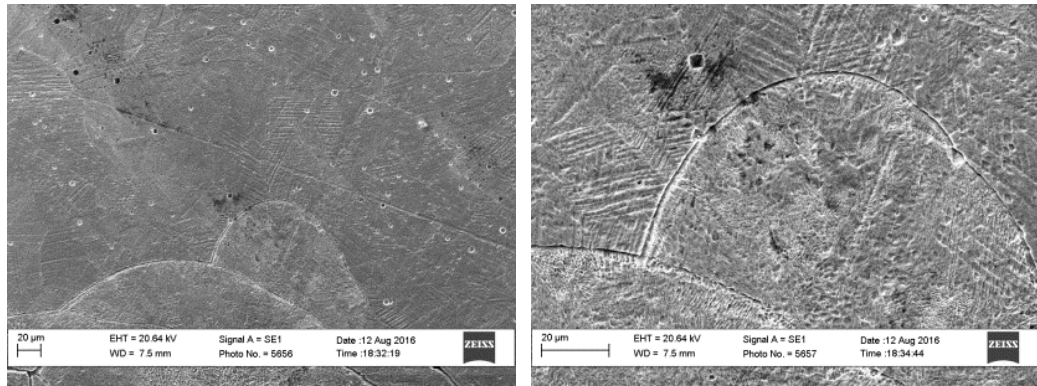
Stainless steels in general are very high corrosion resistant alloys and very difficult to be etched and extra strong etchant must be used. A very severe pitting was observed on some samples as shown in the following figure (left) for sample no. 11. This was avoided by increasing the HCl concentration in the glyceric acid reagent, see the following figure (right).



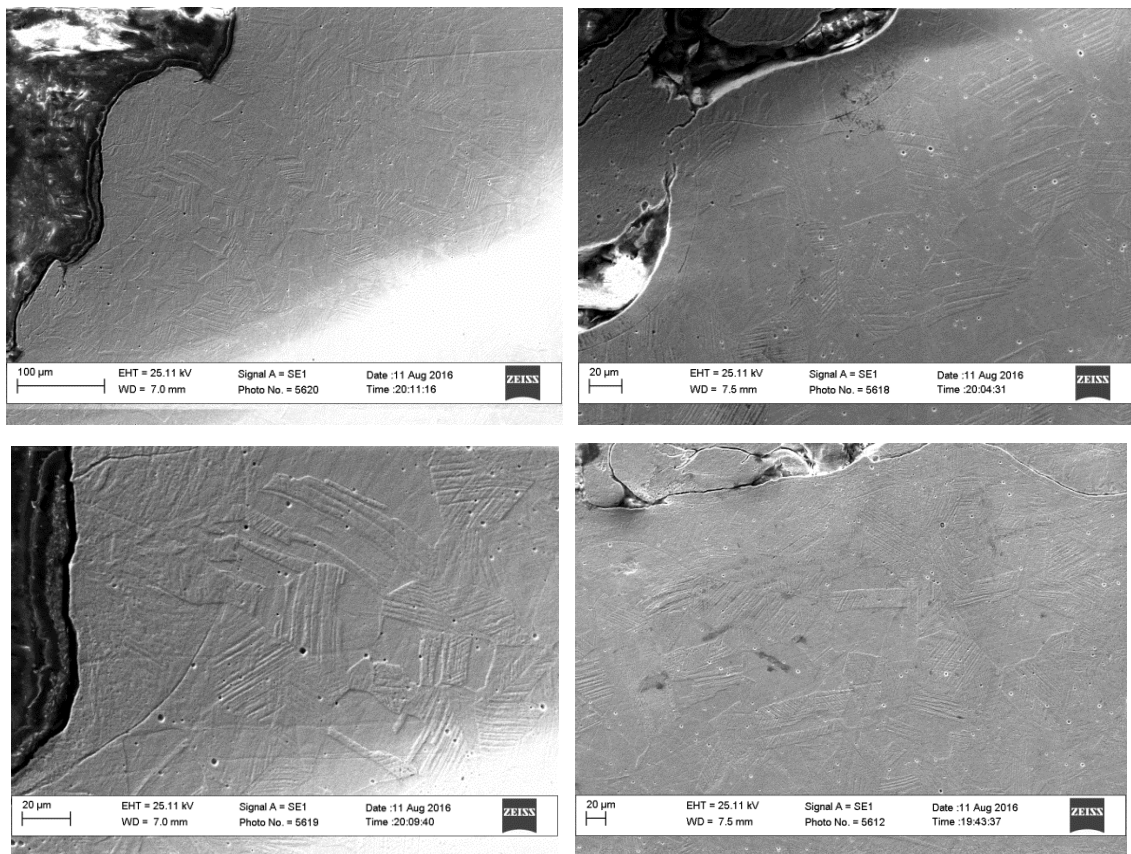
**Figure D-3** Shows the pitting due to strong glyceric acid etchant.

The following figure shows SEM micrographs for samples no. 12. The figure reveals the interfering modified layer after melting and re-solidification. This can be explained by the consecutive pulses in conjunction with the helical movement of the laser beam on the metal surface.

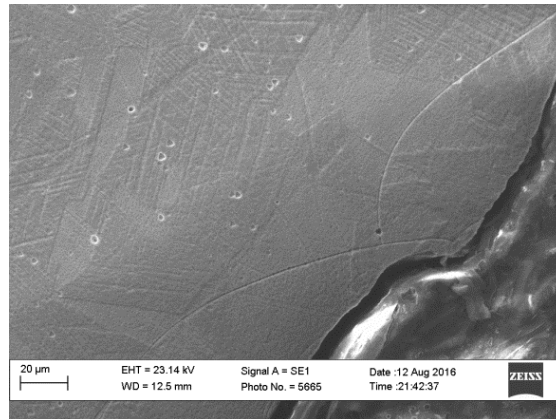




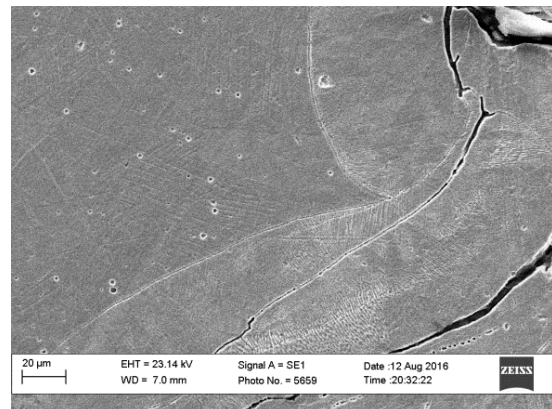
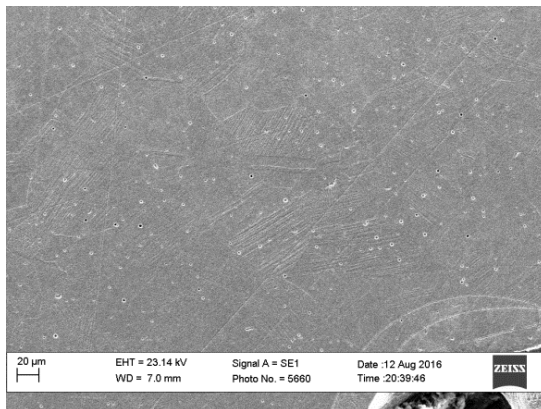
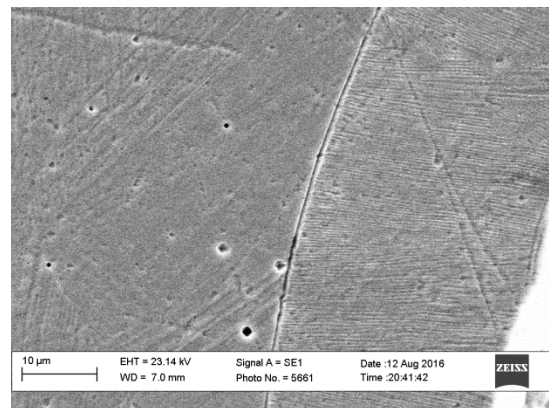
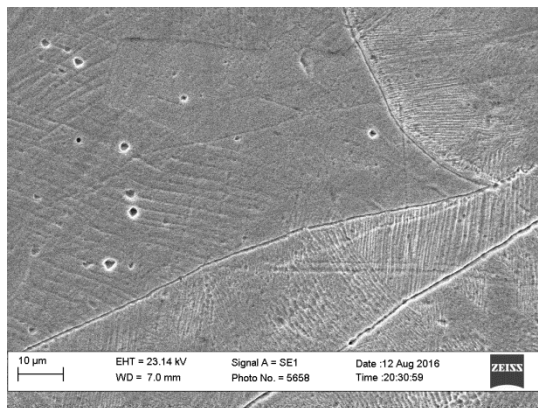
**Figure D-4** Shows the interfering melted layers and the interface with the bulk material



**Sample 11**



**Sample 22**



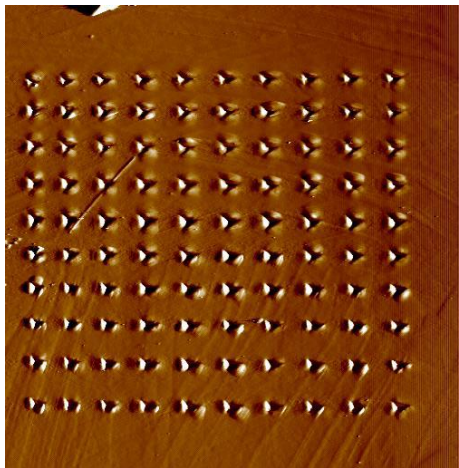
**Sample 26**



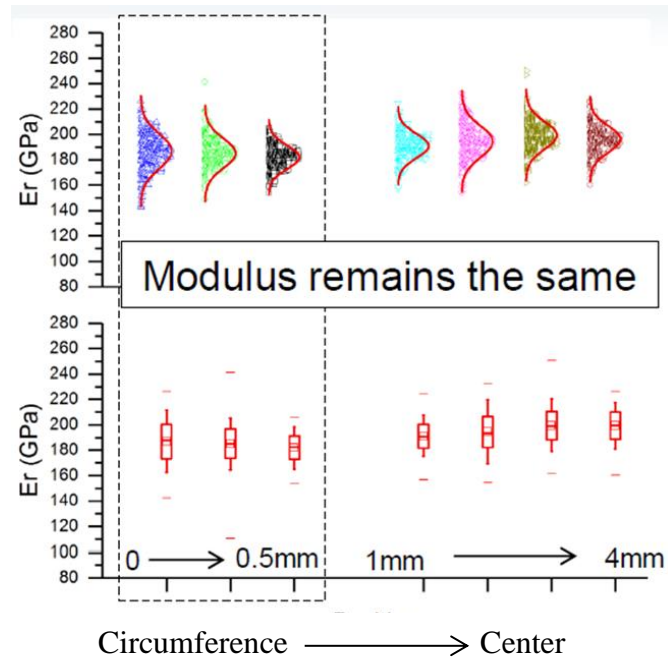
## Appendix E

### E-1 Elastic modulus test

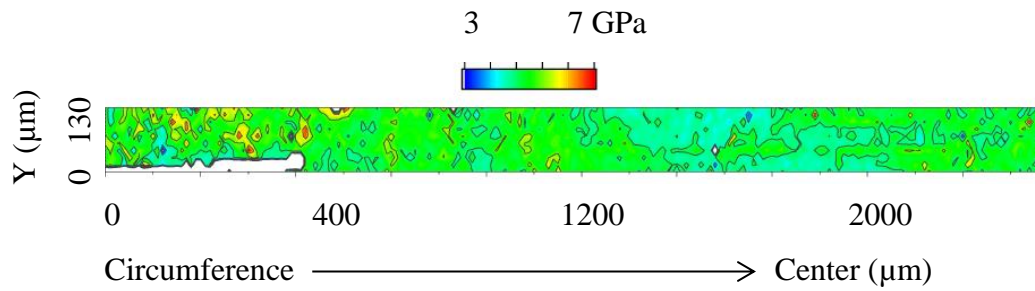
Figure E-1 below shows the elastic modulus investigation was also carried out at Bruker nano surfaces division, Czech Republic, for confirmation. Figure (a) shows the indentations array designed for  $10 \times 10$  indents with  $15 \mu\text{m}$  spacing, one array at the centre and another array near the surface. The test shows no change in the elastic modulus, Figure (b) and a small enhancement in the hardness, Figure (c) near the surface compared to the bulk material. These results agree well with the results obtained by the MSSi, Limerick University, which is detailed in section 5.15.



(a) The indentations array used during the elastic modulus and surface hardness investigations.



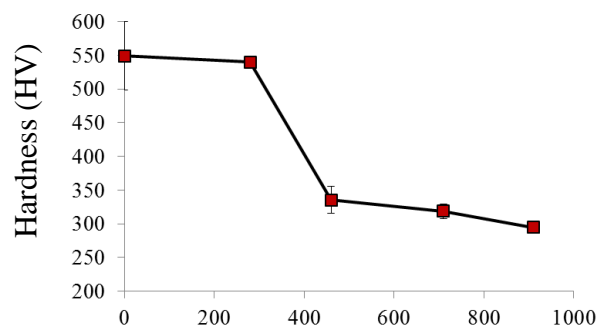
(b) The elastic modulus test results.



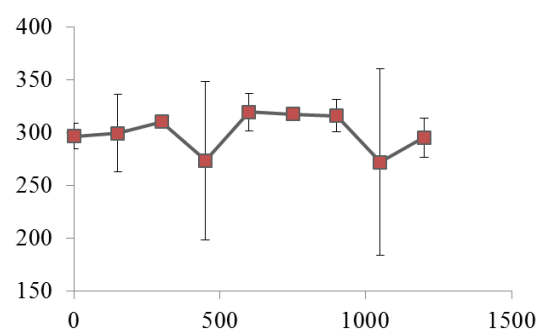
(c) The surface hardness test results.

**Figure E-1** The elastic modulus and surface hardness for sample no. 9 obtained by using the nano-indentation analysis.

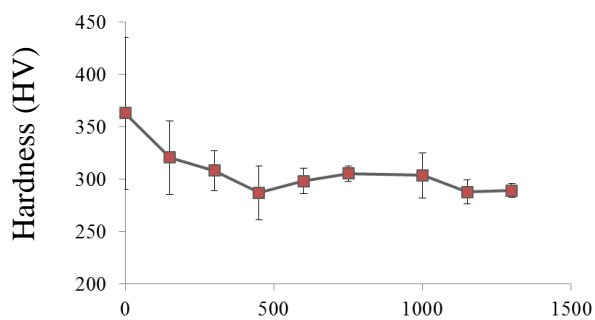
## E-2 Surface hardness of the nitride samples



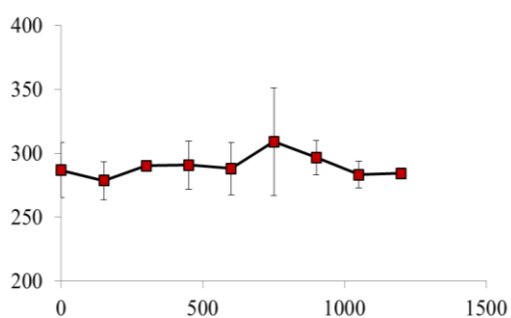
S-3



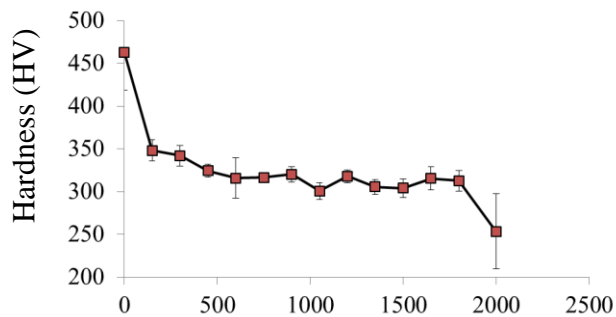
S-5



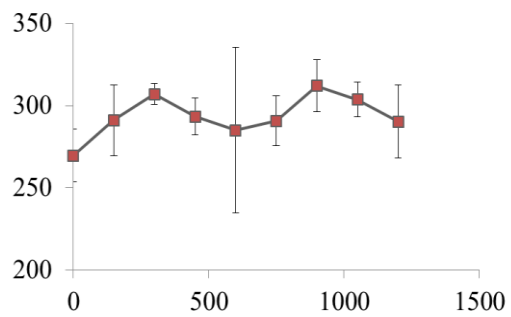
S-6



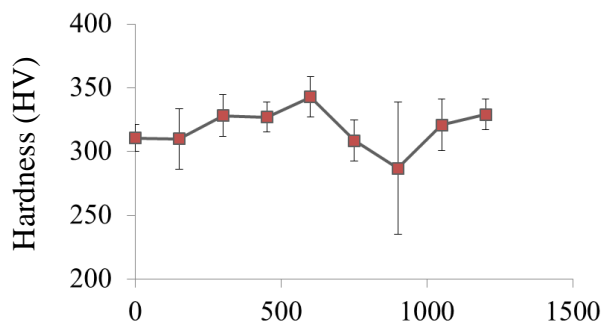
S-8



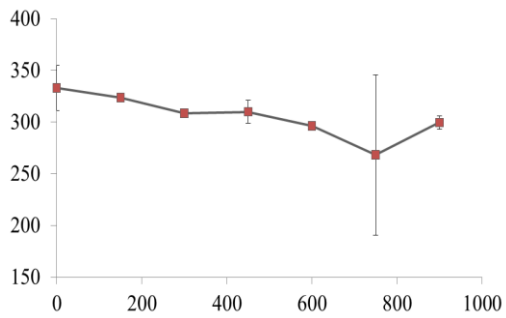
S-9



S-10

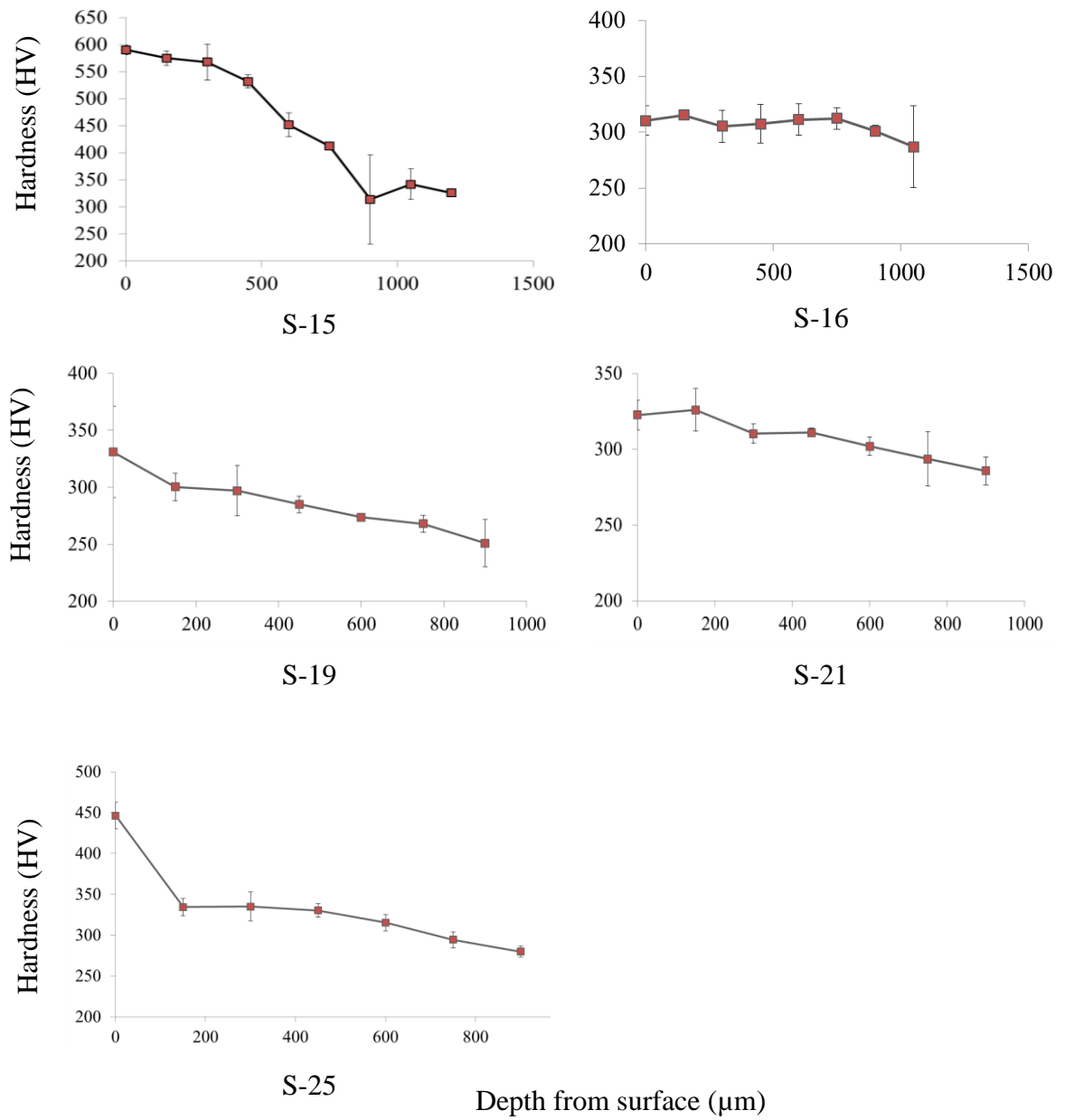


S-13



S-14

Depth from surface (μm)



**Figure D-5** The measured surface hardness for the 316L SST samples processed in 20% argon-80% nitrogen atmosphere.